JACC
Basic to Translational Science

A Journal of the American College of Cardiology

EDITORIAL BOARD

EDITOR-IN-CHIEF	**Douglas L. Mann, MD,** St. Louis, MO	
DEPUTY EDITOR	**L. Kristin Newby, MD,** Durham, NC	
ASSOCIATE EDITORS	**Brian H. Annex, MD,** Charlottesville, VA **Nanette H. Bishopric, MD,** Miami, FL **Daniel P. Kelly, MD,** Philadelphia, PA **William Robb MacLellan, MD,** Seattle, WA	**Peter Libby, MD,** Boston, MA **Geoffrey Pitt, ScM, MD, PhD,** Cornell, NY **Eva van Rooij, PhD,** Utrecht, the Netherlands
GUEST EDITOR-IN-CHIEF	**Robert Roberts, MD,** Tucson, AZ	
GUEST EDITOR	**Juan F. Granada, MD,** Orangeburg, NY	
STATISTICAL EDITOR	**Cindy Green, PhD,** Durham, NC	
VICE PRESIDENT, PUBLISHING	**Kimberly Murphy,** Washington, DC	
EXECUTIVE MANAGING EDITOR	**Monica R. Payne-Emmerson,** Washington, DC	
MANAGING EDITOR	**Kimberly Trevey,** Washington, DC	
EDITORIAL ASSISTANT	**Jennifer Rapp,** Washington, DC	
DIRECTOR, PRODUCT MANAGEMENT, DIGITAL PUBLISHING	**Nandhini Kuntipuram,** Washington, DC	
SOCIAL MEDIA EDITORS	**Reza Ardehali, MD, PhD,** Los Angeles, CA	**Meena S. Madhur, MD, PhD,** Nashville, TN
CME EDITORS	**Amanda Coniglio, MD,** Durham, NC	**Michelle Kelsey, MD,** Durham, NC **Vishal Rao, MD,** Durham, NC
ETHICS COMMITTEE	**Holly Atkinson, MD,** New York, NY **Lawrence S. Cohen, MD,** New Haven, CT **Kim Fox, MD,** London, UK **Robert Frye, MD,** Rochester, MN	**Philip J. Landrigan, MD,** New York, NY **Richard L. Popp, MD,** Palo Alto, CA **Eric Prystowsky, MD,** Indianapolis, IN **James Willerson, MD,** Houston, TX
EDITOR-IN-CHIEF, *JACC*	**Valentin Fuster, MD, PhD,** New York, NY	
EDITOR-IN-CHIEF, *JACC: CARDIOVASCULAR IMAGING*	**Y. Chandrashekhar, MD,** Minneapolis, MN	
EDITOR-IN-CHIEF, *JACC: CARDIOVASCULAR INTERVENTIONS*	**David J. Moliterno, MD,** Lexington, KY	
EDITOR-IN-CHIEF, *JACC: HEART FAILURE*	**Christopher M. O'Connor, MD,** Falls Church, VA	

EDITOR-IN-CHIEF, *JACC: CLINICAL ELECTROPHYSIOLOGY*	**David J. Wilber, MD,** Chicago, IL
EDITOR-IN-CHIEF, *JACC: CASE REPORTS*	**Julia Grapsa, MD, PhD,** London, UK
EDITOR-IN-CHIEF, *JACC: CARDIOONCOLOGY*	**Bonnie Ky, MD, MSCE,** Philadelphia, PA

EDITORIAL CONSULTANTS

Mark Anderson, MD, PhD, Baltimore, MD

Themistocles Assimes, MD, PhD, Palo Alto, CA

Noel Bairey-Merz, MD, Los Angeles, CA

Craig Basson, MD, Needham, MA

Jeffery Berger, MD, New York, NY

Don Bers, PhD, Davis, CA

Michael Bristow, MD, PhD, Aurora, CO

Daniel Burkoff, MD, PhD, Framingham, MA

John Burnett, MD, Rochester, MN

John Canty, MD, Buffalo, NY

Barbara Casadei, MD, Oxford, UK

Karen Christman, PhD, San Diego, CA

Peter Crawford, MD, PhD, Orlando, FL

Craig Emter, PhD, Columbia, MO

Zahi Fayad, PhD, New York, NY

Glenn Fishman, MD, New York, NY

Peter Ganz, MD, San Francisco, CA

Roberta Gottlieb, MD, Los Angeles, CA

Josh Hare, MD, Miami, FL

Ray Hershberger, MD, Columbus, OH

Carolyn Ho, MD, Boston, MA

Jennifer Ho, MD, Boston, MA

Farouc Jaffer, MD, PhD, Boston, MA

Tim Kamp, MD, PhD, Madison, WI

Walter Koch, PhD, Philadelphia, PA

David Lanfear, MD, Detroit, MI

Jin-Moo Lee, MD, St. Louis, MO

Richard Lee, MD, Boston, MA

Jonathan Lindner, MD, Portland, OR

Peter Liu, MD, Ottawa, Ontario, Canada

Eduardo Marban, MD, PhD, Los Angeles, CA

Ali Marian, MD, Houston, TX

Kenneth Margulies, MD, Philadelphia, PA

Peter McCullough, MD, MPH, Dallas, TX

Timothy Mckinsey, MD, Denver, CO

Javid Moslehi, MD, Nashville, TN

Jorge Plutzky, MD, Boston, MA

David Port, PhD, Aurora, CO

Sumanth Prabhu, MD, Birmingham, AL

Hani Sabbath, PhD, Detroit, MI

Paul Simpson, MD, San Francisco, CA

Mark Sussman, PhD, San Diego, CA

Jenny Van Eyk, PhD, Los Angeles, CA

Richard Vega, MD, Orlando, FL

Xander Wehrens, MD, PhD, Houston, TX

Arthur Wilde, MD, PhD, Amsterdam, the Netherlands

Myles Wolf, MD, MMSc, Chicago, IL

Sean Wu, MD, PhD, Stanford, CA

JACC
Basic to Translational Science

A Journal of the American College of Cardiology

2019-2020 OFFICERS

Richard J. Kovacs, MD, FACC, President

Athena Poppas, MD, FACC, Vice President

Howard "Bo" T. Walpole, Jr., MD, MBA, FACC, Treasurer

Akshay Khandelwal, MD, FACC, Secretary and Board of Governors Chair

Timothy W. Attebery, DSc, MBA, FACHE, Chief Executive Officer

2019-2020 PUBLICATIONS AND EDITORIAL COORDINATION COMMITTEE

Viviany R. Taqueti, MD, MPH, FACC, Chair

Rhonda M. Cooper-DeHoff, MD, FACC, Annual Scientific Session Program Committee

Prasad C. Gunasekaran, MD FIT Representative

Fadi G. Hage, MD, FACC

Fred M. Kusumoto, MD, FACC, Awards Committee

Renato D. Lopes, MD, PhD, FACC

Sandra M. Oliver-McNeil, DNP, ACNP-BC, AACC Committee

James E. Tcheng, MD, FACC, (Ex Officio) Chair, Digital Steering Committee

William J. Oetgen, MD, MBA, FACC, FACP, ACC Executive Vice President - Science & Quality, Education and Publications

Kimberly Murphy, ACC Division Vice President, Publishing

CORRESPONDENCE FOR AMERICAN COLLEGE OF CARDIOLOGY

All correspondence for the College, other than that related to *JACC: Basic to Translational Science* should be sent to Resource Center, American College of Cardiology, 2400 N Street, NW, Washington, DC 20037

JACC: BASIC TO TRANSLATIONAL SCIENCE VOL. 4, NO. 2, 2019
© 2019 THE AUTHORS. PUBLISHED BY ELSEVIER ON BEHALF OF THE AMERICAN COLLEGE OF CARDIOLOGY FOUNDATION. THIS IS AN OPEN ACCESS ARTICLE UNDER THE CC BY-NC-ND LICENSE (http://creativecommons.org/licenses/by-nc-nd/4.0/).

LEADING EDGE IN TRANSLATIONAL RESEARCH

Celecoxib Is Associated With Dystrophic Calcification and Aortic Valve Stenosis

Meghan A. Bowler, PhD,[a,*] Michael A. Raddatz, BS,[a,*] Camryn L. Johnson, BS,[a] Brian R. Lindman, MD, MSc,[b] W. David Merryman, PhD[a]

JACC: BASIC TO TRANSLATIONAL SCIENCE CME/MOC/ECME

This article has been selected as this month's *JACC: Basic to Translational Science* CME/MOC/ECME activity, available online at http://www.acc.org/jacc-journals-cme by selecting the *JACC* Journals CME/MOC/ECME tab.

Accreditation and Designation Statement

The American College of Cardiology Foundation (ACCF) is accredited by the Accreditation Council for Continuing Medical Education (ACCME) and the European Board for Accreditation in Cardiology (EBAC) to provide continuing medical education for physicians.

The ACCF designates this Journal-based CME/MOC/ECME activity for a maximum of 1 AMAPRA Category 1 Credit or 1 EBAC Credit. Physicians should only claim credit commensurate with the extent of their participation in the activity.

Successful completion of this CME activity, which includes participation in the evaluation component, enables the participant to earn up to 1 Medical Knowledge MOC point in the American Board of Internal Medicine's (ABIM) Maintenance of Certification (MOC) program. Participants will earn MOC points equivalent to the amount of CME credits claimed for the activity. It is the CME activity provider's responsibility to submit participant completion information to ACCME for the purpose of granting ABIM MOC credit.

Celecoxib Is Associated With Dystrophic Calcification and Aortic Valve Stenosis will be accredited by the European Board for Accreditation in Cardiology (EBAC) for 1 hour of External CME credits. Each participant should claim only those hours of credit that have actually been spent in the educational activity. The Accreditation Council for Continuing Medical Education (ACCME) and the European Board for Accreditation in Cardiology (EBAC) have recognized each other's accreditation systems as substantially equivalent. Apply for credit through the post-course evaluation.

Method of Participation and Receipt of CME/MOC/ECME Certificate

To obtain credit for JACBTS: Basic to Translational Science CME/MOC/ECME, you must:

1. Be an ACC member or JACBTS subscriber.
2. Carefully read the CME/MOC/ECME-designated article available online and in this issue of the *journal*.
3. Answer the post-test questions. At least 2 questions provided must be answered correctly to obtain credit.
4. Complete a brief evaluation.
5. Claim your CME/MOC/ECME credit and receive your certificate electronically by following the instructions given at the conclusion of the activity.

CME/MOC/ECME Objective for This Article: Upon completion of this activity, the learner should be able to: 1) list the criteria for diagnosing severe aortic stenosis by echocardiography; 2) recognize the potential limitations of echocardiography for measuring the degree of aortic stenosis; and 3) describe current treatment options for severe aortic stenosis.

CME/MOC/ECME Editor Disclosure: CME/MOC/ECME Editor L. Kristin Newby, MD, is supported by research grants from Amylin, Bristol-Myers Squibb Company, GlaxoSmithKline, Sanofi, Verily Life Sciences (formerly Google Life Sciences), the MURDOCK Study, NIH, and PCORI; receives consultant fees/honoraria from BioKier, DemeRx, MedScape/TheHeart.org, Metanomics, Philips Healthcare, Roche Diagnostics, CMAC Health Education & Research Institute; serves as an Officer, Director, Trustee, or other fiduciary role for the AstraZeneca HealthCare Foundation and the Society of Chest Pain Centers (now part of ACC); and serves in another role for the American Heart Association and is the Deputy Editor of *JACC: Basic to Translational Science*.

Author Disclosures: This work was funded by NIH grants HL135790, HL115103, and GM007347, American Heart Association grant 18PRE34070125, and NSF grants 1055384 and 2013170175. The datasets used for the analyses described were obtained from Vanderbilt University Medical Center's BioVU, which is supported by numerous sources: institutional funding, private agencies, and federal grants. These include the NIH-funded Shared Instrumentation grant S10RR025141, and CTSA grants UL1TR002243, UL1TR000445, and UL1RR024975. The clinical datasets used for the analyses described were obtained from Vanderbilt University Medical Center's Synthetic Derivative. Dr. Lindman has received research grants from Edwards Lifesciences and Roche Diagnostics; served on scientific advisory boards for Roche Diagnostics; and has been a consultant to Medtronic and Roche Diagnostics. All other authors have reported that they have no relationships relevant to the contents of this paper to disclose.

Medium of Participation: Online (article and quiz).

CME/MOC/ECME Term of Approval

Issue Date: April 2019
Expiration Date: March 31, 2020

ISSN 2452-302X https://doi.org/10.1016/j.jacbts.2018.12.003

JACC: BASIC TO TRANSLATIONAL SCIENCE VOL. 4, NO. 2, 2019
APRIL 2019:135–43

Celecoxib Is Associated With Dystrophic Calcification and Aortic Valve Stenosis

Meghan A. Bowler, PhD,[a,*] Michael A. Raddatz, BS,[a,*] Camryn L. Johnson, BS,[a] Brian R. Lindman, MD, MSc,[b] W. David Merryman, PhD[a]

VISUAL ABSTRACT

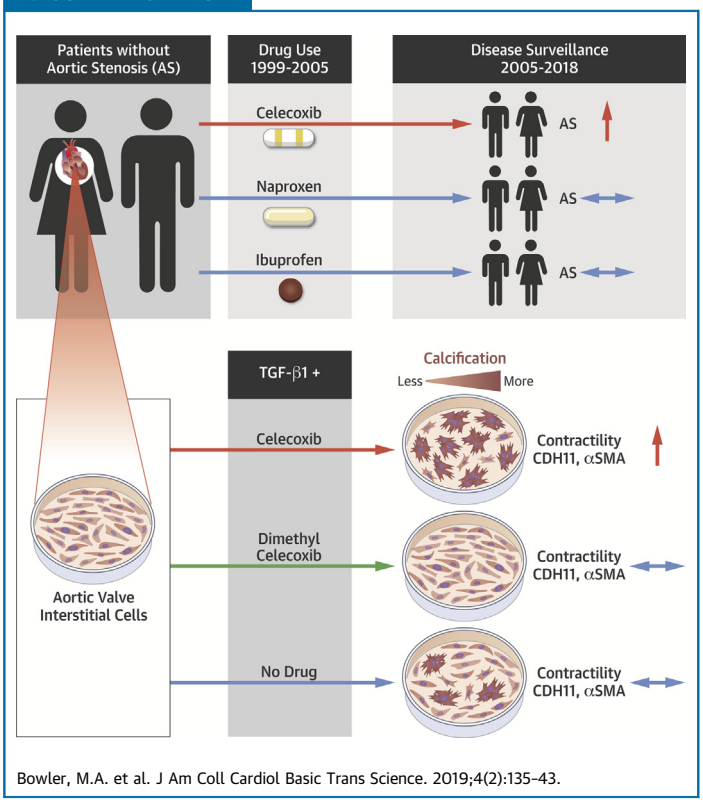

Bowler, M.A. et al. J Am Coll Cardiol Basic Trans Science. 2019;4(2):135–43.

HIGHLIGHTS

- **Celecoxib use is associated with diagnosis of aortic stenosis in analysis of electronic medical records.**
- **Celecoxib treatment increases dystrophic calcification of aortic valve interstitial cells in vitro.**
- **Dimethyl celecoxib, which binds CDH11, prevents TGF-β1–mediated calcification of aortic valve interstitial cells in vitro.**

From the [a]Department of Biomedical Engineering, Vanderbilt University, Nashville, Tennessee; and the [b]Structural Heart and Valve Center, Vanderbilt University Medical Center, Nashville, Tennessee. *Dr. Bowler and Mr. Raddatz contributed equally to this work, and are joint first authors. This content is solely the responsibility of the authors and does not necessarily represent the official views of the National Institutes of Health (NIH), the National Science Foundation (NSF), or Vanderbilt University. This work was funded by NIH grants HL135790, HL115103, and GM007347, American Heart Association grant 18PRE34070125, and NSF grants 1055384 and 2013170175. The datasets used for the analyses described were obtained from Vanderbilt University Medical Center's BioVU, which is supported by numerous sources: institutional funding, private agencies, and federal grants. These include the NIH-funded Shared Instrumentation grant S10RR025141, and CTSA grants UL1TR002243, UL1TR000445, and UL1RR024975. The clinical datasets used for the analyses described were obtained from Vanderbilt University Medical Center's Synthetic Derivative. Dr. Lindman has received research grants from Edwards Lifesciences and Roche Diagnostics; served on scientific advisory boards for Roche Diagnostics; and has been a consultant to Medtronic and Roche Diagnostics. All other authors have reported that they have no relationships relevant to the contents of this paper to disclose.

All authors attest they are in compliance with human studies committees and animal welfare regulations of the authors' institutions and Food and Drug Administration guidelines, including patient consent where appropriate. For more information, visit the *JACC: Basic to Translational Science* author instructions page.

Manuscript received November 13, 2018; revised manuscript received December 11, 2018, accepted December 12, 2018.

SUMMARY

Calcific aortic valve disease is a progressive fibrocalcific process that can only be treated with valve replacement. Cadherin-11 has recently been identified as a potential therapeutic target for calcific aortic valve disease. The already approved drug celecoxib, a cyclooxygenase-2 inhibitor, binds cadherin-11, and was investigated as a therapeutic against calcific aortic valve disease. Unexpectedly, celecoxib treatment led to hallmarks of myofibroblast activation and calcific nodule formation in vitro. Retrospective electronic medical record analysis of celecoxib, ibuprofen, and naproxen revealed a unique association of celecoxib use and aortic stenosis. (J Am Coll Cardiol Basic Trans Science 2019;4:135–43) © 2019 The Authors. Published by Elsevier on behalf of the American College of Cardiology Foundation. This is an open access article under the CC BY-NC-ND license (http://creativecommons.org/licenses/by-nc-nd/4.0/).

ABBREVIATIONS AND ACRONYMS

ANOVA = analysis of variance

AS = aortic stenosis

AVEC = aortic valve endothelial cell

AVIC = aortic valve interstitial cell

CAVD = calcific aortic valve disease

CDH11 = cadherin-11

CN = calcific nodule

COX2 = cyclooxygenase-2

EMR = electronic medical record

FDA = Food and Drug Administration

OR = odds ratio

SMA = smooth muscle actin

TGF = transforming growth factor

VUMC = Vanderbilt University Medical Center

More than 25% of the U.S. population over 65 years of age is affected by calcific aortic valve disease (CAVD) (1). This degenerative disease is the most common cause of aortic stenosis (AS), which eventually requires surgical replacement of the aortic valve because there are no effective pharmaceutical treatments. This lack of medical therapy is a result of our inadequate understanding of the disease mechanism (2). CAVD is believed to be mediated by aortic valve interstitial cells (AVICs), which become activated by transforming growth factor (TGF)-β1 into myofibroblasts (3), characterized by increased contractility, collagen deposition, and expression of α-smooth muscle actin (SMA) and cadherin-11 (CDH11). When these myofibroblasts are subjected to strain, as is normal in the cardiac valve environment, this causes membrane tearing, leading to apoptosis-mediated cell death. This process has been termed the dystrophic pathway of calcification and was evident in 83% of excised human aortic valves (whereas only 13% of those showed osteogenic markers) (4), making dystrophic calcification the most prevalent mechanism of CAVD.

We recently identified and validated CDH11 as a possible therapeutic target for CAVD (5–8). CDH11 is a mechanosensitive transmembrane cell adhesion protein known to have increased expression in calcified human aortic valves (7), to be increased in the AVICs of the *Notch1*$^{+/-}$ murine model of CAVD (5), and to be necessary for in vitro formation of the calcific nodules (CNs) characteristic of CAVD (7). Additionally, recent work has shown that blocking CDH11 with a monoclonal antibody in the *Notch1*$^{+/-}$ model prevents CAVD progression (6). These findings motivated us to evaluate current Food and Drug Administration (FDA)-approved drugs that may block CDH11 activity for CAVD, as the CDH11 antibody research program was recently halted by Roche after disappointing Phase II trials for rheumatoid arthritis. A review of the published reports revealed that celecoxib, brand name Celebrex (Pfizer, New York, New York), and its inactive analog, dimethyl celecoxib, bind CDH11 with high affinity (9). We therefore hypothesized that either of these drugs may prevent CAVD by blocking the homotypic CDH11 bonds between neighboring cells.

To evaluate this hypothesis, we treated porcine AVICs and aortic valve endothelial cells (AVECs) with celecoxib or dimethyl celecoxib. Cells were also treated with TGF-β1 to biochemically induce myofibroblast differentiation. Cells were then subjected to well-established functional assays of CAVD such as CN formation (5,7,10–12) and collagen gel contraction, as well as evaluated for expression of myofibroblast markers α-SMA and CDH11. To assess clinical relevance, we performed a retrospective analysis of celecoxib use and AS incidence in the electronic medical record (EMR) from Vanderbilt University Medical Center (VUMC).

SEE PAGE 144

METHODS

IN VITRO EXPERIMENTS AND STATISTICAL ANALYSIS. Porcine aortic valve cells were isolated as previously described (7,13) and used between passages 3 and 11. Cells were evaluated with a combination of molecular and functional assays in order to understand the role of treatment with celecoxib, dimethyl celecoxib, and TGF-β1 in their propensity to calcify; details of the following in vitro assays are in the Supplemental Appendix. The nodule assay allows for rapid screening of potential drug strategies that may prevent dystrophic calcification in vitro (5,7,12). Briefly, cells were plated onto pronectin (AVICs) or collagen IV (AVECs) Flexcell plates (Flexcell International, Burlington, North Carolina), then treated with TGF-β1, and subsequently strained at 15% using the Flexcell Tension system, as previously described

FIGURE 1 Dimethyl Celecoxib Prevents CN Formation in AVICs but Celecoxib Promotes CN Formation Through Myofibroblast Induction

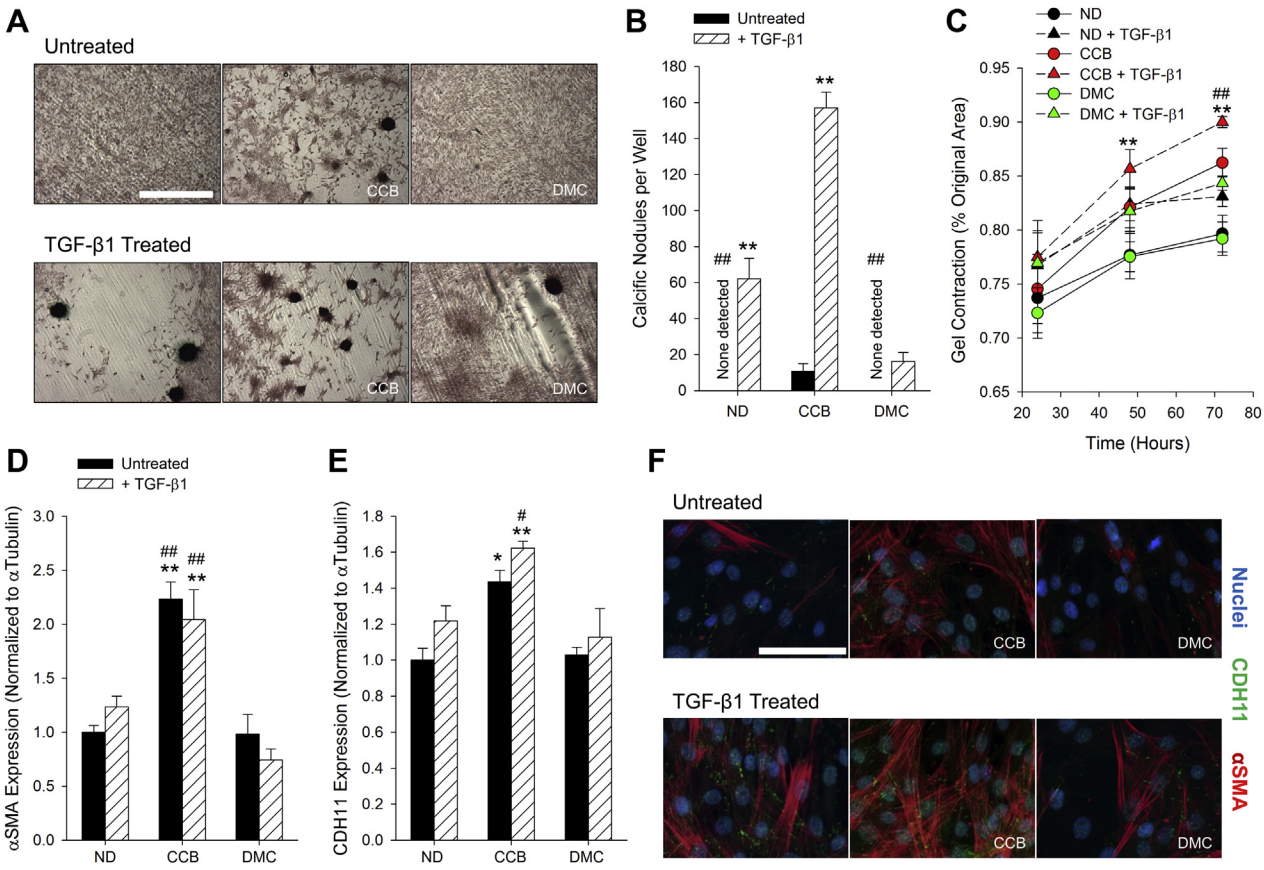

(A) Cyclic biaxial strain and TGF-β1 induce CN formation, identified by Alizarin Red staining. **(B)** Treatment with celecoxib increases the number of CNs formed in the untreated and TGF-β1–treated cases. Dimethyl celecoxib treatment reduces the number of TGF-β1–induced CNs. **(C)** TGF-β1 treatment increases contractility. Celecoxib pre-treatment also increases contractility to the level of ND + TGF-β1. Treatment with celecoxib increases expression of α-SMA **(D and F)** and CDH11 **(E and F)**. n ≥ 3. *p < 0.05 versus ND, #p < 0.05 versus ND + TGF-β1, **p < 0.001 versus same pre-treatment, ##p < 0.001 versus ND + TGF-β1. Scale bars indicate 1 mm **(A)** and 100 μm **(F)**. AVIC = aortic valve interstitial cell; CCB = celecoxib; CN = calcific nodule; DMC = dimethyl celecoxib; ND = no drug; TGF = transforming growth factor.

(10,11). In a separate cohort, AVICs were treated with conditioned medium harvested from AVEC cultures after strain. AVICs were also evaluated for contractility using a free-floating collagen gel system in which cells were plated onto gels and imaged over time to quantify the gel area. Western blots and immunofluorescence were used to evaluate expression of myofibroblast markers CDH11 and α-SMA after various treatments. In all cases, cells were plated simultaneously with celecoxib (Tocris 3786, Tocris Bioscience, Bristol, United Kingdom), dimethyl celecoxib (Sigma-Aldrich D7196, Sigma-Aldrich, St. Louis, Missouri), or no drug to allow for interactions with CDH11 before homotypic bonds were formed. 10 μmol/l celecoxib and dimethyl celecoxib was chosen to match the plasma concentration found after typical doses of celecoxib in humans (9). For all experiments, n ≥ 3; more detailed methodology can be found in the Supplemental Appendix. All groups were compared with analysis of variance (ANOVA) in SigmaPlot software version 11.0 (Systat Software, San Jose, California), and a p value <0.05 was considered significant. Normality (Shapiro-Wilk) and equal variance were tested. Normal datasets with equal variance were analyzed via 1-way ANOVA with pairwise multiple comparisons made using the Holm-Sidak post hoc testing method. Non-normal datasets were analyzed via Kruskal-Wallis 1-way ANOVA on ranks with pairwise multiple comparisons made using Dunn's post hoc testing method. In vitro data are presented as mean ± SEM.

CLINICAL DATA AND STATISTICAL ANALYSIS. AS patients 60 to 89 years of age on January 27, 2018,

FIGURE 2 Retrospective Cohort Study Design

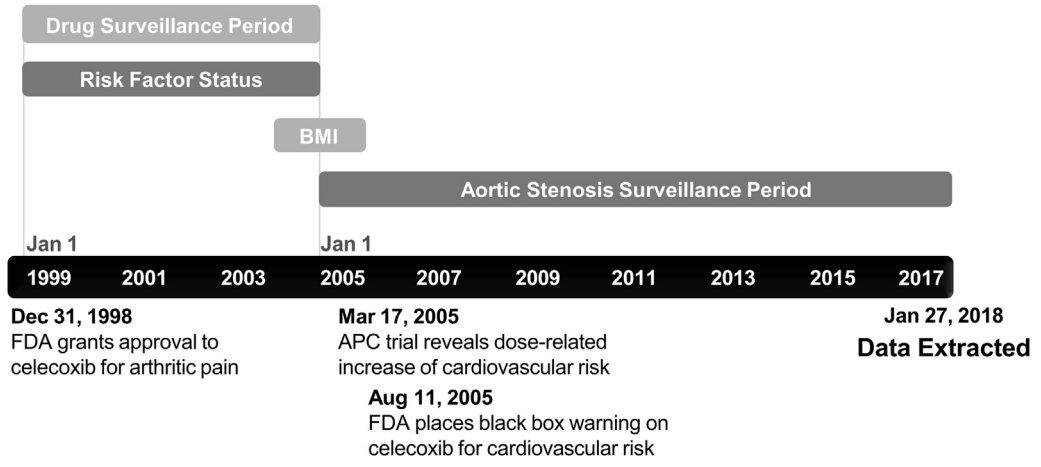

The retrospective clinical analysis described here was designed based on the approval and clinical trial history of celecoxib. Celecoxib was approved on December 31, 1998, and clinical trial results revealed a potential cardiovascular risk in early 2005, defining our drug surveillance period. Body mass index (BMI) data were collected within 1 year of January 1, 2005. The aortic stenosis surveillance period extended from January 1, 2005, to January 27, 2018. APC = Adenoma Prevention With Celecoxib; FDA = Food and Drug Administration.

were identified using the Synthetic Derivative, a de-identified version of VUMC's EMR containing >2.5 million unique records. Date gating and clinical covariates were identified a priori on the basis of celecoxib's approval history and known risk factors for AS, respectively. Ibuprofen and naproxen were chosen for comparison due to their similar indications and pattern of use (14,15), and their previous use

TABLE 1 Celecoxib Use Is Associated With AS

	Cases	Controls	Unadjusted OR (95% CI)	Unadjusted p Value	Adjusted OR (95% CI)	Adjusted p Value
Celecoxib	(n = 574)	(n = 6,397)				
Male	57.49 (330)	43.71 (2,796)	1.73 (1.46-2.06)	<0.001	1.70 (1.43-2.03)	<0.001
Age, yrs	76.70 ± 4.80	72.89 ± 7.91	1.06 (1.05-1.07)	<0.001	1.06 (1.05-1.07)	<0.001
BMI, kg/m^2	30.67 ± 6.94	28.04 ± 6.05	1.02 (1.01-1.03)	0.002	1.02 (1.01-1.03)	0.003
Hypertension	54.88 (315)	40.24 (2,574)	1.81 (1.52-2.14)	<0.001	1.42 (1.19-1.70)	<0.001
Type 2 diabetes	24.74 (142)	15.85 (1,014)	1.75 (1.43-2.13)	<0.001	1.35 (1.09-1.67)	0.006
Celecoxib use	23.34 (134)	18.21 (1,165)	1.36 (1.11-1.67)	0.003	1.24 (1.00-1.53)	0.046
Ibuprofen	(n = 427)	(n = 4,724)				
Male	57.14 (244)	44.86 (2,119)	1.64 (1.34-2.00)	<0.001	1.59 (1.30-1.95)	<0.001
Age, yrs	76.86 ± 7.82	73.15 ± 7.87	1.06 (1.05-1.07)	<0.001	1.06 (1.05-1.07)	<0.001
BMI, kg/m^2	30.83 ± 6.89	29.93 ± 6.94	1.02 (1.00-1.03)	0.011	1.02 (1.01-1.04)	0.006
Hypertension	54.33 (232)	40.60 (1,918)	1.74 (1.43-2.12)	<0.001	1.40 (1.13-1.72)	0.002
Type 2 diabetes	25.76 (110)	16.49 (779)	1.76 (1.40-2.21)	<0.001	1.38 (1.08-1.77)	0.010
Ibuprofen use	26.46 (113)	30.25 (1,429)	0.83 (0.66-1.04)	0.102	0.98 (0.78-1.23)	0.852
Naproxen	(n = 509)	(n = 5,342)				
Male	57.37 (292)	45.17 (2,413)	1.63 (1.36-1.96)	<0.001	1.55 (1.29-1.87)	<0.001
Age, yrs	76.50 ± 7.86	73.07 ± 7.88	1.06 (1.04-1.07)	<0.001	1.05 (1.04-1.07)	<0.001
BMI, kg/m^2	30.58 ± 6.81	29.83 ± 6.96	1.01 (1.00-1.03)	0.021	1.02 (1.00-1.03)	0.025
Hypertension	55.80 (284)	40.21 (2,148)	1.88 (1.56-2.25)	<0.001	1.55 (1.28-1.88)	<0.001
Type 2 diabetes	24.75 (126)	16.17 (864)	1.71 (1.38-2.11)	<0.001	1.35 (1.07-1.88)	0.010
Naproxen use	16.50 (84)	18.12 (968)	0.89 (0.70-1.14)	0.364	0.92 (0.71-1.18)	0.498

Values are % (n) or mean ± SD. Odds ratios (ORs) for age and BMI are reported per unit increase.
AS = aortic stenosis; BMI = body mass index; CI = confidence interval.

as comparators for celecoxib in the PRECISION (Prospective Randomized Evaluation of Celecoxib Integrated Safety vs Ibuprofen or Naproxen) trial (16). Detailed cohort definition criteria can be found in the Supplemental Appendix. Mean available follow-up was 10.16 ± 3.14 years. Unadjusted odds ratios (ORs) and differences between cases and controls were calculated using the Fisher exact and Mann-Whitney *U* tests, respectively. Given the significant association of several clinical variables with incident AS in our preliminary models, a multivariable logistic regression based on age, sex, body mass index, hypertension, diabetes, and drug use was used to calculate adjusted ORs and p values (17). All analyses were performed using the statistical programming language R, version 3.4.4 (18). Clinical data are presented as mean ± SD. Use of the Synthetic Derivative is classified as nonhuman research by Vanderbilt University's institutional review board, and approval was given for this study.

RESULTS

IN VITRO DYSTROPHIC CALCIFICATION ANALYSIS. Alizarin Red staining of calcium shows the characteristic rounded morphology of CNs formed by AVICs (**Figure 1A**). As expected, treatment with TGF-β1 increases the number of CNs under all pre-treatment conditions (**Figures 1A and 1B**). Unexpectedly, celecoxib pre-treatment causes a greater increase in CN number, whereas dimethyl celecoxib pre-treatment, as hypothesized, prevents TGF-β1-induced CN formation (**Figures 1A and 1B**). A gel contraction assay reveals that celecoxib-treated AVICs appear more contractile than their untreated or dimethyl celecoxib-treated counterparts, though not significantly (**Figure 1C**). TGF-β1 treatment increases contractility as well and compounds with celecoxib treatment to cause significantly more contraction than the no drug pre-treated with TGF-β1 (**Figure 1C**). Expression of myofibroblast markers α-SMA and CDH11 were evaluated by Western blot (**Figures 1D and 1E**, Supplemental Figure S1) and immunofluorescence (**Figure 1F**, Supplemental Figure S2). Densitometry demonstrates a significant increase in both markers only in the celecoxib pre-treated AVICs (**Figures 1D and 1F**). We observe no calcification of AVECs alone, as was expected, and very little calcification in AVICs treated with AVEC conditioned medium (Supplemental Figure S3).

RETROSPECTIVE CLINICAL ANALYSIS. The results obtained from these in vitro experiments led us to investigate possible clinical significance of celecoxib use. Approximately 8,300 deidentified patient records from VUMC met inclusion criteria and were queried for possible association of AS with celecoxib, naproxen, or ibuprofen use (**Figure 2**). In unadjusted analyses, celecoxib use is associated with an increased odds of developing AS (OR: 1.36; 95% confidence interval: 1.11 to 1.67; $p = 0.003$) (**Table 1**). After adjustment, this association persists (adjusted OR: 1.24; 95% confidence interval: 1.00 to 1.53; $p = 0.046$). Identical analyses were performed with ibuprofen and naproxen, and no associations were found. To assess the consistency of this cohort with those in other celecoxib studies, we cursorily examined unadjusted ORs of celecoxib with myocardial infarction and ischemic stroke, and found no association, as has been reported previously (Supplemental Table S1) (16).

DISCUSSION

Our investigation was motivated by the need for pharmaceutical alternatives to aortic valve replacement and the unique ability of celecoxib and dimethyl celecoxib to bind CDH11, a recently identified target for CAVD and AS. We have previously demonstrated that targeting CDH11 in vivo prevents the pathological increase in aortic jet maximum velocity (6), a clinical metric used to define the severity of AS. Others have found that celecoxib and its inactive analog, dimethyl celecoxib, were able to bind CDH11 (9), presenting an opportunity to exploit the off-target effects of celecoxib to treat CAVD with an already FDA-approved drug. The main finding of this work was unexpected. Primarily, celecoxib, the FDA-approved drug we anticipated being a potential therapeutic for CAVD, causes calcification in vitro and is associated with AS in patients. Conversely, the inactive analog dimethyl celecoxib showed the expected benefit of CDH11 blockade. Although further studies of dimethyl celecoxib are warranted, the new risk of celecoxib, a commonly prescribed drug, is the focus of our studies and discussion.

CELECOXIB PROMOTES MYOFIBROBLAST DIFFERENTIATION AND CALCIFICATION IN VITRO. Although AVICs are widely believed to be the cells driving CAVD, we evaluated the effects of celecoxib and dimethyl celecoxib on both AVICs and AVECs, as well as effects on AVICs from drug-treated AVEC conditioned medium. Because AVECs showed no response to celecoxib or dimethyl celecoxib (Supplemental Figure S3), we focused on direct effects of the drugs on AVICs. We show here that celecoxib causes an increase in both α-SMA and CDH11 expression, pointing to an induction of the myofibroblast phenotype, which then leads to CN formation. Conversely, although dimethyl

celecoxib treatment does not appear to change the AVIC phenotype—contractility, α-SMA expression, and CDH11 expression remain unchanged—it does significantly reduce CN formation. This supports our hypothesis that this beneficial effect is likely the result of dimethyl celecoxib preventing homotypic interactions of CDH11 between neighboring cells. With CDH11's cell-cell adhesions blocked, the tension between AVICs is reduced, which prevents the membrane tearing and subsequent apoptosis-mediated cell death that leads to CN formation. Given that activity in the cyclooxygenase-2 (COX2) axis is the key difference between celecoxib and dimethyl celecoxib, we attribute celecoxib's promyofibroblast effect to COX2 inhibition, which supports the notion of a protective role for COX2 in dystrophic CN formation.

CELECOXIB IS ASSOCIATED WITH AS. This is not the first investigation into the impact of COX2 inhibitors on heart disease. Most COX2 inhibitors were pulled from the market because of adverse cardiovascular effects by 2005 (19,20). Celecoxib had not displayed the same adverse effects and has retained FDA approval; however, the FDA mandated a cardiovascular safety trial. This study showed no increased risk of cardiovascular death, nonfatal myocardial infarction, or nonfatal stroke with celecoxib use when compared with ibuprofen or naproxen (16). However, these outcomes focus on acute, relatively short-term, and thrombotic events, and do not include valvular pathologies. On the basis of our in vitro data, rather than an acute thrombotic event, we suspected an increase in long-term risk of AS in these patients. Therefore, we tested our hypothesis using longitudinal clinical data. In retrospective analysis, we observed a unique association of celecoxib use with the presence of AS. The association of celecoxib and AS remained significant when adjusted for age, sex, body mass index, and known AS risk factors (17,21). The same is not observed in patients taking ibuprofen or naproxen, which have comparable major indications and clinical uses to celecoxib (acute pain, inflammatory or rheumatoid disorders, osteoarthritis, and primary dysmenorrhea), but inhibit COX1 in addition to COX2. This suggests there is something unique about celecoxib or selective COX2 inhibition that is associated with AS.

THE UNKNOWN ROLE OF COX2 IN AS. COX2 expression is increased in calcified human aortic valves (22), yet there are conflicting data as to whether it is a disease initiator or part of a protective response. COX2 inhibition has been shown in the *Klotho*-deficient mouse to lead to decreased aortic valve calcification via an osteogenic mechanism assessed by cell- and tissue-level pathology (22). Although calcification is the most common pathology finding in AS, clinical decision making is driven by functional measures (such as aortic jet maximum velocity). However, clinical studies of celecoxib have not yet focused on valvular function or pathology, or long-term effects (>4 years) of the drug (16,19,23). We have shown that COX2 inhibition can promote CN formation in porcine AVICs through the more prevalent dystrophic pathway of calcification, and a significant association between celecoxib use and AS in humans.

Collectively, these findings support further investigation of celecoxib or COX2's role in other models of CAVD and AS, such as *Notch1*$^{+/-}$ or *Apoe*$^{-/-}$ mice, to clarify whether COX2 is protective or disease-driving. COX2 also plays a key role in modulating various immune processes, and investigating the impact of celecoxib in immunocompetent CAVD models may provide new insights into the in vivo mechanisms implicated. Clinically, a multifaceted retrospective study of functional and imaging-defined AS progression with celecoxib use may further clarify this risk. It is still unclear whether celecoxib introduces novel risk or is a modifying risk factor in those already at risk. Additionally, although the efficacy of targeting CDH11 in vivo has been shown (6), further studies of dimethyl celecoxib in relevant murine models and eventually humans could reveal a novel therapeutic for CAVD.

STUDY LIMITATIONS. Our in vitro experiments rely on porcine cells, which are a standard model for CAVD research and are potentially better examples of healthy valve cells than samples from humans, because most heart valve donors are not free of other cardiovascular pathologies. Future work in human AVICs or a variety of in vivo mouse models could confirm our proposed mechanism.

Although we have imposed strict time gates and cohort selection criteria, retrospective EMR study does not allow for controlled assessment or follow-up of study participants. The retrospective nature of the clinical analysis does not allow us to quantify dosage of patients included, but contemporary published reports conclude that >80% of users at the time had standard 200 mg prescriptions (14,15). It is difficult to confidently rule in or rule out AS for patients in this large deidentified cohort of clinical records, but we tried to use definitions that would increase the accuracy of these designations. We cannot rule out that CAVD may have been present in some

individuals during the drug exposure period. In addition, the retrospective nature of the study precludes conclusions about causality of CAVD. The various differences between the celecoxib and control cohorts are adjusted for when possible, but may imply additional underlying differences that are better controlled in a randomized controlled trial. For example, in our preliminary models, we assessed the impact of hyperlipidemia on AS incidence, but it was not significantly associated with AS and had no effect on the model. This may be due to incomplete retrospective data or the lack in the era queried of consistent laboratory values such as lipoprotein(a), which has since proven a reliable biomarker for the association of dyslipidemia with AS (21). Additionally, valve morphology is a highly prevalent risk factor for CAVD, but it could not be accurately assessed in this retrospective study without consistent imaging for all subjects. An echo-driven study may provide more clarity on the impact of celecoxib in patients with a bicuspid aortic valve. Reanalysis of the PRECISION trial data may be an effective option for assessing the potential risk outlined in this analysis.

CONCLUSIONS

Overall, these data suggest that celecoxib use is associated with the development of CAVD. Although further studies are necessary, it is likely that dimethyl celecoxib or a monoclonal antibody against CDH11 would be safer therapeutic options than celecoxib to pursue for patients with CAVD or other CDH11-mediated diseases. Considering the indications for celecoxib, these results suggest that physicians must carefully balance the risks of COX1 inhibition in the gut with those of COX2-specific inhibition in the aortic valve when choosing a pain control regimen, and use celecoxib with caution in elderly patients with risk factors for AS.

ADDRESS FOR CORRESPONDENCE: Dr. W. David Merryman, Vanderbilt University, 2213 Garland Avenue, 9445D MRB4, Nashville, Tennessee 37232. E-mail: david.merryman@vanderbilt.edu.

PERSPECTIVES

COMPETENCY IN MEDICAL KNOWLEDGE: A recent cardiovascular safety trial showed that celecoxib is noninferior to ibuprofen and naproxen with regard to cardiovascular death, nonfatal myocardial infarction, and nonfatal stroke, and is associated with a lower risk of gastrointestinal bleeding than those medications. Those findings may encourage more widespread use of celecoxib to treat inflammatory pain. Our findings, including both in vitro studies and a retrospective review of the electronic medical record, indicate that celecoxib is associated with calcific nodule formation and the development of aortic stenosis.

TRANSLATIONAL OUTLOOK: Additional clinical studies are needed to confirm the link between celecoxib use and the development or progression of aortic stenosis, as this could influence prescribing patterns for medications that relieve inflammatory pain. Our studies show that dimethyl celecoxib impedes calcific nodule formation in vitro. Thorough in vivo animal studies should be performed to assess dimethyl celecoxib's translational potential for the prevention or treatment of calcific aortic valve disease.

REFERENCES

1. Rajamannan NM, Evans FJ, Aikawa E, et al. Calcific aortic valve disease: not simply a degenerative process: a review and agenda for research from the National Heart and Lung and Blood Institute Aortic Stenosis Working Group. Executive summary: calcific aortic valve disease-2011 update. Circulation 2011;124:1783–91.

2. Hutcheson JD, Aikawa E, Merryman WD. Potential drug targets for calcific aortic valve disease. Nat Rev Cardiol 2014;11:218–31.

3. Walker GA, Masters KS, Shah DN, Anseth KS, Leinwand LA. Valvular myofibroblast activation by transforming growth factor-beta: implications for pathological extracellular matrix remodeling in heart valve disease. Circ Res 2004;95:253–60.

4. Mohler ER 3rd, Gannon F, Reynolds C, Zimmerman R, Keane MG, Kaplan FS. Bone formation and inflammation in cardiac valves. Circulation 2001;103:1522–8.

5. Chen J, Ryzhova LM, Sewell-Loftin MK, et al. Notch1 mutation leads to valvular calcification through enhanced myofibroblast mechanotransduction. Arterioscler Thromb Vasc Biol 2015;35:1597–605.

6. Clark CR, Bowler MA, Snider JC, Merryman WD. Targeting cadherin-11 prevents notch1-mediated calcific aortic valve disease. Circulation 2017;135:2448–50.

7. Hutcheson JD, Chen J, Sewell-Loftin MK, et al. Cadherin-11 regulates cell-cell tension necessary for calcific nodule formation by valvular myofibroblasts. Arterioscler Thromb Vasc Biol 2013;33:114–20.

8. Bowler MA, Bersi MR, Ryzhova LM, Jerrell RJ, Parekh A, Merryman WD. Cadherin-11 as a regulator of valve myofibroblast mechanobiology. Am J Physiol Heart Circ Physiol 2018;315:H1614–26.

9. Dakshanamurthy S, Issa NT, Assefnia S, et al. Predicting new indications for approved drugs using a proteochemometric method. J Med Chem 2012;55:6832–48.

10. Fisher CI, Chen J, Merryman WD. Calcific nodule morphogenesis by heart valve interstitial cells is strain dependent. Biomech Model Mechanobiol 2013;12:5–17.

11. Chen J, Peacock JR, Branch J, David Merryman W. Biophysical analysis of dystrophic and osteogenic models of valvular calcification. J Biomech Eng 2015;137:020903.

12. Hutcheson JD, Ryzhova LM, Setola V, Merryman WD. 5-HT(2B) antagonism arrests non-canonical TGF-beta1-induced valvular myofibroblast differentiation. J Mol Cell Cardiol 2012;53:707–14.

13. Gould RA, Butcher JT. Isolation of valvular endothelial cells. J Vis Exp 2010;46:2158.

14. Blondell RD, Azadfard M, Wisniewski AM. Pharmacologic therapy for acute pain. Am Fam Physician 2013;87:766–72.

15. Fosbøl EL, Gislason GH, Jacobsen S, et al. The pattern of use of non-steroidal anti-inflammatory drugs (NSAIDs) from 1997 to 2005: a nationwide study on 4.6 million people. Pharmacoepidemiol Drug Saf 2008;17:822–33.

16. Nissen SE, Yeomans ND, Solomon DH, et al. Cardiovascular safety of celecoxib, naproxen, or ibuprofen for arthritis. N Engl J Med 2016;375:2519–29.

17. Yan AT, Koh M, Chan KK, et al. Association between cardiovascular risk factors and aortic stenosis: the CANHEART aortic stenosis study. J Am Coll Cardiol 2017;69:1523–32.

18. R Development Core Team. R: a language and environment for statistical computing. Vienna, Austria: R Foundation for Statistical Computing, 2018.

19. Bresalier RS, Sandler RS, Quan H, et al. Adenomatous Polyp Prevention on Vioxx (APPROVe) Trial Investigators. Cardiovascular events associated with rofecoxib in a colorectal adenoma chemoprevention trial. N Engl J Med 2005;352:1092–102.

20. U.S. Food and Drug Administration. COX-2 Selective (Includes Bextra, Celebrex, and Vioxx) and Non-Selective Non-Steroidal Anti-Inflammatory Drugs (NSAIDs). February 6, 2018. Available at: https://www.fda.gov/drugs/drugsafety/postmarketdrugsafetyinformationforpatientsandproviders/ucm429364.htm. Accessed April 10, 2018.

21. Lindman BR, Clavel MA, Mathieu P, et al. Calcific aortic stenosis. Nat Rev Dis Primers 2016;2:16006.

22. Wirrig EE, Gomez MV, Hinton RB, Yutzey KE. COX2 inhibition reduces aortic valve calcification in vivo. Arterioscler Thromb Vasc Biol 2015;35:938–47.

23. Solomon SD, McMurray JJ, Pfeffer MA, et al. Adenoma Prevention with Celecoxib (APC) Study Investigators. Cardiovascular risk associated with celecoxib in a clinical trial for colorectal adenoma prevention. N Engl J Med 2005;52:1071–80.

KEY WORDS aortic stenosis, aortic valve, calcification, celecoxib

APPENDIX For an expanded Methods section as well as supplemental figures and tables, please see the online version of this paper.

Go to http://www.acc.org/jacc-journals-cme to take the CME/MOC/ECME quiz for this article.

JACC: BASIC TO TRANSLATIONAL SCIENCE VOL. 4, NO. 2, 2019
© 2019 THE AUTHOR. PUBLISHED BY ELSEVIER ON BEHALF OF THE AMERICAN COLLEGE OF CARDIOLOGY FOUNDATION. THIS IS AN OPEN ACCESS ARTICLE UNDER THE CC BY-NC-ND LICENSE (http://creativecommons.org/licenses/by-nc-nd/4.0/).

EDITORIAL COMMENT

Off Target But on Track to New Strategies to Mitigate Calcific Aortic Valve Disease*

Dwight A. Towler, MD, PhD

Approximately 7% of our drugs approved as pharmacotherapy in the United States have no known primary target, and about twice this number have poorly defined mechanisms of action (1). Moreover, chemoinformatics – the combination of chemistry, structural biology, data mining, and computational sciences to define chemical space in present day pharmacology – has revealed that approximately 5% of drugs with well-defined therapeutic targets have high-affinity off-target interactions (2). Off-target molecular interactions molecules may provide either therapeutic benefit or untoward side effects. This drug property, known as polypharmacology, has been well appreciated for years, and on occasion has been clinically useful even when precise mechanisms were initially unclear. For example, the antibiotic demeclocycline arguably found its most unique therapeutic benefit in treatment of the syndrome of inappropriate antidiuretic hormone secretion because of the off-target capacity of demeclocycline to induce mild nephrogenic diabetes insipidus and increase free water excretion. However, polypharmacology can significantly complicate patient management; e.g., the well-known negative side effects of amiodarone on thyroid and pulmonary physiology when deployed to treat life-threatening arrhythmias.

In this issue of *JACC: Basic to Translational Science*, Bowler et al. (3) have innovatively followed through on a chemoinformatic clue that pointed to previously unknown polypharmacology. A prior independent, mass spectrometry-based study recently identified the widely used nonsteroidal anti-inflammatory drug celecoxib as a high-affinity ligand for cadherin 11 (CDH11), also known as osteoblast cadherin (4). Studies from the Merryman lab had previously shown that CDH11 was expressed in valve interstitial cells (VICs), and is a key contributor to VIC-mediated osteogenic mineralization in aortic valves via mechanical modulation of the VIC phenotype. Thus, the investigative team examined porcine aortic VIC-mediated matrix calcification in the presence of celecoxib or dimethyl celecoxib—the latter a methylated congener that also binds CDH11 but does not inhibit cyclooxygenase 2 (Cox2). To the authors' surprise, celcoxib increased, whereas dimethyl celecoxib inhibited, calcified nodule formation in VICs grown under prosclerotic conditions (e.g., transforming growth factor-beta with biaxial mechanical strain) (3).

SEE PAGE 135

Furthermore, celecoxib increased the contractile myofibroblast phenotype of VICs in this relevant culture model. Importantly, aortic valve endothelial cells exhibited little to no procalcific activity or modulation. To further establish the relationship between celecoxib and calcific aortic valve disease (CAVD), the authors queried the Vanderbilt Synthetic Derivative, a powerful de-identified patient database enabling an analysis of celecoxib use and the risk for calcific aortic stenosis (AS) (3). Comparison was made to other nonsteroidal anti-inflammatory drugs such as naproxen or ibuprofen that do not bind CDH11. In the adjusted retrospective analysis, celecoxib use was

*Editorials published in *JACC: Basic to Translational Science* reflect the views of the authors and do not necessarily represent the views of *JACC: Basic to Translational Science* or the American College of Cardiology.

From the Department of Internal Medicine, Endocrine Division, University of Texas Southwestern Medical Center, Dallas, Texas. Dr. Towler is supported by NIH grants HL069229 and HL114806, the American Diabetes Association, the J.D. and Maggie E. Wilson Distinguished Chair in Biomedical Research, and the Louis V. Avioli Endowed Professorship in Mineral Metabolism Research.

The author attests he is in compliance with human studies committees and animal welfare regulations of the author's institutions and Food and Drug Administration guidelines, including patient consent where appropriate. For more information, visit the *JACC: Basic to Translational Science* author instructions page.

ISSN 2452-302X https://doi.org/10.1016/j.jacbts.2019.03.010

associated with a significant 25% increase in AS risk, whereas no such association was found with naproxen or ibuprofen exposure (3). Thus, celecoxib use emerges as a plausible risk factor for calcific AS, potentially related to mechanisms involving VIC Cox2 inhibition in the setting of CDH11 modulation (3).

Why is this paper from Bowler et al. (3) so significant? There are several important features, but 2 stand out as very helpful to consider, including their implications. Firstly and most saliently, celecoxib emerges as a new member in a handful of widely used drugs associated with the CAVD spectrum in humans. Given the high prevalence of calcific AS in our aging population and the failure of statins to favorably impact CAVD (5), close attention must be paid to clinical observations that potentially offer clues to pathogenesis and prevention. The Multiethnic Study of Atherosclerosis revealed that aminobisphosphonate use for osteoporosis was associated with reduced aortic valve calcification in postmenopausal women (6). Because valve calcium accrual portends CAVD progression to clinically relevant AS (5), this suggests that aminobisphosphonates might mitigate progression, but direct evidence is lacking and potential mechanisms unknown. The Japanese Aortic Stenosis Study identified that warfarin use increased, whereas angiotensin receptor blocker use decreased, calcific AS risk (7). As Bowler et al. (3) newly show, Cox2 inhibition in the setting of concomitant Cdh11 antagonism—as occurs with celecoxib—increases risk for AS. This suggests a protective role for Cox2 in limiting VIC calcification; however, this relationship may differ for those Cox2 inhibitors that do not simultaneously impact both Cox2 and CDH11 pathways; for example, naproxen and ibuprofen. Notably, naproxen and ibuprofen use were not associated with increased calcific AS risk (3). Nevertheless, Cox2 generates a spectrum of bioactive oxylipid metabolites—including proinflammatory and proresolving prostaglandins and lipoxins — and pharmacologic modulation or loss of Cox2 markedly perturbs oxylipid metabolism (8). Moreover, oxidized phospholipids (oxPL) also inhibit Cox2 activity as relevant to calcific AS (9). Biochemical and genetic data have converged to reveal oxPL: lipoprotein(a) [Lp(a)] complexes drive calcific AS via lysophosphatidic acid ligand-receptor interactions (10). An important study by Zheng et al. (11) has recently shown that elevated Lp(a) levels (> 35 mg/dl) not only reflect elevated aortic valve calcifying activity as revealed by fluorodeoxyglucose positron-emission tomography/computed tomography, but also portend clinical calcific AS progression (11). As Gotoh first pointed out (12), Lp(a) conveys risk for aortic valve sclerosis and CAVD beyond low-density lipoprotein cholesterol (13), and Lp(a) does not appear to carry risk for coronary artery calcification similar to low-density lipoprotein cholesterol (14). Thus, given the findings of Bowler et al. (3), patients with elevated Lp(a) might be advised to avoid celecoxib, but this clearly requires further study. Tsimika's lab first demonstrated that Lp(a) is the preferred lipoprotein carrier of oxPL in human plasma — and Lp(a) is absent in most preclinical disease models in the absence of transgenic engineering (reviewed in Tsimika et al. [13]). Therefore, in vivo preclinical studies delineating pathomechanisms of celecoxib and Cox2 inhibition—or therapeutic Cox2 modulation—in CAVD should deploy models from which the contributions of Lp(a):oxPL metabolism can be studied as relevant to human disease. Such models also afford the opportunity to determine how the valve cell mechanobiology regulated by CDH11 interacts with Lp(a):oxPL metabolism in VIC phenotypic modulation.

Secondly, this study indicates the power of chemoinformatics to inform and advance human pharmacology. Uniquely keen insight, team science, institutional infrastructure, and chemoinformatics synergized to identify an untoward AS risk associated with celecoxib use (3); this important result is worrisome given give the prevalence of CAVD in our aging population (5), and deserves further investigation and clinical validation. However, the actions of dimethyl celecoxib — a small-molecule antagonist of CDH11 that avoids Cox2—on limiting VIC calcifying nodule formation and myofibroblastic phenotype (3) indicates that targeting CDH11 is feasible and potentially fruitful as a strategy for mitigating human AS. Indeed, the Merryman lab has shown that a monoclonal antibody targeting CDH11 can ameliorate CAVD and valve tissue stiffness due to murine Notch1 haploinsufficiency (15). These are important observations given the absence of proven pharmacotherapy for human CAVD. Dimethyl celecoxib can serve as a tool compound, enabling refinement of structure-activity relationships in small-molecule modulators of VIC biology via CDH11, potentially useful in AS pharmacotherapy. However, tool compounds have their own shortcomings, and dimethyl celecoxib itself also exhibits polypharmacology, sharing with celecoxib the actions in the cellular endoplasmic reticulum stress response. Studying VIC responses to novel CDH11-targeted small-molecule

inhibitors in development for other indications should prove useful as well. In toto, the enlightening study from Bowler et al. (3) has significant translational implications, providing insight that informs novel strategies to mitigate AS risk in our aging, dysmetabolic population.

ADDRESS FOR CORRESPONDENCE: Dr. Dwight A. Towler, University of Texas Southwestern Medical Center, Internal Medicine, Endocrine Division, 5323 Harry Hines Boulevard, Dallas, Texas 75390-8857. E-mail: Dwight.Towler@utsouthwestern.edu.

REFERENCES

1. Gregori-Puigjane E, Setola V, Hert J, et al. Identifying mechanism-of-action targets for drugs and probes. Proc Natl Acad Sci U S A 2012;109:11178–83.

2. Keiser MJ, Setola V, Irwin JJ, et al. Predicting new molecular targets for known drugs. Nature 2009;462:175–81.

3. Bowler MA, Raddatz MA, Johnson CL, Lindman BR, Merryman WD. Celecoxib is associated with dystrophic calcification and aortic valve stenosis. J Am Coll Cardiol Basic Trans Science 2019;4:135–43.

4. Dakshanamurthy S, Issa NT, Assefnia S, et al. Predicting new indications for approved drugs using a proteochemometric method. J Med Chem 2012;55:6832–48.

5. Lindman BR, Clavel MA, Mathieu P, et al. Calcific aortic stenosis. Nat Rev Dis Primers 2016;2:16006.

6. Elmariah S, Delaney JA, O'Brien KD, et al. Bisphosphonate use and prevalence of valvular and vascular calcification in women MESA (The Multi-Ethnic Study of Atherosclerosis). J Am Coll Cardiol 2010;56:1752–9.

7. Yamamoto K, Yamamoto H, Yoshida K, et al. Prognostic factors for progression of early- and late-stage calcific aortic valve disease in Japanese: the Japanese Aortic Stenosis Study (JASS) retrospective analysis. Hypertens Res 2010;33:269–74.

8. Poorani R, Bhatt AN, Dwarakanath BS, Das UN. COX-2, aspirin and metabolism of arachidonic, eicosapentaenoic and docosahexaenoic acids and their physiological and clinical significance. Eur J Pharmacol 2016;785:116–32.

9. Eligini S, Brambilla M, Banfi C, et al. Oxidized phospholipids inhibit cyclooxygenase-2 in human macrophages via nuclear factor-kappaB/IkappaB- and ERK2-dependent mechanisms. Cardiovasc Res 2002;55:406–15.

10. Mathieu P, Arsenault BJ, Boulanger MC, Bosse Y, Koschinsky ML. Pathobiology of Lp(a) in calcific aortic valve disease. Expert Rev Cardiovasc Ther 2017;15:797–807.

11. Zheng KH, Tsimikas S, Pawade T, et al. Lipoprotein(a) and oxidized phospholipids promote valve calcification in patients with aortic stenosis. J Am Coll Cardiol 2019;73:2150–62.

12. Gotoh T, Kuroda T, Yamasawa M, et al. Correlation between lipoprotein(a) and aortic valve sclerosis assessed by echocardiography (the JMS Cardiac Echo and Cohort Study). Am J Cardiol 1995;76:928–32.

13. Tsimikas S. Potential causality and emerging medical therapies for lipoprotein(a) and its associated oxidized phospholipids in calcific aortic valve stenosis. Circ Res 2019;124:405–15.

14. Kamstrup PR, Tybjaerg-Hansen A, Nordestgaard BG. Elevated lipoprotein(a) and risk of aortic valve stenosis in the general population. J Am Coll Cardiol 2014;63:470–7.

15. Clark CR, Bowler MA, Snider JC, Merryman WD. Targeting cadherin-11 prevents Notch1-mediated calcific aortic valve disease. Circulation 2017;135:2448–50.

KEY WORDS cadherin, calcific aortic stenosis, celecoxib, chemoinformatics, polypharmacology

JACC: BASIC TO TRANSLATIONAL SCIENCE VOL. 4, NO. 2, 2019
© 2019 THE AUTHORS. PUBLISHED BY ELSEVIER ON BEHALF OF THE AMERICAN COLLEGE OF CARDIOLOGY FOUNDATION. THIS IS AN OPEN ACCESS ARTICLE UNDER THE CC BY-NC-ND LICENSE (http://creativecommons.org/licenses/by-nc-nd/4.0/).

CLINICAL RESEARCH

Elamipretide Improves Mitochondrial Function in the Failing Human Heart

Kathryn C. Chatfield, MD, PhD,[a,*] Genevieve C. Sparagna, PhD,[b,*] Sarah Chau, BS,[b] Elisabeth K. Phillips, BS,[b] Amrut V. Ambardekar, MD,[b] Muhammad Aftab, MD,[c,d] Max B. Mitchell, MD,[c] Carmen C. Sucharov, PhD,[b] Shelley D. Miyamoto, MD,[a] Brian L. Stauffer, MD[b,e]

VISUAL ABSTRACT

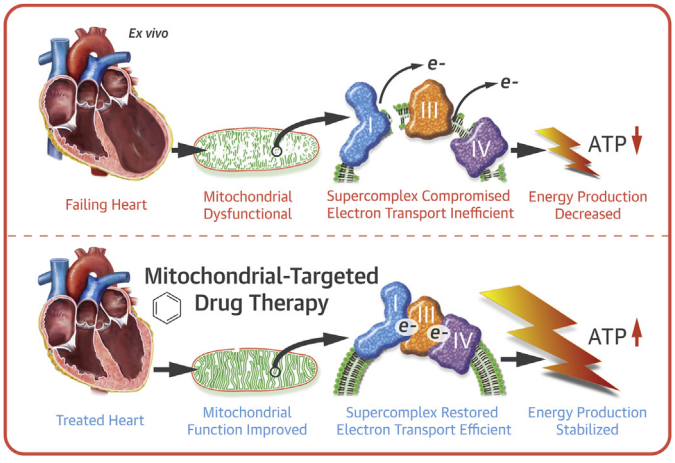

Chatfield, K.C. et al. J Am Coll Cardiol Basic Trans Science. 2019;4(2):147–57.

HIGHLIGHTS

- **Mitochondrial function is impaired in explanted failing pediatric and adult human hearts.**
- **Elamipretide is a novel mitochondria-targeted drug that is targeted to cardiolipin on the inner mitochondrial membrane and improves coupling of the electron transport chain.**
- **Treatment of explanted human hearts with elamipretide improves human cardiac mitochondrial function.**
- **The study provides novel methods to evaluate the influence of compounds on mitochondria in the human heart and provides proof of principle for the use of elamipretide to improve mitochondrial energetics in failing myocardium due to multiple etiologies and irrespective of age.**

From the [a]Department of Pediatrics, University of Colorado School of Medicine, Children's Hospital of Colorado, Aurora, Colorado; [b]Department of Medicine/Division of Cardiology, University of Colorado School of Medicine, Aurora, Colorado; [c]Department of Surgery/Division of Cardiothoracic Surgery, University of Colorado School of Medicine, Aurora, Colorado; [d]Department of Surgery, Veterans Administration Hospital, Denver, Colorado; and the [e]Department of Medicine/Division of Cardiology, Denver Health Medical Center, Denver, Colorado. *Drs. Chatfield and Sparagna have contributed equally to this paper. This work was supported by the Addison Scott Memorial Fund, the Boedecker Foundation Award, the Jack Cooper Millisor Chair in Pediatric Heart Disease, a gift from the Nair Family, research support from Stealth BioTherapeutics, Inc., and the following National Institutes of Health (NIH)/National Heart, Lung, and Blood Institute grants: K08 HL127294, R01 HL107715 (to Dr. Stauffer) and R01 HL126928 (to Dr. Miyamoto). This study was supported by NIH/National Center for Advancing Translational Sciences Colorado CTSA Grant Number UL1 TR001082. The contents are the authors' sole responsibility and do not necessarily represent official NIH views. Drs. Sucharov, Miyamoto, and Stauffer are founders and scientific advisors for CoramiR Biomedical, LLC. Dr. Stauffer received research support from Stealth BioTherapeutics, Inc. All other authors have reported that they have no relationships relevant to the contents of this paper to disclose.

All authors attest they are in compliance with human studies committees and animal welfare regulations of the authors' institutions and Food and Drug Administration guidelines, including patient consent where appropriate. For more information, visit the *JACC: Basic to Translational Science* author instructions page.

Manuscript received October 22, 2018; revised manuscript received December 11, 2018, accepted December 13, 2018.

ISSN 2452-302X https://doi.org/10.1016/j.jacbts.2018.12.005

JACC: BASIC TO TRANSLATIONAL SCIENCE VOL. 4, NO. 2, 2019
APRIL 2019:147–57

ABBREVIATIONS AND ACRONYMS

ADP = adenosine diphosphate

BN-PAGE = blue native polyacrylamide gel electrophoresis

C = mitochondrial respiratory complex

FCCP = carbonyl cyanide p-trifluoromethoxyphenyl hydrazone

HF = heart failure

RCR = respiratory control ratio

SC CCF = supercomplex coupling control factor

SUMMARY

Negative alterations of mitochondria are known to occur in heart failure (HF). This study investigated the novel mitochondrial-targeted therapeutic agent elamipretide on mitochondrial and supercomplex function in failing human hearts ex vivo. Freshly explanted failing and nonfailing ventricular tissue from children and adults was treated with elamipretide. Mitochondrial oxygen flux, complex (C) I and CIV activities, and in-gel activity of supercomplex assembly were measured. Mitochondrial function was impaired in the failing human heart, and mitochondrial oxygen flux, CI and CIV activities, and supercomplex-associated CIV activity significantly improved in response to elamipretide treatment. Elamipretide significantly improved failing human mitochondrial function. (J Am Coll Cardiol Basic Trans Science 2019;4:147–57) © 2019 The Authors. Published by Elsevier on behalf of the American College of Cardiology Foundation. This is an open access article under the CC BY-NC-ND license (http://creativecommons.org/licenses/by-nc-nd/4.0/).

MITOCHONDRIAL DYSFUNCTION AND CARDIOLIPIN IN HEART FAILURE

A substantial body of work has implicated abnormal mitochondrial function and consequent impaired energy production via oxidative phosphorylation as a factor in the development of heart failure (HF), leading to heightened interest in mitochondrial function as a therapeutic target (1–3). Efficient mitochondrial function is considered especially essential in the heart due to the sustained energy requirements of the myocardium. Cardiolipin, a unique phospholipid with 4 fatty acid side chains, is critical for maintaining normal adenosine triphosphate generation by anchoring the proteins of the electron transport chain onto the inner mitochondrial membrane architecture (4). In the heart, a mitochondrial inner membrane enriched with tetralinoleoyl cardiolipin (containing 4 linoleic acid side chains) facilitates the stability of the physical interaction between oxidative phosphorylation complex protein multimers in what has been termed the mitochondrial supercomplex, composed of complex (C) I, CIII, and CIV (5,6). Abnormalities in cardiolipin composition lead to mitochondrial dysfunction in the failing heart through disruption of the supercomplex and can be improved with dietary interventions in rodent models (7–9). These abnormalities in mitochondrial function have led to heightened interest in mitochondria as a therapeutic target in HF (3).

SEE PAGE 158

ELAMIPRETIDE, A MITOCHONDRIAL-TARGETED PEPTIDE

Elamipretide (formerly referred to as Bendavia, MTP-131, and SS-31) is an aromatic-cationic, cell-permeable tetrapeptide in a new class of mitochondrial-targeted drugs and is the first in its class to enter clinical trials in patients with HF (10–12). The peptide is targeted to mitochondria via cardiolipin where it has been shown in animal models to improve energetics and decrease reactive oxygen species, possibly by stabilizing the mitochondrial membrane and cytochrome *c* (13,14). Elamipretide rapidly enters tissue (within minutes of treatment) and has cardioprotective effects in ischemia/reperfusion injury in animal models (15–18). To date, there are no data on the direct effects of elamipretide, or other members of this novel class, on mitochondrial function in the human heart.

ELAMIPRETIDE IN HUMAN HF

The purpose of the present study was to investigate the effects of elamipretide on human cardiac mitochondrial function. Because this study was ex vivo and performed over the course of a few hours (too rapid to induce cardiolipin remodeling), any effects of the drug would likely be independent of cardiolipin molecular species alterations. Using freshly explanted human hearts, the current study found that: 1) elamipretide improves impaired mitochondrial function in HF, with no effect on normal mitochondrial function in nonfailing hearts; 2) elamipretide improves mitochondrial supercomplex function (CI, CIII, and CIV) but does not alter CII or CV activity; and 3) the short-term action of elamipretide is independent of any changes in cardiolipin side chain composition.

METHODS

CHEMICALS AND REAGENTS. Elamipretide was provided by Stealth BioTherapeutics, Inc. (Newton, Massachusetts), resuspended in water at 10 mM, and stored at -80°C. The elamipretide ex vivo treatment

TABLE 1 Characteristics of Cardiac Samples According to Experiment

	High-Resolution Respirometry		Enzyme Activity Assays		BN-PAGE In-Gel Activity		Cardiolipin Mass Spectrometry	
	Nonfailing	Failing	Nonfailing	Failing	Nonfailing	Failing	Nonfailing	Failing
No. of heart samples	13	23	11	12	19	21	5	10
Male	6	15	4	7	8	10	3	7
Female	7	8	7	5	11	11	2	3
Age, yrs	25 ± 7	31 ± 5	20 ± 8	29 ± 8	26 ± 5	25 ± 5	28 ± 13	29 ± 9
Ejection fraction, %	64 ± 5	24 ± 2	64 ± 4	27 ± 3	61 ± 3	22 ± 6	58 ± 2	20 ± 3

Values are n or mean ± SEM.
BN-PAGE = blue native polyacrylamide gel electrophoresis.

concentration was determined by the plateau of a dose-response curve in a subset of samples (data not shown). Unless otherwise noted, all other chemicals were from MilliporeSigma (Burlington, Massachusetts).

PATIENT SAMPLES. Explanted cardiac ventricular tissue from children and adults of all races, sexes, and ethnic backgrounds with informed consent obtained from the subjects or their guardians were available for this study through the institutional review board-approved University of Colorado Pediatric and Adult Cardiac Tissue Banks. Fresh samples were harvested during sequential transplants at Children's Hospital Colorado and University of Colorado Hospital. Additional experiments were performed in previously harvested frozen samples from the University of Colorado Heart Tissue Bank. Sample characteristics for each experiment are given in **Table 1**. More detailed information for each patient is provided in Supplemental Tables 1 and 2. Nonfailing tissue was procured from donors or individuals with normal systolic ventricular function. HF tissue was obtained from patients undergoing transplant for terminal HF with reduced systolic function. Heart tissue was dissected in the operating room immediately after explant and kept in BIOPS preservation solution at 4°C until processing (19). Mitochondria were freshly isolated within 6 h of explant for spectrophotometric assays. Time course experiments showed that after 3 days in BIOPS at 4°C, mitochondrial respiration was unchanged in nonfailing tissue, but increased in HF tissue (Supplemental Figure 1). High-resolution respirometry experiments were performed in fresh permeabilized cardiac fibers. Flash-frozen tissue at time of explant was used for in-gel activity staining using blue native polyacrylamide gel electrophoresis (BN-PAGE) separation.

MITOCHONDRIAL ISOLATION. Subpopulations of myocardial mitochondria, subsarcolemmal located beneath the plasma membrane and interfibrillar residing between the myofibrils, were isolated by using differential centrifugation and trypsin digestion as previously described with the following modifications for human tissue (20,21). Briefly, freshly explanted cardiac tissue in pieces no larger than 5 mm was placed in ice-cold BIOPS solution. Tissue was trimmed of fat, placed into mitochondrial isolation buffer, and minced by using scissors. Low-speed spins were at 1,500*g* and high-speed spins at 4,200*g*. One milligram of trypsin was used per gram of tissue. Mitochondria were resuspended in potassium buffer and protein quantified (BCA, Thermo Fisher Scientific, Waltham, Massachusetts).

ENZYMATIC ACTIVITIES. Isolated mitochondria were diluted to a final protein concentration of 1 mg/ml and incubated with 100 μM elamipretide or an equal volume of vehicle (water) for 1 h on ice. Enzymatic activities of CI, CIV, and citrate synthase were performed at 30°C as previously described (22,23).

BLUE NATIVE POLYACRYLAMIDE GEL ELECTROPHORESIS. Mitochondrial supercomplexes were separated by BN-PAGE using TGX 4-15% gels (Bio-Rad, Hercules, California). In-gel activity assays for CI, CII, CIV, and CV were performed with septal tissue processed according to published methods (22,24). Samples were treated with 100 μM elamipretide for 1 h. Supercomplex and free protein bands were quantified by using ImageJ software (National Institutes of Health, Bethesda, Maryland). Total supercomplex activity was calculated as a sum of all supercomplex bands.

HIGH-RESOLUTION RESPIROMETRY. Respiration of permeabilized cardiac fibers was measured by high-resolution respirometry (Oxygraph, Oroboros Instruments, Innsbruck, Austria) using a stepwise protocol to evaluate various components of the electron transport system (19,25). Approximately 30 mg of ventricular tissue was placed in BIOPS immediately after explant. One-half of the tissue was incubated in BIOPS containing 100 μM elamipretide at 4°C for 1 h. After incubation, tissue was cut into approximately 2-mg pieces and teased using forceps to separate fibers. The tissue was then placed in a solution of BIOPS containing 30 μg/ml saponin for 30 min to permeabilize

FIGURE 1 High-resolution Respirometry of Treated and Untreated Heart Fibers

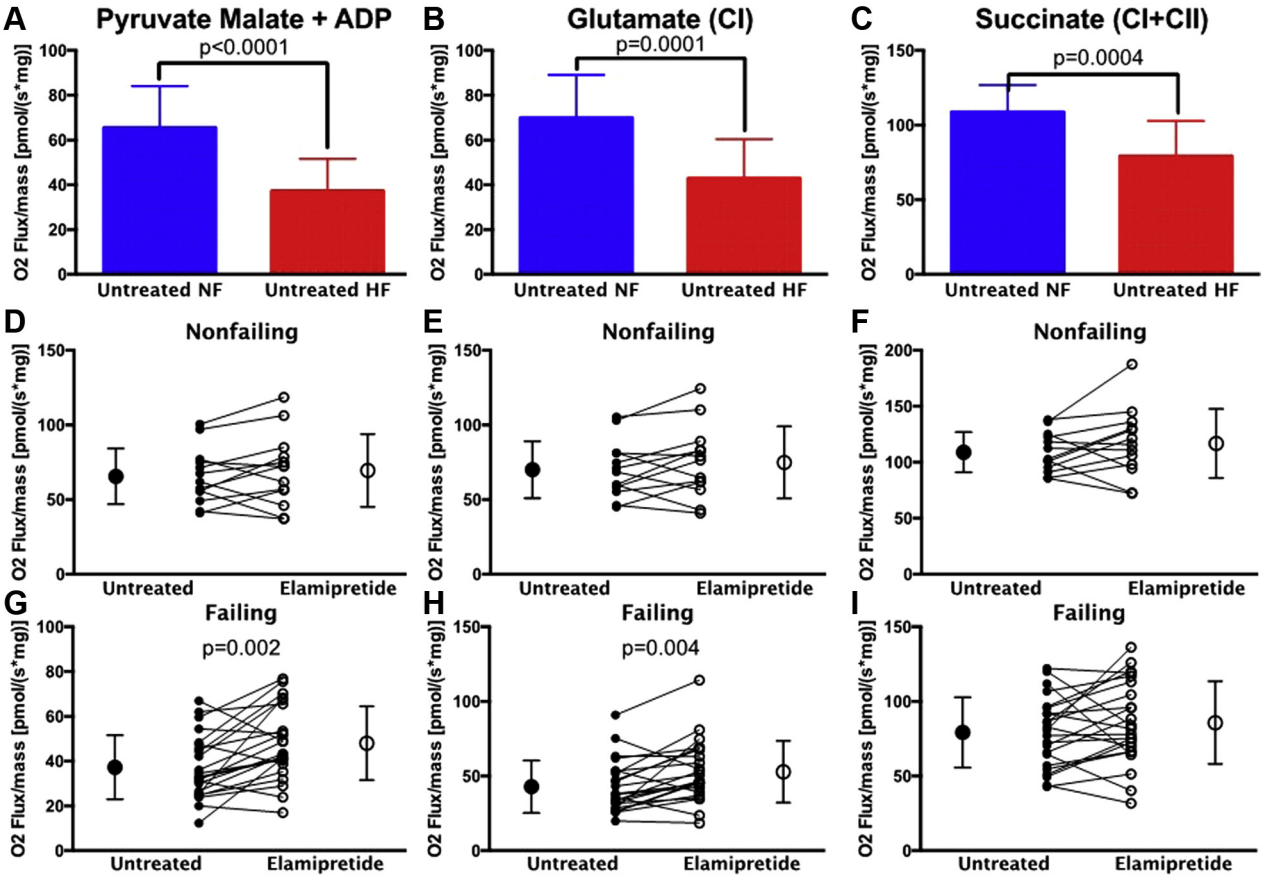

Oxygen (O2) flux normalized to mass in permeabilized heart fibers from untreated heart failure (HF) versus nonfailing (NF) human hearts with additions of: **(A)** pyruvate malate plus adenosine diphosphate (ADP); **(B)** subsequent addition of glutamate acting through complex (C) I; and **(C)** subsequent addition of succinate additionally activating CII. **(D to F)** Elamipretide treatment had no effect on oxygen flux of NF samples **(G to I)** but significantly improved oxygen flux in HF samples after additions of the aforementioned substrates. Untreated hearts in **(D to I)** are shown with **closed circles** and treated hearts with **open circles**. NF, n = 13; HF, n = 23.

the plasma membrane and to allow substrate delivery to the mitochondria. Fibers were washed for 10 min at 4°C in ice-cold mitochondrial respiration medium containing 25 μM blebbistatin ± 100 μM elamipretide (26). Samples were blotted on filter paper, weighed, and placed in the chambers of the Oroboros O2K apparatus at 37°C containing respiration medium and 25 μM blebbistatin ± 100 μM elamipretide. Standard protocols were followed for calibration of the chambers and followed by stepwise addition of 5 mM pyruvate, 1 mM malate, 4 mM adenosine diphosphate (ADP), 10 mM glutamate, 10 mM succinate, 10 μM cytochrome *c*, and either 2 μg/ml oligomycin or 0.5 μM steps of carbonyl cyanide p-trifluoromethoxyphenylhydrazone (FCCP) (until the maximum rate was reached) followed by 2 μM rotenone. Oxygen flux rates were normalized per milligram of tissue wet weight.

CARDIOLIPIN QUANTITATION. Cardiolipin was quantified in a subset of the total cohort by using previously published methods with liquid chromatography coupled to electrospray ionization mass spectrometry in an API 4000 Mass Spectrometer (SCIEX, Framingham, Massachusetts) (20). After BIOPS or BIOPS Plus 100 μM elamipretide treatment for 4 h, heart tissue was frozen without buffer at -80°C. Tissue pieces were homogenized by using a glass-on-glass homogenizer in phosphate-buffered saline and lipids extracted according to previously published methods with 1 mmol tetramyristoyl-cardiolipin as an internal standard (Avanti Polar Lipids, Alabaster, Alabama) (20,27). Cardiolipin species were quantified per milligram of protein.

STATISTICAL ANALYSIS. Statistical analyses were performed by using Prism software version 6.0

FIGURE 2 SC CCF and RCR With Elamipretide Treatment

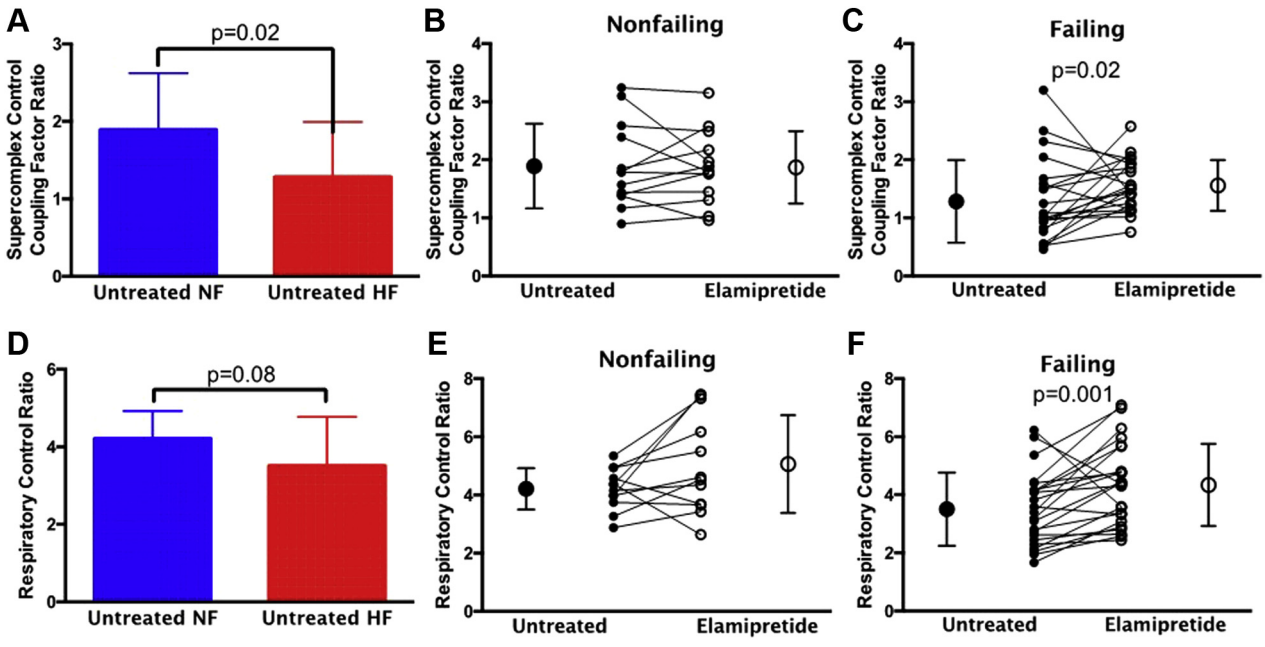

(A) Supercomplex coupling control factor (SC CCF) ratio is lower in untreated HF than NF controls. Elamipretide treatment does not alter SC CCF in **(B)** NF hearts but improves SC CCF in **(C)** HF. **(D)** The respiratory control ratio (RCR) trends lower in untreated NF hearts versus HF hearts. Elamipretide treatment has no effect on RCR in **(E)** NF hearts but increases RCR in **(F)** HF hearts. Untreated hearts in **B, C, E and F** are shown with **closed circles** and treated hearts with **open circles**. NF, n = 13; HF, n = 23. Abbreviations as in Figure 1.

(GraphPad Software, La Jolla, California). Treatment effects were analyzed by using a ratio-paired Student's *t*-test, with $p < 0.05$ being significant and $p < 0.1$ reported as trending toward significance (28). HF or time-based effects were analyzed by using an unpaired Student's *t*-test. Datasets were tested for Gaussian distribution with the D'Agostino and Pearson omnibus test or the Shapiro-Wilk normality test. Data that did not conform to a Gaussian distribution (glutamate and supercomplex coupling control factor data) were log-transformed before analysis.

Graphs with bars show SEM for unpaired Student's *t*-test data, and graphs with paired data show means plus SDs (chosen for clarity) flanked on either side of the paired data. Linear regression analysis was performed to assess for an association between age and significant outcomes (no associations were demonstrated).

RESULTS

ELAMIPRETIDE IMPROVES RESPIRATION OF INTACT MITOCHONDRIA FROM THE FAILING HUMAN HEART. Quantitation of the results of high-resolution respirometry in all samples is shown in Figure 1 with sample traces shown in Supplemental Figure 2. There was significantly lower mitochondrial normalized oxygen flux in HF vs nonfailing samples using pyruvate malate + ADP, glutamate (CI), and succinate (CI + CII) as substrates (Figures 1A to 1C). There were also significantly lower oxygen fluxes in HF with inhibition of flux through CI + CII using oligomycin or the uncoupler FCCP ($p < 0.01$) but not combined with the CI inhibitor rotenone (data not shown).

Elamipretide treatment of nonfailing permeabilized fibers did not alter mitochondrial oxygen flux (Figures 1D to 1F). However, in HF, there was a significant increase in oxygen flux with elamipretide treatment using the substrates pyruvate malate + ADP (Figure 1G) and glutamate (CI) (Figure 1H). Notably, there was no significant difference with elamipretide treatment with the addition of succinate (CI + CII) in HF (Figure 1I). Addition of pyruvate/malate, FCCP, rotenone, or oligomycin did not significantly affect oxygen flux through CI + II (data not shown).

ELAMIPRETIDE INCREASES THE SUPERCOMPLEX COUPLING CONTROL FACTOR AND RESPIRATORY CONTROL RATIO IN FAILING MITOCHONDRIA. The supercomplex coupling control factor ratio (SC CCF) is

FIGURE 3 Individual Total Activity Measurements of CI, CIV, and Citrate Synthase in Subsarcolemmal Mitochondria

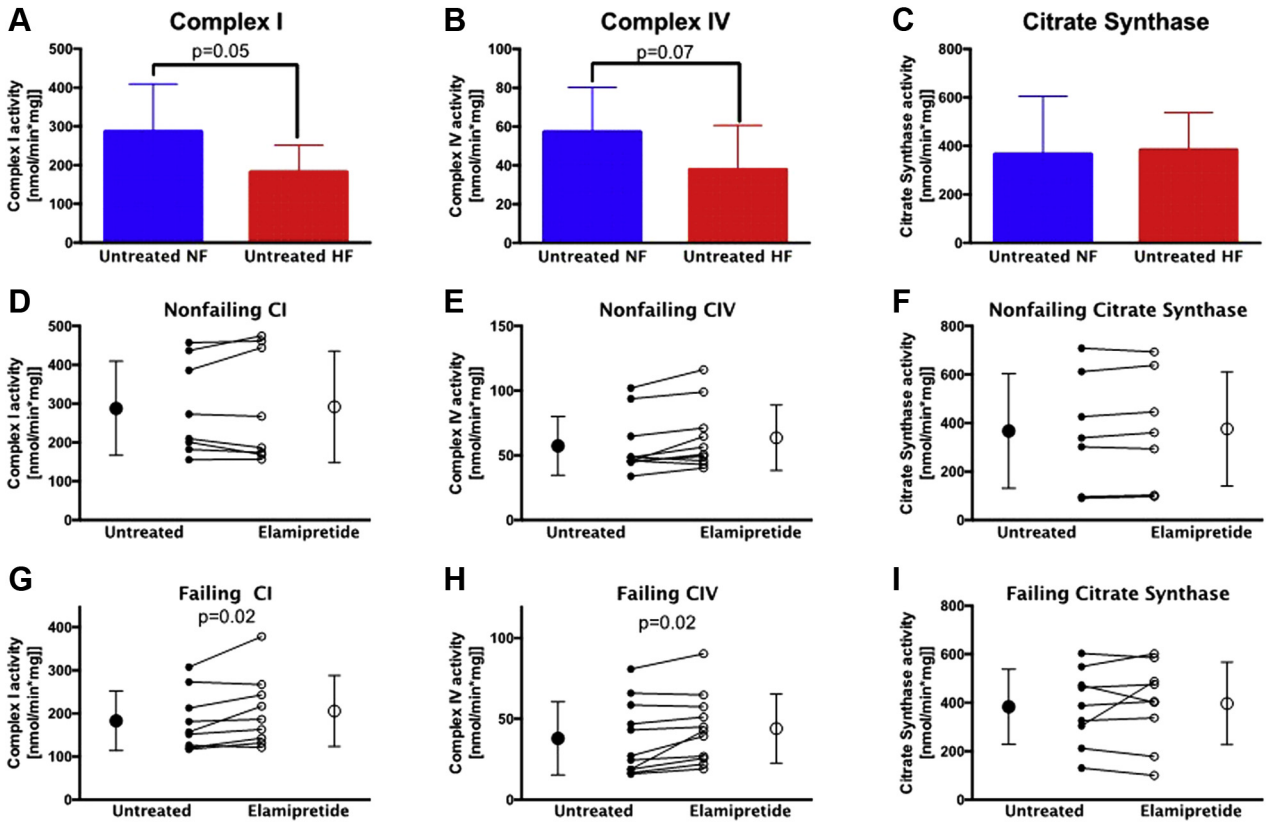

(A to C) Enzyme activities of CI, CIV, and citrate synthase are lower, trending lower, and unchanged, respectively, in untreated HF versus NF controls. **(D to F)** Activities of CI, CIV, and citrate synthase are unaltered with elamipretide treatment in NF hearts. **(G to I)** Individual activities of CI and CIV increase with elamipretide treatment in HF, with citrate synthase unchanged. Untreated hearts in **(C to G)** are shown with **closed circles** and treated hearts with **open circles**. NF, n = 11; HF, n = 12. Abbreviations as in Figure 1.

a mathematical construct to calculate the influence of the supercomplex on a given respirometry measurement and is directly proportional to supercomplex integrity (derivation is given in the Supplemental Methods). The SC CCF was significantly lower with HF (Figure 2A). Elamipretide treatment in nonfailing hearts did not alter SC CCF (Figure 2B). Conversely, in HF, elamipretide treatment significantly increased SC CCF (Figure 2C). The respiratory control ratio (RCR) indicates a trend toward decreasing in HF (Figure 2D). There was no change in RCR with elamipretide treatment in nonfailing hearts (Figure 2E), whereas in HF, RCR was significantly increased with elamipretide treatment (Figure 2F).

ACTIVITIES OF MITOCHONDRIAL CI AND CIV IN SUBSARCOLEMMAL MITOCHONDRIA ARE INCREASED WITH ELAMIPRETIDE. Freshly isolated subsarcolemmal and interfibrillar mitochondria treated with elamipretide were used to measure total activity of CI and CIV as well as citrate synthase, a soluble enzyme in the mitochondrial matrix (29). Total CI activity was significantly lower in HF compared with nonfailing samples (Figure 3A), whereas CIV activity in subsarcolemmal mitochondria showed a trend toward a decrease in HF (Figure 3B). No difference in citrate synthase activity was observed between HF and the nonfailing group (Figure 3C). In nonfailing subsarcolemmal mitochondria, activities of these 3 enzyme complexes were unaffected by elamipretide treatment (Figures 3D to 3F). However, in failing subsarcolemmal mitochondria, both CI and CIV activities exhibited a trend for increase by elamipretide treatment (Figures 3G and 3H), while citrate synthase activity was unchanged (Figure 3I). None of the enzyme activities was altered in the elamipretide-treated interfibrillar mitochondria (data not shown).

SUPERCOMPLEX-ASSOCIATED CIV ACTIVITY IS ALTERED WITH ELAMIPRETIDE. BN PAGE in-gel

FIGURE 4 In-gel Activities of Supercomplex-associated and Free Electron Transport Complexes in Subsarcolemmal Mitochondria

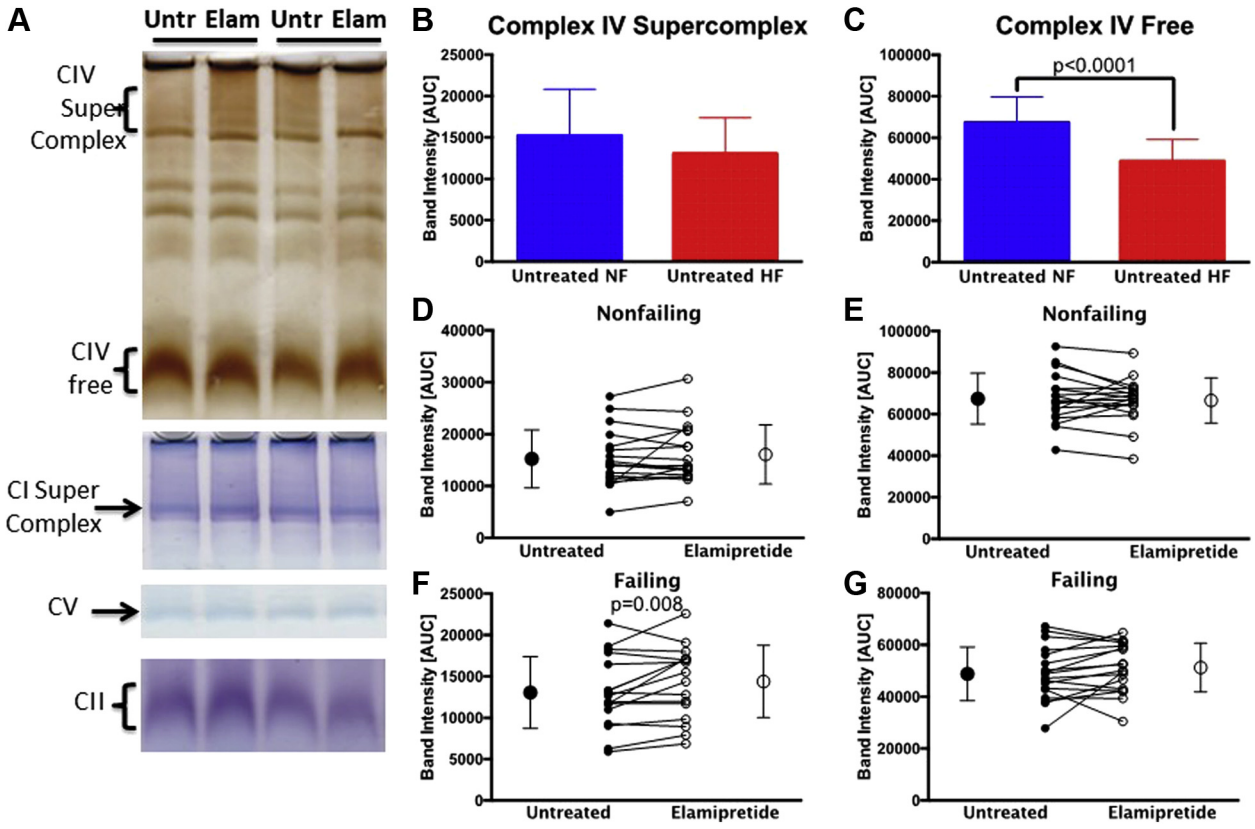

(A) Representative lanes from blue native polyacrylamide gel electrophoresis gels from failing hearts with in-gel activity stains for electron transport complexes CIV, CI, CV, and CII either free or in the supercomplex with **arrows/brackets** showing quantifiable bands on each gel. The 4 lanes represent 2 samples with untreated or elamipretide-treated mitochondria. **(B and C)** Supercomplex CIV activity is unchanged in untreated failing samples, but free CIV is decreased. **(D to G)** Elamipretide treatment of nonfailing samples had no effect on CIV activity **(D, E)** but in failing hearts improves **(F)** supercomplex-associated CIV but **(G)** not free CIV. Untreated hearts in **(D to G)** are shown with **closed circles** and treated hearts with **open circles**. NF, n = 19; HF, n = 21. AUC = area under the curve; Elam = elamipretide treated; Untr = untreated; other abbreviations as in Figure 1.

activity was used to separate supercomplex from free CIV. Figure 4A shows representative gels for CI, CII, CIV, and CV activities. CIV activity is present in a free state, within the supercomplex, and in intermediate molecular weight forms not analyzed in this study. CI is only present in its supercomplex form. When these bands were quantified, the quantity of CIV in the supercomplex was not altered in HF (Figure 4B), whereas the free CIV activity was significantly lower (Figure 4C). In nonfailing samples, elamipretide treatment had no effect on CIV regardless of whether it is bound or free (Figures 4D and 4E). By contrast, in HF, the activity of CIV in the supercomplex was significantly higher after elamipretide treatment, whereas activity of free CIV was unchanged (Figures 4F and 4G). There were no significant changes detected in the activities of CI, CII, or CV in HF or with elamipretide treatment according to this assay (data not shown).

CARDIOLIPIN COMPOSITION IS NOT ALTERED WITH ELAMIPRETIDE TREATMENT. Tetralinoleoyl cardiolipin, the predominant cardiac cardiolipin species, with 4 linoleic acids and a mass-to-charge ratio of 1448, is shown as a percentage of the total (11 major species were used for total) cardiolipin content. The percentage of tetralinoleoyl cardiolipin was significantly lower in HF, consistent with our previously reported findings (Figure 5A), but elamipretide treatment had no effect on tetralinoleoyl cardiolipin in nonfailing or HF samples (Figures 5B and 5C) (7,30). Cardiolipin absolute amounts, percent totals of 8 major cardiolipin species, monolysocardiolipin, or the sum of all cardiolipin species were unaltered after elamipretide treatment (data not shown).

FIGURE 5 Tetralinoleoyl Cardiolipin With Elamipretide Treatment

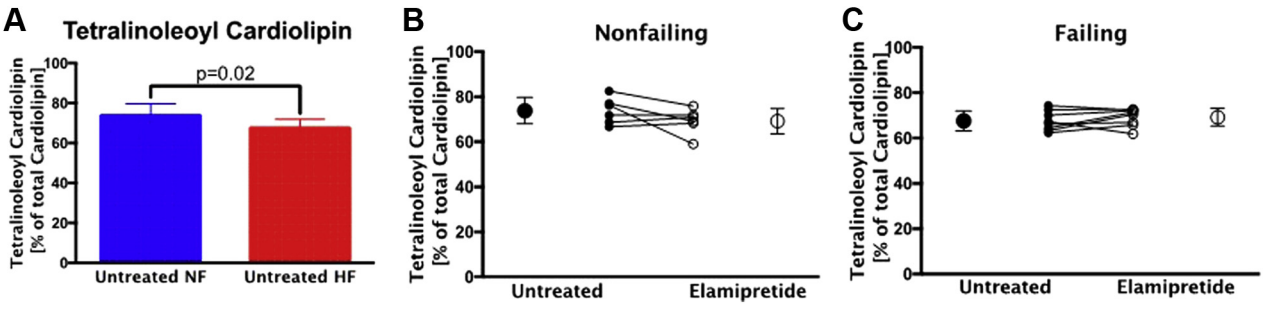

(A) The effect of HF on tetralinoleoyl cardiolipin (mass-to-charge ratio, 1,448) in untreated samples is expressed as a percentage of total cardiolipin. Elamipretide-treated **(B)** NF hearts or **(C)** HF hearts showed no changes in tetralinoleoyl cardiolipin. Untreated hearts in **B and C** are shown with **closed circles** and **treated hearts** with open circles. NF, n = 5; HF, n = 10. Abbreviations as in Figure 1.

DISCUSSION

OVERVIEW OF NOVEL FINDINGS. To the best of our knowledge, this study is the first to investigate the effect of elamipretide on mitochondrial respiration in explanted human heart tissue. Elamipretide treatment improves left ventricular volumes in adults with HF (12), suggesting a potentially new avenue for therapeutic agents in HF (31). We extended these clinical trial data by showing that impaired mitochondrial function in the failing pediatric and adult human heart can be improved with elamipretide treatment. Elamipretide treatment improved the function of components of the electron transport chain when they were associated with the supercomplex in human cardiac mitochondria from the failing ventricle. Finally, acute elamipretide treatment of human cardiac tissue improved mitochondrial and supercomplex function even though the treatment was too rapid to allow remodeling of cardiolipin. This comprehensive analysis in human heart tissue provides additional insight into the mechanism by which elamipretide treatment improves the function of the respiratory chain in human cardiac mitochondria. These findings support the use of supercomplex stabilizing compounds for the treatment of human disease (16,32).

ELAMIPRETIDE IN HUMAN DISEASE. Clinical trials have used elamipretide to address renal, cardiac, and skeletal muscle disease, but this study is the first to show reversal of mitochondrial dysfunction in HF. Elamipretide improved 6-min walk test distances in patients with mitochondrial myopathy (33) and improved left ventricular volumes in patients with HF and left ventricular dysfunction (12). Similarly, elamipretide was associated with improved kidney function after renal angioplasty (34). To our knowledge, there is only 1 other study exploring the influence of elamipretide directly on human mitochondria. Wijermars et al. (35) examined the influence of SS-31 on mitochondrial function in normal renal biopsy samples subjected to ischemic stress. An important difference between their protocol and ours was that the biopsy specimens were pretreated with the compound during the ischemic stress followed by a demonstration of attenuation of mitochondrial dysfunction in the ex vivo study. Similar to our findings in the heart, there was no effect of elamipretide on mitochondrial function in the control renal biopsy specimen. Importantly, our study is the first to report the ability to improve mitochondrial dysfunction in human disease with acute treatment with elamipretide.

ELAMIPRETIDE'S MECHANISM OF ACTION WORKS THROUGH THE ENZYMES OF THE MITOCHONDRIAL SUPERCOMPLEX. Results of high-resolution respirometry showed that elamipretide improves human cardiac mitochondrial function through improved coupling of the supercomplex-associated enzyme complexes CI, CIII, and CIV. Oxygen flux after the addition of supercomplex-specific substrates, pyruvate malate, ADP, and glutamate was impaired in the failing heart. Elamipretide improved oxygen flux in failing samples under these conditions, indicating direct activity on the supercomplex. Succinate, the next substrate added in our experimental protocol, forces the majority of electron flow through CII, a component of the respiratory chain not associated with the supercomplex (36,37). CII-mediated oxygen flux was not influenced by HF, nor was it altered by

elamipretide treatment. Furthermore, addition of rotenone, which inhibits CI and blocks all supercomplex-mediated respiration, permitted CII-mediated oxygen flux that cannot be augmented by elamipretide treatment of tissues (Supplemental Figure 3). These data show that the effect of elamipretide treatment occurs via its effect on CI/CIII/CIV supercomplex activity.

In the complementary spectrophotometry studies, total mitochondrial enzymatic activities of complexes CI and CIV were increased with elamipretide in the failing heart, with no effect on citrate synthase, a soluble enzyme not in the membrane that serves as a marker of mitochondrial content and nonmembrane-associated mitochondrial activity. Enzyme activities of CI and CIV assayed by using BN-PAGE analysis revealed increased supercomplex-associated CIV activity but not CI activity with elamipretide treatment. This result may indicate a stronger effect of elamipretide on recruitment of CIV to the supercomplex. Alternatively, BN-PAGE may not have the sensitivity to detect improvement in CI activity recorded with the enzymatic assay. Taken together, these data suggest that elamipretide improves mitochondrial function by directly affecting respiratory complexes specifically associated with the mitochondrial supercomplex, perhaps by recruiting free CIV into the supercomplex.

IMPROVEMENT OF MITOCHONDRIAL FUNCTION BY ELAMIPRETIDE IS INDEPENDENT OF CARDIOLIPIN REMODELING. Elamipretide reportedly rapidly targets mitochondria through the attraction between the positively charged residues of the peptide with the negatively charged cardiolipin head group, which is believed to improve phospholipid-dependent bioenergetics (13). Indeed, long-term treatment with elamipretide in animal models has been associated with increased mitochondrial cardiolipin remodeling to its tetralinoleoyl form (16,38). To date, however, it is unclear if cardiolipin remodeling after chronic treatment is a cause or a consequence of elamipretide's mechanism of action. We would not anticipate that elamipretide could acutely alter cardiolipin isoforms in an ex vivo system, and in fact we report here that drug treatment can improve mitochondrial function in the absence of any change in cardiolipin species.

We instead hypothesize that elamipretide may elicit its acute effects by improving the stabilization of cardiolipin-protein interactions, allowing the maintenance of the mitochondrial supercomplex.

IMPROVEMENT OF MITOCHONDRIAL FUNCTION IS INDEPENDENT OF AGE AND HF ETIOLOGY. There is a growing body of literature characterizing the unique adaptations that exist between the failing pediatric heart and the adult heart (39–45). These studies, combined with the differential response of children to adult-based HF therapies and limited improvement in pediatric HF outcomes over the past decade, suggest that investigations of pediatric-specific HF treatments are needed (46–48). Importantly, the present study included both pediatric and adult failing hearts and showed that elamipretide improves mitochondrial function across a number of different pathologic phenotypes on current evidence-based therapy. This finding is unique and provides encouraging evidence that the mitochondria may represent one final common pathway in HF and that mitochondrial-targeted therapies may have more generalizable efficacy complementary to existing HF therapies.

STUDY LIMITATIONS. First, this study was unable to elucidate the mechanisms underlying chronic exposure to elamipretide. Although this study concluded that elamipretide does have a positive effect on mitochondrial function via the enzymes of the supercomplex, and this mechanism does not involve changes in quantity or quality of cardiolipin, the exposure time to elamipretide was limited to a few hours. Future studies are needed to determine the influence of chronic treatment on human mitochondrial function. Second, this study was performed with all hearts that were sequentially collected by our tissue bank over the course of several years. Additional research in larger populations will be necessary to determine if specific disease phenotypes derive greater benefit than others. Third, systemic administration of elamipretide could affect all other mitochondrial-containing tissues and could cause off-target effects not measured by these assays. Fourth, because the experiments were performed in heart tissue in isolation, concentrations of elamipretide in the ex vivo experiments cannot be extrapolated to in vivo treatment. Lastly, because elamipretide binds to the mitochondrial membrane, other membrane-dependent processes such as cross-talk with the endoplasmic reticulum and calcium signaling could be involved; however, this study was limited in scope to the effect of elamipretide on the supercomplex and electron transport system. Any additional effects of elamipretide on human mitochondrial calcium transport and endoplasmic reticulum–mitochondria interactions would need to be analyzed in future studies.

CONCLUSIONS

A new class of mitochondrial-targeted drugs, which includes elamipretide, represents a promising new strategy for the treatment of HF (49). A central

problem in HF is the inability of the heart to adequately meet its own metabolic demands due to altered mitochondrial function and metabolism. These drugs offer targeted benefits through improvement of mitochondrial function and energy production. The present study is the first to assess the impact of a member of this new class of compounds directly on human heart tissue. The findings of the current study are the first to report rapid improvement in mitochondrial function in the human heart, likely through improved coupling of the mitochondrial supercomplex. These data support the use of mitochondrial-targeted pharmaceutical agents to improve energetics and mitochondrial function in the failing heart.

ADDRESS FOR CORRESPONDENCE: Dr. Brian L. Stauffer, University of Colorado Anschutz Medical Campus, 12700 East 19th Avenue, B139, Aurora, Colorado 80045. E-mail: brian.stauffer@ucdenver.edu.

PERSPECTIVES

COMPETENCY IN MEDICAL KNOWLEDGE: Elamipretide, a premier member of a new class of mitochondrial-targeted compounds, improves mitochondrial function in failing myocardium via increased activity of respiratory CI and IV, and efficiency of these complexes in a respiratory supercomplex, improving overall mitochondrial oxygen flux. These data support the use of mitochondrial-targeted therapies to augment oxidative phosphorylation and provide a novel approach to the treatment of human HF.

TRANSLATIONAL OUTLOOK: Mitochondrial-targeted drugs such as elamipretide show promise as novel therapies that improve efficiency of mitochondrial energy production in HF caused by structural or myocardial disease.

REFERENCES

1. Ingwall JS, Weiss RG. Is the failing heart energy starved? On using chemical energy to support cardiac function. Circ Res 2004;95:135–45.

2. Bayeva M, Gheorghiade M, Ardehali H. Mitochondria as a therapeutic target in heart failure. J Am Coll Cardiol 2013;61:599–610.

3. Brown DA, Perry JB, Allen ME, et al. Expert consensus document: mitochondrial function as a therapeutic target in heart failure. Nat Rev Cardiol 2017;14:238–50.

4. Xu Y, Phoon CK, Berno B, et al. Loss of protein association causes cardiolipin degradation in Barth syndrome. Nature Chem Biol 2016;12:641–7.

5. Mileykovskaya E, Dowhan W. Cardiolipin-dependent formation of mitochondrial respiratory supercomplexes. Chem Phys Lipids 2014;179:42–8.

6. Zhang M, Mileykovskaya E, Dowhan W. Gluing the respiratory chain together. Cardiolipin is required for supercomplex formation in the inner mitochondrial membrane. J Biological Chemistry 2002;277:43553–6.

7. Chicco AJ, Sparagna GC. Role of cardiolipin alterations in mitochondrial dysfunction and disease. Am J Physiol Cell Physiol 2007;292:C33–44.

8. Paradies G, Paradies V, Ruggiero FM, Petrosillo G. Cardiolipin and mitochondrial function in health and disease. Antioxidants Redox Signaling 2014;20:1925–53.

9. Chicco A, Sparagna G, McCune S, et al. Linoleate-rich high-fat diet decreases mortality in hypertensive heart failure rats compared to lard and low-fat diets. Hypertension 2008;52:549–55.

10. Ajith TA, Jayakumar TG. Mitochondria-targeted agents: future perspectives of mitochondrial pharmaceutics in cardiovascular diseases. World J Cardiol 2014;6:1091–9.

11. Szeto HH. First-in-class cardiolipin-protective compound as a therapeutic agent to restore mitochondrial bioenergetics. Br J Pharmacol 2014;171:2029–50.

12. Daubert MA, Yow E, Dunn G, et al. Novel mitochondria-targeting peptide in heart failure treatment: a randomized, placebo-controlled trial of elamipretide. Circ Heart Fail 2017;10.

13. Zhao K, Zhao GM, Wu D, et al. Cell-permeable peptide antioxidants targeted to inner mitochondrial membrane inhibit mitochondrial swelling, oxidative cell death, and reperfusion injury. J Biol Chem 2004;279:34682–90.

14. Birk AV, Chao WM, Bracken C, Warren JD, Szeto HH. Targeting mitochondrial cardiolipin and the cytochrome c/cardiolipin complex to promote electron transport and optimize mitochondrial ATP synthesis. Br J Pharmacol 2014;171:2017–28.

15. Dai W, Shi J, Gupta RC, Sabbah HN, Hale SL, Kloner RA. Bendavia, a mitochondria-targeting peptide, improves postinfarction cardiac function, prevents adverse left ventricular remodeling, and restores mitochondria-related gene expression in rats. J Cardiovasc Pharmacol 2014;64:543–53.

16. Sabbah HN, Gupta RC, Kohli S, Wang M, Hachem S, Zhang K. Chronic therapy with elamipretide (MTP-131), a novel mitochondria-targeting peptide, improves left ventricular and mitochondrial function in dogs with advanced heart failure. Circ Heart Fail 2016;9:e002206.

17. Shi J, Dai W, Hale SL, et al. Bendavia restores mitochondrial energy metabolism gene expression and suppresses cardiac fibrosis in the border zone of the infarcted heart. Life Sci 2015;141:170–8.

18. Cho J, Won K, Wu D, et al. Potent mitochondria-targeted peptides reduce myocardial infarction in rats. Coron Artery Dis 2007;18:215–20.

19. Veksler VI, Kuznetsov AV, Sharov VG, Kapelko VI, Saks VA. Mitochondrial respiratory parameters in cardiac tissue: a novel method of assessment by using saponin-skinned fibers. Biochim Biophys Acta 1987;892:191–6.

20. Sparagna GC, Johnson CA, McCune SA, Moore RL, Murphy RC. Quantitation of cardiolipin molecular species in spontaneously hypertensive heart failure rats using electrospray ionization mass spectrometry. J Lipid Res 2005;46:1196–204.

21. Palmer JW, Tandler B, Hoppel CL. Biochemical properties of subsarcolemmal and interfibrillar mitochondria isolated from rat cardiac muscle. J Biol Chem 1977;252:8731–9.

22. Chatfield KC, Coughlin CR 2nd, Friederich MW, et al. Mitochondrial energy failure in HSD10 disease is due to defective mtDNA transcript processing. Mitochondrion 2015;21:1–10.

23. Friederich MW, Erdogan AJ, Coughlin CR 2nd., et al. Mutations in the accessory subunit NDUFB10 result in isolated complex I deficiency and illustrate the critical role of intermembrane space import for complex I holoenzyme assembly. Hum Mol Genet 2017;26:702–16.

24. Van Coster R, Smet J, George E, et al. Blue native polyacrylamide gel electrophoresis: a powerful tool in diagnosis of oxidative phosphorylation defects. Pediatr Res 2001;50:658–65.

25. Letellier T, Malgat M, Coquet M, Moretto B, Parrot-Roulaud F, Mazat JP. Mitochondrial myopathy studies on permeabilized muscle fibers. Pediatr Res 1992;32:17–22.

26. Gnaiger EKA, Schneeberger S, Seiler R, Brandacher G, Steurer W, Margreiter R. Mitochondria in the cold. In: Heldmaier GKM, editor.

Life in the Cold. Berlin, Germany: Heidelberg/New York, NY: Springer, 2000:431–42.

27. Bligh EG, Dyer WJ. A rapid method of total lipid extraction and purification. Can J Biochem Physiol 1959;37:911–7.

28. Curran-Everett D, Benos DJ. Guidelines for reporting statistics in journals published by the American Physiological Society. Am J Physiol Regulatory Integrative Comparative Physiol 2004; 287:R247–9.

29. Lanza IR, Nair KS. Functional assessment of isolated mitochondria in vitro. Methods Enzymol 2009;457:349–72.

30. Chatfield KC, Sparagna GC, Sucharov CC, et al. Dysregulation of cardiolipin biosynthesis in pediatric heart failure. J Mol Cell Cardiol 2014;74: 251–9.

31. Mann DL. Targeting myocardial energetics in the failing heart: are we there yet? Circ Heart Fail 2017;10.

32. Dai DF, Chen T, Szeto H, et al. Mitochondrial targeted antioxidant peptide ameliorates hypertensive cardiomyopathy. J Am Coll Cardiol 2011; 58:73–82.

33. Karaa A, Haas R, Goldstein A, Vockley J, Weaver WD, Cohen BH. Randomized dose-escalation trial of elamipretide in adults with primary mitochondrial myopathy. Neurology 2018; 90:e1212–21.

34. Saad A, Herrmann SMS, Eirin A, et al. Phase 2a clinical trial of mitochondrial protection (elamipretide) during stent revascularization in patients with atherosclerotic renal artery stenosis. Circ Cardiovasc Interv 2017;10.

35. Wijermars LG, Schaapherder AF, de Vries DK, et al. Defective postreperfusion metabolic recovery directly associates with incident delayed graft function. Kidney Int 2016;90:181–91.

36. Lapuente-Brun E, Moreno-Loshuertos R, Acin-Perez R, et al. Supercomplex assembly determines electron flux in the mitochondrial electron transport chain. Science (New York, NY) 2013;340: 1567–70.

37. Lancaster CR, Kroger A. Succinate: quinone oxidoreductases: new insights from X-ray crystal structures. Biochimica et biophysica acta 2000; 1459:422–31.

38. Eirin A, Ebrahimi B, Zhang X, et al. Mitochondrial protection restores renal function in swine atherosclerotic renovascular disease. Cardiovasc Res 2014;103:461–72.

39. Miyamoto SD, Stauffer BL, Polk J, et al. Gene expression and beta-adrenergic signaling are altered in hypoplastic left heart syndrome. J Heart Lung Transplant 2014;33:785–93.

40. Nakano SJ, Miyamoto SD, Movsesian M, Nelson P, Stauffer BL, Sucharov CC. Age-related differences in phosphodiesterase activity and effects of chronic phosphodiesterase inhibition in idiopathic dilated cardiomyopathy. Circ Heart Fail 2015;8:57–63.

41. Nakano SJ, Sucharov J, van Dusen R, et al. Cardiac adenylyl cyclase and phosphodiesterase expression profiles vary by age, disease, and chronic phosphodiesterase inhibitor treatment. J Card Fail 2017;23:72–80.

42. Stauffer BL, Russell G, Nunley K, Miyamoto SD, Sucharov CC. miRNA expression in pediatric failing human heart. J Mol Cell Cardiol 2013;57:43–6.

43. Sucharov CC, Sucharov J, Karimpour-Fard A, Nunley K, Stauffer BL, Miyamoto SD. Micro-RNA expression in hypoplastic left heart syndrome. J Card Fail 2015;21:83–8.

44. Tatman PD, Woulfe KC, Karimpour-Fard A, et al. Pediatric dilated cardiomyopathy hearts display a unique gene expression profile. JCI Insight 2017;2.

45. Patel MD, Mohan J, Schneider C, et al. Pediatric and adult dilated cardiomyopathy represent distinct pathological entities. JCI Insight 2017;2.

46. Rossano JW, Shaddy RE. Update on pharmacological heart failure therapies in children: do adult medications work in children and if not, why not? Circulation 2014;129:607–12.

47. Shaddy RE, Boucek MM, Hsu DT, et al. Carvedilol for children and adolescents with heart failure: a randomized controlled trial. JAMA 2007; 298:1171–9.

48. Kantor PF, Abraham JR, Dipchand AI, Benson LN, Redington AN. The impact of changing medical therapy on transplantation-free survival in pediatric dilated cardiomyopathy. J Am Coll Cardiol 2010;55:1377–84.

49. Steggall A, Mordi IR, Lang CC. Targeting metabolic modulation and mitochondrial dysfunction in the treatment of heart failure. Diseases (Basel, Switzerland) 2017;5.

KEY WORDS heart failure, high-resolution respirometry, mitochondrial-targeted compounds, supercomplex

APPENDIX For supplemental tables and figures, please see the online version of this paper.

JACC: BASIC TO TRANSLATIONAL SCIENCE VOL. 4, NO. 2, 2019
© 2019 THE AUTHORS. PUBLISHED BY ELSEVIER ON BEHALF OF THE AMERICAN COLLEGE OF CARDIOLOGY FOUNDATION. THIS IS AN OPEN ACCESS ARTICLE UNDER THE CC BY-NC-ND LICENSE (http://creativecommons.org/licenses/by-nc-nd/4.0/).

EDITORIAL COMMENT

Targeting Mitochondrial Function in Heart Failure

Makes Sense But Will it Work?*

Muhammad Shahzeb Khan, MD,[a] Javed Butler, MD, MPH, MBA[b]

Humans produce approximately their body weight equivalent adenosine triphosphate (ATP) (~65 kg) each day, and although the heart is only ~0.5% of body weight, it consumes roughly 8% of ATP generated (1). The heart possesses the highest content of mitochondria of any tissue. Approximately 90% of cellular ATP is used to support the contraction-relaxation cycle (2). Calcium sequestration into the sarcoplasmic reticulum also requires ATP. Production of energy in the human heart is a dynamic process because the heart stores only enough energy to support a few heartbeats. Mitochondria therefore must operate efficiently to respond promptly to the ever-changing energy needs as required by the rest of the body's function. Mitochondrial abnormalities and reduced capacity to generate ATP can have a profound impact in heart failure (HF). Abnormal mitochondria are also linked to myocyte injury because they are a major source of reactive oxygen species production that can induce cellular damage. Abnormal mitochondria also promote programmed cell death through the release of cytochrome *c* into the cytosolic compartment and activation of caspases (3).

Progression to HF is associated with a decline in energy reserve capacity that ultimately reaches a threshold after which compensatory mechanisms can no longer support the decreasing energy supply. Moreover, skeletal muscles also show mitochondrial dysfunction in HF, thus contributing to exercise intolerance (4). Mitochondrial dysfunction is also seen in patients with renal insufficiency (5) and in insulin resistance (6). Because patients with HF often have both renal insufficiency and insulin resistance, treating mitochondrial dysfunction in HF hold promise to help through cardiac and extracardiac mechanisms.

SEE PAGE 147

In this issue of *JACC: Basic to Translational Science*, Chatfield et al. (7) describe mitochondrial function impairment in failing ventricular tissue and investigate the impact of elamipretide on mitochondrial and supercomplex function in failing pediatric and adult human hearts ex vivo. These investigators report that elamipretide improved mitochondrial oxygen flux, complex (C) I and IV activities, and supercomplex-associated CIV activity in failing human hearts, whereas the drug had no significant effect on normal mitochondrial function in nonfailing human hearts. Previous studies with elamipretide showed that the drug directly improved energetics in various animal models (8,9). The study by Chatfield et al. (7) is 1 of the studies to demonstrate direct acute effects of elamipretide on ex vivo human hearts.

*Editorials published in *JACC: Basic to Translational Science* reflect the views of the authors and do not necessarily represent the views of *JACC: Basic to Translational Science* or the American College of Cardiology.

From the [a]Department of Medicine, Cook County Hospital, Chicago, Illinois; and the [b]Department of Medicine, University of Mississippi, Jackson, Mississippi. Dr. Butler has received research support from the National Institutes of Health, Patient Centered Outcomes Research, and the European Union; serves on the Speakers Bureau for Novartis, Janssen, and NovoNordisk; and is a consultant for Abbott, Adrenomed, Amgen, Array, AstraZeneca, Bayer, Berlin Cures, Boehringer Ingelheim, Bristol-Myers Squibb, Cardiocell, Corvidia, CVRx, G3 Pharmaceutical, Innolife, Janssen, Lantheus, LinaNova, Luitpold, Medscape, Medtronic, Merck, Novartis, NovoNordisk, Relypsa, Roche, Sanofi, StealthPeptide, South Carolina Pharma, V-Wave Limited, Vifor, and ZS Pharma. Dr. Khan has reported that he has no relationships relevant to the contents of this paper to disclose.

All authors attest they are in compliance with human studies committees and animal welfare regulations of the authors' institutions and Food and Drug Administration guidelines, including patient consent where appropriate. For more information, visit the *JACC: Basic to Translational Science* author instructions page.

ISSN 2452-302X https://doi.org/10.1016/j.jacbts.2019.03.003

The study by Chatfield et al. (7) also gives additional insight into the mechanism of action of elamipretide, thereby suggesting that the drug improves human cardiac function through better coupling of supercomplex-associated enzyme complexes, CI, CIII, and CIV, instead of cardiolipin remodeling. The main mechanism of elamipretide benefits is believed to arise from stabilizing cardiolipin through inhibition of cytochrome *c*-cardiolipin peroxidase complex and thus allowing maximum energy production (10,11). However, Chatfield et al. (7) report that cardiolipin absolute amounts and the sum of all cardiolipin species were unaltered after elamipretide treatment, a finding indicating that the drug may improve mitochondrial function without an effect on cardiolipin. These findings should be considered with caution because the exposure time to the intervention was limited, and the concentrations of elamipretide needed to produce such results could well vary ex vivo and in vivo. The current study also highlights that elamipretide improves mitochondrial function independent of age and HF etiology, thus suggesting that mitochondria may represent 1 common final pathway in HF.

Although the study by Chatfield et al. (7) elegantly provides evidence that elamipretide improves myocardial energetics in failing myocardium, the question remains whether this mechanistic benefit will translate into clinical benefit, given that previous attempts to restore myocardial energetics have inconsistently led to clinical benefit. Fatty acid oxidation reduction with the use of trimetazidine and inhibition of excitation-contraction coupling with ranolazine did not improve HF outcomes (12,13). Although reactive oxygen species damage cardiolipin and result in mitochondrial dysfunction, none of the antioxidants have proved to be beneficial in HF; in fact, long-term supplementation of vitamin E (tocopherol) conferred an increased risk for HF (14,15). On the contrary, several trials have shown benefit of intravenous iron supplementation in patients with HF (16).

In the EMBRACE STEMI (Evaluation of Myocardial Effects of Bendavia for Reducing Reperfusion Injury in Patients With Acute Coronary Events-ST-Segment Elevation Myocardial Infarction) trial, elamipretide did not improve the primary or secondary outcomes (17). In the randomized placebo-controlled trial of elamipretide in HF (18), the drug was shown to reduce left ventricular volumes; however, the confidence intervals were wide in this small study, and there were no changes in biomarker data. Elamipretide is currently being investigated (NCT02788747, NCT02814097, and NCT02914665) in larger HF studies to determine its effect on cardiac remodeling and clinical outcomes.

HF is a complex syndrome involving multiple altered physiological mechanisms and organ systems that interact. The results reported by Chatfield et al. (7) are encouraging, and mitochondria remain a promising therapeutic target. Data from carefully designed and conducted clinical trials are now needed to show whether the promise is actually fulfilled.

ADDRESS FOR CORRESPONDENCE: Dr. Javed Butler, Department of Medicine, L-605, University of Mississippi Medical Center, 2500 North State Street, Jackson, Mississippi 39216. E-mail: jbutler4@umc.edu.

REFERENCES

1. Tornroth-Horsefield S, Neutze R. Opening and closing the metabolite gate. Proc Natl Acad Sci U S A 2008;105:19565–6.

2. Opie L. The Heart: Physiology, from Cell to Circulation. 3rd ed. Philadelphia: Lippincott-Raven, 1998.

3. Brown DA, Perry JB, Allen ME, et al. Expert consensus document: mitochondrial function as a therapeutic target in heart failure. Nat Rev Cardiol 2016;14:238–50.

4. Abozguia K, Phan TT, Shivu GN, et al. Reduced in vivo skeletal muscle oxygen consumption in patients with chronic heart failure — a study using near infrared spectrophotometry (NIRS). Eur J Heart Fail 2008;10:652–7.

5. Eirin A, Ebrahimi B, Zhang X, et al. Mitochondrial protection restores renal function in swine atherosclerotic renovascular disease. Cardiovasc Res 2014;103:461–72.

6. Anderson EJ, Lustig ME, Boyle KE, et al. Mitochondrial H_2O_2 emission and cellular redox state link excess fat intake to insulin resistance in both rodents and humans. J Clin Invest 2009;3:573–81.

7. Chatfield KC, Sparagna GC, Chau S, et al. Elamipretide improves mitochondrial function in the failing human heart. J Am Coll Cardiol Basic Trans Science 2019;4:147–57.

8. Sabbah HN, Gupta RC, Kohli S, Wang M, Hachem S, Zhang K. Chronic therapy with elamipretide (MTP-131), a novel mitochondria-targeting peptide, improves left ventricular and mitochondrial function in dogs with advanced heart failure. Circ Heart Fail 2016;9:e002206.

9. Shi J, Dai W, Hale SL, et al. Bendavia restores mitochondrial energy metabolism gene expression and suppresses cardiac fibrosis in the border zone of the infarcted heart. Life Sci 2015;141:170–8.

10. Dai DF, Hsieh EJ, Chen T, et al. Global proteomics and pathway analysis of pressure-overload-induced heart failure and its attenuation by mitochondrial-targeted peptides. Circ Heart Fail 2013;6:1067–76.

11. Birk A, Chao W, Bracken C, Warren J, Szeto H. Targeting mitochondrial cardiolipin and the cytochrome c/cardiolipin complex to promote electron transport and optimize mitochondrial ATP synthesis. Br J Pharmacol 2014;171:2017–28.

12. Mann DL. Targeting myocardial energetics in the failing heart: are we there yet? Circ Heart Fail 2017;10:4658.

13. Steggall A, Mordi IR, Lang CC. Targeting metabolic modulation and mitochondrial

dysfunction in the treatment of heart failure. Diseases 2017;5:E14.

14. Marchioli R, Levantesi G, Macchia A, et al. Vitamin E increases the risk of developing heart failure after myocardial infarction: results from the GISSI-Prevenzione trial. J Cardiovasc Med (Hagerstown) 2006;7:347–50.

15. Bayeva M, Gheorghiade M, Ardehali H. Mitochondria as a therapeutic target in heart failure. J Am Coll Cardiol 2013;61:599–610.

16. Rocha BML, Cunha GJL, Menezes Falcao LF. The burden of iron deficiency in heart failure: therapeutic approach. J Am Coll Cardiol 2018;71:782–93.

17. Gibson CM, Giugliano RP, Kloner RA, et al. EMBRACE STEMI study: a phase 2a trial to evaluate the safety, tolerability, and efficacy of intravenous MTP-131 on reperfusion injury in patients undergoing primary percutaneous coronary intervention. Eur Heart J 2016;37:1296–303.

18. Daubert MA, Yow E, Dunn G, et al. Novel mitochondria-targeting peptide in heart failure treatment: a randomized, placebo-controlled trial of elamipretide. Circ Heart Fail 2017;10:e004389.

KEY WORDS ATP, elamipretide, heart failure, mitochondria, novel agents

JACC: BASIC TO TRANSLATIONAL SCIENCE VOL. 4, NO. 2, 2019
© 2019 THE AUTHORS. PUBLISHED BY ELSEVIER ON BEHALF OF THE AMERICAN COLLEGE OF CARDIOLOGY FOUNDATION. THIS IS AN OPEN ACCESS ARTICLE UNDER THE CC BY-NC-ND LICENSE (http://creativecommons.org/licenses/by-nc-nd/4.0/).

PRECLINICAL RESEARCH

Glucagon Receptor Antagonism Ameliorates Progression of Heart Failure

Chen Gao, PhD,[a] Shuxun Vincent Ren, MD, PhD,[a] Junyi Yu, MD,[a,b] Ulysis Baal,[a] Dung Thai, MD, PhD,[c,d] John Lu, MD, PhD,[c,d] Chunyu Zeng, MD, PhD,[b] Hai Yan, PhD,[c,d] Yibin Wang, PhD[a]

VISUAL ABSTRACT

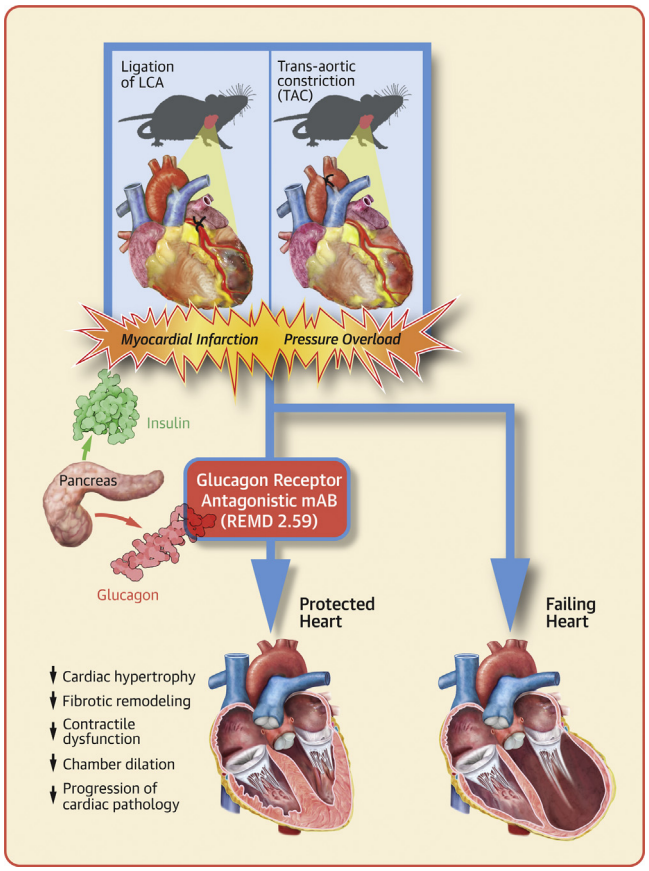

Gao, C. et al. J Am Coll Cardiol Basic Trans Science. 2019;4(2):161–72.

HIGHLIGHTS

- **Systemic treatment of an antibody-based glucagon receptor antagonist confers cardioprotection against myocardial infarction and post-myocardial infarction remodeling in mice.**
- **Systemic treatment of glucagon receptor antagonist prevents pressure overload induced cardiac remodeling and dysfunction in mice.**
- **Glucagon receptor antagonist treatment attenuates the pathological progression of heart failure induced by pressure overload in mice.**
- **Long-term suppression of glucagon signaling is potentially an effective therapy for heart failure with different etiologies independent of metabolic disorders.**

From the [a]Department of Anesthesiology, Cardiovascular Research Laboratories, David Geffen School of Medicine, University of California, Los Angeles, Los Angeles, California; [b]Department of Cardiology, Daping Hospital, The Third Military Medical University, Chongqing, China; [c]REMD Biotherapeutics, Camarillo, California; and [d]Beijing Cosci-REMD Biotherapeutics, Beijing, China. This work is supported in part by National Institutes of Health grants HL140116 to Dr. Wang. Dr. Gao is a recipient of Postdoctoral Fellowship from American Heart Association (17POST33661136). Drs. Thai, Lu, and Yan are employees of REMD Biotherapeutics. Dr. Wang has served as consultant for REMD Biotherapeutics. All other authors have reported that they have no relationships relevant to the contents of this paper to disclose.

ISSN 2452-302X https://doi.org/10.1016/j.jacbts.2018.11.001

JACC: BASIC TO TRANSLATIONAL SCIENCE VOL. 4, NO. 2, 2019
APRIL 2019:161–72

ABBREVIATIONS AND ACRONYMS

GCGR = glucagon receptor

GLC = glucagon

MI = myocardial infarction

PBS = phosphate-buffered saline

PCR = polymerase chain reaction

TAC = transaortic constriction

SUMMARY

Mice were treated with a fully human monoclonal glucagon receptor antagonistic antibody REMD2.59 following myocardial infarction or pressure overload. REMD2.59 treatment blunted cardiac hypertrophy and fibrotic remodeling, and attenuated contractile dysfunction at 4 weeks after myocardial infarction. In addition, REMD2.59 treatment at the onset of pressure overload significantly suppressed cardiac hypertrophy and chamber dilation with marked preservation of cardiac systolic and diastolic function. Initiation of REMD2.59 treatment 2 weeks after pressure overload significantly blunted the progression of cardiac pathology. These results provide the first in vivo proof-of-concept evidence that glucagon receptor antagonism is a potentially efficacious therapy to ameliorate both onset and progression of heart failure. (J Am Coll Cardiol Basic Trans Science 2019;4:161–72) © 2019 The Authors. Published by Elsevier on behalf of the American College of Cardiology Foundation. This is an open access article under the CC BY-NC-ND license (http://creativecommons.org/licenses/by-nc-nd/4.0/).

Heart failure affects approximately 6.5 million people over 20 years of age in the United States, with its prevalence estimated to increase about 45% by 2030 to almost 8 million (1). It is a chronic disease with complex etiology and heterogeneity in its pathological manifestations. Major risk factors for heart failure include smoking, hypertension, and obesity, as well as lifestyle and dietary influences. Despite significant advancement in the standard care of heart failure, the 5-year mortality rate of the disease remains at nearly 50% (1). The new effective therapies for heart failure are critically needed for such a major unmet need.

SEE PAGE 173

Glucagon (GLC) is a peptide hormone produced by pancreatic α-cells (2–6). As a major catabolic hormone, GLC stimulates glucose production from glycogen in liver and promotes gluconeogenesis while it inhibits glycolysis and glycogen synthesis (4). It increases blood glucose and energy expenditure as part of the energy mobilization process in response to hypoglycemia and other bioenergetic stress. Consequently, GLC serves as a counterbalancing hormone with insulin to regulate glucose homeostasis depending on nutrient conditions and available energy sources (7). The GLC receptor (GCGR) is a member of the G protein-coupled receptor family (3,6,8,9). The canonical function of GCGR elicited by GLC is mediated by G protein-coupled protein kinase A activation; however, tissue-specific function of GCGR has been implicated in different cellular processes (2,3,10). Elevated GLC is observed in chronic hyperglycemia associated with type 1 or type 2 diabetes (11–13). Overactivated GLC signaling may contribute to disease progression of diabetes by enhancing glucose production and aggravating systemic hyperglycemia, as well as impairing insulin signaling. Therefore, GCGR inhibition, using either small molecules or antagonistic antibodies, is potentially efficacious to treat diabetes as demonstrated in both preclinical studies as well as several recent clinical trials (11–21). However, much of the previous studies on GLC signaling are in the liver and brain, involving glucose metabolic regulation (2,3,22). Its specific and cell-autonomous role in cardiac tissue has just begun to be appreciated.

Other than glucose regulation in liver, GCGR is also widely expressed in multiple other tissues, including the heart (3,15,18,23–28). In a recent study by Ali et al. (29), GLC stimulation was shown to promote ischemia injury in mouse heart while cardiomyocyte specific GCGR inactivation protected the heart from pathological remodeling following myocardial infarction. This study highlights the potential cardiomyocyte cell-autonomous effect of GCGR overactivation in cardiac pathological remodeling, and GCGR antagonism as a potential therapy for heart failure. REMD-477 is a fully human anti-GCGR antibody that competitively blocks GLC binding to the GCGR with 30-pM binding affinity, and can effectively inhibit the receptor activity at low nanomolar concentrations in cell-based functional assays (14,17,20). Compared with small-molecule approaches (30), antibody-based GCGR antagonism such as REMD-477 is a competitive antagonist and does not have deleterious effects on serum lipid profiles (11,12,19,21,31). Finally, REMD-477

All authors attest they are in compliance with human studies committees and animal welfare regulations of the authors' institutions and Food and Drug Administration guidelines, including patient consent where appropriate. For more information, visit the *JACC: Basic to Translational Science* author instructions page.

Manuscript received April 2, 2018; revised manuscript received November 1, 2018, accepted November 2, 2018.

has been shown to be safe in a phase I study (NCT02715193) and is being tested in 2 phase II clinical studies (NCT03117998 and NCT02455011 for type 1 and type 2 diabetes, respectively). In short, anti-GCGR antibody offers a novel tool to effectively and specifically inhibit GCGR with proven record of clinical safety and efficacy at molecular and metabolic levels.

Functionally identical as REMD-477, REMD2.59 is a surrogate human antibody specifically generated for preclinical studies in rodents (32). In a recent study, weekly treatment with REMD2.59 is shown to reverse diabetes in *ob/ob* mice and improves cardiac function associated with diabetic cardiomyopathy (32). Although this study supports the cardioprotective effect of GCGR antagonism, it is not clear whether the beneficial effect is a direct consequence of cardioprotection on cardiomyocyte or an indirect result of improved global glucose homeostasis and insulin signaling. In the current study, we employed 2 mechanistically divergent and diabetes-independent murine disease models for heart failure, myocardial infarction, and pressure overload, to test whether the cardioprotection by the GCGR antibody is the primary effect of the receptor inhibition. Based on morphological, functional, and molecular parameters, treatment with GCGR antibody REMD2.59 significantly ameliorated the development of heart failure, by attenuating pathological remodeling and cardiac hypertrophy while preventing functional deterioration and pathological gene expression. These novel and exciting observations implicate a potential role of GLC-mediated signaling in heart failure via a cardiomyocyte cell-autonomous mechanism. It raises the prospect of targeting GCGR as potential therapy to treat common forms of heart failure independent of the confounding status of global glucose metabolic disorders.

METHODS

ANIMALS. C57BL/6 male mice (Jackson Laboratory, Bar Harbor, Maine) were used in this study, and all mice were housed in groups of 4 to 5 mice per cage in a room maintained at 23 ± 1°C and 55 ± 5% humidity with a 12-h light-dark cycle and given ad libitum access to food and water.

MYOCARDIAL INFARCTION. Myocardial infarction (MI) was induced in mice by ligation of the left anterior coronary artery. Briefly, the chest was opened via a left thoracotomy. The left coronary artery was identified visually using a stereo microscope, and a 7-0 suture (Ethicon, Inc., Somerville, New Jersey) was placed around the artery 1 to 2 mm below the left auricle. The electrocardiogram was monitored continuously. Permanent occlusion of the left coronary artery resulted from its ligation with the suture. Myocardial ischemia was confirmed by pallor in heart color and ST-segment elevation. The chest was closed with 6-0 silk suture. Once spontaneous respiration resumed, the endotracheal tube was removed.

TRANSAORTIC CONSTRICTION. In the transaortic constriction (TAC) study, after intubation using a 20-gauge plastic needle, mice were placed on a volume ventilator (80 breaths/min, 1.2 ml/g/min) and the anesthesia maintained by isoflurane. The chest was opened via a limited incision in the third intercostal space. The aorta was identified at the T8 region. A 6-0 silk suture was passed around the transverse aorta and tightened against a 27-gauge needle followed by the removal of the needle. Pressure gradient was evaluated by transaortic Doppler.

TREATMENT PROTOCOL. For the MI study, a total of 56 C57BL/6 male mice 8 to 10 weeks of age were operated on by occluding the left anterior coronary artery. Then they were randomly divided into 3 groups: 1) vehicle-treated (phosphate-buffered saline [PBS]) control mice (n = 20); 2) monoclonal antibody against GCGR-treated (mAb REMD2.59) mice (n = 18; 7 mg/kg, subcutaneously, 2 injections at 2 h and 14 days post-MI); and 3) GLC-treated mice (n = 18; 30 μg/kg body weight in 10% gelatin, 4 times/day for the first 6 days). For the TAC study, C57BL6 mice at 6 to 7 weeks of age were randomly divided into 2 groups: 5 sham operated as baseline control mice and 29 mice operated for TAC. The TAC-operated animals were randomly divided into 3 treatment groups: 1) vehicle treated (n = 11; antibody dilation buffer A: 10-mM NaAcetate, 5% sorbitol, 0.004% Tween 20, pH 5.2, weekly subcutaneous injection); 2) REMD2.59 treated (n = 7; 7 mg/kg, subcutaneous injection, weekly started at the onset of TAC); and 3) REMD2.59 therapy (n = 11; 7 mg/kg, subcutaneous injection, weekly started 2 weeks after the onset of TAC).

CARDIAC PHYSIOLOGY. For echocardiography, in vivo cardiac function was assessed by transthoracic echocardiography (Acuson P300, 18-MHz transducer, Siemens [Siemens Healthcare Diagnostics, Tarrytown, New York] and VisualSonics 2100 [Fujifilm Visualsonics, Toronto, Ontario, Canada]) in conscious mice for the MI study and anesthetized mice for the TAC study. From left ventricle short-axis view, an M-mode echocardiogram was acquired to measure left ventricular end-systolic and diastolic diameters. Ejection fraction and fractional shortening were calculated using onboard software package (Vevo Imaging System 2100 [Fujifilm Visualsonics]).

Imaging acquisition and analyses were performed by investigators blinded to treatments. For hemodynamic measurements, a Mikro-tip catheter (SPR1000, Millar Instruments, Houston, Texas) was inserted into the left ventricle. Left ventricular pressure was recorded with the Powerlab Data Acquisition System (ADInstruments Inc., Colorado Springs, Colorado) and calculated into left ventricular developed pressure as end-systolic pressure minus end-diastolic pressure, as well as positive maximal left ventricular pressure derivative (+dp/dtmax) and negative maximal left ventricular pressure derivative (−dp/dtmax) using Chart 7 software (AD Instruments, Colorado Springs, Colorado).

HISTOLOGICAL STUDIES. Hearts were fixed with 10% buffered formalin, embedded in paraffin, and sectioned at 4 μm. One middle longitudinal section per heart was stained with Masson's trichrome (HT-15, Sigma-Aldrich, St. Louis, Missouri). Eight randomly selected fields (400×) from the noninfarct area in the left ventricle were examined for fibrosis and myocyte size under a microscope. Each group comprised 5 to 6 hearts, and a minimum of 40 fields were analyzed in each group by computerized planimetry (ImageJ, National Institutes of Health, Bethesda, Maryland). To assess fibrosis, fibrotic blue area and whole myocardial area were measured. The fibrotic area was presented as a percentage of fibrotic area to the myocardial area. Myocyte size was measured in cross-sectioned muscle cells. In total, 100 to 150 cells/heart were analyzed based on wheat germ agglutinin staining. Two methods were used to assess the size of the infarcted heart. Infarct area was calculated as a percentage of infarcted ventricular area to total ventricular area using the front and back sides of the heart photos. Infarct size was measured as a percentage of infarcted ventricular wall length to total ventricular wall length using cardiac sections. The observer was blinded to the origin of the cardiac sections.

TUNEL assay was performed with the In-Situ Apoptosis Detection Kit (Thermo Fisher Scientific, Waltham, Massachusetts). Briefly, hearts were fixed by perfusion with 10% formalin solution, embedded in paraffin, and sectioned at 6 μm. One middle longitudinal section per heart was taken for TUNEL staining. Proteinase K (20 μg/ml) was added to each slide. Endogenous peroxidases were inactivated by covering sections with 2% hydrogen peroxide. After fixation, sections were incubated with terminal deoxynucleotidyl transferase buffer at 37°C for 30 min. Reactions were terminated with 1× saline-sodium citrate buffer. After being washed, slides were incubated with RTU streptavidin-horseradish peroxidase for 30 min. Positive signal was developed by adding DAB solution. After counterstained with RTU hematoxylin, slides were covered by mounting medium and analyzed under a microscope. Each group comprised 5 to 6 hearts. Eight fields (400×) from the infarct area per heart were analyzed for positive cells and total cells using computerized planimetry (ImageJ). The degree of apoptosis was presented as a percentage of positive cells to total cells.

TABLE 1 Reverse-Transcription-Polymerase Chain Reaction Primer Oligonucleotides

Primer Name	Sequence
BNP RT-F	TAGCCAGTCTCCAGAGCAATTC
BNP RT-R	TTGGTCCTTCAAGAGCTGTCTC
18s F	TCAAGAACGAAAGTCGGAGG
18s R	GGACATCTAAGGGCATCAC

REAL-TIME POLYMERASE CHAIN REACTION. 1 μg RNA was used for first-strand complementary DNA synthesis using Random Primer (Thermo Fisher Scientific) and SuperScriptII Reverse Transcriptase (Thermo Fisher Scientific) according to manufacturer's instruction. Real-time polymerase chain reaction (PCR) was performed using IQ SYBR Green Supermix (Bio-Rad Laboratories, Hercules, California) with CFX-96 Real-time PCR Detection System (Bio-Rad Laboratories) with primers as described in Table 1.

STATISTICAL ANALYSIS METHODS. We used student Wilcoxon rank sum test or analysis of variance to perform statistical analysis between 2 groups or among multiple groups, and a p value <0.05 was considered significant. The specific p values are depicted in the figures according to the following symbols, unless specified in individual figure legend: # indicates $p < 0.05$, * indicates $p < 0.01$, ** indicates $p < 0.001$.

RESULTS

GCGR ANTAGONISM ATTENUATES MI-INDUCED CARDIAC REMODELING. Eight-week to 10-week-old C57BL/J6 male mice were operated by permanent occlusion of left coronary artery descending artery and then randomized into 3 experimental groups, which were treated with PBS (control group; subcutaneous injection twice at 2 h, and 14 days post-MI) or monoclonal anti-GCGR antibody REMD2.59 (REMD group; subcutaneous injection of 7 mg/kg twice at 2 h and 14 days post MI) and GLC (GLC group; subcutaneous injection of 30 μg/kg 4 times/day for the first 6 days), as

illustrated in Figure 1A. REMD2.59 treatment modestly but significantly reduced fasting blood glucose level, indicating the expected GLC antagonistic effect of REMD2.59 in mice (Figure 1B). As shown in Figures 2A and 2B, in the vehicle-treated control group, histopathology analysis at the end of the experiment period of 4 weeks post-MI showed approximately 39% infarct scar size relative to total heart size. In contrast, the REMD-treated heart showed an average of 32% scar area and GLC-treated hearts showed an average of 48% scar area. Although GLC-treated hearts trended to have larger infarct sizes and REMD-treated hearts trended to smaller infarct sizes, the differences did not reach statistical significance, indicating that myocardium sparing may not be the major basis of protection GCGR effects in the post-MI hearts. The REMD2.59-treated heart showed a significant reduction in the apoptotic events detected by TUNEL (Figures 2C and 2D) as well as the level of myocardial fibrosis measured by trichrome staining (Figures 2E and 2F). However, the cellular identities of the apoptotic cells remain to be determined. Finally, REMD2.59 treatment also significantly reduced cardiac hypertrophy versus the vehicle-treated group based on heart weight (Figure 3A), or myocyte cross-sectional area measurements (Figure 3B). However, treatment of unoperated mice with REMD2.59 for 2 weeks did not affect basal heart weight (Figure 3C). These data support the notion that GCGR antagonism can prevent and attenuate the onset of pathological remodeling in response to myocardial injury, by reducing fibrosis and attenuating cardiomyocyte pathological hypertrophy.

GCGR ANTAGONISM PRESERVES CARDIAC FUNCTION AFTER MI. In addition to morphological and histological analysis, we measured cardiac function in each experimental group by both noninvasive echocardiogram and catheter based hemodynamic analysis. As shown in Figures 4A and 4B, a serial echocardiogram showed progressive deterioration of systolic function from 26% fractional shortening at week 1 to 16% at week 4 after MI in the vehicle-treated mice. In contrast, the REMD2.59 treatment almost completely preserved cardiac function from 30% fractional shortening at week 1 to 38% at week 4. In contrast, the mice treated with GLC showed earlier contractile dysfunction than the vehicle-treated group, losing fractional shortening from 26% at week 1 to 17.9% at week 1 after MI. Consistent with the impact on systolic function, significant chamber dilation was observed in the vehicle- and GLC-treated groups, which was almost completely blunted by REMD2.59 treatment (Figure 4B). Using catheter-based invasive hemodynamic measurements (Figures 4C–E), we observed that REMD2.59 treatment significantly elevated left ventricular developed pressure, and systolic pressure and improved both systolic (+dP/dtmax; $p < 0.05$) and diastolic (-dP/dtmax; $p = 0.06$) parameters in the post-MI hearts compared with the vehicle-treated control mice. These data suggest that GCGR inhibition can prevent loss of cardiac function in post-MI hearts. It is noted that the mice from hemodynamic studies had average heart rates (378 ± 94 beats/min, 363 ± 71 beats/min, 431 ± 114 beats/min for vehicle-, REMD-, and GLC-treated groups, respectively). In contrast, the average heart rates of mice for the echocardiograph studies were 626 ± 18 beats/min, 657 ± 9 beats/min, and 662 ± 7 beats/min for the same groups, respectively. Therefore, the hemodynamic measurements were measured under a significantly depressed state, likely due to anesthesia. Nevertheless, there were no differences in heart rates among the 3 experiment groups in either measurements, suggesting that the differences observed in the hemodynamic or echocardiographic parameters were not the results of differential degrees of anesthesia levels.

GCGR INHIBITION ON PRESSURE OVERLOAD–INDUCED CARDIAC HYPERTROPHY. To demonstrate the applicability of GCGR antagonism therapy to heart failure with different etiologies, we investigated the impact of REMD2.59 on pressure overload induced cardiac hypertrophy, dysfunction, and remodeling. Pressure overload was induced by TAC as described previously (33,34) in C57BL/6 male mice 8 to 10 weeks of age

FIGURE 1 Glucagon and Glucagon Receptor Antagonism in Myocardial Infarction

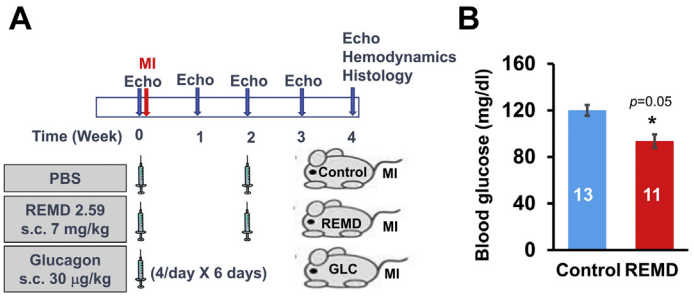

(A) Illustration of experimental design to investigate the effect of glucagon (GLC) and REMD2.59 treatment on myocardial infarction (MI). **(B)** Blood glucose level 14 days after vehicle (Control) or REMD treatment as indicated. The statistical significance and the specific p values depicted in this and the following figures are described in the Methods section according to the following symbols, unless specified for specific comparison among specific groups: #$p < 0.05$, *$p < 0.01$, **$p < 0.001$. Echo = echocardiography; PBS = phosphate-buffered saline; s.c. = subcutaneous.

FIGURE 2 Impact of GLC and GLC Receptor Antagonism on Myocardial Infarction

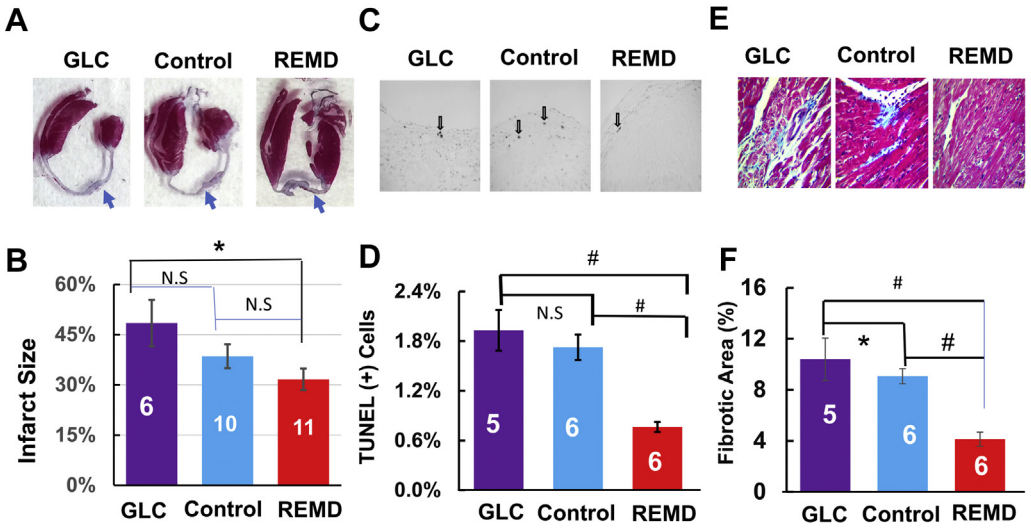

(A) Representative hematoxylin and eosin section of cardiac tissue 4 weeks after MI treated with PBS (Control), GLC, and GLC receptor antagonist (REMD). **(B)** Quantification of infarct scar sizes based on histological analysis; group sizes are indicated in each bar graph. **(C)** Representative TUNEL staining images of left ventricle with apoptotic cells indicated by **arrows**. **(D)** Quantification of percent TUNEL-positive cells with group sizes indicated. #$p < 0.01$. **(E)** Representative trichrome staining of left ventricular tissue. **(F)** Quantification of fibrotic area in the noninfarcted left ventricle from each group with group sizes indicated. Abbreviations as in Figure 1.

FIGURE 3 Impact of GLC and GLC Receptor Antagonist on Cardiac Hypertrophy in Post-Myocardial Infarct Heart

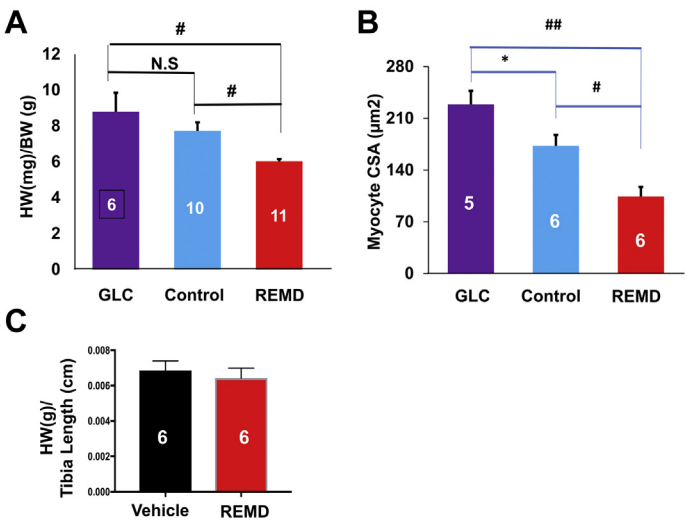

(A) Heart weight (HW) versus body weight (BW) 4 weeks after MI treated with PBS (Control), GLC, and GLC receptor antagonist (REMD). Groups sizes are indicated. **(B)** Myocyte cross-sectional areas (CSA) in left ventricles of the same mouse groups as in pane **A**. Group sizes are indicated. ## $p < 0.001$, #$p < 0.01$, *$p < 0.05$. Abbreviations as in Figure 1.

followed by weekly treatment of vehicle or anti-GCGR antibody (REMD2.59, 7 mg/kg body weight, subcutaneous injection) starting at the same time or starting at 2-weeks post TAC (REMD2.59 therapy) (Figure 5). Compared with the sham-operated group, TAC induced a significant increase in heart sizes as demonstrated in histological sections of the left ventricle, and tissue weights and cardiomyocyte cross-sectional morphometric data of cardiac chamber weight and the left ventricle (Figure 6). Concurrent treatment with REMD2.59 significantly blunted the increase of heart weight and myocyte enlargement compared with the TAC group. In contrast, starting REMD2.59 treatment at 2 weeks post-TAC (REMD2.59 therapy) failed to block left ventricular hypertrophy. These data indicate that GCGR inhibition can prevent the onset of cardiac hypertrophy induced by pressure overload, but has limited effect to reverse established cardiac hypertrophy.

GCGR INHIBITION IN PRESSURE OVERLOAD–INDUCED CARDIAC DYSFUNCTION. Using serial echocardiogram analysis, we found cardiac function, as measured from ejection fraction and percent fractional shortening, was significantly impaired by chronic pressure overload as early as 2 weeks post-TAC and deteriorated further at 5 weeks post-TAC (Figure 7),

FIGURE 4 Impact of GLC and GLC Receptor Antagonist on Cardiac Function and Chamber Dilation in Post-Myocardial Heart

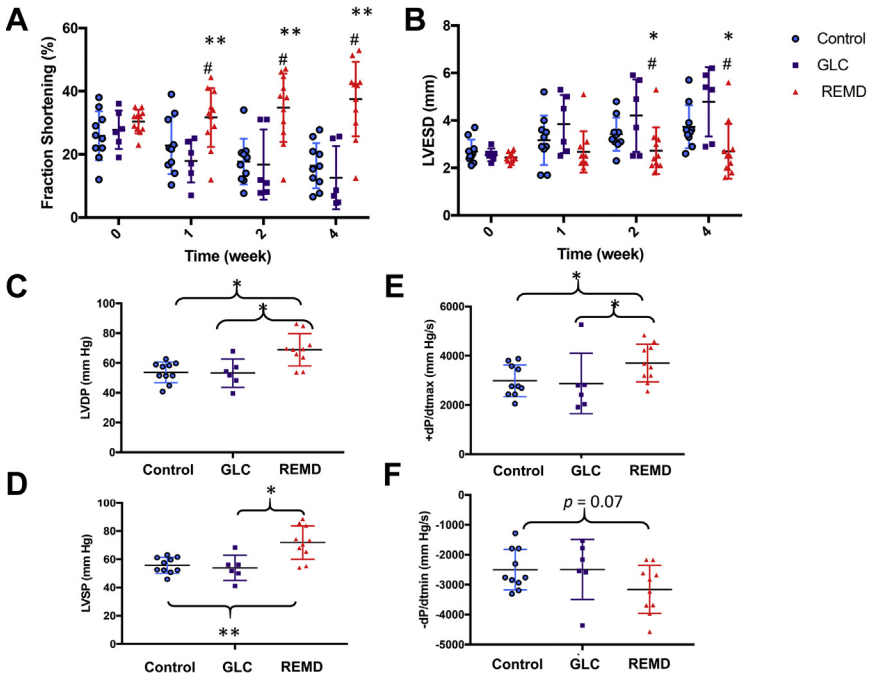

(A) Fractional shortening and **(B)** left ventricular end-systolic dimension (LVESD) in MI hearts treated with PBS (Control; n = 10, **blue**), GLC (n = 6, **purple**), and GLC receptor antagonist (REMD; n = 11; **red**) at different time points recorded by echocardiogram. #p < 0.05 REMD versus Control; REMD versus GLC. **(C)** Left ventricular developed pressure (LVDP). **(D)** Left ventricular systolic pressure (LVSP). **(E)** Maximum pressure derivative (+dP/dtmax) and **(F)** Minimum pressure derivative (-dP/dtmin) as measured by conductance catheter. Abbreviations as in Figure 1.

along with pulmonary congestion (Figure 6B). Treating mice with REMD2.59 at the onset of pressure overload largely preserved the contractile function in the pressure-overloaded hearts with ejection fraction and percent fractional shortening statistically unchanged comparing with the sham-operated mice at 5 weeks post-TAC (Figure 7). Starting REMD2.59 treatment 2 weeks after TAC, when functional impairment had already manifested, blunted further deterioration comparing to the vehicle-treated group. Using speckle tracking-based tissue-strain analysis from echocardiographic images (Figure 8), we observed that REMD2.59 treatment from the onset of TAC prevented the pressure overload-induced systolic and diastolic dysfunction as demonstrated in both systolic strain and diastolic strain rate. In contrast, REMD2.59 treatment starting 2 weeks post-TAC had limited success to reverse these parameters. The cardioprotective effect of REMD2.59 treatment was also manifested in significantly blunted pulmonary congestion (Figure 6B). All these evidences suggest that GCGR antagonism exerts significant protection against pressure overload induced cardiac dysfunction and blunts progression of heart failure.

GCGR ANTAGONISM ON PATHOLOGICAL REMODELING IN THE PRESSURE-OVERLOADED HEART. As a common feature of cardiac remodeling, chronic

FIGURE 5 Glucagon and Glucagon Antagonism in Pressure-Overload Induced Cardiac Hypertrophy

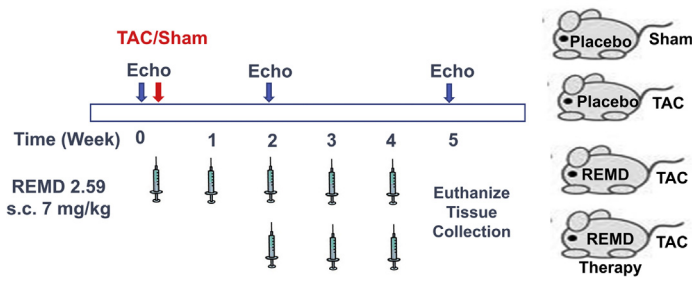

Illustration of treatment regiments for pressure overload-induced heart failure by GLC receptor antagonist either at the onset of the transaortic surgery (transaortic constriction [TAC] + REMD) or 2 weeks after (TAC + REMD therapy). Abbreviations as in Figure 1.

FIGURE 6 Impact of GLC Receptor Antagonist on Cardiac Hypertrophy

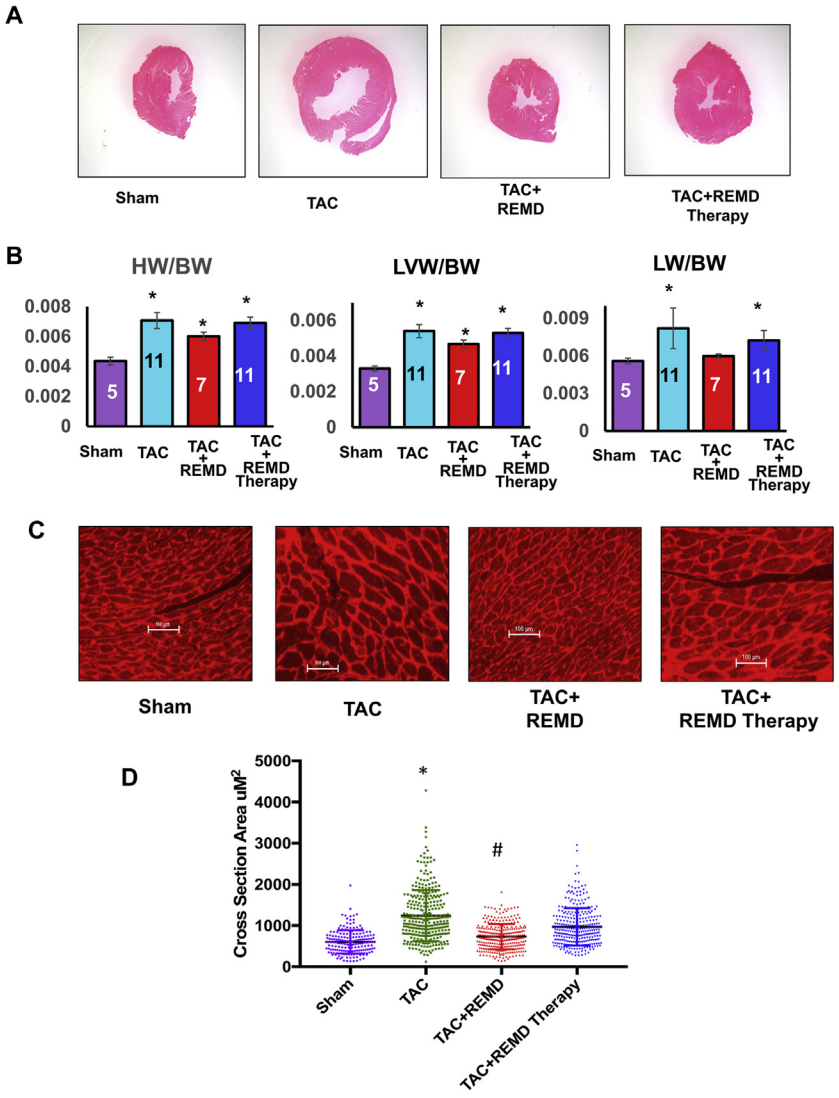

(A) Representative histological section of ventricle by hematoxylin and eosin staining of the heart from each treatment group as indicated. **(B)** Tissue weight measured at week 5 post-TAC from each treatment group as indicated, including HW versus BW (HW/BW), left ventricle weight versus BW (LVW/BW), and lung weight versus BW (LW/BW). *p < 0.05 versus sham. **(C)** Representative images of tissue section of left ventricles stained with wheat germ agglutinin from each treatment group as indicated. **(D)** Quantification of cardiomyocyte cross-sectional area in left ventricles of hearts from different treatment groups as indicated. *p < 0.05 versus Control, #p < 0.05 versus TAC. Abbreviations as in Figures 1, 3, and 5.

pressure overload induced significant level of cardiac fibrosis, as detected by trichrome staining (Figures 9A and 9B) and the expression of a pathological marker gene B-type natriuretic peptide measured by quantitative reverse transcription PCR (Figure 9C). REMD2.59 treatment started either at the onset of pressure overload or 2 weeks post-TAC completely blocked these changes. Therefore, GCGR inhibition can significantly block pathological remodeling in stressed heart in terms of extracellular matrix remodeling or gene expression.

DISCUSSION

In this report, the therapeutic effect of a GCGR antagonistic antibody REMD2.59 was tested in 2 mechanistically divergent disease models of heart failure without confounding defects in global

FIGURE 7 Functional Impact of GLC Receptor Antagonist on Contractile Function Measured by Echocardiogram

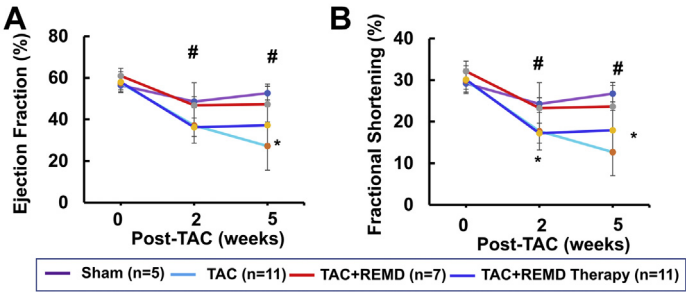

(A) Ejection fraction and **(B)** fractional shortening were measured at basal (week 0), 2 weeks post-TAC (week 2) and 5 weeks post-TAC from each treatment group as indicated. *p < 0.05 TAC versus TAC + REMD; #p < 0.05 TAC versus TAC + REMD therapy. Abbreviations as in Figures 1 and 5.

FIGURE 8 Impact of GLC Receptor Antagonist on Pressure-Overloaded Heart Measured by Tissue Strain

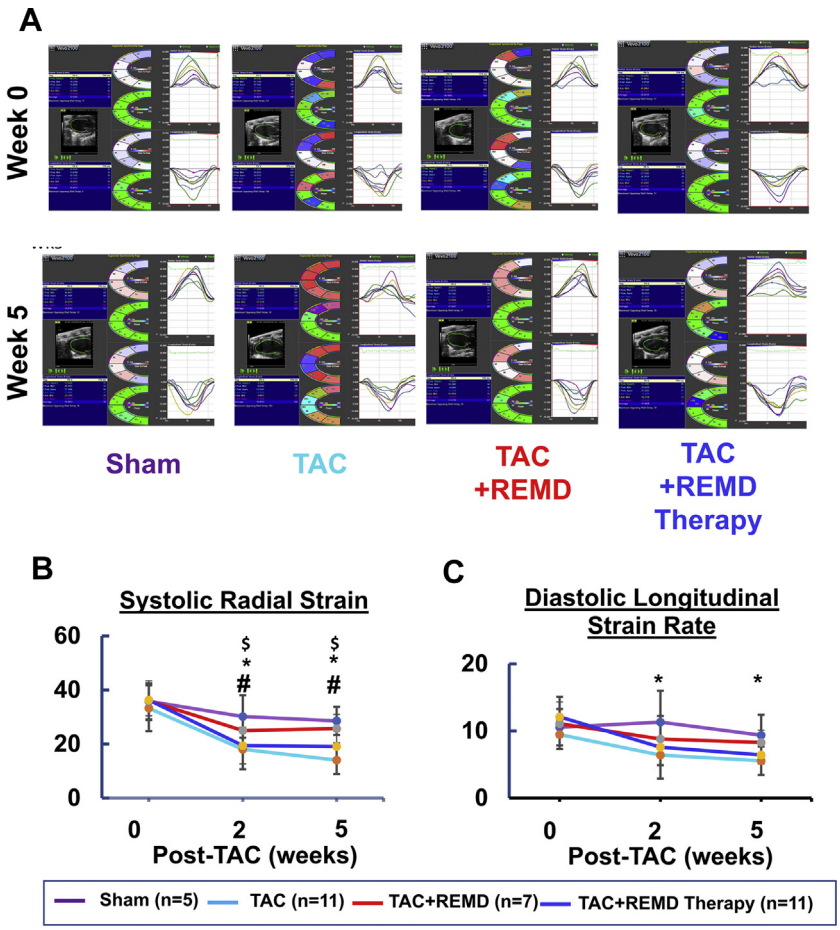

(A) Representative images of long-axis echo recording **(left panel)**, with cross-sectional segment synchronicity map **(middle panels)**, and radial and longitudinal endocardial strain **(right panel)**. **(B)** Average systolic radial strain and **(C)** average diastolic longitudinal strain rates at week 0, 2, and 5 post-TAC from each experimental group as indicated. *p < 0.05 Control versus TAC; #p < 0.05 TAC versus TAC+REMD; $p < 0.05 Control versus TAC + REMD therapy. Abbreviations as in Figures 1 and 5.

FIGURE 9 Impact of GLC Receptor Antagonist on Pathological Remodeling

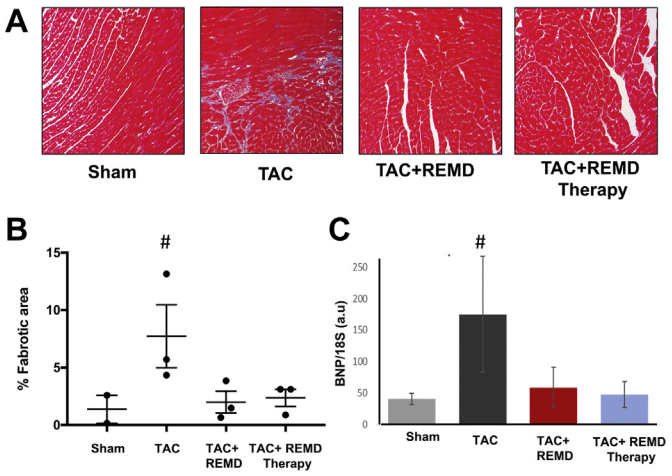

(A) Representative images of trichrome-stained tissue section from hearts of different experimental groups as indicated. **(B)** Quantification of cardiac fibrosis from panel **A**. **(C)** messenger RNA expression level of B-type natriuretic peptide as measured by quantitative reverse transcriptase polymerase chain reaction in heart tissue from different experimental groups as indicated. n = 3/group. #p < 0.05 versus Sham. Abbreviations as in Figures 1 and 5.

metabolism. Based on histological and functional analyses in both MI-injured and pressure-overloaded hearts, REMD2.59 treatment showed significant protection against cardiac hypertrophy and fibrosis remodeling with better preserved contractile function. These findings support a broadly applicable cardioprotective effect of GCGR inhibition against heart failure with different etiologies. As both these pathological stressors are imposed specifically and directly on heart rather in a systemic fashion, the observed cardioprotection of REMD2.59 is likely the result of its direct impact on GCGR signaling in cardiomyocytes rather than its impact on global glucose metabolic activities. This observation is consistent with the previous observations made in the cardiomyocyte-specific GCGR knockout mice, which have demonstrated the cardioprotective effect of GCGR antagonism against myocardial infarction in a receptor-dependent and cardiomyocyte cell-autonomous manner (29,32).

GLC and insulin are both pancreatic but counterbalancing hormones important to maintain systemic glucose regulation. GLC exerts its function via a peptide G protein-coupled receptor, GCGR. The canonical GCGR-mediated signaling involves classic G protein-coupled cAMP-dependent protein kinase A activation in hepatocytes, leading to induction of gluconeogenesis and glycogen catabolism, while inhibiting glycolysis (7,35). In addition to its predominant expression in liver, GCGR is also expressed at modest to low levels in the kidney, heart, pancreas, and many other tissues (3,8,36). Although G protein-coupled canonical signaling for GLC is well established in hepatocytes, other mechanisms involving intracellular calcium regulation have also been reported in nonhepatocytes including cardiomyocytes (3,10,28,36). In this report, we investigated GCGR inhibition in 2 mechanistically divergent disease models (i.e., myocardial infarction vs. pressure overload), the treatment resulted in similar cardioprotective effects against a broad spectrum of sequential pathological features in the failing heart, including cardiomyocyte hypertrophy, marker gene induction, interstitial fibrosis, and most importantly, cardiomyocyte contractile dysfunction. Apparently, GCGR antagonism is affecting cellular processes shared by different etiologies of cardiac pathology, including diabetes (32), ischemic injury, and mechanical overload. It is conceivable that abnormal GCGR activity may impact on cellular metabolism and energetic status via AMPK-dependent modulation in working heart as shown by Sharma et al. (32). However, our understanding to noncanonical signaling mechanism of GCGR is still very limited, and more studies are needed to illustrate the mechanistic basis of GCGR antagonism-mediated cardioprotection in response to different pathological stressors and energy homeostasis in failing hearts.

It is important to note that when REMD2.59 was applied 2 weeks after the onset of pressure overload,

GCGR antagonism no longer had any significant impact on cardiac hypertrophy, but still preserved the residual functions of the heart (**Figures 6 and 7**). This is consistent with previously reported observation that cardiomyocyte hypertrophy is established rather early in response to pressure overload while contractile dysfunction and fibrotic remodeling will continue to manifest (33). Our results highlight the potential limitation in the therapeutic window for heart failure. Nevertheless, REMD treatment can halt the further progression of heart failure and remodeling despite the limitation that GCGR antagonism may not be sufficient to reverse established cardiac hypertrophy and to fully restore contractile function. It is clear that more studies will be needed to fully establish the therapeutic efficacy of GCGR antagonism. Clinically relevant large animal models with established heart failure will be needed, and longer-term treatment and better outcome-based measurements (e.g., death and exercise tolerance) will be required.

Extensive pharmacological and structural analysis shows GCGR antibody REMD-477 competitively blocks GLC binding to the GCGR with 30-pM binding affinity, and can fully inhibit the receptor activity at low nanomolar concentrations in cells (14,17,20). Functionally identical to REMD-477, REMD2.59 is a surrogate human antibody specifically generated for chronical preclinical studies in rodents and primates. Unlike previous small-molecule approaches (30), REMD-477 does not have deleterious effects on serum lipid profiles (11,12,19,21,31) in both ongoing clinical trials in diabetes patients. In short, the anti-GCGR antibody as tested here offers a novel and powerful therapeutic tool to effectively and specifically inhibit GCGR with proven record of clinical safety and efficacy at molecular and metabolic levels.

Several other diabetic therapies, including GLC-like peptide-1 agonists (37,38), dipeptidyl peptidase 4 inhibition (39), and sodium glucose cotransporter 2 inhibitors (40,41), have demonstrated various degrees of cardiovascular benefits along with ameliorated metabolic defects in glucose homeostasis. Yet, not all glucose-lowering therapies have such significant cardiovascular protective effects as sodium glucose cotransporter 2 inhibition (42–46). It is also unclear if these therapies will be efficacious for common forms of heart failure without the confounding metabolic disorders. Our current study in 2 heart failure disease models free from systemic metabolic disorders further supports that GCGR inhibition may be repurposed as an effective therapy for common forms of heart failure.

ACKNOWLEDGMENT The authors wish to thank Ms. Haiying Pu for excellent technical assistance.

ADDRESS FOR CORRESPONDENCE: Dr. Yibin Wang or Dr. Chen Gao, Department of Anesthesiology, Cardiovascular Research Laboratories, David Geffen School of Medicine, University of California, Los Angeles, 650 Charles E. Young Drive, Room CHS 37-200J, Los Angeles, California 90095. E-mail: yibinwang@mednet.ucla.edu OR gaochen0813@g.ucla.edu.

PERSPECTIVES

COMPETENCY IN MEDICAL KNOWLEDGE: Systemic treatment of an antibody-based GCGR antagonist is currently in phase I and II clinical trials for type 1 and type 2 diabetes. The current study demonstrates for the first time that systemic treatment of GCGR antagonist can also exert potent cardioprotection against ischemic injury in the heart, and prevents pathological remodeling and heart failure induced by mechanic overload in nonobese and nondiabetic mice.

TRANSLATIONAL OUTLOOK: Systemic treatment of GCGR antagonist can be considered as a potential therapy for heart failure with different etiologies without concurrent metabolic disorders.

REFERENCES

1. Benjamin EJ, Blaha MJ, Chiuve SE, et al. Heart Disease and Stroke Statistics-2017 Update: a report From the American Heart Association. Circulation 2017;135:e146–603.

2. Vuguin PM, Charron MJ. Novel insight into glucagon receptor action: lessons from knockout and transgenic mouse models. Diabetes Obes Metab 2011;13 Suppl 1:144–50.

3. Authier F, Desbuquois B. Glucagon receptors. Cell Mol Life Sci 2008;65:1880–99.

4. Jiang G, Zhang BB. Glucagon and regulation of glucose metabolism. American journal of physiology Endocrinol Metab 2003;284:E671–8.

5. Nakamura S, Rodbell M. Glucagon induces disaggregation of polymer-like structures of the alpha subunit of the stimulatory G protein in liver membranes. Proc Natl Acad Sci U S A 1991;88:7150–4.

6. Levey GS, Weiss SR, Ruiz E. Characterization of the glucagon receptor in a pheochromocytoma. J Clin Endocrinol Metab 1975;40:720–3.

7. Holst JJ, Holland W, Gromada J, et al. Insulin and glucagon: partners for life. Endocrinology 2017;158:696–701.

8. Yamato E, Ikegami H, Takekawa K, et al. Tissue-specific and glucose-dependent expression of receptor genes for glucagon and glucagon-like peptide-1 (GLP-1). Horm Metab Res 1997;29:56–9.

9. MacNeil DJ, Occi JL, Hey PJ, Strader CD, Graziano MP. Cloning and expression of a human

glucagon receptor. Biochem Biophys Res Commun 1994;198:328–34.

10. Xu Y, Xie X. Glucagon receptor mediates calcium signaling by coupling to G alpha q/11 and G alpha i/o in HEK293 cells. J Recept Sig Transduct Res 2009;29:318–25.

11. Bagger JI, Knop FK, Holst JJ, Vilsboll T. Glucagon antagonism as a potential therapeutic target in type 2 diabetes. Diabetes Obes Metab 2011;13:965–71.

12. Gu W, Yan H, Winters KA, et al. Long-term inhibition of the glucagon receptor with a monoclonal antibody in mice causes sustained improvement in glycemic control, with reversible alpha-cell hyperplasia and hyperglucagonemia. J Pharmacol Exp Ther 2009;331:871–81.

13. Ali S, Drucker DJ. Benefits and limitations of reducing glucagon action for the treatment of type 2 diabetes. Am J Physiol Endocrinol Metab 2009;296:E415–21.

14. Pettus J, Reeds D, Santos Cavaiola T, et al. Effect of a glucagon receptor antibody (REMD-477) in type 1 diabetes: a randomized controlled trial. Diabetes Obes Metab 2018;20:1302–5.

15. Dean ED, Li M, Prasad N, et al. Interrupted glucagon signaling reveals hepatic alpha cell axis and role for L-glutamine in alpha cell proliferation. Cell Metab 2017;25:1362–73.e5.

16. Yang DH, Zhou CH, Liu Q, Wang MW. Landmark studies on the glucagon subfamily of GPCRs: from small molecule modulators to a crystal structure. Acta Pharmacol Sin 2015;36:1033–42.

17. Wang MY, Yan H, Shi Z, et al. Glucagon receptor antibody completely suppresses type 1 diabetes phenotype without insulin by disrupting a novel diabetogenic pathway. Proc Natl Acad Sci U S A 2015;112:2503–8.

18. Lefebvre PJ, Paquot N, Scheen AJ. Inhibiting or antagonizing glucagon: making progress in diabetes care. Diabetes Obes Metab 2015;17:720–5.

19. Mu J, Qureshi SA, Brady EJ, et al. Anti-diabetic efficacy and impact on amino acid metabolism of GRA1, a novel small-molecule glucagon receptor antagonist. PLoS One 2012;7:e49572.

20. Yan H, Gu W, Yang J, et al. Fully human monoclonal antibodies antagonizing the glucagon receptor improve glucose homeostasis in mice and monkeys. J Pharmacol Exp Ther 2009;329:102–11.

21. Lau YY, Ma P, Gibiansky L, et al. Pharmacokinetic and pharmacodynamic modeling of a monoclonal antibody antagonist of glucagon receptor in male ob/ob mice. AAPS J 2009;11:700–9.

22. Hollenstein K, de Graaf C, Bortolato A, Wang MW, Marshall FH, Stevens RC. Insights into the structure of class B GPCRs. Trends Pharmacol Sci 2014;35:12–22.

23. Pujadas G, Drucker DJ. Vascular biology of glucagon receptor superfamily peptides: mechanistic and clinical relevance. Endocr Rev 2016;37:554–83.

24. Zhang H, Qiao A, Yang D, et al. Structure of the full-length glucagon class B G-protein-coupled receptor. Nature 2017;546:259–64.

25. Li Y, Sun J, Li D, Lin J. Activation and conformational dynamics of a class B G-protein-coupled glucagon receptor. Phys Chem Chem Phys 2016;18:12642–50.

26. Yang L, Yang D, de Graaf C, et al. Conformational states of the full-length glucagon receptor. Nat Commun 2015;6:7859.

27. Charron MJ, Vuguin PM. Lack of glucagon receptor signaling and its implications beyond glucose homeostasis. J Endocrinol 2015;224:R123–30.

28. Siu FY, He M, de Graaf C, et al. Structure of the human glucagon class B G-protein-coupled receptor. Nature 2013;499:444–9.

29. Ali S, Ussher JR, Baggio LL, et al. Cardiomyocyte glucagon receptor signaling modulates outcomes in mice with experimental myocardial infarction. Mol Metab 2015;4:132–43.

30. Filipski KJ, Bian J, Ebner DC, et al. A novel series of glucagon receptor antagonists with reduced molecular weight and lipophilicity. Bioorg Med Chem Lett 2012;22:415–20.

31. Gu W, Lloyd DJ, Chinookswong N, et al. Pharmacological targeting of glucagon and glucagon-like peptide 1 receptors has different effects on energy state and glucose homeostasis in diet-induced obese mice. J Pharmacol Exp Ther 2011;338:70–81.

32. Sharma AX, Quittner-Strom EB, Lee Y, et al. Glucagon receptor antagonism improves glucose metabolism and cardiac function by promoting AMP-mediated protein kinase in diabetic mice. Cell Rep 2018;22:1760–73.

33. Gao C, Ren S, Lee JH, et al. RBFox1-mediated RNA splicing regulates cardiac hypertrophy and heart failure. J Clin Invest 2016;126:195–206.

34. Lee JH, Gao C, Peng G, et al. Analysis of transcriptome complexity through RNA sequencing in normal and failing murine hearts. Circ Res 2011;109:1332–41.

35. Wu F, Song G, de Graaf C, Stevens RC. Structure and function of peptide-binding G protein-coupled receptors. J Mol Biol 2017;429:2726–45.

36. Rodgers RL. Glucagon and cyclic AMP: time to turn the page? Curr Diabetes Rev 2012;8:362–81.

37. Drucker DJ. The cardiovascular biology of glucagon-like peptide-1. Cell Metab 2016;24:15–30.

38. Seferovic PM, Petrie MC, Filippatos GS, et al. Type 2 diabetes mellitus and heart failure: a position statement from the Heart Failure Association of the European Society of Cardiology. Eur J Heart Fail 2018;20:853–72.

39. Nauck MA, Meier JJ, Cavender MA, Abd El Aziz M, Drucker DJ. Cardiovascular actions and clinical outcomes with glucagon-like peptide-1 receptor agonists and dipeptidyl peptidase-4 inhibitors. Circulation 2017;136:849–70.

40. Tanaka H, Hirata KI. Potential impact of SGLT2 inhibitors on left ventricular diastolic function in patients with diabetes mellitus. Heart Fail Rev 2018;23:439–44.

41. Kaplan A, Abidi E, El-Yazbi A, Eid A, Booz GW, Zouein FA. Direct cardiovascular impact of SGLT2 inhibitors: mechanisms and effects. Heart Fail Rev 2018;23:419–37.

42. Packer M. Worsening heart failure during the use of DPP-4 inhibitors: pathophysiological mechanisms, clinical risks, and potential influence of concomitant antidiabetic medications. J Am Coll Cardiol HF 2018;6:445–51.

43. Packer M. Contrasting effects on the risk of macrovascular and microvascular events associated with anti-hyperglycaemic drugs that enhance sodium excretion and lower blood pressure. Diabet Med 2018;35:707–13.

44. Lim S, Eckel RH, Koh KK. Clinical implications of current cardiovascular outcome trials with sodium glucose cotransporter-2 (SGLT2) inhibitors. Atherosclerosis 2018;272:33–40.

45. Bistola V, Lambadiari V, Dimitriadis G, et al. Possible mechanisms of direct cardiovascular impact of GLP-1 agonists and DPP4 inhibitors. Heart Fail Rev 2018;23:377–88.

46. Nassif M, Kosiborod M. Effect of glucose-lowering therapies on heart failure. Nat Rev Cardiol 2018;15:282–91.

KEY WORDS glucagon receptor antagonism, heart failure, myocardial infarction, pressure overload

JACC: BASIC TO TRANSLATIONAL SCIENCE VOL. 4, NO. 2, 2019
© 2019 THE AUTHOR. PUBLISHED BY ELSEVIER ON BEHALF OF THE AMERICAN COLLEGE OF CARDIOLOGY FOUNDATION. THIS IS AN OPEN ACCESS ARTICLE UNDER THE CC BY-NC-ND LICENSE (http://creativecommons.org/licenses/by-nc-nd/4.0/).

EDITORIAL COMMENT

Modulation of Glucagon Signaling

A Metabolic Approach for Heart Failure?*

Alessandro Pocai, MD

Glucagon is secreted mainly from the α-cells of the pancreas and regulates glucose homeostasis through modulation of hepatic glucose production. As elevated glucagon levels contribute to the pathophysiology of hyperglycemia in patients with type 2 diabetes (T2D) (1), there have been several attempts to develop small-molecule glucagon receptor (GCGR) antagonists. Although promising glucose-lowering effects have been reported, dose-dependent increase in LDL-cholesterol, blood pressure, body weight, and plasma transaminases have been observed (2–4). In recent years, and thanks also to the information obtained from these clinical trials, more under-acknowledged pleiotropic effects of glucagon on lipids and body weight have become clearer (5). Glucagon is also reported to have effects on the cardiovascular system, but a thorough understanding of the impact of modulation of GCGR on the heart is still lacking (6). Several drugs already used in patients with T2D result in increased or decreased circulating glucagon and have been tested in cardiovascular outcome trials. The data obtained so far have not established a clear beneficial or deleterious directionality for glucagon. Dipeptidyl peptidase-4 inhibitors that have a glucagonostatic effect have shown cardiovascular neutrality or higher risk of hospitalization for heart failure (7), whereas glucagon-like peptide-1 receptor (GLP1R) agonists lower glucagon but also have additional effects on body weight and blood pressure and are either neutral or cardioprotective (7). Sodium glucose cotransporter-2 inhibitors (SGLT2i), which have been reported to increase plasma glucagon (8), result in reduction of the rates of hospitalization for heart failure (7).

SEE PAGE 161

In this issue of *JACC: Basic to Translational Science*, Gao et al. (9) report the consequences of antagonizing glucagon receptors with a monoclonal antibody (REMD2.59) in 2 nondiabetic rodent models of heart failure.

Mice with myocardial infarction (MI)-induced by ligation of the left coronary artery were treated with PBS, REMD2.59, or glucagon. Histopathologic and morphological analysis of heart post-MI showed reduced infarct size areas in animals treated with REMD2.59, whereas glucagon-injected animals showed a trend toward larger infarct size areas. REMD2.59 also reduced myocardial fibrosis, heart weight, and myocyte cross-sectional area. Consistent with impact on systolic function, chamber dilation was observed in vehicle- and glucagon-treated groups and was blunted by treatment with REMD2.59. REMD2.59 also improved both systolic and diastolic parameters in the post-MI heart. The authors concluded that REMD2.59 reduces pathological remodeling post-MI by reducing fibrosis and cardiomyocyte hypertrophy, leading to improvement of cardiac function.

Treatment with REMD2.59 (REMD) at the onset of pressure-overload (TAC) partially prevented cardiac hypertrophy and chamber dilation with preservation of systolic and diastolic function. Two weeks after pressure overload, REMD2.59 (REMD therapy) reduced the progression of cardiac pathology but no longer had any effects on left ventricle hypertrophy

*Editorials published in *JACC: Basic to Translational Science* reflect the views of the authors and do not necessarily represent the views of *JACC: Basic to Translational Science* or the American College of Cardiology.

From Cardiovascular and Metabolism, Janssen Research and Development, Spring House, Pennsylvania. Dr. Pocai is an employee of Janssen Pharmaceutical Companies of Johnson and Johnson.

The author attests that he is in compliance with human studies committees and animal welfare regulations of the author's institutions and Food and Drug Administration guidelines including patient consent when appropriate. For more information, visit the *JACC: Basic to Translational Science* author instructions page.

ISSN 2452-302X https://doi.org/10.1016/j.jacbts.2019.03.006

JACC: BASIC TO TRANSLATIONAL SCIENCE VOL. 4, NO. 2, 2019
APRIL 2019:173–5

while partially preserving residual function of the heart. REMD and REMD-therapy reduced chronic pressure-overload-induced cardiac fibrosis, suggesting reduction in pathological remodeling.

The authors proposed glucagon receptor antagonism as a new therapeutic approach to treat onset and progression of heart failure with different etiologies, independently of any improvements on metabolic status.

The data presented herein are consistent with cardiomyocyte-specific deletion of GCRG (10), demonstrating that heart-specific elimination of GCGR signaling reduces mortality that is induced by experimental ischemia in normal mice.

However, there are some experimental caveats and questions that need to be explored further.

Glucagon was administered as 4 injections a day for the first 6 days to post-MI mice and is expected to increase glucose production with changes in overall metabolic status (5). Also, a placebo group to control for vehicle composition and frequency of administration was not included in this study. Consistent with the above-mentioned metabolic changes in normal mice, the authors reported decreased fasting plasma glucose in mice treated with REMD2.59. Although the animals were nondiabetic, and the injury was localized to the heart, it is unclear if these metabolic changes contributed to the effects observed.

An important consideration is the potential for transability of these findings from mice to humans. Ligation of the left coronary artery is 1 of the preferred methods of inducing local injury and subsequent heart failure. However, contrary to the clinical situation, in which the patient has progressive nonocclusive coronary artery obstruction, MI in this model is due to occlusion of a normal artery. Although the latter is 1 of the strengths of this work—as it allows the evaluation of a potential direct effect on the heart, limiting systemic metabolic changes—it reduces the translational relevance of the model. It would be important to generate mechanistic data supporting a direct effect of REMD2.59 on the heart: for example, by evaluating REMD2.59 in isolated cardiomyocytes. This last experiment would be helpful also because pharmacological blockade may not entirely replicate cardiomyocytes genetic ablation of GCGR (10). As mentioned above, small-molecule GCGR antagonists in patients with T2D have shown increased plasma LDL-cholesterol, blood pressure, weight, and plasma transaminase (2–4). Of note, preliminary assessment of a GCGR antisense did not result in any of these adverse events in patients with T2D, opening the possibility that some actions may not be mediated by GCGR (11). However, there are additional changes observed in humans that need to be evaluated carefully, such as the impact on pancreatic abnormalities including α-cell hyperplasia reported in patients with loss of function of the GCGR (12,13). REMD 2.59 is a surrogate human antibody generated for preclinical studies and is functionally identical to REMD-477 (9). REMD-477 was tested in a short-term study in patients with T1D, and the effects on glucose and circulating hormones were monitored between day 6 and 12 post-treatment (14). Longer-term studies are required to demonstrate that the antibody approach does not have similar liabilities that might offset any direct and indirect benefit on the heart.

In a previous publication, the same authors reported that REMD2.59 activates adenosine monophosphate-activated protein kinase (AMPK) in the heart, leading to improved diabetic cardiomyopathy (15). Activation of heart AMPK has been shown to result in cardiac hypertrophy without apparent functional consequences, reminiscent of cardiac hypertrophy observed in athletes. Whether this effect is tolerable in humans with heart failure of different etiologies has yet to be determined (16).

Recent data suggest a potential beneficial action of ketone bodies in the failing heart (17) and, because glucagon stimulates ketone bodies formation through the liver, it is important to consider that GCGR antagonism may deprive the heart of a key fuel it requires under failing conditions.

Many questions remain regarding the potential beneficial effects of GCGR antagonism on the failing heart. For the reasons highlighted above, these results must be interpreted with caution.

Several combinations with metabolic targets such as GLP-1 and SGLT2i are currently in clinical trials, with the promise of achieving profound weight loss and glucose lowering while leveraging their cardioprotective effects (18–20). These novel approaches are expected to have important bidirectional effects on GCGR. Modulation of metabolic pathways with direct and indirect action on the heart may be critical for the treatment of heart failure with and without concurrent metabolic disorders and support the need for continued mechanistic work to define the pathways involved.

ADDRESS FOR CORRESPONDENCE: Dr. Alessandro Pocai, Janssen Research and Development, Cardiovascular and Metabolism, 1516 Welsh and McKean Roads, Spring House, Pennsylvania 19477. E-mail: apocai1@ITS.JNJ.com.

REFERENCES

1. Ali S, Drucker DJ. Benefits and limitations of reducing glucagon action for the treatment of type 2 diabetes. Am J Physiol Endocrinol Metab 2009;296:e415–21.

2. Engel SS, Xu L, Andryuk PJ, et al. Efficacy and tolerability of MK-0893, a glucagon receptor antagonist (GRA), in patients with type 2 diabetes (T2DM). Diabetes 2011;60 suppl 1:A85.

3. Guzman CB, Zhang XM, Liu R, et al. Treatment with LY2409021, a glucagon receptor antagonist, increases liver fat in patients with type 2 diabetes. Diabetes Obes Metab 2017;19:1521–8.

4. Bergman A, Tan B, Somayaji VR, et al. A 4-week study assessing the pharmacokinetics, pharmacodynamics, safety, and tolerability of the glucagon receptor antagonist PF-06291874 administered as monotherapy in subjects with type 2 diabetes mellitus. Diabetes Res Clin Pract 2017;126:95–104.

5. Müller TD, Finan B, Clemmensen C, et al. The new biology and pharmacology of glucagon. Physiol Rev 2017;97:721–66.

6. Petersen KM, Bøgevig S, Holst JJ, et al. Hemodynamic effects of glucagon: a literature review. J Clin Endocrinol Metab 2018;103:1804–12.

7. Sinha B, Ghosal S. Meta-analyses of the effects of DPP-4 inhibitors, SGLT2 inhibitors and GLP1 receptor analogues on cardiovascular death, myocardial infarction, stroke and hospitalization for heart failure. Diabetes Res Clin Pract 2019;20;150:8–16.

8. Saponaro C, Pattou F, Bonner C. SGLT2 inhibition and glucagon secretion in humans. Diabetes Metab 2018;44:383–5.

9. Gao C, Ren VS, Yu J, et al. Glucagon receptor antagonism ameliorates progression of heart failure. J Am Coll Cardiol Basic Trans Science 2019;4:161–72.

10. Ali S, Ussher JR, Baggio LL, et al. Cardiomyocyte glucagon receptor signaling modulates outcomes in mice with experimental myocardial infarction. Mol Metab 2015;4:132–43.

11. Morgan E, Smith A, Watts L, et al. ISIS-GCGRRX, an antisense glucagon receptor antagonist, caused rapid, robust, and sustained improvements in glycemic control without changes in BW, BP, lipids, or hypoglycemia in T2DM patients on stable metformin therapy. (Abstr109-LB). Diabetes 2014;63 Suppl 1:LB28.

12. Zhou C, Dhall D, Nissen NN, et al. Homozygous P86S mutation of the human glucagon receptor is associated with hyperglucagonemia, alpha cell hyperplasia, and islet cell tumor. Pancreas 2009;38:941–6.

13. Larger E, Wewer Albrechtsen NJ, Hansen LH, et al. Pancreatic alpha cell hyperplasia and hyperglucagonemia due to a glucagon receptor splice mutation. Endocrinol Diabetes Metab Case Rep 2016;2016:16–0081.

14. Pettus J, Reeds D, Cavaiola TS, et al. Effect of a glucagon receptor antibody (REMD-477) in type 1 diabetes: A randomized controlled trial. Diabetes Obes Metab 2018;20:1302–5.

15. Sharma AX, Quittner-Strom EB, Lee Y, et al. Glucagon receptor antagonism improves glucose metabolism and cardiac function by promoting AMP-mediated protein kinase in diabetic mice. Cell Rep 2018;22:1760–73.

16. Myers RW, Guan HP, Ehrhart J, et al. Systemic pan-AMPK activator MK-8722 improves glucose homeostasis but induces cardiac hypertrophy. Science 2017;357:507–11.

17. Horton JL, Davidson MT, Kurishima C, et al. The failing heart utilizes 3-hydroxybutyrate as a metabolic stress defense. JCI Insight 2019;21:4.

18. Gasbjerg LS, Gabe MBN, Hartmann B, et al. Glucose-dependent insulinotropic polypeptide (GIP) receptor antagonists as anti-diabetic agents. Peptides 2018;100:173–81.

19. Clemmensen C, Finan B, Müller TD, DiMarchi RD, Tschöp MH, Hofmann SM. Emerging hormonal-based combination pharmacotherapies for the treatment of metabolic diseases. Nat Rev Endocrinol 2019;15:90–104.

20. Hollander P, Bays HE, Rosenstock J, et al. Coadministration of canagliflozin and phentermine for weight management in overweight and obese individuals without diabetes: a randomized clinical trial. Diabetes Care 2017;40:632–9.

KEY WORDS glucagon, heart failure, metabolism

JACC: BASIC TO TRANSLATIONAL SCIENCE VOL. 4, NO. 2, 2019
© 2019 THE AUTHORS. PUBLISHED BY ELSEVIER ON BEHALF OF THE AMERICAN COLLEGE OF CARDIOLOGY FOUNDATION. THIS IS AN OPEN ACCESS ARTICLE UNDER THE CC BY-NC-ND LICENSE (http://creativecommons.org/licenses/by-nc-nd/4.0/).

PRECLINICAL RESEARCH

Perioperatively Inhaled Hydrogen Gas Diminishes Neurologic Injury Following Experimental Circulatory Arrest in Swine

Alexis R. Cole, BS,[a] Dorothy A. Perry, MBChB,[a,b] Ali Raza, MD,[a,b] Arthur P. Nedder, DVM,[c] Elizabeth Pollack, DVM Candidate,[c] William L. Regan, CCP, LP,[d] Sarah J. van den Bosch, MS,[a] Brian D. Polizzotti, PhD,[a,b] Edward Yang, MD,[e,f] Daniel Davila, MD,[g,h] Onur Afacan, MD,[e,f] Simon K. Warfield, PhD,[e,f] Yangming Ou, PhD,[b,e,f] Brenda Sefton, PA,[d] Allen D. Everett, MD,[i] Jeffrey J. Neil, MD, PhD,[e,f] Hart G.W. Lidov, MD, PhD,[h,j,k] John E. Mayer, MD,[d,l] John N. Kheir, MD[a,b]

VISUAL ABSTRACT

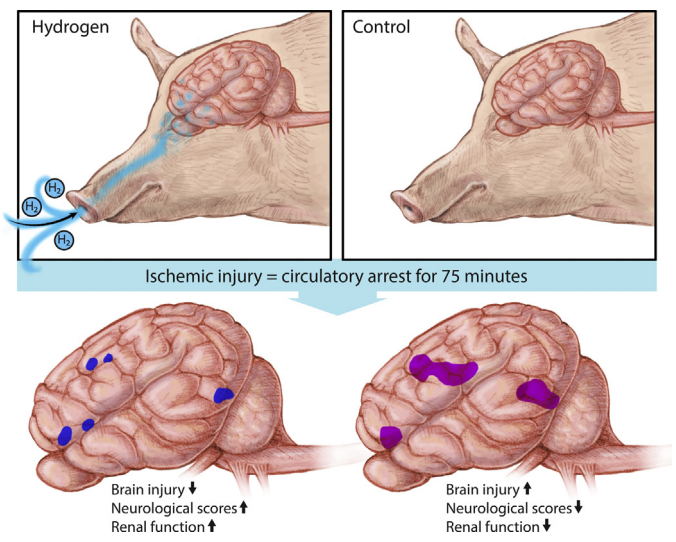

Cole, A.R. et al. J Am Coll Cardiol Basic Trans Science. 2019;4(2):176–87.

HIGHLIGHTS

- **Inhaled hydrogen gas has been shown to temper the sequelae of ischemic insults. Its application in cardiopulmonary bypass has not been investigated.**
- **Neonatal swine were cannulated to cardiopulmonary bypass and exposed to prolonged circulatory arrest (75 min at 25°C). Swine were randomized to treatment with or without inhaled 2.4% hydrogen gas mixtures for 24 h during and following ischemic injury. Hydrogen-treated swine exhibited significantly less severe brain injury than controls, as quantified by clinical examination, serology, magnetic resonance-graded volume of injury, and histopathology. Hydrogen treatment also decreased renal injury.**
- **The administration of inhaled 2.4% hydrogen gas mixtures through a standard ventilator and anesthesia machine were safe, even in the setting of electrocautery.**

From the [a]Department of Cardiology, Boston Children's Hospital, Boston, Massachusetts; [b]Department of Pediatrics, Harvard Medical School, Boston, Massachusetts; [c]Animal Resources at Children's Hospital, Boston Children's Hospital, Boston, Massachusetts; [d]Department of Cardiovascular Surgery, Boston Children's Hospital, Boston, Massachusetts; [e]Department of Radiology, Boston Children's Hospital, Boston, Massachusetts; [f]Department of Radiology, Harvard Medical School, Boston, Massachusetts; [g]Department of Neurology, Boston Children's Hospital, Boston, Massachusetts; [h]Department of Neurology, Harvard Medical School, Boston, Massachusetts; [i]Division of Pediatric Cardiology, Johns Hopkins University School of Medicine, Baltimore, Maryland; [j]Department of Pathology, Boston Children's Hospital, Boston, Massachusetts; [k]Department of Pathology, Harvard Medical School, Boston, Massachusetts; and the [l]Department of Surgery, Harvard Medical School, Boston, Massachusetts. Dr. Kheir is supported by American Heart Association grant 15GRNT25700161; and by philanthropic donations from the Hess Family

ISSN 2452-302X https://doi.org/10.1016/j.jacbts.2018.11.006

SUMMARY

This study used a swine model of mildly hypothermic prolonged circulatory arrest and found that the addition of 2.4% inhaled hydrogen gas to inspiratory gases during and after the ischemic insult significantly decreased neurologic and renal injury compared with controls. With proper precautions, inhalational hydrogen may be administered safely through conventional ventilators and may represent a complementary therapy that can be easily incorporated into current workflows. In the future, inhaled hydrogen may diminish the sequelae of ischemia that occurs in congenital heart surgery, cardiac arrest, extracorporeal life-support events, acute myocardial infarction, stroke, and organ transplantation. (J Am Coll Cardiol Basic Trans Science 2019;4:176–87)
© 2019 The Authors. Published by Elsevier on behalf of the American College of Cardiology Foundation. This is an open access article under the CC BY-NC-ND license (http://creativecommons.org/licenses/by-nc-nd/4.0/).

ABBREVIATIONS AND ACRONYMS

CPB = cardiopulmonary bypass

GFAP = glial fibrillatory acidic protein

H_2 = hydrogen gas

•OH = hydroxyl radical

PDI = Psychomotor Development Index

SNDS = Swine Neurodevelopment Score

Newborns with critical congenital heart disease often undergo major surgical interventions in the neonatal period that require the use of cardiopulmonary bypass (CPB). Several studies have provided radiographic evidence showing that new ischemic injury occurs following CPB (1–7). Neonates with the diagnosis of left heart obstructive lesions are consistently at the highest risk of cerebral injury (5,8). In 1 study (1), new white matter injury (i.e., not present preoperatively) was evident in more than 70% of neonates undergoing aortic arch reconstruction. Cerebral injuries included moderate or severe white matter injury in 40% to 50% of patients; new infarctions were found in one-third of patients. Further, clinically evident seizures have been reported in up to 20% of neonates following surgery for congenital heart disease and are more common in patients undergoing prolonged deep hypothermic circulatory arrest (9,10). Subclinical seizures occur in an even higher fraction (1,10,11). The presence of postoperative seizures is an important marker of underlying ischemic injury, which may manifest as radiologic injury and developmental delay years later (12). Thus, although abnormal neurodevelopment in infants with critical congenital heart disease is multifactorial (including in utero, genetic, and socioeconomic risk factors) (13), injury occurring during CPB represents a significant contributor to neurologic impairment.

To mitigate this problem, nearly all operations are performed under some degree of hypothermia, which suppresses cerebral oxygen consumption (14), and enhances preservation of high-energy phosphates, and reduces the accumulation of toxic metabolites (15). Cerebral hypoxia can be monitored using cerebral near-infrared spectroscopy and the degree and duration of cerebral hypoxia have been associated with subsequent neurologic impairment. For example, newborns experiencing a regional cerebral oxyhemoglobin saturation index <40 exhibited worse receptive communication at 2 years of age than those who did not (16). Efforts to minimize cerebral hypoxia during congenital heart surgery have resulted in improvements in neurologic outcomes. For example, the addition of carbon dioxide during hypothermia (i.e., pH-stat, which promotes cerebral vasodilation during bypass) was associated with a more rapid return of normal electroencephalographic activity (17). In another study (18), target hematocrit during CPB was significantly associated with Psychomotor Development Index (PDI) scores at 1 year of age (18).

At a cellular level, cerebral hypoxia during CPB creates a complex cascade of changes within the inner mitochondrial membrane, causing formation of the superoxide anion radical ($O_2^{-\bullet}$) (19), which in turn generates hydroxyl radicals (•OH) by the Fenton reaction. The •OH is the strongest of the oxidant species and reacts indiscriminately with nucleic acids, lipids, and proteins, causing direct cellular injury and stimulating apoptosis. Because there is no known detoxification system for •OH, scavenging

Cardiac Innovation Fund, the Furber Family Innovative Therapies Fund, and Lindsay Bartels (a donor who provided some financial support for the study). Dr. Everett is a consultant for Immunarray LLC; and holds patents through Johns Hopkins University assigned to Immunarray, Inc. All other authors have reported that they have no relationships relevant to the contents of this paper to disclose.

All authors attest they are in compliance with human studies committees and animal welfare regulations of the authors' institutions and U.S. Food and Drug Administration guidelines, including patient consent where appropriate. For more information, visit the *JACC: Basic to Translational Science* author instructions page.

Manuscript received September 26, 2018; revised manuscript received November 6, 2018, accepted November 6, 2018.

FIGURE 1 Presumed Mechanism of H_2 Action in the Setting of Ischemia

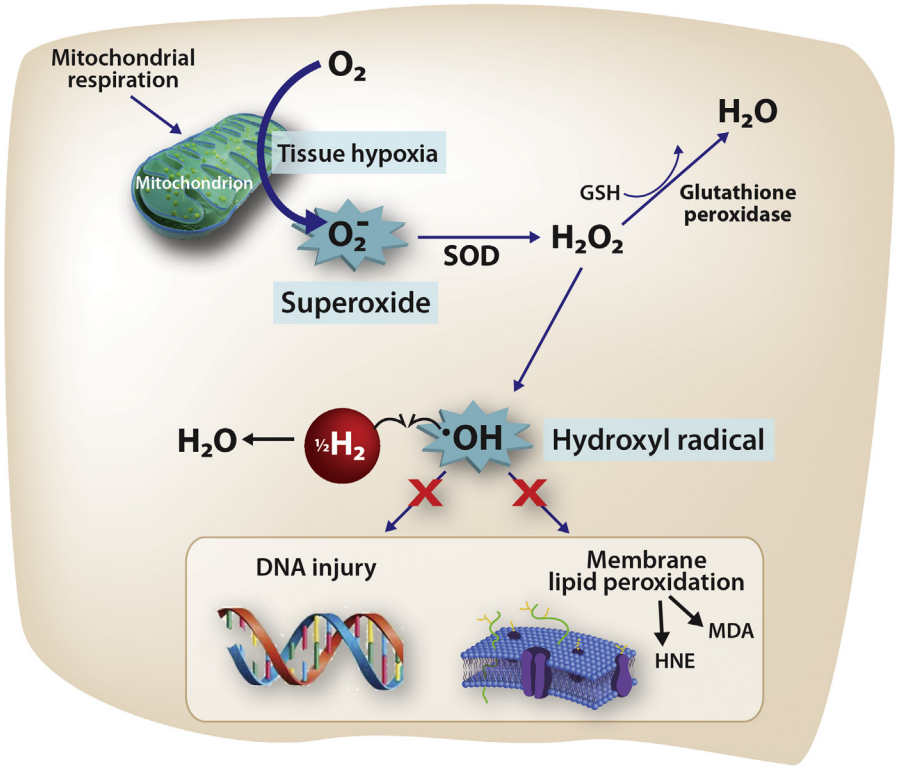

Ischemic insults create tissue hypoxia, stimulating a complex cascade (not shown) that results in the release of superoxide ($O_2^{-\bullet}$). When $O_2^{-\bullet}$ is present in excess (i.e., when compensatory mechanisms become saturated), it directly causes the reduction of transition metal ions, including Fe^{3+} and Cu^{2+}, which in turn, generates hydroxyl radicals (•OH) by the Fenton reaction. The •OH is the strongest of the oxidant species and is the direct effector of DNA injury and lipid membrane peroxidation, which releases HNE and MDA, causing direct cellular injury and stimulating apoptosis. Unlike $O_2^{-\bullet}$ and H_2O_2, there is no known detoxification system for •OH; therefore, scavenging •OH is a critical antioxidant process. Molecular hydrogen (H_2), which freely permeates the cell wall and diffuses into the cytosol and mitochondria, reduces the hydroxyl radical to water and thus mitigates •OH-mediated tissue injury. HNE = 4-hydroxyl-2-nonenal; MDA = malondialdehyde; SOD = superoxide dismutase.

•OH is a critical antioxidant process (20). Recently, it has been discovered that hydrogen gas (i.e., molecular dihydrogen [H_2]) selectively reduces •OH in vivo (**Figure 1**) (21). For example, rodents breathing either 2% or 4% H_2 for 90 min following a period of middle cerebral artery occlusion exhibited a substantially smaller infarct volume, improved neurologic scores, weight gain, and thermoregulation relative to controls (21), findings that were repeated by an independent group (22). In another study (23), H_2-treated rodents undergoing a 5-min period of asphyxial cardiac arrest exhibited more favorable neurologic scores, improved myocardial function, and improved 96-h survival than did those treated with targeted temperature management alone. Here, we studied the effects of inhalational H_2 gas on neurologic outcomes in neonatal swine undergoing cerebral hypoxic-ischemic injury in the setting of hypothermic CPB. We hypothesized that the inhalation of H_2 gas surrounding a CPB-related ischemic injury would diminish the degree of neurologic injury in subject animals relative to that in control animals.

METHODS

The following protocol was approved by the Institutional Animal Care and Use Committee at Boston Children's Hospital (protocol 15-08-2990) (**Figure 2**), which included a review of hydrogen-related environmental hazard concerns.

EXPERIMENTAL PROTOCOL. Sixteen neonatal female Yorkshire swine (3.8 to 5.8 kg; post-natal age: 6 to 10 days of life) were acclimated to their surroundings

FIGURE 2 Study Protocol

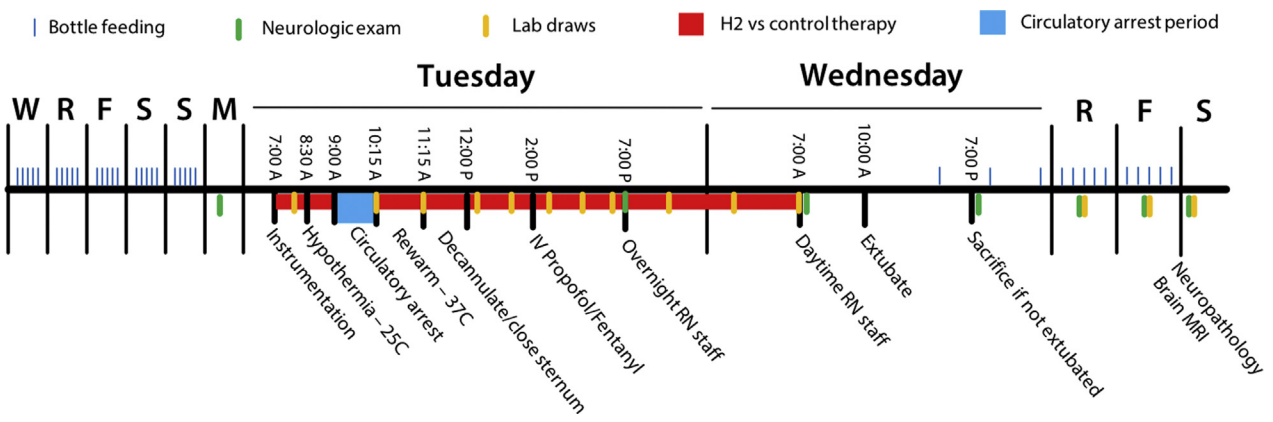

Neonatal swine were acclimated with bottle feedings 5 time per day **(blue marks)** for 5 days prior to experimentation. On the day of experimentation, swine were anesthetized and instrumented for cardiopulmonary bypass. Ischemic injury included circulatory arrest for 75 min at 25°C. Swine were then rewarmed and decannulated and underwent mechanical ventilation using a standardized intensive care protocol. Swine were ventilated for a total of 24 h (including pre- and postoperative treatments) with or without 2.4% inhaled hydrogen therapy (n = 8 swine per group). Videotaped neurologic examinations **(green marks)** took place prior to and daily following the circulatory arrest period. Swine underwent sedated brain MRI followed by terminal cerebral perfusion for histopathologic examination on postoperative day 3. F = Friday; M = Monday; MRI = magnetic resonance imaging; R = Thursday; RN = nursing care; S = Saturday/Sunday; W = Wednesday.

and bottle fed 5 times daily by research staff for 6 days. On the day of experimentation, swine were anesthetized by intramuscular injections of tiletamine (Telazol), xylazine and atropine, and tracheally intubated. Swine were then sedated by using inhaled isoflurane (0.25% to 2%). Neuromuscular blockade (cisatracurium) was administered upon anesthetic induction and then again prior to sternotomy incision. A right femoral arterial (3-F sheath) catheter and a right internal jugular venous (4-F, 5 cm) catheter were placed and continuously transduced. Esophageal and rectal temperature probes were placed. A median sternotomy was performed, a subtotal thymectomy performed, and the pericardium opened. A sterile human infant-sized CPB circuit (S5 infant perfusion pack, Sorin Group, Arvada, Colorado) was primed with blood from an adult donor swine sacrificed on the previous day. The right atrium and ascending aorta were cannulated (18-F DLP malleable single-stage venous and 10-F arterial cannulas, Medtronic-Biomedicus, Eden Prairie, Minnesota), and full-flow CPB was instituted. As is our institution's clinical practice, a dose of methylprednisolone (30 mg/kg intravenous [IV]) was administered upon initiation of CPB. Swine were then cooled to 25°C (measured rectally) over 30 min, using a pH-stat management strategy (carbon dioxide added). Following cooling, the aorta was cross-clamped, and a solution of cold blood, potassium, magnesium, and lidocaine were administered into the aortic root, and cardioplegia was induced (del Nido Cardioplegia Solution [24]), causing prompt diastolic arrest. Circulation was then discontinued for a 75-min period of circulatory arrest. Rectal temperature was maintained as close to 25°C as possible by using surface cooling as needed. Following circulatory arrest, circulation was restored, and swine were warmed to 37°C over 60 min. Swine were then weaned from CPB using inotropic support as needed to maintain systolic blood pressure >80 mm Hg. Cannulas were removed, hemostasis ensured, and the sternum closed.

SURVIVAL PERIOD. Sedation was then transitioned to infusions of propofol (1 to 3 mg/kg/h) and fentanyl (1 to 2 μg/kg/h), and inhalational isoflurane was discontinued for an 18-h period of regimented intensive care staffed by intensive care nursing staff. During this time, esophageal temperature was continuously monitored and maintained below 38°C by using a cooling blanket. Blood pressure was maintained with an infusion of dopamine (3 to 5 μg/kg/min, titrated to systolic blood pressure >70 mm Hg). Diuresis was achieved by using furosemide (1 mg/kg every 12 h). Mechanical ventilation was continued by using synchronized, intermittent mandatory ventilation with a fraction of inspired oxygen, required to maintain pulse oximetry saturation of 95% and target tidal volumes of 8 ml/kg. Animals were continuously

monitored for clinical seizure activity. Seizures lasting longer than 2 min were treated according to a protocol of lorazepam (0.1 mg/kg IV every 5 min up to 3 doses), then phenobarbital (20 mg/kg IV every 20 min for 2 doses), then fosphenytoin (20 mg/kg IV every 20 min for 2 doses), then an increase in the rate of propofol infusion (up to 10 mg/kg/h). Inotrope score was calculated as: [dopamine (μg/kg/min) + dobutamine (μg/kg/min) + 100× epinephrine (μg/kg/min)] (25).

After the animals underwent 18 h of intensive care, the arterial catheter, thoracic drain, and tracheal tube were removed. Swine were then observed for 3 days, with quantification of neurologic status by daily neurologic examinations. Blood drawn prior to and daily after the injury was analyzed for complete blood count, chemistry profile, hepatic transaminases, and venous blood gas analysis. Glial fibrillatory acidic protein (GFAP) was assessed using an electrochemiluminescent sandwich immunoassay (Meso Scale Diagnostics, Rockville, Maryland), with a detection range of 0.001 to 40.0 ng/ml (26).

INHALED HYDROGEN THERAPY. Animals were randomized to treatments as described above with or without inhaled hydrogen (2.40%) for a 24-h period during and after the ischemic injury (n = 8 per group). At the beginning of the study, we created a table that dictated the treatment allocation for each experiment in random order, according to which patients were treated. Due to environmental hazards and logistical considerations, members of the veterinary, perfusion, and overnight nursing staff were not blinded to treatment group allocation, whereas surgical staff, neurologists, and histopathologists were blinded to treatment allocation. Premixed, certified hydrogen gas blends containing 2.40 ± 0.05% of grade-6 purity (99.9999%) hydrogen gas with either balance medical air or medical oxygen (Praxair Distribution, Inc., Jessup, Maryland) were obtained and received as nonflammable gas mixtures. These tanks were fitted with a 50-psi regulator and a flash arrestor and then attached directly to the air and oxygen (respectively) inlets of the anesthesia machine (Dräger Apollo, Coppell, Texas) during the experimental period and to the mechanical ventilator (Servo I model, Maquet, Gothenburg, Sweden) during the survival period (Supplemental Figure S1). Additional hydrogenated "carbogen" mixtures were made, including 0%, 4%, 6%, and 8% carbon dioxide, 2.40% hydrogen, and balance oxygen for use during hypothermic perfusion. Ambient hydrogen concentrations were measured continuously (Eagle 2 model, RKI Instruments, Union City, California).

SWINE NEUROLOGIC DEFICIT SCORES. Swine were evaluated prior to and following each 24-h period after the injury using a previously described swine neurologic deficit score (SNDS) (27) by 2 research technicians, present for each examination (unblinded to treatment allocation), and 2 neurologists (by review of videotaped examinations, blinded to treatment allocation). The mean of the 4 scores was taken at each time point. The examination assessed cranial nerve function, respiratory pattern, motor and sensory function, level of consciousness, and behavior, each assigned a total of 100 points. Points were assigned based on specific abnormal neurologic findings (Supplemental Table 1), such that a score of 0 was normal, and a score of 500 represented brain death. The presence or absence of clinical seizures was not part of the scoring system.

BRAIN MAGNETIC RESONANCE IMAGING. On day 3 post-injury, swine were anesthetized for brain magnetic resonance imaging (MRI) (3-T Skyra model scanner, 64-channel head and neck coil, Siemens, Corp., Munich, Germany). High-resolution T1, T2, fluid-attenuated inversion recovery, and diffusion-weighted images were obtained. Areas of enhancement on axial and coronal T2 and apparent diffusion coefficient images were manually assessed on a voxel-per-voxel basis and outlined (itk-SNAP software application, Penn Image Computing and Science Laboratory, University of Pennsylvania, Philadelphia, Pennsylvania, and Scientific Computing and Imaging Institute, University of Utah, Salt Lake City, Utah) by a radiology technician (Mr. Abdelhakim Ouaalam, Department of Radiology, Boston Children's Hospital, Boston, Massachusetts), a radiologist (E.Y.), and a clinical neurologist (J.N.), all of whom were blinded to treatment allocation. From these values, total volumes of cranial injuries per swine were calculated using in-house software normalized to brain volume, and the total volumes of injuries were compared between groups by using the Mann-Whitney *U* test.

NEUROHISTOPATHOLOGY. Following brain MRI of the swine on post-injury day 3, both carotid arteries and jugular veins were then cannulated by cutdown and perfused with normal saline (2 l), followed by 4% paraformaldehyde (4 l). The heads of swine were fixed in 10% formaldehyde for 24 h and then removed and paraffin embedded and then stained for hematoxylin and eosin. Hypoxic-ischemic injuries of the frontal cortex, temporal cortex, hippocampus, dentate gyrus, caudate nucleus, and thalamus were graded according to a previously defined scale by a pathologist (H.G.W.L.) blinded to treatment allocation. Briefly, histologic injury was evaluated by using

both light and fluorescence microscopy (28) on a scale of 0 through 5 for each of 6 regions, as follows: 0 = normal, no injury; 1 = rare hypereosinophilic neurons; 2 = small clusters of hypereosinophilic neurons; 3 = majority of neurons (>50%) are hypereosinophilic; 4 = significant damage to neurons; and 5 = cavitated infarction with histologic necrosis. Animals that did not survive for 3 days (due to refractory status epilepticus) were assigned the median histologic score for animals in the control group.

STATISTICAL ANALYSIS. The primary outcome of this study was neurologically intact survival, which was defined as an SNDS of ≤120 at 3 days, compared between groups using a log-rank test (Gehan-Breslow-Wilcoxon test). On the basis of a previous series of pilot experiments, 15% of animals in the control group were expected to meet this endpoint, and the study was powered to identify the fact that 70% or more in the hydrogen treatment group met this endpoint at 5 days with 80% power and an alpha level of 0.05.

Between-group differences in SNDS, regional neurohistologic scores, body temperatures, regional oxyhemoglobin saturation index values, hemodynamics, inotrope scores, serum lactic acid concentrations, blood gas concentrations, PaO_2/FiO_2 ratios, chemistry values, and hematologic parameters were assessed over time by using 2-way repeated measures analysis of variance (ANOVA), using Prism version 7.00 software (for MacIntosh [Cupertino, California], GraphPad, La Jolla, California). In order to complete ANOVA, missing values for the 2 animals which were sacrificed early were estimated to be the median values across controls for that time point. When results were statistically significant, time-dependent differences between groups were assessed by using Sidak's multiple comparisons test. Interobserver reliability for SNDS was assessed by Pearson coefficient between blinded versus unblinded observers for time-matched pairs. Single time point values, such as differences in cerebral infarct volumes or changes in GFAP relative to baseline, were compared between groups by Student's *t*-test or Mann-Whitney *U* test, as appropriate. For all tests, a p value of <0.05 was considered statistically significant.

RESULTS

HYDROGEN HAZARDS. Hydrogen-oxygen and hydrogen-air mixtures were administered via the anesthesia machine and mechanical ventilator without malfunction or incident. Electrocautery was used with no subjective difference in performance between controls and the hydrogen-treated animals. Measurements of ambient hydrogen concentrations were below the lower limit of detection (<1 ppm) at all time points.

CLINICAL OUTCOMES. All animals were successfully weaned from CPB. The degrees to which hypothermia was achieved were similar between the groups (mean rectal temperature: 27.4 ± 1.8°C vs. 26.5 ± 1.9°C in controls and hydrogen-treated groups, respectively; p = 0.2387) (Supplemental Figure S2). Cerebral and somatic near infrared spectroscopy values were also similar between groups, frequently reaching a nadir of <20 during the deep hypothermic circulatory arrest period (Supplemental Figure S3). Two swine in the control group exhibited refractory status epilepticus and were sacrificed at 32 and 36 h post-injury following a failed trial of extubation; no hydrogen-treated animals exhibited seizures. Survival to 3 days was similar between groups (log rank test: p = 0.1435). Hydrogen-treated swine exhibited a higher rate of neurologically intact survival, defined as an SNDS of ≤120 at the time of death (log-rank test; p = 0.0035) (**Figure 3A**). SNDSs were significantly improved in hydrogen-treated swine in the postoperative period (p < 0.0001) (**Figure 3B**). Interobserver reliability was excellent among in-person scorers (i.e., unblinded research team members) and videotaped reviewers (i.e., blinded neurologists) (Pearson correlation coefficient: 0.895). The increase in serum GFAP concentrations relative to those at baseline was significantly higher in controls than in H_2-treated swine at 60 min post-injury (p = 0.0068) (Supplemental Figure S4).

Relative to controls, H_2-treated swine exhibited a significantly lower level of serum creatinine during the survival period (p = 0.0152), an average of 0.38 mg/dl lower by postoperative day 3. There were no differences in serum markers of hepatic injury or function (Supplemental Figure S5). There were no significant differences in acute hemodynamics, and inotrope scores were similar between the groups (Supplemental Figure S6). In the postoperative period, there were no differences in PaO_2/FiO_2 ratios as a marker of lung function (p = 0.92), nor were there significant differences in blood gas values during the postoperative period (Supplemental Figure S7). Similarly, there were no significant differences in hematologic endpoints between groups during the survival period (Supplemental Figure S8).

NEURORADIOLOGY. Swine in both groups exhibited a radiographic predominance of frontal and temporal lobe injuries. However, H_2-treated swine exhibited significantly lower volumes of white matter injury on T2 imaging than did controls (median: 134 mm^3

[interquartile range [IQR]: 84 to 200 mm^3] in H_2-treated swine vs. 383 mm^3 [IQR: 77 to 639 mm^3] in controls; p = 0.0460) (Figure 4).

NEUROPATHOLOGY. Regions of radiographically apparent injury correlated well with histologically apparent injury, with a predominance of injury in the frontal cortex. As a group, H_2-treated swine exhibited significantly lower histologic injury scores than did controls (p = 0.0044) (Figure 5), with a predominance of injury in the frontal cortex. There was no evidence of thalamic injury in this model.

DISCUSSION

We have shown that the perioperative administration of 2.40% H_2 is safe and diminishes neurologic injury in an experimental model of circulatory arrest. Although the combination of temperature and duration of circulatory arrest used is not used clinically, the model did successfully establish the degree of neurologic injury manifested in the most severely affected neonates, including perioperative seizures and radiographically apparent injury. In that setting, the perioperative administration of H_2 improved clinical neurologic scores, decreased serum markers of brain injury, decreased radiographically apparent volumes of brain injury, and lessened the degree of histopathologic injury. In addition, H_2-treated swine exhibited a significantly lower concentration of serum creatinine during the survival period, suggesting that hydrogen may diminish the effects of renal ischemia. Notably, there were minimal differences between groups in injury measures of cardiac performance, such as venous oxyhemoglobin saturation. This may be because, in essence, animals underwent a 75-min period of cardioplegic aortic cross-clamping, an ischemic insult that is known to be well tolerated.

This work adds to a growing body of preclinical studies supporting the therapeutic efficacy of inhalational H_2 gas. As mentioned previously, inhalational H_2 gas has been shown to diminish the volume of brain injury in rodent models of middle cerebral artery occlusion (21) and asphyxial cardiac arrest (23). H_2 inhalation has also been shown to decrease cellular injury and improve post-ischemic organ function in several animal models. For example, the administration of 1.3% H_2 in dogs for 6 h following a 90-min occlusion of the left anterior descending artery resulted in a 50% reduction in infarct size (29). A similarly protective effect has been shown following experimental ischemia-reperfusion injury in liver (30), lung (31), heart (32), and small intestine (33) and in models of septic shock (34). Still other studies have examined the intravenous administration of H_2-saturated saline (35) and the oral administration of H_2 in tablet or water form (36), although the serum concentration achieved by the oral route is orders of magnitude lower than that in the inhalational route (37).

Recently, a series of bold first-in-human studies of inhalational H_2 gas has been described. The first study (38) was a case series describing the administration of 2% H_2 in 5 mechanically ventilated survivors of witnessed out-of-hospital cardiac arrest, which found that 4 of 5 patients exhibited favorable

FIGURE 3 Clinical Neurologic Outcomes

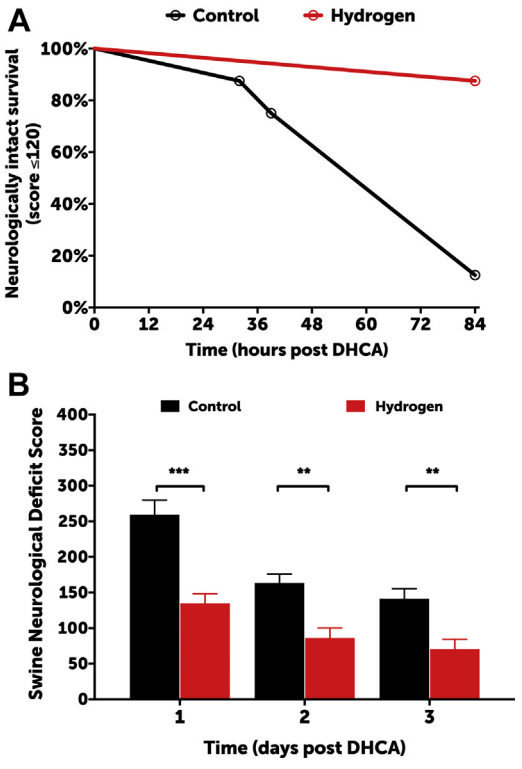

(A) Hydrogen-treated swine exhibited significantly higher rates of neurologically intact survival, which was defined as an SNDS ≤120 at the time of death (log-rank test: p = 0.0035). The overall rates of survival were similar between groups (log-rank test: p = 0.1435). **(B)** Hydrogen-treated swine exhibited significantly lower SNDS at 1, 2, and 3 days post injury (2-way ANOVA: p < 0.0001). Data for day 1 represent 8 swine per group; data for days 2 and 3 represent 8 swine in the hydrogen group and 6 in the control group (2 swine allocated to the control group died from refractory seizures and could not be successfully extubated). ***p < 0.001; **p < 0.01 for daily differences according to Sidak's multiple comparisons post test. ANOVA = analysis of variance; DHCA = deep hypothermic circulatory arrest; SNDS = Swine Neurodevelopment Score.

FIGURE 4 **Radiographic Differences Between Groups**

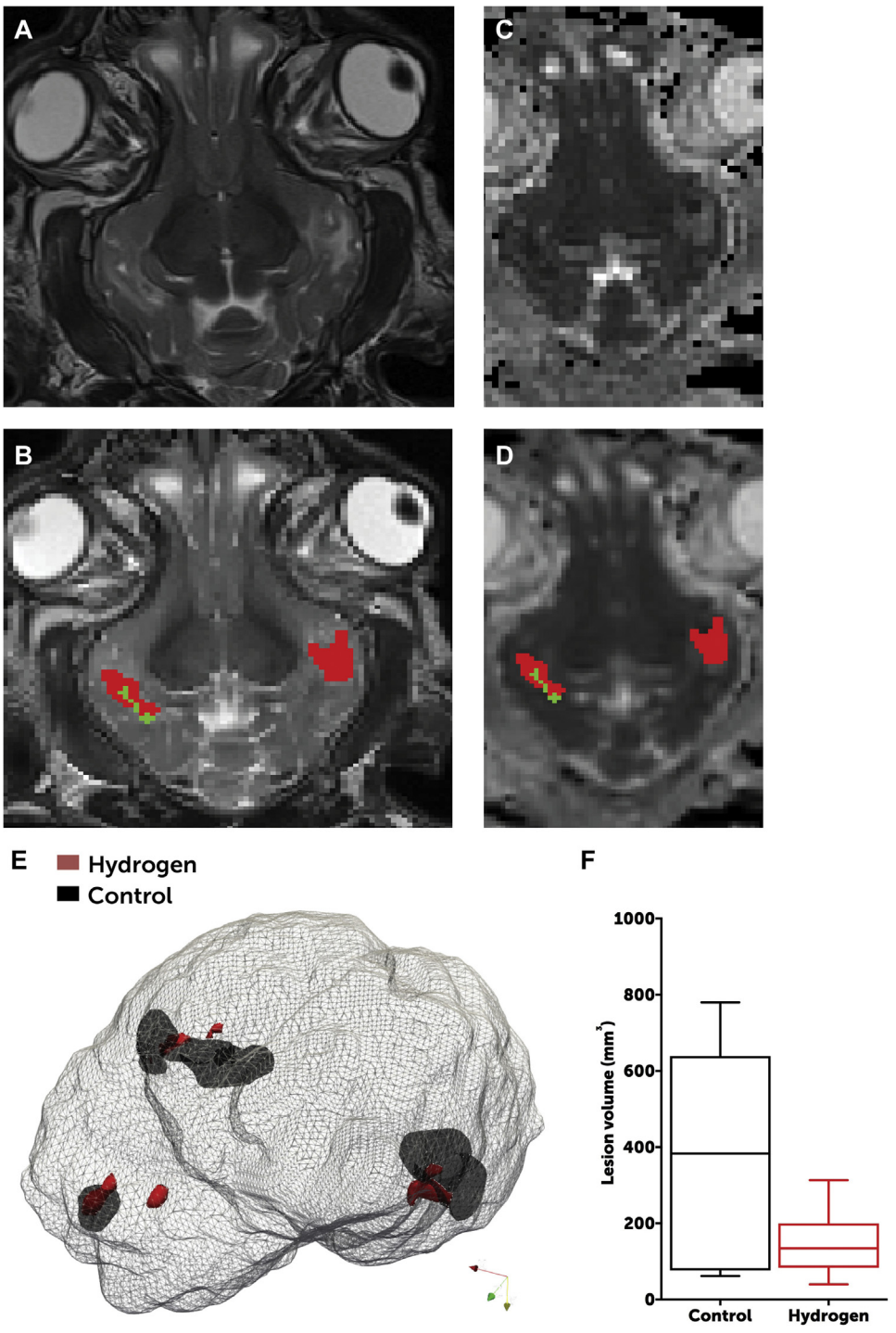

Axial T2 images **(A)** were assessed for radiographically apparent injuries **(B)**, which were outlined as moderate **(green)** or severe **(red)** on a voxel-per-voxel basis. These areas of injury were corroborated by review of apparent diffusion coefficient mapping **(C)**, which were similarly outlined **(D)**. **(E)** Areas of injury were rendered in 3 dimensions and overlaid onto an image of the brain to provide a visual image of the differences in the volume of cranial injury. Data were based on brain MRI of 8 swine in the hydrogen-treated group and 6 in the control group (2 swine allocated to the control group died from refractory seizures and could not survive to day 3). **(F)** H_2-treated animals exhibited a significantly lower volume of injury than did control animals (Student *t*-test: $p = 0.0463$). The **line** represents median, **boxes** are interquartile ranges, and **error bars** are minimum and maximum values.

FIGURE 5 Histopathologic Differences Between Groups

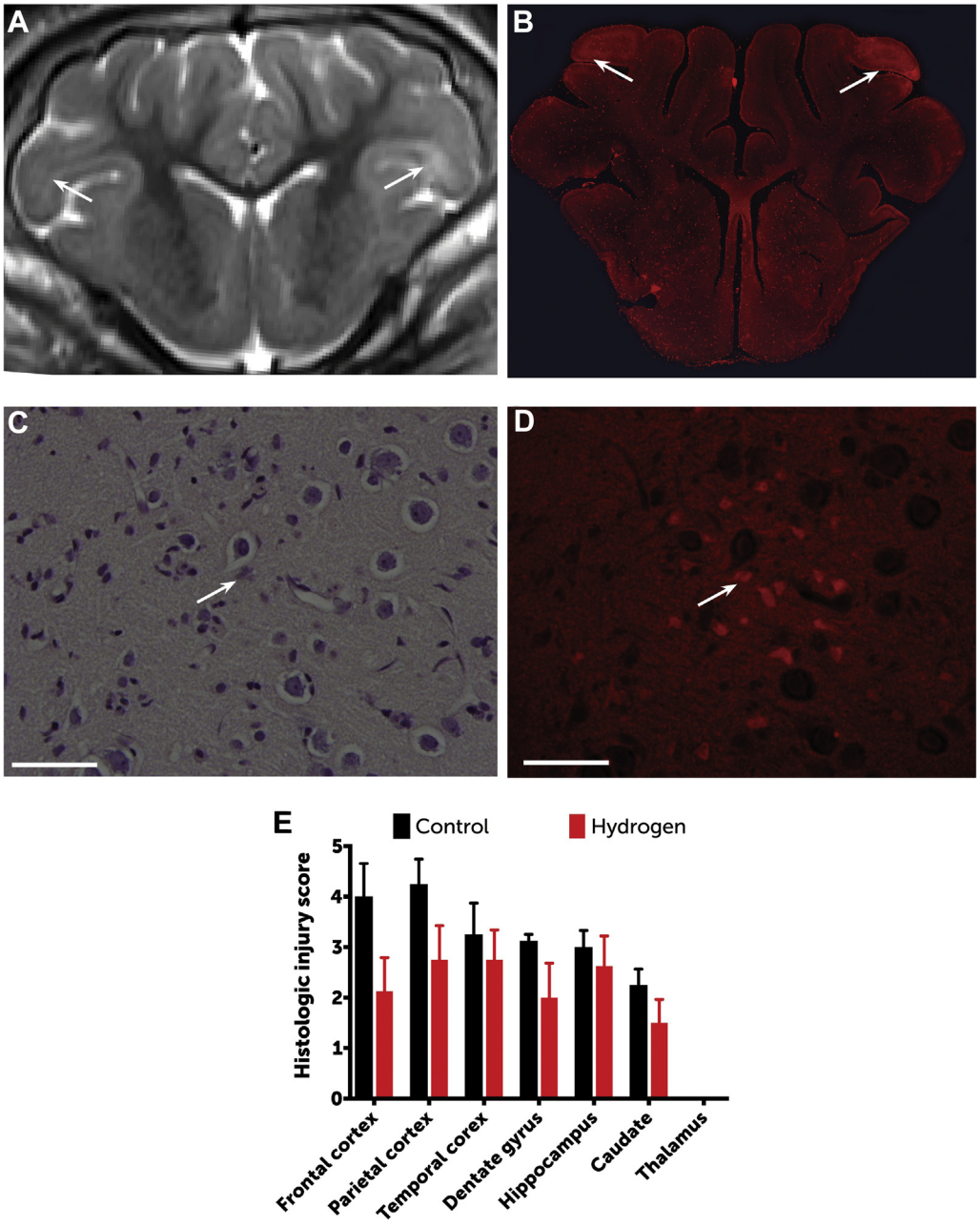

Regions of radiographically apparent injury **(A) (arrows)** correlated well with histologically apparent injury **(B)**, shown here by fluorescence microscopy (original magnification: ×1, using a Rhodamine filter). Neuronal injury was scored between 0 (normal) and 5 (severe neuronal injury, necrosis) for each region through identification of hypereosinophilic and/or apoptotic neurons by using both light **(C)** and fluorescence **(D)** microscopy (original magnification: ×60; bars = 50 μm). **Open arrows** = hypereosinophilic and apoptotic neurons. **(E)** As a group, hydrogen-treated swine exhibited significantly lower histologic injury scores than controls (2-way repeated measures ANOVA according to Sidak's test results: $p = 0.0044$). Data are based on histopathology for 8 swine in the hydrogen-treated group and 6 in the control group (2 swine allocated to the control group died from refractory seizures and did not survive to day 3). Data are means; error bars are SEM.

neurologic function (cerebral performance category 1) at hospital discharge. There were no environmental hazards reported. The second study (39) describes the face mask administration of 1.3% H_2 in 10 adults (plus 10 controls) undergoing percutaneous coronary reperfusion for ST-segment elevation myocardial infarction, finding that H_2 significantly improved ejection fraction at 6-month follow-up examination (39). A third study (40) described 25 patients (plus 25 controls) who presented with acute mild-to-moderately severe stroke, who underwent inhalation of 3% H_2 gas through face masks for 1 h twice per day for 7 days, which resulted in significant improvements in U.S. National Institutes of Health Stroke Scale scores and volumes of cerebral infarction by diffusion-weighted MRI imaging (40).

The application of H_2 administration in infants undergoing CPB is attractive for several reasons. First, it appears to be safe and easy to use. The dose tested here (2.4%) is a nonflammable gas mixture, even when mixed with balance (i.e., 97.6%) oxygen; hydrogen concentrations above 4% are known to be flammable. Following due diligence, we were able to attach these source gases were directly to the anesthesia machine and mechanical ventilator, and did not note any adverse effects on the delivery of anesthetic gas or on the function of either device. This represents an improvement on prior delivery techniques (which add a hydrogen-nitrogen mixture to inspiratory gas following passage through the ventilator) (38) in several ways. The setup described in the present study ensured delivery of a constant concentration of H_2 regardless of the patient's oxygen requirements. Administration of H_2 gas mixtures to the ventilator inlet would likely be required to treat infants due to their high bias flow and rapid respiratory rate, factors that would cause excessive dilution of even the most concentrated hydrogen-nitrogen mixture. Second, H_2 appears to be well tolerated at the doses tested. Consistent with prior reports (40,41), we did not find that the administration of H_2 had a measurable effect on hemodynamics or lung function. In the future, it will be important to study the effects of more extended durations of exposure (e.g., 72 h continuously) on these endpoints. Third, the application of H_2 may be practically added to current therapies, including hypothermia. For these reasons, a clinical trial of perioperative H_2 administration in neonates at high risk for neurologic injury may be warranted.

STUDY LIMITATIONS. 1) Although the newborn piglet has become an accepted model for the term neonate, we note that the maturity of myelination in these animals was approximately that of an 12-18 month old infant. 2) The protective effects of inhalational anesthetics and of intravenous sedatives (e.g. propofol) are well appreciated and may have affected the degree of neuronal injury, although the dosing was protocolized and equally applied to both groups. 3) Because we did not perform electroencephalography, we are unable to comment on hydrogen's effect on subclinical seizure activity. 4) Although previously well-characterized, we did not quantify the arterial concentrations of hydrogen gas during administration. Based on prior work, we expect that the arterial concentration of 2.4% H2 (which was a certified gas mixture and therefore the concentration was independently verified) in mechanically ventilated swine would reach a plateau between 5-10 μM/l within 20 min of inhalation (41). The number of animals included in each group was small, such that less common adverse effects of hydrogen administration may not have been detected. A properly powered safety study is warranted.

CONCLUSIONS

In a small series of neonatal swine, the perioperative administration of inhalational H_2 gas diminishes neurologic injury following experimental circulatory arrest.

ACKNOWLEDGMENTS The authors thank veterinary staff Cara Pimental, Madeleine Woomer, and Hugh Simonds; clinical perfusion staff Greg Matte, Kevin Connor, Natalie Toutenel, and Molly Bryant; overnight nursing staff Jay Hartford, Danielle Healey, and Stephanie Pietrafitta; clinical radiology staff Peter Morriss and Joseph Zmuda; and feeding volunteers Abigail Moore, Lindsay Thomson, Katherine Black, Andrew Lock, Jemima Lamothe, Yifeng Peng, Raymond Seekell, and Cameron Russell. The authors also thank Jie Zhu for performing GFAP assays; institutional safety officer Chad Pires, Boston Fire Department; and Centers for Disease Control and Prevention consultant Isaac Zlochower for assistance with the technical implementation of this work.

ADDRESS FOR CORRESPONDENCE: Dr. John Kheir, Department of Cardiology, Harvard Medical School, 300 Longwood Avenue, Boston, Massachusetts 02115. E-mail: john.kheir@childrens.harvard.edu.

PERSPECTIVES

COMPETENCY IN MEDICAL KNOWLEDGE: The use of inhaled hydrogen gas to diminish ischemic injury has been applied successfully in several rodent models and was recently described in humans following stroke, acute myocardial infarction, and cardiac arrest. A demonstration of safety in healthy volunteers is warranted, followed by a prospective study of hydrogen inhalation during congenital heart surgery and other clinical scenarios.

TRANSLATIONAL OUTLOOK: The favorable side effect profile and ease of administration make hydrogen a potentially appealing ancillary therapy.

REFERENCES

1. Algra SO, Jansen NJG, van der Tweel I, et al. Neurological injury after neonatal cardiac surgery: a randomized, controlled trial of 2 perfusion techniques. Circulation 2014;129:224–33.

2. Dent CL, Spaeth JP, Jones BV, et al. Brain magnetic resonance imaging abnormalities after the Norwood procedure using regional cerebral perfusion. J Thorac Cardiovasc Surg 2006;131:190–7.

3. Mahle WT, Tavani F, Zimmerman RA, et al. An MRI study of neurological injury before and after congenital heart surgery. Circulation 2002;106:I109–14.

4. McQuillen PS, Barkovich AJ, Hamrick SEG, et al. Temporal and anatomic risk profile of brain injury with neonatal repair of congenital heart defects. Stroke 2007;38:736–41.

5. Andropoulos DB, Hunter JV, Nelson DP, et al. Brain immaturity is associated with brain injury before and after neonatal cardiac surgery with high-flow bypass and cerebral oxygenation monitoring. J Thorac Cardiovasc Surg 2010;139:543–56.

6. Beca J, Gunn JK, Coleman L, et al. New white matter brain injury after infant heart surgery is associated with diagnostic group and the use of circulatory arrest. Circulation 2013;127:971–9.

7. Galli KK, Zimmerman RA, Jarvik GP, et al. Periventricular leukomalacia is common after neonatal cardiac surgery. J Thorac Cardiovasc Surg 2004;127:692–704.

8. Creighton DE, Robertson CMT, Sauve RS, et al. Neurocognitive, functional, and health outcomes at 5 years of age for children after complex cardiac surgery at 6 weeks of age or younger. Pediatrics 2007;120:e478–86.

9. Clancy RR, McGaurn SA, Wernovsky G, et al. Risk of seizures in survivors of newborn heart surgery using deep hypothermic circulatory arrest. Pediatrics 2003;111:592–601.

10. Bellinger DC, Jonas RA, Rappaport LA, et al. Developmental and neurologic status of children after heart surgery with hypothermic circulatory arrest or low-flow cardiopulmonary bypass. N Engl J Med 1995;332:549–55.

11. Naim MY, Gaynor JW, Chen J, et al. Subclinical seizures identified by postoperative electroencephalographic monitoring are common after neonatal cardiac surgery. J Thorac Cardiovasc Surg 2015;150:169–80.

12. Rappaport LA, Wypij D, Bellinger DC, et al. Relation of seizures after cardiac surgery in early infancy to neurodevelopmental outcome. Boston Circulatory Arrest Study Group. Circulation 1998;97:773–9.

13. Morton PD, Ishibashi N, Jonas RA. Neurodevelopmental abnormalities and congenital heart disease: insights into altered brain maturation. Circ Res 2017;120:960–77.

14. Ferradal SL, Yuki K, Vyas R, et al. Non-invasive assessment of cerebral blood flow and oxygen metabolism in neonates during hypothermic cardiopulmonary bypass: feasibility and clinical implications. Sci Rep 2017;7:44117.

15. Lanier WL. Cerebral metabolic rate and hypothermia: their relationship with ischemic neurologic injury. J Neurosurg Anesthesiol 1995;7:216–21.

16. Simons J, Sood ED, Derby CD, Pizarro C. Predictive value of near-infrared spectroscopy on neurodevelopmental outcome after surgery for congenital heart disease in infancy. J Thorac Cardiovasc Surg 2012;143:118–25.

17. Duplessis A, Jonas R, Wypij D, et al. Perioperative effects of alpha-stat versus ph-stat strategies for deep hypothermic cardiopulmonary bypass in infants. J Thorac Cardiovasc Surg 1997;114:991–1001.

18. Wypij D, Jonas RA, Bellinger DC, et al. The effect of hematocrit during hypothermic cardiopulmonary bypass in infant heart surgery: results from the combined Boston hematocrit trials. J Thorac Cardiovasc Surg 2008;135:355–60.

19. Chinopoulos C, Adam-Vizi V. Calcium, mitochondria and oxidative stress in neuronal pathology. Novel aspects of an enduring theme. FEBS J 2006;273:433–50.

20. Sheu S-S, Nauduri D, Anders MW. Targeting antioxidants to mitochondria: a new therapeutic direction. Biochimica et Biophysica Acta 2006;1762:256–65.

21. Ohsawa I, Ishikawa M, Takahashi K, et al. Hydrogen acts as a therapeutic antioxidant by selectively reducing cytotoxic oxygen radicals. Nat Med 2007;13:688–94.

22. Nagatani K, Wada K, Takeuchi S, et al. Effect of hydrogen gas on the survival rate of mice following global cerebral ischemia. Shock 2012;37:645–52.

23. Wang P, Jia L, Chen B, et al. Hydrogen inhalation is superior to mild hypothermia in improving cardiac function and neurological outcome in an asphyxial cardiac arrest model of rats. Shock 2016;46:312–8.

24. Matte GS, del Nido PJ. History and use of del Nido cardioplegia solution at Boston Children's Hospital. J Extra Corpor Technol 2012;44:98–103.

25. Wernovsky G, Wypij D, Jonas RA, et al. Postoperative course and hemodynamic profile after the arterial switch operation in neonates and infants. A comparison of low-flow cardiopulmonary bypass and circulatory arrest. Circulation 1995;92:2226–35.

26. Magruder JT, Hibino N, Collica S, et al. Association of nadir oxygen delivery on cardiopulmonary bypass with serum glial fibrillary acidic protein levels in pediatric heart surgery patients. Interact Cardiovasc Thorac Surg 2016;23:531–7.

27. Forbess JM, Ibla JC, Lidov HG, et al. University of Wisconsin cerebroplegia in a piglet survival model of circulatory arrest. Ann Thor Surg 1995;60:S494–500.

28. Castellanos MR, Nehru VM, Pirog EC, Optiz L. Fluorescence microscopy of H&E stained cervical biopsies to assist the diagnosis and grading of CIN. Pathol Res Pract 2018;214:605–11.

29. Yoshida A, Asanuma H, Sasaki H, et al. H2 Mediates cardioprotection via involvements of katp channels and permeability transition pores of mitochondria in dogs. Cardiovasc Drugs Ther 2012;26:217–26.

30. Fukuda K-I, Asoh S, Ishikawa M, Yamamoto Y, Ohsawa I, Ohta S. Inhalation of hydrogen gas suppresses hepatic injury caused by ischemia/reperfusion through reducing oxidative stress. Biochem. Biophys Res Commun 2007;361:670–4.

31. Kawamura T, Huang C-S, Tochigi N, et al. Inhaled hydrogen gas therapy for prevention of lung transplant-induced ischemia/reperfusion injury in rats. Transplantation 2010;90:1344–51.

32. Nakao A, Kaczorowski DJ, Wang Y, et al. Amelioration of rat cardiac cold ischemia/reperfusion injury with inhaled hydrogen or carbon monoxide, or both. J Heart Lung Transplant 2010; 29:544–53.

33. Buchholz BM, Kaczorowski DJ, Sugimoto R, et al. Hydrogen inhalation ameliorates oxidative stress in transplantation induced intestinal graft injury. Am J Transplant 2008;8:2015–24.

34. Yu Y, Yang Y, Bian Y, et al. Hydrogen gas protects against intestinal injury in wild type but not NRF2 knockout mice with severe sepsis by regulating HO-1 and HMGB1 release. Shock 2017; 48:364–70.

35. Huo T-T, Zeng Y, Liu X-N, et al. Hydrogen-rich saline improves survival and neurological outcome after cardiac arrest and cardiopulmonary resuscitation in rats. Anesth Analg 2014;119: 368–80.

36. Ostojic SM, Vukomanovic B, Calleja-Gonzalez J, Hoffman JR. Effectiveness of oral and topical hydrogen for sports-related soft tissue injuries. Postgrad Med 2014;126:187–95.

37. Liu C, Kurokawa R, Fujino M, Hirano S, Sato B, Li X-K. Estimation of the hydrogen concentration in rat tissue using an airtight tube following the administration of hydrogen via various routes. Sci Rep 2014;4:5485.

38. Tamura T, Hayashida K, Sano M, et al. Feasibility and safety of hydrogen gas inhalation for post-cardiac arrest syndrome–first-in-human pilot study. Circ J 2016;80:1870–3.

39. Katsumata Y, Sano F, Abe T, et al. The effects of hydrogen gas inhalation on adverse left ventricular remodeling after percutaneous coronary intervention for ST-elevated myocardial infarction—first pilot study in humans. Circ J 2017;81: 940–7.

40. Ono H, Nishijima Y, Ohta S, et al. Hydrogen gas inhalation treatment in acute cerebral infarction: a randomized controlled clinical study on safety and neuroprotection. J Stroke Cerebrovasc Dis 2017;26:2587–94.

41. Ono H, Nishijima Y, Adachi N, et al. A basic study on molecular hydrogen (H2) inhalation in acute cerebral ischemia patients for safety check with physiological parameters and measurement of blood H2 level. Medical Gas Research 2012;2:1.

KEY WORDS circulatory arrest, hydrogen gas, ischemia-reperfusion injury, neuroprotection

APPENDIX For supplemental figures and a table, please see the online version of this paper.

JACC: BASIC TO TRANSLATIONAL SCIENCE VOL. 4, NO. 2, 2019
© 2019 THE AUTHORS. PUBLISHED BY ELSEVIER ON BEHALF OF THE AMERICAN COLLEGE OF CARDIOLOGY FOUNDATION. THIS IS AN OPEN ACCESS ARTICLE UNDER THE CC BY-NC-ND LICENSE (http://creativecommons.org/licenses/by-nc-nd/4.0/).

PRECLINICAL RESEARCH

Phosphorylation of Hsp20 Promotes Fibrotic Remodeling and Heart Failure

George T. Gardner, PhD,[a] Joshua G. Travers, PhD,[b] Jiang Qian, PhD,[a] Guan-Sheng Liu, PhD,[a] Kobra Haghighi, PhD,[a] Nathan Robbins, MS,[c] Min Jiang, BS,[c] Yutian Li, MS,[a] Guo-Chang Fan, PhD,[a] Jack Rubinstein, MD,[c] Burns C. Blaxall, PhD,[b] Evangelia G. Kranias, PhD[a,d]

VISUAL ABSTRACT

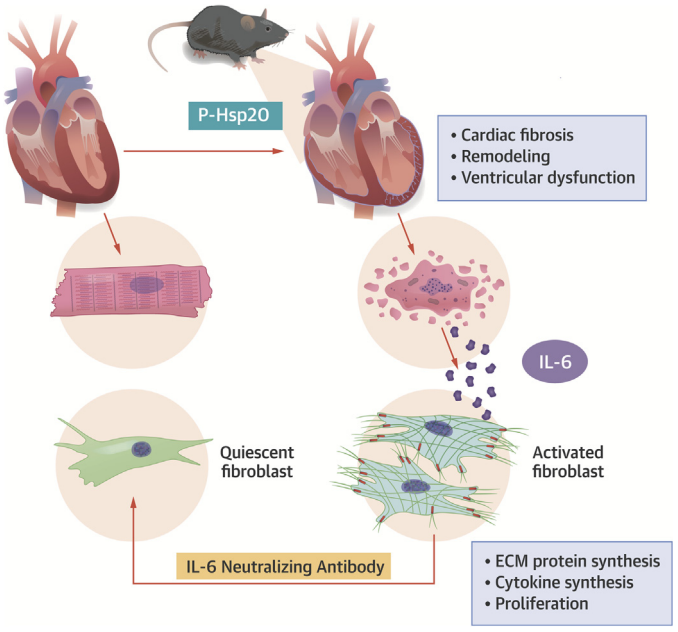

Gardner, G.T. et al. J Am Coll Cardiol Basic Trans Science. 2019;4(2):188–99.

HIGHLIGHTS

- **PKA-phosphorylation of Hsp20 is elevated in human failing hearts.**
- **Increases in phosphorylated Hsp20 in vivo are associated with fibrotic remodeling and reduced left ventricular function.**
- **The phosphorylated Hsp20 in cardiomyocyte promotes upregulation of IL-6 and its subsequent paracrine actions on the cardiac fibroblast.**
- **Blockade of IL-6 effects ex vivo and in vivo reduces the pro-fibrotic effects of phosphorylated Hsp20.**
- **Targeting phosphorylated Hsp20 in the cardiomyocyte may represent a potential therapeutic strategy to mitigate fibrotic remodeling and preserve function in the failing heart.**

From the [a]Department of Pharmacology and Systems Physiology, University of Cincinnati College of Medicine, Cincinnati, Ohio; [b]Department of Pediatrics, Division of Molecular Cardiovascular Biology, The Heart Institute, Cincinnati Children's Hospital Medical Center, Cincinnati, Ohio; [c]Department of Internal Medicine, University of Cincinnati College of Medicine, Cincinnati, Ohio; and the [d]Molecular Biology Division, Center for Basic Research, Biomedical Research Foundation of the Academy of Athens, Athens, Greece. This research was supported by U.S. National Institutes of Health (NIH) grants R01 HL26057, R01 HL64018 (EGK), R01 HL132551, R01 HL133695, R01 HL134321 to Dr. Blaxall; and predoctoral fellowship grants 15PRE25090055 and NIH grant T32 HL125204 from the American Heart Association Great Rivers Affiliate to Dr. Gardner. All other authors have reported that they have no relationships relevant to the contents of this paper to disclose.

All authors attest they are in compliance with human studies committees and animal welfare regulations of the authors' institutions and U.S. Food and Drug Administration guidelines, including patient consent where appropriate. For more information, visit the *JACC: Basic to Translational Science* author instructions page.

Manuscript received August 22, 2018; revised manuscript received September 27, 2018, accepted November 14, 2018.

ISSN 2452-302X https://doi.org/10.1016/j.jacbts.2018.11.007

SUMMARY

Cardiomyocyte-specific increases in phosphorylated Hsp20 (S16D-Hsp20) to levels similar to those observed in human failing hearts are associated with early fibrotic remodeling and depressed left ventricular function, symptoms which progress to heart failure and early death. The underlying mechanisms appear to involve translocation of phosphorylated Hsp20 to the nucleus and upregulation of interleukin (IL)-6, which subsequently activates cardiac fibroblasts in a paracrine fashion through transcription factor STAT3 signaling. Accordingly, treatment of S16D-Hsp20 mice with a rat anti-mouse IL-6 receptor monoclonal antibody (MR16-1) attenuated interstitial fibrosis and preserved cardiac function. These findings suggest that phosphorylated Hsp20 may be a potential therapeutic target in heart failure. (J Am Coll Cardiol Basic Trans Science 2019;4:188–99) © 2019 The Authors. Published by Elsevier on behalf of the American College of Cardiology Foundation. This is an open access article under the CC BY-NC-ND license (http://creativecommons.org/licenses/by-nc-nd/4.0/).

ABBREVIATIONS AND ACRONYMS

Ccl2 = C-C motif chemokine ligand 2

Ccl3 = C-C motif chemokine ligand 3

Col1a1 = collagen 1A1

Col3A1 = collagen 3A1

ECM = extra-cellular matrix

Hsp = heat shock protein

I/R = ischemia/reperfusion

IL = interleukin

Postn = periostin

SMA = smooth muscle actin

STAT3 = signal transducer and activator of transcription 3

TG = transgenic

TGF = transforming growth factor

TNF = tumor necrosis factor

TUNEL = terminal deoxynucleotidyl transferase dUTP nick end labeling

WT = wild type

Heart failure is a world-wide health problem affecting approximately 26 million people (1). Although significant advances have been made in the management of disease symptoms, morbidity and mortality rates remain high throughout the world (1). Studies aiming to understand the mechanisms, the underlying causes, and the progression of heart failure have implicated several signaling pathways. Specifically, the β-adrenergic axis, including its downstream regulatory phosphorylation substrates, has been shown to play a major role in cardiac remodeling (2). However, it is puzzling that some cyclic adenosine monophosphate-dependent phosphoproteins are downregulated, whereas others are increased in failing hearts (3). These altered responses may reflect the fine balance between protein kinase and phosphatase activities in subcellular compartments during heart failure progression (4). Among the cardiac phosphoproteins in the β-adrenergic transduction pathway is the small heat shock protein 20 (Hsp20 or HspB6), which has recently drawn particular attention.

SEE PAGE 200

Hsp20 belongs to the subfamily Hsps, which consists of 10 members whose molecular masses range from 12 to 43 kDa (5). It is a highly conserved protein and can be detected in all tissues but is most abundant in cardiac, skeletal, and smooth muscles (6). The levels of Hsp20 are mostly upregulated in human failing hearts (7) and in animal models upon oxidative stress, ischemia-reperfusion (I/R) injury, exercise training, and chronic β-adrenergic stimulation (8). These findings suggest that Hsp20 may play a critical role in cellular stress resistance as an adaptive response after exposure to stress stimuli. Indeed, adenoviral studies and studies in transgenic (TG) mice with cardiac-specific increases in Hsp20 have demonstrated a protective role for this protein against β-agonist-induced apoptosis (9,10), chronic doxorubicin-induced oxidative stress (11), and I/R injury (12).

Hsp20 was initially discovered as a phosphoprotein induced upon prolonged β-adrenergic stimulation of cardiomyocytes (13). Proteomic analysis revealed that phosphorylation occurs at Ser16 by protein kinase A, a phenomenon unique to Hsp20 among the small Hsp family (13). Subsequent investigations have shown that phosphorylation at Ser16 was elevated in human failing hearts as well as in murine hearts after I/R injury (7,12), suggesting that Hsp20 may function as an innate protector. Indeed, studies from the present authors' laboratory have indicated that overexpression of a constitutively phosphorylated form of Hsp20 (S16D) in cultured cardiomyocytes conferred protection against isoproterenol-induced cellular apoptosis, whereas overexpression of constitutively dephosphorylated Hsp20 (S16A) offered no anti-apoptotic benefits (9). Moreover, TG mice with cardiac-specific overexpression of the dephosphorylated S16A-Hsp20 exhibited diminished functional recovery and greater infarct size following I/R injury, both of which were associated with increased cardiomyocyte necrosis and apoptosis (7). These findings implicated phosphorylation of Hsp20 as a potential cardioprotector.

The critical role of Hsp20 in the heart and the potential benefits of its phosphorylation prompted examination of the functional significance and long-term effects of Hsp20 phosphorylation at Ser16 in vivo. To this end, the present authors generated a model with cardiac-specific overexpression of a constitutively phosphorylated Hsp20 form (S16D-Hsp20) and chose a mouse line with levels similar to those observed in human failing hearts for

characterization (7). Surprisingly, and in contrast to previous findings, S16D-Hsp20 mice exhibited early fibrotic remodeling and dysfunction, which progressed to the development of heart failure. Ex vivo studies have revealed that these effects were linked to the pro-fibrotic role of phosphorylated Hsp20, which induced synthesis of interleukin (IL)-6 in cardiomyocytes and its subsequent paracrine activation of cardiac fibroblasts through transcription factor STAT3 signaling. Accordingly, treatment of S16D mice using a rat anti-mouse IL-6 receptor monoclonal antibody (MR16-1) attenuated interstitial fibrosis and preserved left ventricular (LV) function. Taken together, these results reveal a novel functional role for Hsp20 in the heart and indicate that increases in Hsp20 phosphorylation appear to be maladaptive and may exacerbate the progression to heart failure.

METHODS

Additional detailed methods are available in the Supplemental Appendix.

EXPERIMENTAL MODELS. All animal procedures were performed according to guidelines set forth by the U.S. National Institutes of Health and those of the Institutional Animal Care and Use Committee at the University of Cincinnati. TG mice with cardiac-specific overexpression of constitutively phosphorylated Hsp20 (S16D-Hsp20) were generated as previously described (7) and carried the mouse cardiac S16D-Hsp20 cDNA under the control of the α-myosin heavy chain promoter. Male TG and wild-type (WT) age-matched control mice were used for all studies. For endpoint studies, mouse hearts were excised following anesthesia (200 mg/kg intraperitoneally [IP], Euthasol, Virbac AH, Inc., Fort Worth, Texas) and used for further analysis.

CARDIOMYOCYTE AND CARDIAC FIBROBLAST CROSS-TALK EXPERIMENTAL DESIGN. Cardiomyocyte and cardiac fibroblast isolation procedures were performed as described in the Supplemental Methods. Following cardiomyocyte isolation, the cardiomyocyte pellet was resuspended in a solution of plating medium (Dulbecco's modified Eagle medium [DMEM]), 10% fetal bovine serum [FBS], and 1% penicillin-streptomycin [Pen/Strep, ThermoFisher Scientific, Waltham, Massachusetts] plus 0.2% 2,3-butanedione monoxime), which was plated on laminin-coated dishes and incubated for 1 h at 37°C. The medium was replaced with infection medium (plating medium with no FBS), and cardiomyocytes were infected with adenovirus-infected green fluorescent protein (Ad.GFP), and with Ad.S16D or adenovirus-infected constitutively dephosphorylated Hsp20A (Ad.S16A) at a multiplicity of infection of 100. After 2 h of infection, the cells were transferred to culture medium consisting of a solution of DMEM plus 5 mg/l insulin-transferrin-selenium (Sigma-Aldrich, St. Louis, Missouri), 100 U/ml penicillin/streptomycin, 2 mM of L-glutamine, 4 mM $NaHCO_3$, 10 mM Hepes, 0.2% bovine serum albumin, and 25 μM blebbistatin (Cayman Chemical, Ann Arbor, Michigan) for 48 h. Medium was replaced after 24 h, after which the cardiomyocytes were collected for protein and RNA isolation. The conditioned medium was obtained and centrifuged at 5,000 *g* for 10 min to remove cell debris and stored at −80°C.

The ventricular fibroblasts were plated in growth medium and allowed to grow for 4 to 5 days until confluent. After fibroblasts were passaged in dishes appropriately sized for subsequent experiments, they were cultured in growth medium containing the cardiomyocyte-conditioned medium at a dilution of 1:1. Fibroblast proliferation was determined by using the MTT cell growth assay (catalog number CT02, MilliporeSigma, Burlington, Massachusetts) as previously described (14). Gene expression of pro-fibrotic markers was assessed using quantitative polymerase chain reaction (qPCR), and alpha-smooth muscle actin (SMA) stress fiber formation was evaluated using immunofluorescence. IL-6 inhibition was achieved through addition of an IL-6-neutralizing antibody (catalog number MAB406, R & D Systems, Minneapolis, Minnesota) to the conditioned medium upon application to the fibroblasts at a concentration of 0.60 μg/ml, based on a previously established protocol (15).

MR16-1 TREATMENT. Four-week old male S16D and WT control mice were injected with the rat anti-mouse IL-6 receptor monoclonal antibody MR16-1 (Genentech, San Francisco, California), as described later, using previously established protocols with minor modifications (16,17). Echocardiography was performed before the first injection and subsequently at 2 and 4 weeks afterward. Immediately after baseline echocardiography was performed, mice were given 2 mg/body MR16-1 or phosphate-buffered saline (PBS) as control by IP injection. During the first, second, and third weeks after the initial injection, mice received 0.5 mg/week MR16-1 or PBS (0.25 mg/body × 2 injections/week). At 8 weeks of age, following the final echocardiographic assessment, mice were sacrificed, and hearts were removed for examination of fibrosis using PicroSirius Red staining (Abcam, Cambridge, Massachusetts). Cardiac fibroblasts and

FIGURE 1 S16D-Hsp20 Transgenic Mice Exhibit Reduced Survival, Left Ventricular Remodeling, and Dysfunction

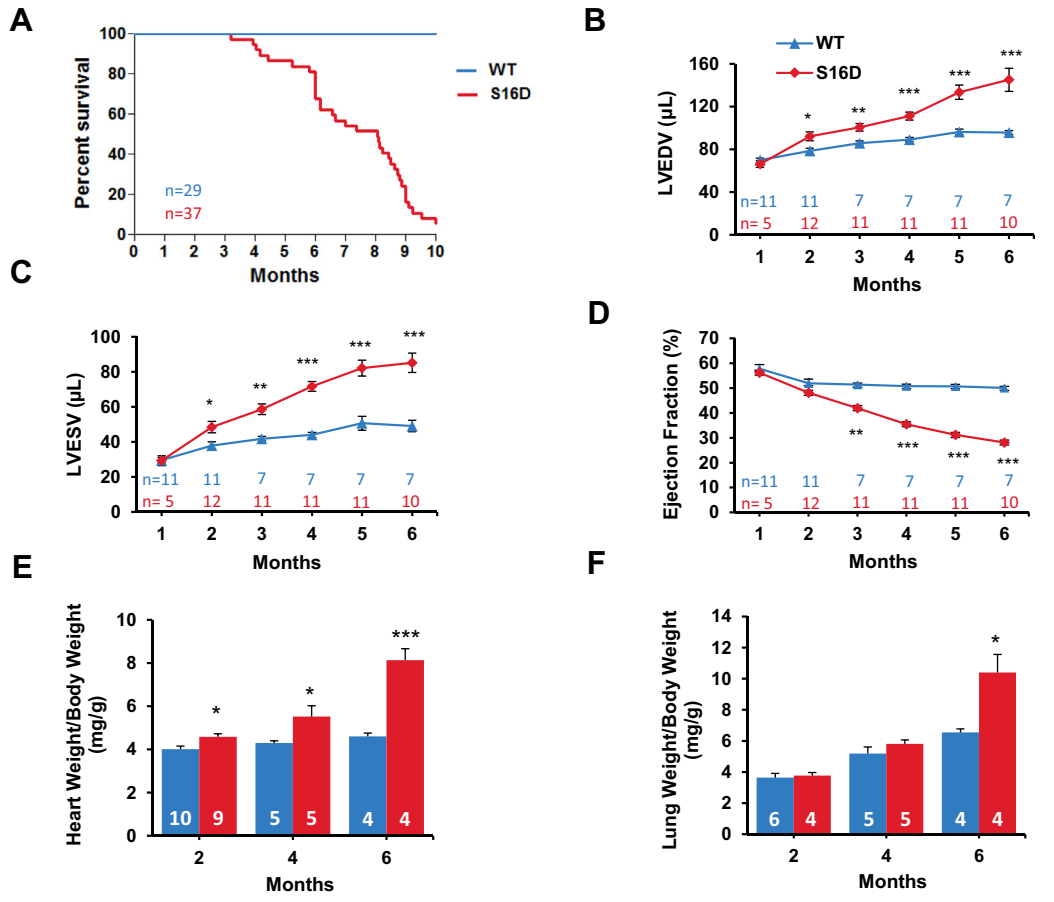

(A) Kaplan-Meier survival curve of S16D and WT control mice. Longitudinal echocardiographic assessment of S16D and WT mice at 2, 4, and 6 months of age: **(B)** LVEDV; **(C)** LVESV; and **(D)** EF. Gravimetric analysis of S16D and WT control mice at 2, 4, and 6 months of age. Ratios of **(E)** heart weight/body weight and **(F)** lung weight/body weight in S16D and WT control mice. Values are mean ± SEM. *$p < 0.05$; **$p < 0.01$; ***$p < 0.001$ versus WT. The number of samples (n) per group is indicated on the bar graphs. EF = ejection fraction; LVEDV = left ventricular end diastolic volume; LVESV = left ventricular end systolic volume; S16D = phosphorylated Hsp20; WT = wild type.

cardiomyocytes were isolated from a second cohort of treated and nontreated WT and S16D mice, as described in the Supplemental Methods. STAT3 signaling was assessed in the isolated fibroblasts by Western blotting, and expression of remodeling markers (*ANP*, *BNP*, and *β-MHC*) were measured using qPCR.

STATISTICS. Data were expressed as mean ± SEM. Comparisons between the means of 2 groups were evaluated using an unpaired Student *t*-test at each time point (**Figures 1B to 1F and 2D**) or the Mann-Whitney *U* test for data sets shown in **Figure 2B**, due to the small sample size (n = 3). Comparisons of more than 2 groups were performed using 1-way analysis of variance (ANOVA) followed by the Tukey multiple comparison test (**Figures 3B to 3E and 5F**). Alternatively, the Kruskal-Wallis test followed by Dunn's multiple comparison test was used for data shown in **Figure 5H**, due to the small sample size (n = 3). Groups which originated from the same heart were compared using a paired Student *t*-test (**Figure 4B**) or 1-way repeated measures ANOVA, followed by Tukey's multiple comparison test (**Figure 3A**). Data in **Figure 3G** were analyzed by using the Friedman test followed by Dunn's multiple comparison test, because of the small sample size (n = 3). Comparisons among the expression levels of 4 genes in the adenovirus-infected cardiomyocytes (**Figure 4A**) were performed by 2-way repeated measures ANOVA, followed by Bonferroni correction. Comparisons among groups in the MR16-1 treatment study (**Figure 5D**) were performed using 2-way repeated measures ANOVA, followed by the Neuman-Keuls multiple

FIGURE 2 Extensive Interstitial Fibrosis Evident in S16D-Hsp20 Hearts

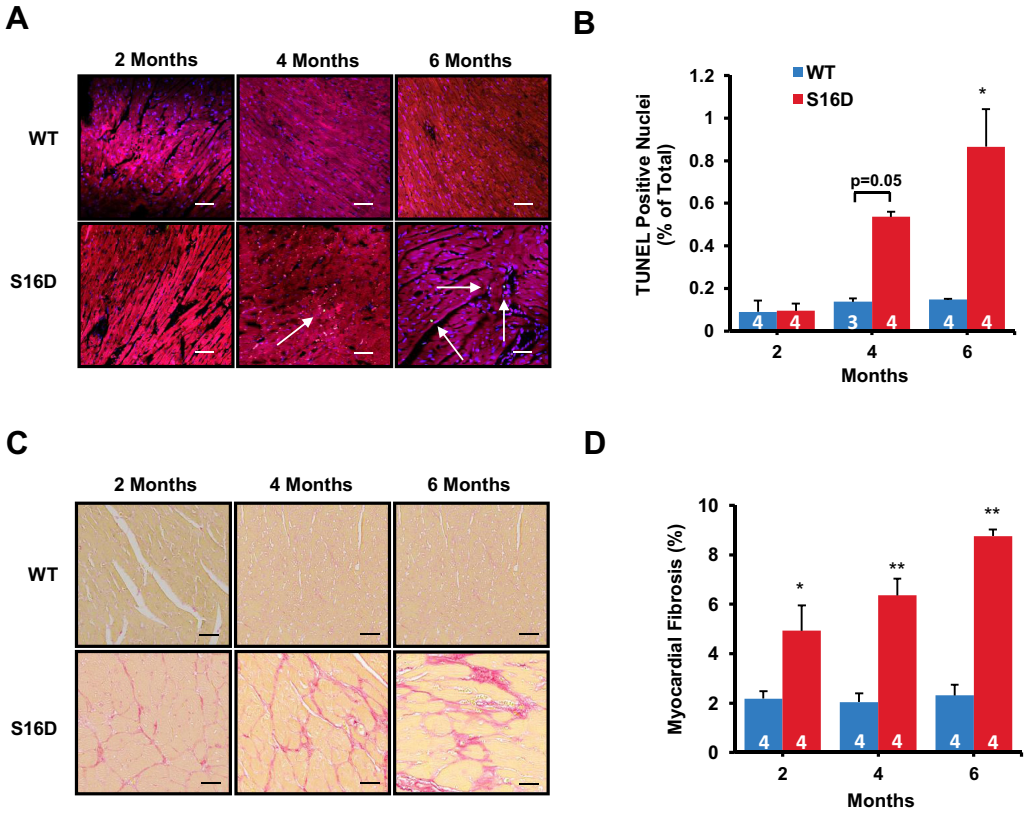

(A) Representative confocal images (original magnification: ×20) for TUNEL staining **(green)** counterstained with actin **(red)** and DAPI to visualize nuclei **(blue)**. **Arrows** indicate TUNEL-positive cells; scale bar: 50 μm. **(B)** Quantitative analysis of TUNEL-positive nuclei (expressed as a percentage of total nuclei) in S16D and WT ventricular sections at 2, 4, and 6 months of age. **(C)** Representative images (original magnification: ×20) of ventricular sections stained with Picrosirius red; scale bar: 50 μm. **(D)** Quantitative analysis of ventricular fibrosis (expressed as a percentage of total area) in S16D and WT hearts at 2, 4, and 6 months of age. The number of samples (n) per group is indicated on the bar graphs. DAPI = 4′,6-diamidino-2-phenylindole; TUNEL = terminal deoxynucleotidyl transferase dUTP nick end labeling; other abbreviations as in Figure 1.

comparison test. Analysis of survival was performed using the Kaplan-Meier method (using 29 WT control and 37 S16D mice). The following statistical thresholds were applied: $p < 0.05$, $p < 0.01$, and $p < 0.001$. Comparisons were made among the experimental groups and WT or GFP or among the indicated groups. Statistical analyses were performed using Prism version 8 software (GraphPad, San Diego, California).

RESULTS

S16D-Hsp20 TRANSGENIC MICE EXHIBITED CARDIAC REMODELING, DYSFUNCTION, AND EARLY MORTALITY. Hsp20 is upregulated and hyperphosphorylated in human heart failure and experimental I/R injury (7,12). To determine the functional significance of increases in Hsp20 phosphorylation, TG mice with cardiac-specific overexpression of a constitutively phosphorylated mutation (S16D-Hsp20) were generated (Supplemental Figure S1A). A TG mouse line was chosen that expressed increases in S16D-Hsp20 levels similar to those observed in human failing hearts (7) (Supplemental Figures S1B and S1C) for further characterization studies. Interestingly, S16D mice exhibited significantly reduced survival, with a mortality rate of approximately 50% by 7 months and 100% by 10 months of age (Figure 1A). There were no parallel deaths in either WT (Figure 1A) or TG mice with similar levels of WT-Hsp20 overexpression (12). Longitudinal assessment of LV geometry using echocardiography indicated significant chamber

FIGURE 3 S16D-Hsp20 Cardiomyocyte-Conditioned Medium Activates Myofibroblast Differentiation

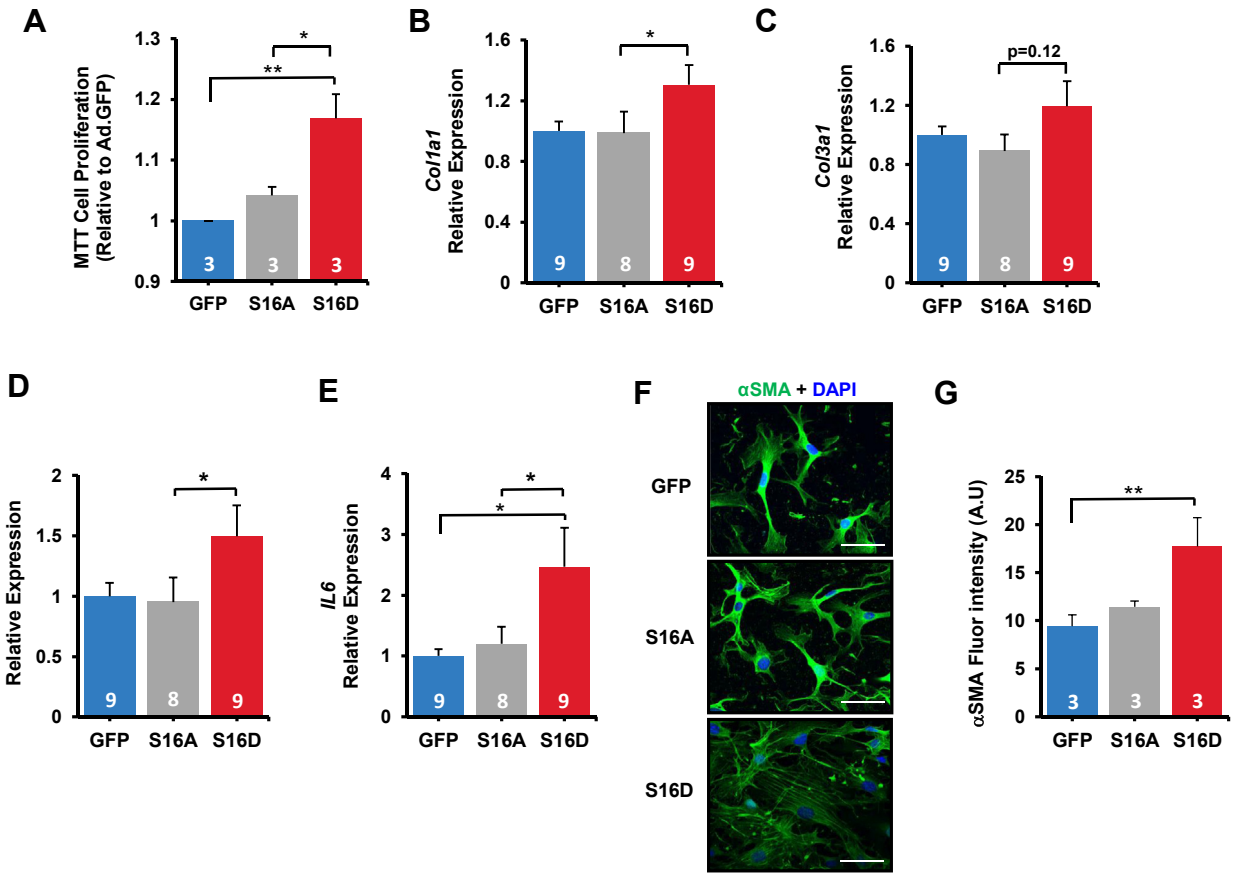

Adult mouse cardiac fibroblasts were cultured in conditioned medium from Ad.GFP, Ad.S16D, Ad.S16A. Fibroblast proliferation and markers of myofibroblast differentiation were assessed. **(A)** Quantification of fibroblast proliferation was determined using the MTT assay. Values are fold changes relative to those of Ad.GFP. Relative gene expression levels are shown for **(B)** *Col1a1*; **(C)** *Col3a1*; **(D)** *TGFβ1*; and **(E)** *IL-6*. Values are fold-changes relative to those of Ad.GFP. **(F)** Representative confocal images (original magnification: ×40) of fibroblasts stained with αSMA **(green)** plus DAPI to visualize nuclei **(blue)**; scale bar: 50 μm. **(G)** Quantification of αSMA fluorescence intensity. The number of samples (n) per group is indicated on the bar graphs. SMA = smooth muscle actin; Ad.GFP = adenovirus-infected green fluorescent protein; Ad.S16D = adenovirus-infected phosphorylated Hsp16D; Ad.S16A = adenovirus-infected dephosphorylated Hsp16A; *Col1a1* = collagen 1a1; *Col3a1* = collagen 3a1; *IL* = interlukin-6; *TGF* = transforming growth factor; other abbreviations as in Figure 2.

dilation (i.e., LV end-diastolic volume and LV end-systolic volume) in S16D mice, which became evident as early as 2 months of age (Figures 1B and 1C). These geometrical alterations were accompanied by a decrease in ejection fraction (EF) by 3 months of age (Figure 1D). The EF continued to deteriorate over time to <50% of normal by 6 months, concomitant with 50% mortality (Figure 1D). In contrast, TG mice overexpressing nonphosphorylated Hsp20 (S16A) at levels similar to those of S16D-Hsp20 mice did not exhibit any alterations in LV function and geometry up to 6 months of age (Supplemental Figure S2A to S2C). Further morphological, histological, and cellular studies were concentrated at the following 3 time points: at 2 months of age, at which point no change in LV function and slight chamber dilation occurred; at 4 months of age, when a significant decline in LV function and chamber dilation were exhibited but minimal deaths; and at 6 months, when severe dysfunction, extensive chamber dilation, and close to 50% mortality occurred (Figure 1A). Gravimetric analysis revealed a 13% increase in heart weight/body weight ratio as early as 2 months, which further increased at 4 and 6 months in S16D mice compared to those in WT mice (Figure 1E). Accordingly, cardiomyocyte hypertrophy, determined by wheat germ agglutinin staining, was increased at 2 months and was further augmented at 4 and 6 months

FIGURE 4 Acute Overexpression of S16D-Hsp20 in Cardiomyocytes Promotes Upregulation of the *IL-6* Gene Expression and Secretion

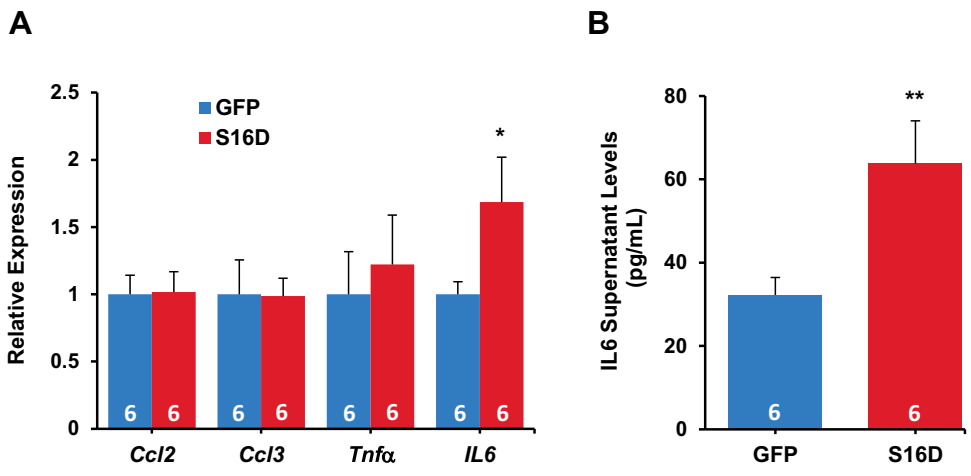

(A) Assessment of the following cytokine gene expression levels in Ad.GFP and Ad.S16D cardiomyocytes *Ccl2*, *Ccl3*, *TNF-α*, and *IL-6*. *TGFβ1* and *IL-1β* were not detectable in either group. Values were normalized to those of the internal control, 18 S, and expressed as fold-changes relative to those of Ad.GFP. **(B)** Quantification of IL-6 secretion into the conditioned medium from Ad.GFP and Ad.S16D cardiomyocytes was determined by using an ELISA assay. The number of samples (n) per group is indicated on the bar graphs. *Ccl2* = C-C motif chemokine ligand 2; *Ccl3* = C-C motif chemokine ligand 3; ELISA = enzyme-linked immunosorbent assay; MR16-1 = rat anti-mouse IL-6 receptor monoclonal antibody; *TNF* = tumor necrosis factor; WT = wild type; other abbreviations as in Figure 3.

(Supplemental Figures S3A and S3B). Analysis of gene expression of remodeling markers indicated that only the atrial natriuretic peptide (*ANP*) level was significantly elevated at 2 months of age. However, by 6 months of age, *ANP*, brain natriuretic peptide (*BNP*), and β-myosin heavy chain (*MHC*) levels were all significantly increased in S16D hearts (Supplemental Figure S3). Assessment of lung congestion indicated significant increases only at 6 months of age in S16D mice (**Figure 1F**). These results suggested that cardiac overexpression of S16D promoted early LV dilation, culminating in cardiac dysfunction and development of heart failure, resulting in early death.

EARLY INTERSTITIAL FIBROSIS. Evidence indicates that the advancement of cardiac remodeling is associated with myocyte apoptosis and interstitial fibrosis (18). Thus, cardiomyocyte loss in S16D hearts was assessed by terminal deoxynucleotidyl transferase dUTP nick end labeling (TUNEL) assay. There were significant levels of apoptosis at 4 and 6 months compared to WT control mice, whereas there was no evidence of TUNEL-positive nuclei at 2 months (**Figures 2A and 2B**). The absence of cardiomyocyte death at 2 months was further confirmed by lack of alterations in serum levels of cardiac troponin I (Supplemental Figure S4A) as well as caspase-3 activity (Supplemental Figure S4B) and the apoptotic markers Bak, Bcl-2, and Bax (Supplemental Figures S4C and S4D). Surprisingly, although there was no evidence of cell death at 2 months, significant interstitial fibrosis was observed by PicroSirius Red (Abcam) staining (**Figures 2C and 2D**). Collagen deposition was further determined through assessment of hydroxyproline content in S16D hearts. This assessment demonstrated a significant increase at 2 months, which was further increased at 6 months of age (Supplemental Figure S5A). These increases were accompanied by significant upregulation of the profibrotic markers collagen 1A1 (*Col1a1*) and transforming growth factor *(TGF)-β1* and by a trend toward increased expression of periostin (*Postn*) (Supplemental Figures S5B to S5D). Collectively, the data suggest that S16D-Hsp20 promotes early interstitial fibrosis in the absence of cardiomyocyte death in the heart.

CROSSTALK BETWEEN S16D CARDIOMYOCYTES AND FIBROBLASTS. Cardiac fibroblasts are responsible for extracellular matrix homeostasis, providing structural support for cardiomyocytes (18,19). Upon pathological stimulation, fibroblasts transition to the myofibroblast phenotype, which can promote excessive collagen secretion, leading to pathological remodeling (19). Recent studies have identified-dynamic crosstalk between cardiomyocytes and

fibroblasts, which occurs through secreted factors (20–22). Thus, these authors sought to determine whether S16D overexpression in the cardiomyocytes promote myofibroblast transition through a paracrine mechanism. To this end, isolated ventricular cardiomyocytes and fibroblasts from adult mouse hearts were used and with the cardiomyocytes were Ad.GFP and Ad.S16D or the constitutively dephosphorylated Hsp20, Ad.S16A, as an additional control. The Hsp20 overexpression levels in S16D and S16A cardiomyocytes were similar (Supplemental Figures S6A and S6B). Then, the conditioned medium from the infected cardiomyocytes was used to culture fibroblasts, and their potential activation was assessed using key markers (19). Fibroblasts in the S16D medium exhibited significantly enhanced proliferation (**Figure 3A**) and significant upregulation of *Col1a1*, *(TGF)-β1*, and *IL-6*, as well as a trend toward upregulation of collagen 3A1 (*Col13a1*) (**Figures 3B to 3E**). Further analysis using immunofluorescence revealed the presence of prominent αSMA-positive stress fibers in S16D fibroblasts (**Figures 3F and 3G**), a reliable indicator of myofibroblast activation in culture. Importantly, the effects observed on fibroblast differentiation were specific to S16D as there were no alterations elicited by the S16A medium (**Figures 3A to 3G**). To exclude cardiomyocyte death as a contributing factor to fibroblast activation (22), the levels of lactate dehydrogenase were determined in the conditioned medium. There were no differences in the levels of lactate dehydrogenase released among the 3 groups (Supplemental Figure S6C). These findings demonstrate that overexpression of S16D in the cardiomyocytes may promote the secretion of a factor(s) which stimulates differentiation of fibroblasts to myofibroblasts.

IL-6 IS UPREGULATED IN S16D CARDIOMYOCYTES. The findings described above coupled with previous evidence indicating that secretion of cytokines from the cardiomyocyte (23) can activate myofibroblast differentiation (24) prompted an examination of the expression levels of C-C motif chemokine ligand 2 (*Ccl2)*, C-C motif chemokine ligand 3 (*Ccl3*), *IL-6*, tumor necrosis factor *(TNF)-α, TGFβ1*, and *IL-1β* in Ad.S16D cardiomyocytes. Interestingly, only IL-6 expression was upregulated (**Figure 4A**), and this upregulation was associated with its increased secretion into the medium from the cardiomyocytes (**Figure 4B**). Taken together, these data indicate that increases in S16D in cardiomyocytes promote IL-6 transcriptional upregulation and its subsequent secretion to the extracellular space.

BLOCKING IL-6 REDUCES PRO-FIBROTIC EFFECTS OF S16D. To determine the role of IL-6 in the pro-fibrotic effects elicited by the S16D cardiomyocytes, an IL-6-neutralizing antibody, M16-1, was included in the conditioned medium that was applied to fibroblasts. There was a reduction in the expression levels of collagens and cytokines in the fibroblasts treated with the IL-6 antibody, although statistical significance was not reached (Supplemental Figures S6D and S7A). Furthermore, αSMA stress fiber formation was abrogated in the presence of the IL-6 antibody (Supplemental Figures S7E and S7F). To further confirm the role of IL-6 in the transition of fibroblasts to myofibroblasts, the question of whether STAT3 localized to the nucleus was examined, as its phosphorylation and nuclear translocation occurred upon stimulation of the IL-6 receptor (IL-6R) (25). Indeed, nuclear accumulation of phosphorylated STAT3 (P-STAT3) was significantly greater in fibroblasts treated with the S16D medium (Supplemental Figure S7G). Accordingly, inclusion of the IL-6 antibody abrogated this effect (Supplemental Figure S7G). These results suggested that S16D overexpression in the cardiomyocyte promotes myofibroblast differentiation through a paracrine mechanism by activation of the IL-6/STAT3 signaling pathway in the fibroblast.

TREATMENT OF S16D MICE WITH MR16-1 ATTENUATED FIBROSIS AND IMPROVED CARDIAC FUNCTION. Our ex vivo findings led to an investigation of whether IL-6 was contributing to the excessive collagen deposition and cardiac remodeling in the S16D mice, which was observed as early as 2 months of age. Indeed, both cardiac and serum IL-6 levels were higher in S16D mice than in WT mice (**Figures 5A and 5B**). Because IL-6 has been implicated in fibrotic ventricular remodeling (26), the authors hypothesized that treatment of S16D mice with an IL-6 receptor antagonist (MR16-1) would reduce ventricular fibrosis and preserve function. Therefore, S16D and WT mice were treated with MR16-1 or PBS for 4 weeks, starting at 1 month of age, when no ventricular dysfunction or remodeling was evident (**Figure 5C**). Treatment with MR16-1 prevented deterioration of function (EF) in S16D mice (**Figure 5D**), although it had no effects on ventricular chamber dilation, cardiomyocyte hypertrophy, or remodeling markers (Supplemental Figures S8A to S8F), indicating that a separate mechanism might have been contributing to remodeling in S16D hearts. Importantly, MR16-1 completely prevented ventricular fibrosis in S16D hearts (**Figures 5E and 5F**). To confirm the fact that IL-6 signaling was inhibited by MR16-1 in S16D hearts, cardiac fibroblasts were isolated, and P-STAT3/total STAT3 levels were assessed through

FIGURE 5 MR16-1 Treatment Attenuates Fibrosis and Improves Cardiac Function

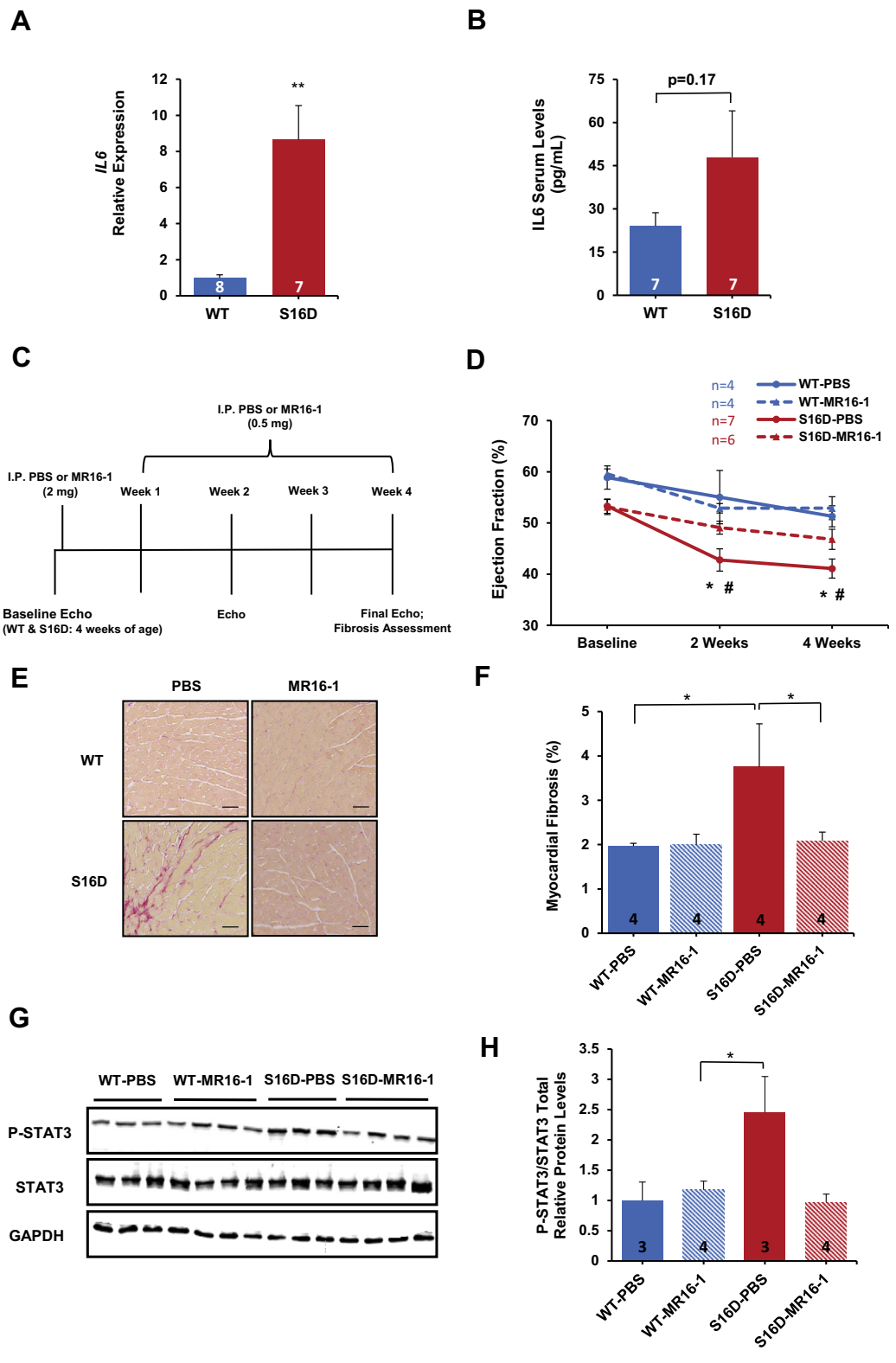

Continued on the next page

Western blotting. Indeed, fibroblasts isolated from S16D-PBS-treated hearts showed an increase in P-STAT3 levels, which was abrogated by treatment with the MR16-1 antibody. These results suggested that upregulation of IL-6 contributes to the acceleration of cardiac fibrosis and dysfunction in S16D TG mice.

DISCUSSION

The current study reveals a novel pro-fibrotic role of phosphorylated Hsp20 (S16D-Hsp20) through regulation of myocyte-synthesized IL-6 and subsequent paracrine activation of myofibroblast differentiation. These insights were acquired through characterization of a TG mouse model with cardiac-specific overexpression of constitutively phosphorylated Hsp20 (S16D-Hsp20), which demonstrated fibrotic ventricular remodeling at an early age.

Cardiac fibroblasts are essential for maintaining normal cardiac function, as they provide a structural network for cardiomyocytes, distribute mechanical forces through the cardiac tissue, and mediate electric conduction (19). In response to pathological stimuli, these cells undergo a transition to a myofibroblast phenotype, which can secrete elevated levels of extracellular matrix (ECM) proteins aimed at maintaining the structural integrity of the heart (19). However, a sustained fibrotic response can lead to reduced ventricular compliance, cardiac dysfunction, and ultimately heart failure (19). There are 2 distinct types of cardiac fibrosis: 1) reactive interstitial fibrosis, which is an expansion of the ECM in the absence of cardiomyocyte loss; and 2) replacement fibrosis, which results in extensive cardiomyocyte death (27). In the present study, S16D was associated with extensive cardiac interstitial fibrosis as early as 2 months of age, without evidence of cardiomyocyte apoptosis. Thus, it appears that cell death was not the initial driving force behind the early interstitial fibrosis, consistent with previous in vitro findings indicating that S16D renders cardiomyocyte protection from apoptosis (9).

The fine communication between cardiac myocytes and fibroblasts plays a key role in cardiac remodeling mediated by paracrine factors (21). These factors include numerous cytokines such as TGF-β1, IL-6, IL-1β, and TNF-α, which have been implicated in fibroblast proliferation and myofibroblast activation (21,22,26). Findings of the present study indicate that the S16D overexpression in cardiomyocytes also activated myofibroblast differentiation in a paracrine fashion. This was shown by enhanced proliferation and upregulation in expression of collagens, cytokines, and αSMA stress fibers. The pro-fibrotic effects were specific to S16D, as medium from Ad.S16A (constitutively dephosphorylated) cardiomyocytes had no effects. Further assessment of the S16D-infected cardiomyocytes indicated the transcriptional upregulation of IL-6. These effects were specific to IL-6, as there were no alterations in gene expression of other cytokines. Accordingly, secretion of IL-6 from the cardiomyocytes contributed to activation of fibroblasts to myofibroblasts, as shown by a reduction of the pro-fibrotic effects when using the IL-6 neutralizing antibody.

IL-6 is a pleiotropic cytokine whose expression in the heart has received particular interest, as its circulatory and intracardiac levels are elevated in congestive heart failure and are powerful predictors of LV remodeling (28,29). IL-6 signaling occurs through the transcription factor STAT3, which, upon phosphorylation at tyrosine 705, translocates to the nucleus and activates a broad array of target genes (25). In the cardiac fibroblast, STAT3 activation has been demonstrated to promote fibroblast proliferation in addition to synthesis of ECM proteins (25). Results of the present study show that S16D overexpression in cardiomyocytes promotes IL-6 secretion, which subsequently activates nuclear

FIGURE 5 Continued

(A) Quantification of *IL-6* gene expression levels in S16D hearts and WT control hearts. Values were normalized to those of the internal control GAPDH and expressed as fold-changes relative to those of WT mice. **(B)** Quantification of *IL-6* serum levels in S16D and WT control mice was determined by using an ELISA assay. **(C)** Schematic presentation of S16D and WT control mice treated with MR16-1 or PBS (control) starting at 1 month of age. Following the baseline echocardiographic assessment, mice were injected with 2 mg/body weight MR16-1 or PBS. Subsequently, mice received 0.5 mg/body per week (2 injections of 0.25 mg/body) during weeks 1, 2, and 3. **(D)** Left ventricular ejection fraction at baseline and at 2 and 4 weeks; *$p < 0.05$ versus WT-PBS; #$p < 0.05$ versus S16D-MR16-1. **(E)** Representative images (original magnification: ×20) of Picrosirius **red** staining following 4 weeks of treatment; scale bar: 50 μm. **(F)** Quantification of percent of ventricular fibrosis (fibrotic area/total ventricular area). **(G)** Representative Western blots and **(H)** quantification of P-STAT3 (Y705)/total STAT3 protein levels of the indicated groups. Values are fold-changes relative to those of WT-PBS. The number of samples (n) per group is indicated on the bar graphs. GAPDH = glyceraldehyde 3-phosphate dehydrogenase; I.P. PBS = intraperitoneal phosphate buffered saline; P-STAT3 = phosphorylated STAT3; other abbreviations as in Figures 3 and 4.

translocation of phosphorylated STAT3 (P-STAT3) in fibroblasts and increased expression of collagen and cytokines. Importantly, addition of the IL-6 neutralizing antibody reduced the P-STAT3 and attenuated the pro-fibrotic effects of S16D. Thus, IL-6/STAT3 signaling appears to mediate the paracrine effects of the S16D cardiomyocyte.

The ex vivo findings described previously led to the hypothesis that IL-6 may contribute to cardiac remodeling and dysfunction observed in the S16D mouse model. Indeed, cardiac gene expression as well as serum levels of IL-6 were elevated in S16D hearts as early as 2 months of age. To confirm the contribution of IL-6 in cardiac remodeling and dysfunction, S16D mice were treated with the selective IL-6 receptor antagonist monoclonal antibody MR16-1. Isolated cardiac fibroblasts revealed that STAT3 signaling was elevated in the nontreated S16D hearts, although this effect was abolished by treatment with the MR16-1 antibody. Accordingly, MR16-1 prevented the development of interstitial fibrosis and preserved EF. However, MR16-1 treatment had no effects on the observed alterations of LV chamber dilation, cardiomyocyte hypertrophy, or remodeling markers, as these parameters were similar to those in nontreated S16D mice. Taken together, IL-6/STAT3 signaling appears to contribute to fibroblast activation and the resultant development of interstitial fibrosis in S16D hearts. Nonetheless, the lack of protection against remodeling in the MR16-1-treated S16D hearts indicates that these pathological alterations are driven by additional factors other than the IL-6/STAT3 pathway.

These results suggest that chronic phosphorylation of Hsp20 is associated with ventricular remodeling and dysfunction, partially mediated through the pro-fibrotic action of cardiomyocyte-synthesized IL-6. Thus, targeting the levels of S16D-Hsp20 in human heart failure may represent an effective strategy for limiting fibrotic remodeling.

STUDY LIMITATIONS. Although the current findings highlight the significance of chronic Hsp20 phosphorylation in cardiac fibrosis, use of the TG mouse model in this study may be criticized as limiting. Generation of a gene-targeted knock-in mouse model would have been a more elegant model for examining the significance of Hsp20 phosphorylation in vivo. However, transgenesis was chosen because the aim was to overexpress S16D-Hsp20 at levels similar to those observed in human heart failure. The authors recognize that additional mechanisms might have contributed to cardiac remodeling in the S16D hearts. For the purpose of this study, the authors focused specifically on the regulation of IL-6 in the cardiomyocyte and its subsequent paracrine effects on the cardiac fibroblast.

CONCLUSIONS

Ex vivo and in vivo studies have revealed a novel role for phosphorylated Hsp20 in the heart involving upregulation of IL-6 in the cardiomyocyte and the associated paracrine activation of cardiac fibroblasts. Thus, hyperphosphorylation of Hsp20 in human failing hearts coupled with findings from the current study suggest that it may play a role in pathological remodeling and, thus, may provide a new therapeutic opportunity.

ACKNOWLEDGEMENTS The authors thank the Live Microscopy Core in the Department of Pharmacology and Systems Physiology, University of Cincinnati, for providing technical assistance with confocal microscopy.

ADDRESS FOR CORRESPONDENCE: Dr. Evangelia G. Kranias, Department of Pharmacology and Systems Physiology, University of Cincinnati College of Medicine, 231 Albert Sabin Way, Cincinnati, Ohio 45267-0575. E-mail: KRANIAEG@ucmail.uc.edu.

PERSPECTIVES

COMPETENCY IN MEDICAL KNOWLEDGE: Cardiac fibrosis, characterized by excessive deposition of extracellular matrix proteins, is a key component in ventricular remodeling and the pathophysiology of heart failure. Crosstalk between cardiomyocytes and cardiac fibroblasts through paracrine factors has emerged as a factor in this remodeling process. However, there is a need to gain further insights into this apparent cardiac myocyte/fibroblast communication to prevent heart failure progression. Findings from the present study demonstrate that phosphorylated Hsp20 may act as a regulator in paracrine-induced fibrotic remodeling.

TRANSLATIONAL OUTLOOK: Hsp20 phosphorylation is chronically elevated in human and experimental heart failure. Explorations in the relevance of these increases in a murine model indicates that they associate with fibrotic ventricular remodeling and contractile dysfunction. Therefore, Hsp20 may serve as a novel therapeutic target in heart failure.

REFERENCES

1. Savarese G, Lund LH. Global public health burden of heart failure. Card Fail Rev 2017;3:7–11.

2. Lohse MJ, Engelhardt S, Eschenhagen T. What is the role of beta-adrenergic signaling in heart failure? Circ Res 2003;93:896–906.

3. Lou Q, Janardhan A, Efimov IR. Remodeling of calcium handling in human heart failure. Adv Exp Med Biol 2012;740:1145–74.

4. Nicolaou P, Hajjar RJ, Kranias EG. Role of protein phosphatase-1 inhibitor-1 in cardiac physiology and pathophysiology. J Mol Cell Cardiol 2009;47:365–71.

5. Kappé G, Franck E, Verschuure P, Boelens WC, Leunissen JA, De jong WW. The human genome encodes 10 alpha-crystallin-related small heat shock proteins: HspB1-10. Cell Stress Chaperones 2003;8:53–61.

6. Fan GC, Chu G, Kranias EG. Hsp20 and its cardioprotection. Trends Cardiovasc Med 2005;15:138–41.

7. Qian J, Ren X, Wang X, et al. Blockade of Hsp20 phosphorylation exacerbates cardiac ischemia/reperfusion injury by suppressed autophagy and increased cell death. Circ Res 2009;105:1223–31.

8. Fan GC, Kranias EG. Small heat shock protein 20 (HspB6) in cardiac hypertrophy and failure. J Mol Cell Cardiol 2011;51:574–7.

9. Fan GC, Chu G, Mitton B, et al. Small heat-shock protein Hsp20 phosphorylation inhibits beta-agonist-induced cardiac apoptosis. Circ Res 2004;94:1474–82.

10. Fan GC, Yuan Q, Song G, et al. Small heat-shock protein Hsp20 attenuates beta-agonist-mediated cardiac remodeling through apoptosis signal-regulating kinase 1. Circ Res 2006;99:1233–42.

11. Fan GC, Zhou X, Wang X, et al. Heat shock protein 20 interacting with phosphorylated Akt reduces doxorubicin-triggered oxidative stress and cardiotoxicity. Circ Res 2008;103:1270–9.

12. Fan GC, Ren X, Qian J, et al. Novel cardioprotective role of a small heat-shock protein, Hsp20, against ischemia/reperfusion injury. Circulation 2005;111:1792–9.

13. Chu G, Egnaczyk GF, Zhao W, et al. Phosphoproteome analysis of cardiomyocytes subjected to beta-adrenergic stimulation: identification and characterization of a cardiac heat shock protein p20. Circ Res 2004;94:184–93.

14. Travers JG, Kamal FA, Valiente-alandi I, et al. Pharmacological and activated fibroblast targeting of Gβγ-GRK2 after myocardial ischemia attenuates heart failure progression. J Am Coll Cardiol 2017;70:958–71.

15. Fredj S, Bescond J, Louault C, Delwail A, Lecron JC, Potreau D. Role of interleukin-6 in cardiomyocyte/cardiac fibroblast interactions during myocyte hypertrophy and fibroblast proliferation. J Cell Physiol 2005;204:428–36.

16. Ueda O, Tateishi H, Higuchi Y, et al. Novel genetically-humanized mouse model established to evaluate efficacy of therapeutic agents to human interleukin-6 receptor. Sci Rep 2013;3:1196.

17. Hartman MH, Vreeswijk-baudoin I, Groot HE, et al. Inhibition of interleukin-6 receptor in a murine model of myocardial ischemia-reperfusion. PLoS One 2016;11:e0167195.

18. Liu T, Song D, Dong J, et al. Current understanding of the pathophysiology of myocardial fibrosis and its quantitative assessment in heart failure. Front Physiol 2017;8:238.

19. Travers JG, Kamal FA, Robbins J, Yutzey KE, Blaxall BC. Cardiac fibrosis: the fibroblast awakens. Circ Res 2016;118:1021–40.

20. Martin ML, Blaxall BC. Cardiac intercellular communication: are myocytes and fibroblasts fair-weather friends? J Cardiovasc Transl Res 2012;5:768–82.

21. Pellman J, Zhang J, Sheikh F. Myocyte-fibroblast communication in cardiac fibrosis and arrhythmias: mechanisms and model systems. J Mol Cell Cardiol 2016;94:22–31.

22. Talman V, Ruskoaho H. Cardiac fibrosis in myocardial infarction-from repair and remodeling to regeneration. Cell Tissue Res 2016;365:563–81.

23. Aoyagi T, Matsui T. The cardiomyocyte as a source of cytokines in cardiac injury. J Cell Sci Ther 2011;2012(S5).

24. Porter KE, Turner NA. Cardiac fibroblasts: at the heart of myocardial remodeling. Pharmacol Ther 2009;123:255–78.

25. Haghikia A, Ricke-Hoch M, Stapel B, Gorst I, Hilfiker-Kleiner D. STAT3, a key regulator of cell-to-cell communication in the heart. Cardiovasc Res 2014;102:281–9.

26. Meléndez GC, Mclarty JL, Levick SP, Du Y, Janicki JS, Brower GL. Interleukin 6 mediates myocardial fibrosis, concentric hypertrophy, and diastolic dysfunction in rats. Hypertension 2010;56:225–31.

27. Piek A, De Boer RA, Silljé HH. The fibrosis-cell death axis in heart failure. Heart Fail Rev 2016;21:199–211.

28. Kanda T, Takahashi T. Interleukin-6 and cardiovascular diseases. Jpn Heart J 2004;45:183–93.

29. Kobara M, Noda K, Kitamura M, et al. Antibody against interleukin-6 receptor attenuates left ventricular remodelling after myocardial infarction in mice. Cardiovasc Res 2010;87:424–30.

KEY WORDS fibroblast, heart failure, Hsp20, IL-6, remodeling

APPENDIX For an expanded methods section and supplemental figures, please see the online version of this paper.

JACC: BASIC TO TRANSLATIONAL SCIENCE VOL. 4, NO. 2, 2019
© 2019 THE AUTHORS. PUBLISHED BY ELSEVIER ON BEHALF OF THE AMERICAN COLLEGE OF CARDIOLOGY FOUNDATION. THIS IS AN OPEN ACCESS ARTICLE UNDER THE CC BY-NC-ND LICENSE (http://creativecommons.org/licenses/by-nc-nd/4.0/).

EDITORIAL COMMENT

Putting the Heat on Cardiac Fibrosis

Hsp20 Regulates Myocyte-To-Fibroblast Crosstalk*

Jennifer L. Major, PhD, Timothy A. McKinsey, PhD

Fibrosis is a wound-healing process that is triggered by tissue injury or stress. Cardiac fibrosis is associated with adverse outcomes in several forms of heart failure (HF), including HF with reduced ejection fraction, HF with preserved ejection fraction, and genetically driven cardiomyopathies (1,2). Although the increased extracellular matrix (ECM) deposition that accompanies fibrotic responses may acutely serve to stabilize a focal area of myocardial damage, excessive, diffuse, or chronic activation of fibrosis can be deleterious to long-term cardiac function and patient survival. For example, fibrosis can increase the passive stiffness of the myocardium, which contributes to diastolic dysfunction (3,4), and can disrupt electrical conduction in the heart, which causes arrhythmias and sudden cardiac death (5). Unfortunately, despite the well-accepted roles of fibrosis in cardiac dysfunction, no targeted antifibrotic drugs for the heart exist. Thus, it is crucial to understand the fundamental mechanisms that drive cardiac fibrosis so that novel approaches to thwart this pathogenic process can be discovered.

Resident fibroblasts in the heart are major contributors to cardiac fibrosis (6,7). In response to stress, these cells undergo a cell state transition to become activated fibroblasts, sometimes referred to as myofibroblasts, which produce high levels of ECM. Inflammatory cues from dead myocytes, leukocytes, vascular cells, and resident fibroblasts themselves have historically been viewed as the major drivers of fibroblast activation in the heart. However, there is a growing body of evidence to support a role for myocyte-derived secreted factors in the control of the cardiac fibroblast activation (8,9). In this issue of *JACC: Basic to Translational Science,* Gardner et al. (10) reveal a function for heat shock protein 20 (Hsp20) in the regulation of pro-fibrotic cardiomyocyte-to-fibroblast crosstalk.

SEE PAGE 188

Hsp20 is a member of the small heat shock superfamily of proteins that function as chaperones to prevent protein misfolding through adenosine triphosphate–independent processes (11,12). Over the last decade, several studies have demonstrated cardioprotective functions of Hsp20. Work by Chu et al. (13) and Fan et al. (14) established that cardiomyocyte Hsp20 levels and phosphorylation at serine-16 were increased by β-adrenergic stimulation, which resulted in protection against apoptosis. Subsequently, they discovered that transgenic mice with cardiomyocyte-specific expression of Hsp20 were protected from ischemia-reperfusion injury (15). The protective effects of Hsp20 in the heart were corroborated by other groups using distinct cell-based and in vivo models of cardiac stress (16). Furthermore, cell culture studies that used Hsp20 derivatives harboring a phosphomimetic or a non-phosphorylatable amino acid in place of serine-16, and S16D and S16A, respectively, implicated protein kinase A (PKA)– or protein kinase D–mediated phosphorylation of this site as a beneficial signaling event in cardiomyocytes (16).

Paradoxically, in the current study, Gardner et al. (10) showed that cardiomyocyte-specific expression of Hsp20-S16D in mice led to systolic dysfunction and 100% mortality in <1 year. In contrast, there were no

*Editorials published in *JACC: Basic to Translational Science* reflect the views of the authors and do not necessarily represent the views of *JACC: Basic to Translational Science* or the American College of Cardiology.

From the Department of Medicine, Division of Cardiology and Consortium for Fibrosis Research & Translation, University of Colorado, Aurora, Colorado. Dr. Major has received funding from the Canadian Institutes of Health Research (FRN-395620). Dr. McKinsey was supported by the National Institutes of Health (HL116848, HL127240 and DK119594) and the American Heart Association (16SFRN31400013).

All authors attest they are in compliance with human studies committees and animal welfare regulations of the authors' institutions and Food and Drug Administration guidelines including patient consent when appropriate. For more information, visit the *JACC: Basic to Translational Science* author instructions page.

ISSN 2452-302X https://doi.org/10.1016/j.jacbts.2019.03.007

FIGURE 1 Model for Hsp20-Mediated Cardiomyocyte-to-Fibroblast Crosstalk

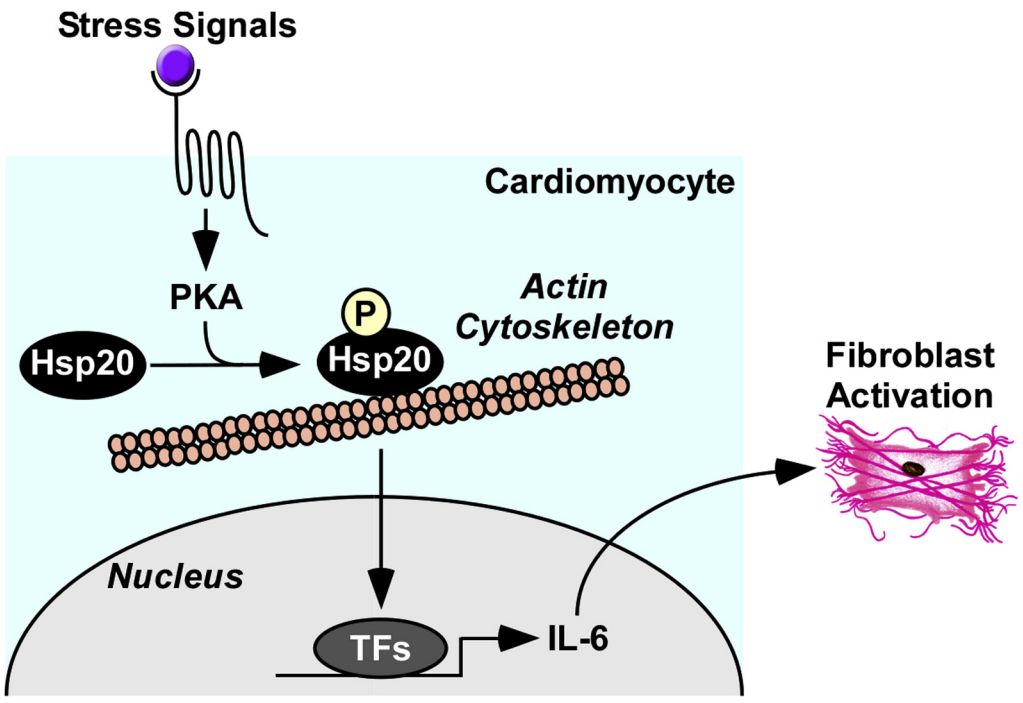

Stress signals lead to protein kinase A (PKA)–mediated phosphorylation of heat shock protein 20 (Hsp20) in cardiomyocytes. Phospho-Hsp20 associates with the actin cytoskeleton and transmits activating signals to nuclear transcription factors (TFs) that stimulate production of interleukin (IL)-6. IL-6, secreted from cardiomyocytes, functions in a paracrine manner to stimulate resident cardiac fibroblasts.

deleterious effects of transgene-mediated expression of non-phosphorylatable Hsp20-H16A in the heart. Hsp20-S16D transgenic mice exhibited significant interstitial fibrosis before evidence of myocyte apoptosis, which led the investigators to postulate that phospho-Hsp20 could be triggering reactive interstitial fibrosis through paracrine activation of resident fibroblasts. Consistent with this notion, exposure of cultured cardiac fibroblasts to medium from cultured cardiomyocytes ectopically expressing Hsp20-S16D, but not Hsp20-S16A, led to a modest increase in fibroblast activation markers. The investigators went on to show that Hsp20-S16D promotes production and secretion of interleukin-6 (IL-6), which has the capacity to stimulate cardiac fibroblasts in vitro and in vivo. A 1-month treatment with a neutralizing antibody against IL-6 was found to block pathological cardiac fibrosis in Hsp20-S16D transgenic mice.

The current findings further establish the importance of myocyte-derived paracrine signaling in the control of fibroblast activation in the heart, and suggest novel approaches for therapeutically targeting cardiac fibrosis based on IL-6 inhibition or altering Hsp20 phosphorylation and/or function. Although inhibiting IL-6 signaling has yielded contradictory results in murine models by either blunting or exacerbating cardiac disease, a recent phase 2 clinical trial demonstrated that tocilizumab, a humanized monoclonal antibody against the IL-6 receptor, reduced inflammation and cardiac damage in patients post-myocardial infarction (17,18). In the future, cardiac cardiac magnetic resonance, which is the current gold standard modality for noninvasive evaluation of cardiac fibrosis, could be used to evaluate the ability of tocilizumab and other IL-6 targeted therapies to reduce ECM deposition in the heart.

Regarding Hsp20, most efforts to date have focused on enhancing phosphorylation of this chaperone as a therapeutic strategy for HF. Hsp20 is found in multiprotein complexes that include phosphodiesterase-4 (PDE4), which degrades cyclic adenosine monophosphate and thereby dampens PKA-mediated phosphorylation of substrates, including Hsp20. Peptide disrupters of the Hsp20–PDE4 interaction have been shown to increase Hsp20 phosphorylation and block cardiomyocyte hypertrophy and fibrosis, which suggests

that, counter to the conclusions of the current study, Hsp20 phosphorylation is cardioprotective (19,20).

Because of potential translational significance of Hsp20 phosphorylation, it will be critical to extend the findings of Gardner et al. (10) to further address the question of whether this post-translational modification is beneficial or detrimental to the heart. The answer likely lies somewhere in the middle, with the cost-to-benefit ratio of Hsp20 phosphorylation being determined by factors such as the stoichiometry and duration of the phospho-modification. Because Hsp20-S16D was expressed in >10-fold excess of the endogenous protein, most of the pool of this chaperone in cardiomyocytes represents the phospho form. It is possible that balancing the amount of transgene-produced S16D versus endogenous Hsp20 to more closely match physiological levels of phospho-Hsp20 will yield distinct effects, which may be salutary. Additionally, implementation of an inducible transgene system that enables temporal modulation of S16D expression acutely following myocardial infarction could uncover the protective effects of Hsp20 phosphorylation. This latter system would enable investigators to address the possibility that acute increases in phospho-Hsp20 exert beneficial effects in the context of a pathogenic insult, but disrupt cardiac homeostasis in the absence of stress.

It will also be important to determine if the discrepancy between the current findings and previous work, which suggested favorable consequences of Hsp20 phosphorylation, is due to the use of the S16D construct. Aspartic and glutamic acid are frequently used to mimic the negative charge of a phospho group, but these substitutions do not always recapitulate the consequences of site-specific phosphorylation (21). Knock-in mice harboring an alanine codon for amino acid 16 in the endogenous Hsp20 locus should be particularly informative.

Additional investigation of the mechanisms by which Hsp20 controls IL-6 expression in cardiac muscle also has the potential to guide translational efforts. Previous studies have demonstrated that β-adrenergic receptor signaling in cardiomyocytes leads to PKA-dependent recruitment of Hsp20 to the actin cytoskeleton, which is coupled to enhanced cellular contraction (14). Presumably, the actin-associated pool of phospho-Hsp20 conveys signals to nuclear transcription factors that control IL-6 gene expression (**Figure 1**). Details about the molecular basis for this cytoskeleton-to-nucleus communication in cardiomyocytes could reveal regulatory nodes that could be manipulated to blunt the transcriptional network that governs pathogenic cardiomyocyte-to-fibroblast crosstalk. As alluded to by the investigators, phospho-Hsp20 might also function within the cardiomyocyte nucleus to stimulate IL-6 gene expression.

In summary, the compelling study described by Gardner et al. (10) has advanced our understanding of the mechanisms that control fibrosis of the heart and has shed light on possible avenues for therapeutic intervention, while concurrently uncovering new and exciting questions. Answers to these questions will undoubtedly be forthcoming as investigators continue to put the heat on the problem of cardiac fibrosis.

ACKNOWLEDGMENTS The authors thank M.B. Felisbino and Y.H. Lin for helpful discussions.

ADDRESS FOR CORRESPONDENCE: Dr. Timothy A. McKinsey, Department of Medicine, Division of Cardiology and Consortium for Fibrosis Research & Translation, University of Colorado Anschutz Medical Campus, 12700 East 19th Avenue, Aurora, Colorado 80045-0508. E-mail: timothy.mckinsey@ucdenver.edu.

REFERENCES

1. Schuetze KB, McKinsey TA, Long CS. Targeting cardiac fibroblasts to treat fibrosis of the heart: focus on HDACs. J Mol Cell Cardiol 2014;70:100–7.

2. Travers JG, Kamal FA, Robbins J, Yutzey KE, Blaxall BC. Cardiac fibrosis: the fibroblast awakens. Circ Res 2016;118:1021–40.

3. Diez J, Querejeta R, Lopez B, Gonzalez A, Larman M, Martinez Ubago JL. Losartan-dependent regression of myocardial fibrosis is associated with reduction of left ventricular chamber stiffness in hypertensive patients. Circulation 2002;105:2512–7.

4. Mohammed SF, Hussain S, Mirzoyev SA, Edwards WD, Maleszewski JJ, Redfield MM. Coronary microvascular rarefaction and myocardial fibrosis in heart failure with preserved ejection fraction. Circulation 2015;131:550–9.

5. Francis Stuart SD, De Jesus NM, Lindsey ML, Ripplinger CM. The crossroads of inflammation, fibrosis, and arrhythmia following myocardial infarction. J Mol Cell Cardiol 2016;91:114–22.

6. Alex L, Frangogiannis NG. The cellular origin of activated fibroblasts in the infarcted and remodeling myocardium. Circ Res 2018;122:540–2.

7. Tallquist MD. Cardiac fibroblasts: from origin to injury. Curr Opin Physiol 2018;1:75–9.

8. Martin ML, Blaxall BC. Cardiac intercellular communication: are myocytes and fibroblasts fair-weather friends? J Cardiovasc Transl Res 2012;5:768–82.

9. Zhang P, Su J, Mende U. Cross talk between cardiac myocytes and fibroblasts: from multiscale investigative approaches to mechanisms and functional consequences. Am J Physiol Heart Circ Physiol 2012;303:H1385–96.

10. Gardner GT, Travers JG, Qian J, et al. Phosphorylation of Hsp20 promotes fibrotic

remodeling and heart failure. J Am Coll Cardiol Basic Trans Science 2019;4:188–99.

11. Jakob U, Gaestel M, Engel K, Buchner J. Small heat shock proteins are molecular chaperones. J Biol Chem 1993;268:1517–20.

12. Lee S, Carson K, Rice-Ficht A, Good T. Hsp20, a novel alpha-crystallin, prevents Abeta fibril formation and toxicity. Protein Sci 2005;14:593–601.

13. Chu G, Egnaczyk GF, Zhao W, et al. Phosphoproteome analysis of cardiomyocytes subjected to beta-adrenergic stimulation: identification and characterization of a cardiac heat shock protein p20. Circ Res 2004;94:184–93.

14. Fan GC, Chu G, Mitton B, Song Q, Yuan Q, Kranias EG. Small heat-shock protein Hsp20 phosphorylation inhibits beta-agonist-induced cardiac apoptosis. Circ Res 2004;94:1474–82.

15. Fan GC, Ren X, Qian J, et al. Novel cardioprotective role of a small heat-shock protein, Hsp20, against ischemia/reperfusion injury. Circulation 2005;111:1792–9.

16. Martin TP, Currie S, Baillie GS. The cardioprotective role of small heat-shock protein 20. Biochem Soc Trans 2014;42:270–3.

17. Hartman MHT, Groot HE, Leach IM, Karper JC, van der Harst P. Translational overview of cytokine inhibition in acute myocardial infarction and chronic heart failure. Trends Cardiovasc Med 2018;28:369–79.

18. Kleveland O, Kunszt G, Bratlie M, et al. Effect of a single dose of the interleukin-6 receptor antagonist tocilizumab on inflammation and troponin T release in patients with non-ST-elevation myocardial infarction: a double-blind, randomized, placebo-controlled phase 2 trial. Eur Heart J 2016;37:2406–13.

19. Martin TP, Hortigon-Vinagre MP, Findlay JE, Elliott C, Currie S, Baillie GS. Targeted disruption of the heat shock protein 20-phosphodiesterase 4D (PDE4D) interaction protects against pathological cardiac remodelling in a mouse model of hypertrophy. FEBS Open Bio 2014;4:923–7.

20. Sin YY, Edwards HV, Li X, et al. Disruption of the cyclic AMP phosphodiesterase-4 (PDE4)-HSP20 complex attenuates the beta-agonist induced hypertrophic response in cardiac myocytes. J Mol Cell Cardiol 2011;50:872–83.

21. McKinsey TA, Zhang CL, Olson EN. Activation of the myocyte enhancer factor-2 transcription factor by calcium/calmodulin-dependent protein kinase-stimulated binding of 14-3-3 to histone deacetylase 5. Proc Natl Acad Sci U S A 2000;97:14400–5.

KEY WORDS fibroblast, heart failure, Hsp20, interleukin-6, remodeling

JACC: BASIC TO TRANSLATIONAL SCIENCE VOL. 4, NO. 2, 2019
© 2019 THE AUTHORS. PUBLISHED BY ELSEVIER ON BEHALF OF THE AMERICAN COLLEGE OF CARDIOLOGY FOUNDATION. THIS IS AN OPEN ACCESS ARTICLE UNDER THE CC BY-NC-ND LICENSE (http://creativecommons.org/licenses/by-nc-nd/4.0/).

PRECLINICAL RESEARCH

Characterization of a Unique Form of Arrhythmic Cardiomyopathy Caused by Recessive Mutation in LEMD2

Nelly Abdelfatah, PHD,[a,*] Ruping Chen, PHD,[b,*] Henry J. Duff, MD,[a] Colette M. Seifer, MB,[c] Ilan Buffo, MD,[d] Cathleen Huculak, MSc,[e] Stephanie Clarke, MSc,[f] Robin Clegg, MD,[g] Davinder S. Jassal, MD,[c] Paul M.K. Gordon, PHD,[h] Carole Ober, PHD,[i] Care4Rare Canada Consortium, Patrick Frosk, PHD, MD,[f,j] Brenda Gerull, MD[a,b,k]

VISUAL ABSTRACT

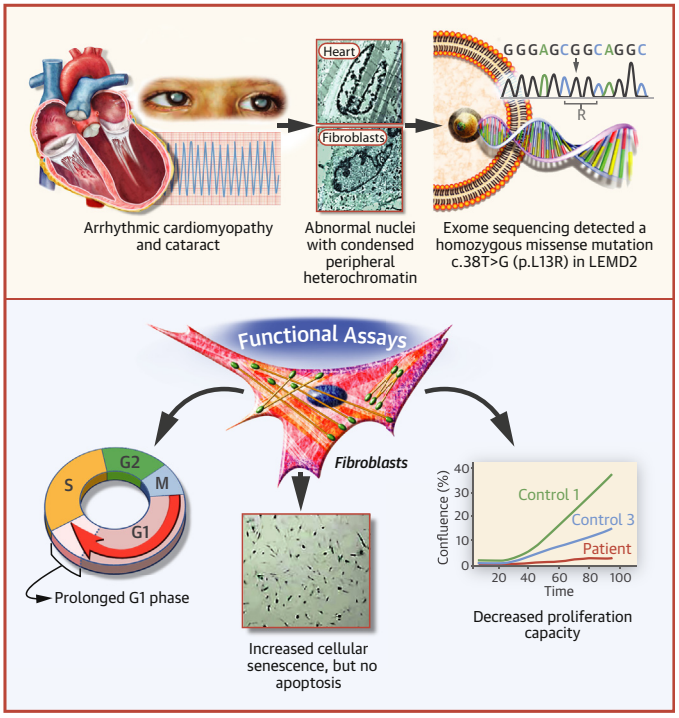

Abdelfatah, N. et al. J Am Coll Cardiol Basic Trans Science. 2019;4(2):204–21.

HIGHLIGHTS

- **The homozygous c.38T>G mutation in the *LEMD2* gene causes arrhythmic cardiomyopathy with bilateral juvenile cataract in the Hutterite population.**
- **The cardiac phenotype is characterized by localized inferior and inferolateral fibrosis of the left ventricle and mild impairment of left ventricular systolic function but severe ventricular arrhythmias leading to sudden cardiac death.**
- **Affected heart tissue and fibroblasts exhibit abnormally shaped nuclei with condensed peripheral heterochromatin.**
- **Functional assays on affected fibroblasts show decreased proliferation capacity, cellular senescence, and a prolonged G1 phase, suggesting premature aging and cellular senescence in proliferating cells.**

From the [a]Department of Cardiac Sciences, Libin Cardiovascular Institute of Alberta, Cumming School of Medicine, University of Calgary, Calgary, Alberta, Canada; [b]Comprehensive Heart Failure Center, University Hospital Würzburg, Würzburg, Germany; [c]Section of Cardiology, Department of Internal Medicine, Max Rady College of Medicine, Rady Faculty of Health Sciences, University of Manitoba, Winnipeg, Manitoba, Canada; [d]Variety Children's Heart Centre, University of Manitoba, Winnipeg, Manitoba, Canada; [e]Department of Medical Genetics, Alberta Health Services, Calgary, Alberta, Canada; [f]Department of Biochemistry and Medical Genetics, Max Rady College of Medicine, Rady Faculty of Health Sciences, University of Manitoba, Winnipeg, Manitoba, Canada; [g]Department of Pediatrics, University of Calgary, Calgary, Alberta, Canada; [h]Cumming School of Medicine Centre for Health Genomics and Informatics, University of Calgary, Calgary, Alberta, Canada; [i]Department of Human Genetics, The University of Chicago, Chicago, Illinois; [j]Department of Pediatrics and Child Health, Max Rady College of Medicine, Rady Faculty of Health Sciences, University of Manitoba, Winnipeg, Manitoba, Canada; and the [k]Department of Internal Medicine I, University

ISSN 2452-302X https://doi.org/10.1016/j.jacbts.2018.12.001

SUMMARY

Nuclear envelope proteins have been shown to play an important role in the pathogenesis of inherited dilated cardiomyopathy. Here, we present a remarkable cardiac phenotype caused by a homozygous *LEMD2* mutation in patients of the Hutterite population with juvenile cataract. Mutation carriers develop arrhythmic cardiomyopathy with mild impairment of left ventricular systolic function but severe ventricular arrhythmias leading to sudden cardiac death. Affected cardiac tissue from a deceased patient and fibroblasts exhibit elongated nuclei with abnormal condensed heterochromatin at the periphery. The patient fibroblasts demonstrate cellular senescence and reduced proliferation capacity, which may suggest an involvement of LEM domain containing protein 2 in chromatin remodeling processes and premature aging. (J Am Coll Cardiol Basic Trans Science 2019;4:204–21) © 2019 The Authors. Published by Elsevier on behalf of the American College of Cardiology Foundation. This is an open access article under the CC BY-NC-ND license (http://creativecommons.org/licenses/by-nc-nd/4.0/).

ABBREVIATIONS AND ACRONYMS

ACM = arrhythmogenic cardiomyopathy
BANF = barrier to autointegration factor
CMR = cardiac magnetic resonance
DAPI = 4′,6′-diamidino-2-phenylindole
DCM = dilated cardiomyopathy
DNA = deoxyribonucleic acid
eGFP = enhanced green fluorescent protein
EMD = emerin
ICD = implantable cardioverter-defibrillator
LEMD2 = LEM domain containing protein 2
LGE = late gadolinium enhancement
LMNA = lamin A/C
LV = left ventricular
PBS = phosphate-buffered saline
NE = nuclear envelope
P = passage
SAHF = senescence-associated heterochromatin foci
SNV = single nucleotide variant

Dilated cardiomyopathy (DCM) is characterized by left ventricular (LV) or biventricular dilatation and systolic dysfunction that often leads to heart failure and sudden cardiac death (1). Genetic forms of DCM are heterogeneous, which became more evident with the widespread use of next-generation sequencing panels or exome sequencing (2). To date, >50 disease-related genes have been reported, although relatively few are supported by robust segregation analyses or experimental data. Mutations in genes encoding inner nuclear membrane (INM) proteins lamin A/C (*LMNA*) and emerin (*EMD*) have been shown to be involved in the pathogenesis of DCM. *LMNA* encodes A-type lamins, which are intermediate filaments that, together with B-type lamins, form a filamentous structure that underlies the nuclear envelope (NE) (3). Dominant *LMNA* mutations cause a variety of phenotypes involving skeletal muscle, cardiac muscle, adipose tissue, and peripheral nerves, including a form of Emery-Dreifuss muscular dystrophy and isolated DCM. *LMNA* mutations account for 6% to 10% of genetically determined DCM and are frequently associated with arrhythmias and conduction system disturbances (4). *EMD* encodes an LEM domain protein located in the nuclear lamina and has a role in assembly of the nuclear lamina and structural organization of the NE. *EMD* mutations are associated with an X-linked form of Emery-Dreifuss muscular dystrophy, which usually includes a severe form of cardiomyopathy (5). Moreover, variants in genes encoding other nuclear membrane components have also been implicated in cardiomyopathy, including SYNE1, SYNE2, and LAP2α (1).

LEM domain containing protein 2 (LEMD2) is a member of the group II LEM domain proteins, which contain ~40 conserved amino acids representing the LEM domain, a domain discovered previously in other INM proteins (6–9). It is ubiquitously expressed in the INM of the NE with an increase during telophase and lower expression in the endoplasmic reticulum (10–13). LEMD2 binds the deoxyribonucleic acid (DNA)-binding protein barrier to autointegration factor (BANF) mediated by the LEM domain and interacts with nuclear lamins by its N-terminal and transmembrane domains (14). Complete disruption in mice causes embryonic lethality by embryonic day 11.5, leading to reduced sizes of most tissues. Neural and heart structures appeared to be less developed and/or

Hospital Würzburg, Würzburg, Germany. *Drs. Abdelfatah and Chen contributed equally to this work and are joint first authors.
This research was supported by the Care4Rare Canada Consortium funded by Genome Canada, the Canadian Institutes of Health Research, and the Ontario Genomics Institute with additional funding provided to the predecessor of Care4Rare, FORGE Canada, by Genome Quebec, Genome British Columbia, and the McLaughlin Centre to Dr. Frosk. The study was further supported by Alberta Innovates Health Solutions (grant no. 201200822), the Canadian Institutes of Health Research (FRN: 123351), and the Libin Cardiovascular Institute of Alberta to Drs. Gerull and Abdelfatah. Support was also provided by the German Ministry of Education and Research, Berlin, Germany (grant no. 01EO1504 to Dr. Gerull). All other authors have reported that they have no relationships relevant to the contents of this paper to disclose.
All other authors attest they are in compliance with human studies committees and animal welfare regulations of the authors' institutions and Food and Drug Administration guidelines, including patient consent where appropriate. For more information, visit the *JACC: Basic to Translational Science* author instructions page.

Manuscript received October 4, 2018; revised manuscript received November 2, 2018, accepted December 3, 2018.

abnormal. Studies of knock-out embryos exhibited thin myocardium with underdeveloped trabeculae, consistent with a role for LEMD2 in cardiac development. Moreover, knockdown of it in an immortalized mouse myoblast cell line (C2C12) causes a myogenesis defect (13,15).

Recently, a mutation in *LEMD2* has been associated with juvenile cataract and a risk for sudden cardiac death in the Hutterite population (16). The Hutterite population is a genetic isolate who originated in Europe in the 16th century and emigrated to the United States and Canada in the 1870s. They can be traced back to <100 founders and are divided into 3 branches: Dariusleut, Lehrerleut (L-leut), and Schmiedeleut (S-leut) (17,18).

In the present study, we clinically and genetically characterized 2 large Hutterite families with LEMD2-associated disease from the L-leut and S-leut branches. Individuals carrying the homozygous mutation (c.38T>G; p.L13R) in the *LEMD2* gene exhibited a new form of arrhythmic cardiomyopathy with localized inferior and inferolateral myocardial scarring and severe arrhythmias but only mild impairment of systolic LV function. Cardiac tissue and fibroblasts from affected patients exhibited abnormally shaped and elongated nuclei as well as heterochromatin disorganization. Mutant fibroblasts showed a proliferation defect and cell senescence but no increased apoptosis, suggesting an involvement of mutant LEMD2 in chromatin remodeling processes and premature aging.

METHODS

PATIENT CHARACTERIZATION. The study conformed to the principles outlined in the Declaration of Helsinki and was approved by institutional review boards of the University of Calgary and University of Manitoba (ID-E23515, ID-E20729, HS16978). All participating individuals provided written informed consent. Clinical evaluation included 12-lead electrocardiography, signal-averaged electrocardiography, and exercise testing according to the Bruce protocol, 24-h Holter monitoring, and 2-dimensional transthoracic echocardiography and/or cardiac magnetic resonance (CMR) imaging. In some cases, additional investigations and/or records such as reports from implantable cardioverter-defibrillators (ICDs) were obtained. Medical records of deceased individuals have been collected when possible to reconstruct their phenotypes. Tissue blocks of heart and liver of the deceased individual 600, II-16 have been further investigated. A skin biopsy was taken from individual 600, II-18, indicated as "Pat" and 2 volunteers at an age of 40 years (age-matched control subjects: Ctrl1 and Ctrl2) and 61 years ("old" senescent control: Ctrl3) for isolating dermal fibroblasts.

GENETIC STUDIES. DNA from 4 affected individuals of family 600 (II-2, II-3, II-18, and III-4) were extracted and underwent exome sequencing. Sequence enrichment was performed by using the Agilent SureSelect Whole Human Exon 50 Mb XT (version 3) kit (Agilent Technologies, Santa Clara, California) and sequenced on a 5500xl SOLiD system (Thermo Fisher Scientific, Waltham, Massachusetts). Raw color space sequences were error-corrected and aligned to the human reference genome version hg19 with version 2.5 of the 5500xl manufacturer's LifeScope software version 2.5, using the "targeted.resequencing.pe" workflow (19). The aligned sequences were deduplicated, realigned, and genotypes called by using multiple third-party programs, using the validated workflow described previously (20). Nonsynonymous single nucleotide variants (SNVs) and insertions and deletions in coding regions were retained for the downstream analysis, which were further annotated with functional impact. Minor allele frequencies of the control subjects were evaluated by using the Genome Aggregation Database (21). Rare homozygous variants (population allele frequency <0.05) that were shared among all 4 individuals were identified as potential causal variants. Fine mapping was undertaken in 4 affected family members of family 600 and 2 affected family members of family 290 (III-12 and III-13) using 8 SNVs that flanked the 18.3 Mb homozygous region at chr.6p21.3 containing LEMD2.

MOLECULAR MODELING. The PyMOL Molecular Graphics System, version ~1.3r1 (August 2010) by Schrödinger LLC (Cambridge, Massachusetts), was used to introduce the p.L13R mutation into the LEMD2 domain with the atomic structure PDB ID 2ODC (22). The Swiss Model Homology Server was used to generate a model of this domain, including the mutant p.L13R using LEM domain template (PDB ID 2ODC).

HISTOLOGY AND TRANSMISSION ELECTRON MICROSCOPY. Heart tissue was embedded in paraffin, and 5-μm thick slices were deparaffinized and stained with hematoxylin and eosin, Masson's trichrome, and picro sirius red (1% sirius red in saturated aqueous picric acid) as previously described (23). An Olympus Bx54 microscope equipped with an UPlanSApo 100x/1.4NA objective (Olympus, Tokyo, Japan) was used for imaging. Samples for the transmission electron microscopy were fixed, dehydrated,

and embedded in resin blocks. Blocks were split to 50- to 70-nm thin sections and imaged by using a Hitachi H-7650 transmission electron microscope (Hitachi High Technologies America, Inc., Schaumburg, Illinois).

PLASMID GENERATION AND CELL CULTURE. A plasmid containing the full-length human *LEMD2* complementary DNA fused to an enhanced green fluorescent protein (eGFP)-tag on the C terminus was purchased (GeneCopoeia, Rockville, Maryland). The mutation c.38T>G was introduced by using the QuikChange Lightning Kit (Agilent Technologies). The mCherry-tagged Lamin A plasmid (Addgene, Cambridge, Massachusetts) was purchased and used for co-transfection. C2C12 and HEK293 cells were cultured in Dulbecco's modified Eagle's medium (L-glutamine, 4.5 g/l glucose; Lonza Group, Basel, Switzerland) supplemented with10% fetal calf serum and 500 U/ml penicillin and 500 μg/ml streptomycin. Fibroblast cell lines were cultured in gelatin 0.01% (MilliporeSigma, Burlington, Massachusetts) coated plates and incubated in fibroblast media consisting of Dulbecco's modified Eagle's medium (L-glutamine, 4.5 g/l glucose; Lonza Group) supplemented with 10% fetal calf serum, 500 U/ml penicillin, 500 μg/ml streptomycin, and MEM Non-Essential Amino Acids Solution 100× (Thermo Fisher Scientific).

IMMUNOCYTOCHEMISTRY, IMMUNOHISTOCHEMISTRY, AND CONFOCAL MICROSCOPY. C2C12 cells were transfected with either eGFP-LEMD2 or mCherry-Lamin A/C or co-transfected with both by using Lipofectamine 2000 (Thermo Fisher Scientific). Forty-eight hours after transfection, cells were fixed for 20 min in 4% paraformaldehyde at 4°C, washed 3 times with phosphate-buffered saline (PBS) for 10 min each) and blocked for 1 h with goat serum. Afterwards, the slides were washed, and Prolong Gold Antifade Mountant with 4′,6′-diamidino-2-phenylindole (DAPI) (Thermo Fisher Scientific) was added. Fibroblast cells were spread on 0.01% gelatin-coated cover slides and incubated at 37°C for 48 h and fixed with 4% paraformaldehyde for 20 min at 4°C. Paraffin-embedded tissue slides (5 μm) were deparaffinized by using xylene and ethanol. Tissue and fixed fibroblast cells were washed with PBS, blocked with goat serum, and stained overnight with primary antibodies followed by secondary antibodies conjugated with Alexa-488 and Alexa-555 dyes for 2 h at room temperature (Supplemental Table 1 and Supplemental Figure 1 for isotype control staining) and embedded in ProLong Gold Antifade Mountant with DAPI. The LSM5 Exciter (Carl Zeiss AG, Oberkochen, Germany) was used for confocal imaging. All images were processed with Zen software v6,0,0,303 (MDaemon Technologies, Ltd., Grapevine, Texas).

WESTERN BLOT ANALYSIS. Transfected HEK293 cells were collected 48 h after transfection. Fibroblasts were harvested after reaching 80% confluence. Both were collected in radio-immunoprecipitation assay buffer supplemented with proteinase inhibitor cocktail (Roche, Mannheim, Germany) and homogenized. Protein samples were separated by using sodium dodecyl sulfate polyacrylamide gel electrophoresis, transferred to the membrane and incubated with primary antibodies overnight at 4°C followed by the horseradish peroxidase-conjugated secondary antibody at room temperature for 2 h (Supplemental Table 1). Bands were detected on the ChemiDoc equipment (Bio-Rad, Hercules, California) after adding Amersham ECL Western Blotting Detection Reagent (GE Healthcare, Life Sciences, Chicago, Illinois). Bands were quantified by using Image Lab Touch Software version 6.0 (Bio-Rad, Hercules, California).

FIBROBLAST CELL PROLIFERATION ASSAY. Fibroblast cells from a 38-year-old patient (family 600, II-18), a 40-year-old age-matched control subject (Ctrl1), and a 61-year-old male control subject (Ctrl3) at different passage numbers were used for the proliferation assay. Cells were diluted to 20,000 cells/ml with fibroblast medium and seeded into a 96-well flat bottom plate coated with gelatin and incubated at 37°C for 2 h before scanning. The plate was placed into the IncuCyte ZOOM system (Essen BioScience Inc., Ann Arbor, Michigan) and scanned under the phase 4× object with a 2-h interval. Collected data were analyzed by using the IncuCyte ZOOM's confluence processing analysis tool (basic analysis).

APOPTOSIS ASSAY FROM TISSUE. Paraffinized sectioned slices from heart and liver of the deceased patient (family 600, II-16) and a control were stained with 5-bromo-2′-deoxyuridine 5′-triphosphate according to the APO-BRDU-IHC Colorimetric kit (MilliporeSigma) instructions (24). Images were conducted by using the Olympus Bx54 microscope equipped with an UPlanSApo 100x/1.4NA objective (Olympus, Tokyo, Japan).

TERMINAL DEOXYNUCLEOTIDYLTRANSFERASE-MEDIATED dUTP NICK END LABELING AND CELL SENESCENCE ASSAY OF FIBROBLASTS. Fibroblasts were harvested and fixed with freshly prepared 2% paraformaldehyde for 1 h at room temperature. Cells were suspended in permeabilization solution and

incubated with terminal deoxynucleotidyltransferase-mediated dUTP nick end labeling reaction mixture for 1 h at 37°C in the dark. For the staining, the *in situ* cell death detection kit (Roche) was used. Cells were sorted with the fluorescence-activated cell sorting (FACS) Calibur (Becton Dickinson) flow cytometer, and the results were analyzed with FlowJo software version 7.6.1 (FlowJo, Ashland, Oregon). Cultured fibroblasts with identical passage number were subjected to β-galactosidase staining by using a senescence β-galactosidase staining kit (CS0030, MilliporeSigma) following the manufacturer's instructions.

CELL CYCLE ANALYSIS. Harvested fibroblasts were fixed by -20°C pre-cooled 75% ethanol and stored at -20°C overnight. Fixed cells were rinsed twice with PBS, re-suspended in PBS containing 100 μg/ml RNase A (Takara Bio, Kusatsu, Japan), and incubated at 37°C for 30 min. Propidium iodide 40 μg/ml plus 0.25% Triton X-100 was added to the cell suspension, and cells were incubated in the dark at 37°C for 30 min. Stained DNA was analyzed by using a FACS Calibur flow cytometer and FlowJo software version 7.6.1.

STATISTICAL ANALYSIS. All datasets are expressed as mean ± SEM. The replicates and numbers (N) of experiments are indicated with each experiment. Two-way analysis of variance was used for all the assays with multiple samples. Statistical analyses were performed by using Prism 7 software (version 7.0a; GraphPad Software, La Jolla, California), if not otherwise indicated.

RESULTS

ARRHYTHMIC CARDIOMYOPATHY WITH REGIONAL INFERIOR AND INFEROLATERAL MYOCARDIAL SCARRING IS ASSOCIATED WITH JUVENILE CATARACT. We clinically investigated 20 members of 2 extended families (family 600 and family 290) of the L-leut and S-leut branches of the Hutterite population who have a history of bilateral juvenile cataract (**Figure 1A, Table 1**). The phenotype of bilateral juvenile cataract was reported previously in family 600 (16,25,26); however, it became obvious that cardiac disease may also be associated with it after 2 individuals from the original publications died suddenly at the ages of 28 and 43 years (family 600, III-2 and II-16).

Eighteen additional individuals from both families with a history of bilateral juvenile cataract were identified. Those who were available for study underwent detailed cardiac investigations (**Table 1**). Six individuals aged 8 to 22 years had normal clinical findings. The remainder exhibited some form of cardiac disease that appeared to be age dependent. A group of 4 people (family 290, II-20, II-21, III-20, and III-21) aged 15 to 46 years demonstrated a subclinical phenotype with normal cardiac function and no arrhythmias but a pattern of fibrosis detected by late gadolinium enhancement (LGE) in the cardiac magnetic resonance imaging (MRI) (**Figure 1B, a,c,d**). Interestingly, the LGE pattern and location appeared to be very specific and was also seen in more severely affected individuals (**Figure 1B, b**).

In the entire cohort, 5 individuals died of sudden cardiac death ranging in ages from 28 to 51 years (family 600, III-2 and II-16; family 290, II-3, II-4, and II-6). One additional individual had a sudden cardiac arrest on exertion at the age of 36 years and was resuscitated (family 290, II-22). This patient along with 3 other individuals between 29 and 38 years of age (family 600, II-2, II-3, and II-18) also exhibited a significant pattern of scarring in the CMR imaging in the inferior and lateral wall segments with transmural LGE. All 4 individuals had wall motion abnormalities and mildly reduced systolic LV function ranging between 43% and 48% on CMR imaging. A similar pattern of LGE can also be observed in inferior/inferolateral myocardial infarction. Therefore, 2 of the patients underwent a computed tomography angiogram (family 600, II-18) or a coronary angiogram (family 290, II-22), and normal coronary arteries were found. Patient 600, II-18 had an ICD placed for primary prevention and had ventricular arrhythmias terminated by an ICD shock ~1 year later (**Figure 1C**).

Two patients had phenotypes more consistent with progressive dilation and heart failure rather than having a sudden arrhythmogenic event (family 290, II-3 and II-5). Patient 290, II-5 presented at 25 years of age due to shortness of breath and was found to have a phenotype of DCM with severe mitral regurgitation and significant systolic dysfunction. His disease progressed over the next 2 years despite medical therapy, and he eventually received a heart transplant. He is currently doing well in his 40s but unfortunately many of his medical records reporting the clinical phenotype were not available for this study, including cardiac pathology findings. His sisters (family 290, II-3 [mentioned earlier] and II-4) reportedly had similar clinical phenotypes and were being medically managed when they died suddenly of presumed arrhythmias.

Although not assessed by a neuromuscular specialist, none of the homozygous carriers

FIGURE 1 **Clinical Features of 2 Extended Hutterite Families With Arrhythmic Cardiomyopathy and Juvenile Cataract**

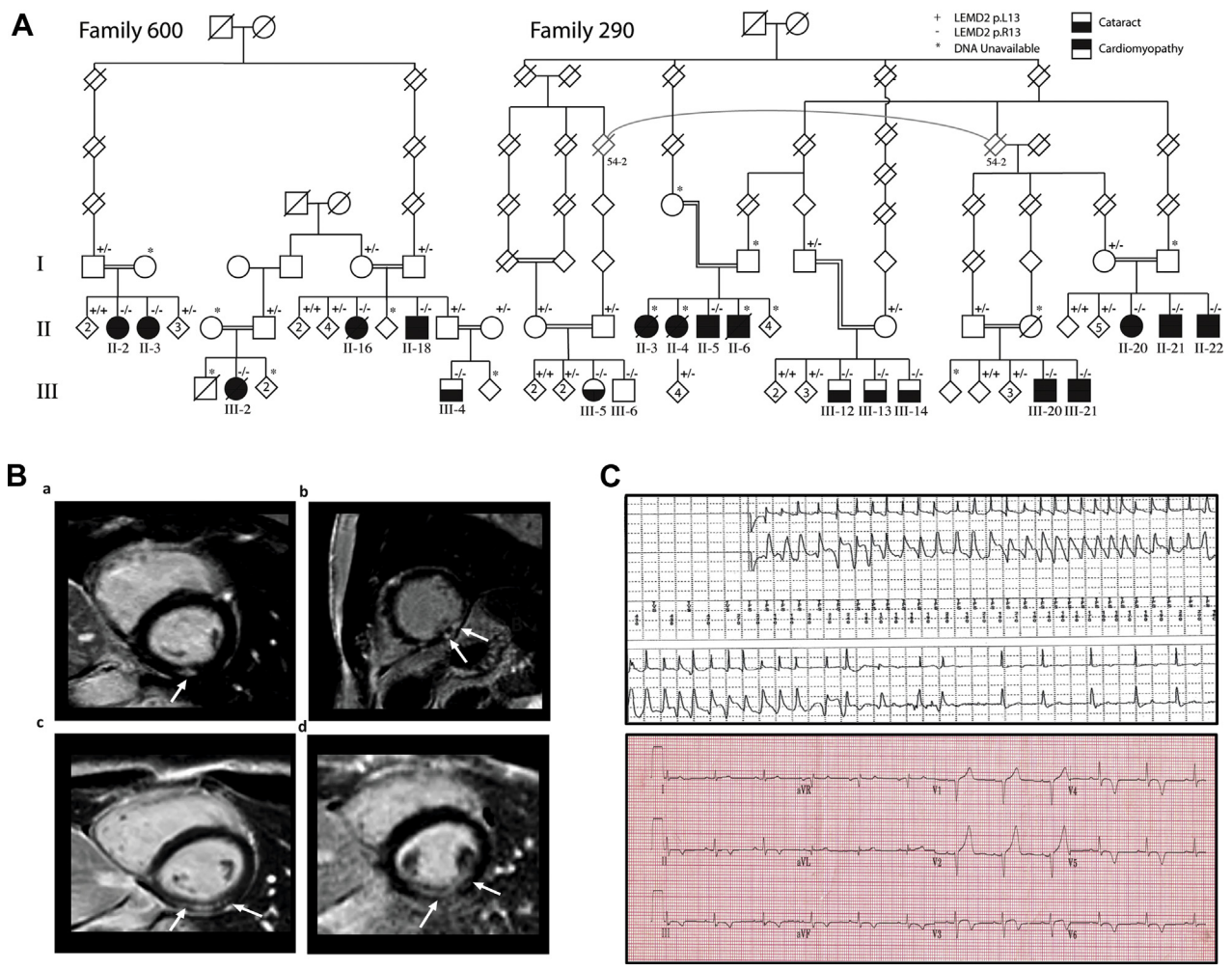

(A) Pedigrees of 2 multigenerational Hutterite families of L-leut (family 600) and S-leut (family 290) descendants. **Filled black squares** (male subjects) and **circles** (female subjects) refer to affected individuals with cataract and arrhythmic cardiomyopathy. **Filled upper half symbols** indicate individuals diagnosed with arrhythmic cardiomyopathy. **Filled lower half symbols** refer to individuals with juvenile cataract. **Diagonal lines** indicate deceased individuals. **Double lines** refer to known consanguinity. The genotype indicated by a "+" is the p.L13 (wild-type) allele and that indicated by a "-" is the mutant p.R13 allele. **(B)** Short-axis views of late gadolinium enhancement cardiac magnetic resonance imaging of family 290, II-20 (a), II-22 (b), III-20 (c), and III-21 (d) confirming nearly transmural delayed enhancement of the inferior/inferolateral walls as indicated by the arrows. **(C)** Rhythm strip of individual 600, II-18 recorded by the implantable cardioverter-defibrillator before delivering an appropriate shock **(upper panel)**. Representative 12-lead electrocardiogram of the same individual showing deep T-wave inversions inferior and lateral corresponding to areas of fibrosis in the cardiac magnetic resonance image **(lower panel)**. DNA = deoxyribonucleic acid; LEMD2 = LEM domain containing protein 2.

demonstrated clinically evident skeletal muscle disease. Of note, several heterozygous carriers of family 600 underwent clinical investigations with electrocardiography and echocardiography (e.g., all siblings and the parents of patient 600, II-16); no cardiac abnormalities have been observed.

Overall, the cardiac phenotype can be summarized as a LV cardiomyopathy with or without dilatation with a localized inferior and inferolateral pattern of fibrosis and subsequent wall motion abnormalities in this region. The main clinical phenotype is characterized by ventricular arrhythmias and sudden death, suggesting the term arrhythmic cardiomyopathy although a subset presented with a phenotype more consistent with classic DCM. The earliest signs of the disease were detected in individual 290, III-21

TABLE 1 Clinical Characteristics of Individuals With Bilateral Juvenile Cataract

		CMR					
	Age of Investigation (yrs)	Tissue Characterization (Scar) and Wall Motion Abnormalities	RVEDVi	RVEF	LVEDVi	LVEF	Echocardiography
Family 600							
II-2	31	Inferior and inferolateral scar, thinned and a kinetic, fibrosis subendocardial and subepicardial	74 ml/m^2	52%	84 ml/m^2	47%	LA dilated, mildly reduced LV function, hypokinetic apex, LVEDD 5.0 cm (normal), normal RV function
II-3	29	Fibrosis inferior and inferolateral with corresponding hypokinesis, fibrosis subendocardial and subepicardial	72 ml/m^2	57%	84 ml/m^2	48%	Normal LA, LVEF 45%, inferolateral wall akinetic, LVEDD 4.7 cm (normal), normal RV function
III-2	28 deaths	NA	NA	NA	NA	NA	Moderate decreased LV and RV function, LVEF 36%
II-16 AR-900A 62†	42 deaths	NA	NA	NA	NA	NA	NA
II-18 AR-900A 31†	38	Basal and mid inferolateral and apical lateral hypokinetic, apex dyskinetic, same segments transmural scarring	101 ml/m^2	54%	94 ml/m^2	43%	Normal LA, LVEF 45%, mild global hypokinesis, apex akinetic, LVEDD 4.2 cm (normal), normal RV function
III-4 AR-900A 37†	9	NA	NA	NA	NA	NA	Normal
Family 290							
III-12	21	None	84 ml/m^2	63%	97 ml/m^2	56%	Normal
III-13	19	None	108 ml/m^2	51%	100 ml/m^2	58%	Normal
III-14	10	None	84 ml/m^2	55%	78 ml/m^2	56%	Normal
III-20	20	Delayed enhancement inferolateral wall	62 ml/m^2	51%	67 ml/m^2	64%	Normal
III-21	15	Delayed enhancement inferolateral wall	57.5 ml/m^2	58%	64 ml/m^2	57%	Normal
II-20	46	Delayed enhancement, epi-mid myocardial, inferolateral wall mid-level	66 ml/m^2	58%	57 ml/m^2	68%	Normal
II-21	43	Delayed enhancement, epi-mid myocardial, inferolateral wall at base	64 ml/m^2	54%	68 ml/m^2	57%	Normal
II-22	36	LV basal inferolateral wall akinesis, LBBB (abnormal septal motion), delayed enhancement basal inferior lateral walls	38 ml/m^2	70%	93 ml/m^2	45%	Regional wall motion abnormalities, moderately dilated LA
III-5	8	NA	NA	NA	NA	NA	Normal
III-6	13	None	109.3 ml/m^2	56%	79.6 ml/m^2	56%	Normal
II-5	25	NA	NA	NA	NA	NA	Dilatation of both ventricles, severe MV regurgitation, severe systolic dysfunction
II-4	44 deaths	NA	NA	NA	NA	NA	NA
II-6	30 deaths	NA	NA	NA	NA	NA	NA
II-3	51 deaths	NA	NA	NA	NA	NA	NA

All living individuals are homozygous mutation carriers of the LEMD2 mutation. *Autopsy report summary: Heart was not enlarged but showed area of scarring at left ventricular (LV) free wall. Microscopic findings: Extensive transmural scar with neovascularization. Myocytes at the edge of scar are hypertrophied. The fibrosis extends around the myocytes and appears to expand interstitial spaces from the endocardium to the epicardial surface. There was no gross or microscopic vascular disease as well as no acute inflammation (no myocarditis). †Corresponding individual described by Boone et al. (16).

CMR = cardiac magnetic resonance imaging; ICD = implantable cardioverter-defibrillator; ILR = internal loop recorder; LA = left atrium; LBBB = left bundle branch block; LVEDi = left ventricular end-diastolic volume index; LVEF = left ventricular ejection fraction; LVEDD = left ventricular end-diastolic diameter; MV = mitral valve; nsVT = no sustained ventricular tachycardia; NA = not available; RV = right ventricular; RBBB = right bundle branch block; RVEDVi = right ventricular end-diastolic volume index; RVEF = right ventricular ejection fraction; SA-ECG = signal averaged electrocardiogram; SR = sinus rhythm; PAC = premature atrial beat; PVCs = premature ventricular complexes.

Continued on the next page

with mild changes in the CMR imaging at 15 years of age (Figure 1B, d), whereas 6 individuals, all ≤22 years of age, have not yet shown any signs of the disease (Table 1).

GENETIC ANALYSES CONFIRMED A HOMOZYGOUS MUTATION IN LEMD2 (c.38T>G; p.L13R) IN ALL CLINICALLY AFFECTED INDIVIDUALS. Recently, a homozygous mutation in the inner nuclear membrane

TABLE 1 Continued

ECG	Arrhythmias (24 Holter)	SA-ECG	ICD or ILR	Cataract	Clinical History	Other
SR, T-wave inversions III, aVF, V_4-V_6	2,757 isolated PVCs, 51 couplets, slow runs of nsVT, no pauses	3/3 positive for late potential	ILR: no significant arrhythmias	Yes	No symptoms, no fainting	NA
SR, incomplete RBBB, T-wave inversions II, III, aVF, V_5, V_6, delayed R V_2-V_4	1,984 isolated PVCs, 38 couplets, no nsVT, no pauses	3/3 positive	ILR: no significant arrhythmias	Yes	No symptoms, no fainting	NA
SR, RBBB, abnormal R-wave progression V_3-V_5, T-wave inversion across all leads	NA	NA	NA	Yes	Died suddenly during work; felt unwell few hours before, 3 yrs ago diagnosed with peripartum cardiomyopathy	NA
NA	NA	NA	NA	Yes	Died suddenly during kitchen work; no previous symptoms	Autopsy*
SR, T-wave inversions III, aVF, V_3-V_6, delayed R-wave progression V_2-V_6	nsVT runs of 10 and 13 beats, monomorphic, frequent PVCs (2286), no pauses	NA	ICD: 1× shock fast polymorphic VT	Yes	Syncope associated with ICD shock	CT angiogram: no coronary artery disease
Normal for age	None	3/3 negative	NA	Yes	No symptoms, no fainting	Normal exercise stress test
Early repolarization	1 isolated PAC, no nsVT	1/3 positive	NA	Yes	No symptoms, no fainting	NA
Normal for age	Normal	1/3 positive	NA	Yes	No symptoms, no fainting	NA
Normal for age	Normal	2/3 positive	NA	Yes	No symptoms, no fainting	NA
Normal for age	650 PVCs, 1 couplet, no nsVT	1/3 positive	NA	Yes	No symptoms, no fainting	Normal Exercise stress test
Normal for age	Normal	Normal	NA	Yes	No symptoms, no fainting	NA
Normal	Normal	Normal	NA	Yes	No symptoms, no fainting	Normal exercise stress test
Normal	4,800 PVCs	Normal	NA	Yes	No symptoms, no fainting	Normal exercise stress test
LBBB, T inversions V_4-V_6	NA	NA	ICD, no shocks	Yes	Collapsed with exertion, required resuscitation, cardioversion for sustained VT	Normal coronary angiogram
Normal for age	Normal	Normal	NA	Yes	No symptoms, no fainting	NA
SR RBBB	Rare PVCs of 2 dominant morphologies	Abnormal repolarization	NA	Not at age 13 yrs	No symptoms, no fainting	Homozygous for LEMD2 p.L13R
LBBB with left-axis deviation	NA	NA	NA	Yes	Followed up from age 25 yrs, heart transplant at age 27 yrs, today age 44 yrs	No cardiac pathology available
NA	NA	NA	NA	Yes	Died suddenly at kitchen table at age 44 yrs, history of "enlarged heart"	No autopsy done
NA	NA	NA	NA	Yes	Died suddenly at age 30 yrs while skating	No autopsy done
NA	NA	NA	NA	Yes	Died suddenly at age 51 yrs, was followed up for "cardiac condition"	No autopsy done

protein LEMD2 (c.38T>G; p.L13R) was reported by Boone et al. (16) in individuals of the Hutterite population with juvenile cataract and sudden death. The cohort we report here consists of 3 affected individuals reported from the original publication by Boone et al. (II-16, II-18, and III-4 in family 600) (**Table 1**) and an additional 17 unique affected individuals. We independently confirmed the region of homozygosity on chromosome 6p21.31 between genomic positions 24,784,436 and 43,044,640, covering 18.3 Mb. Eight SNVs with a minor allele frequency <0.01 located in the shared region were used for fine mapping of 4 affected family members of family 600 and 2 affected family members (III-12 and III-13) of family 290, which narrowed down the region of homozygosity on chr.6p.21 to 6.8 Mb containing

~60 genes (Supplemental Table 2). *LEMD2* was the only gene containing a novel homozygous missense mutation c.38T>G; p.L13R (chr.6: 33,772.202), which was not found in the Genome Aggregation Database (21). All individuals from both families with juvenile cataracts were found to be homozygous for the c.38T>G mutation, except 1 carrier, who we believe is pre-symptomatic at 13 years of age (family 290, III-6).

The p.L13R mutation is located in the LEM domain at a highly evolutionary conserved position (**Figure 2A**). Three-dimensional protein remodeling of the mutated protein showed that the amino acid residue substitution R13 leads to steric hindrance to form a proper three-dimensional structure (**Figure 2B**).

To determine the carrier frequency of the p.L13R mutation in the Hutterite population, we used a previously published resource available through the University of Chicago (27,28). Briefly, this resource consists of a database of 98 healthy Hutterite individuals from the S-leut branch who have had full genome sequencing (i.e., complete allele ascertainment) and another 1,317 healthy Hutterites from the S-leut branch who had a more limited analysis but were imputed for every possible genotype in the genome. The imputed genotypes were all calculated with high confidence by using linkage disequilibrium and pedigree analysis as previously described (28). The database was interrogated for the disease allele, and 8 individuals from the fully sequenced cohort were found to carry 1 copy, yielding an estimated carrier frequency of 1 of 13 (0.0769) assuming Hardy-Weinberg equilibrium. However, this frequency was even higher at 1 of 8 (0.125) when the larger cohort with imputed genotypes was used, suggesting this disease may have a very large impact in this population.

AFFECTED HEART TISSUE OF A DECEASED PATIENT AND FIBROBLASTS SHOW ELONGATED AND INVAGINATED NUCLEI WITH CONDENSED PERIPHERAL HETEROCHROMATIN. We next analyzed heart tissue of the left ventricle from the deceased patient (family 600, II-16). Histology from specimens from patient 600, II-16 and a control LV heart sample demonstrated significantly more myocyte hypertrophy and interstitial fibrosis, as well as an increase in collagen deposits in the deceased patient tissue compared with control myocardium (**Figure 2C**). It has been previously reported that muscle cell nuclei from patient tissue with DCM due to mutations in the NE protein LMNA exhibit an alteration of nuclear morphology (29). To examine the structure of the nuclei, we performed transmission electron microscopy from cardiac tissue as well as from patient fibroblasts (family 600, II-18) compared with an aged-matched control (Ctrl1) at 2 different passage numbers (P2 and P15). The nuclei of the affected heart tissue appeared to be very abnormal in shape and heterochromatin structure. They were elongated and showed an invagination of the nuclear membrane as well as condensed clumping of peripheral heterochromatin (**Figure 2D**). All observed nuclei in cardiac tissue demonstrated those abnormalities (n = 100 nuclei examined). In patient fibroblast cells, the invagination of the nuclear membrane was also frequently noticed, but the peripheral chromatin was less condensed compared with the nuclei of the heart tissue. Abnormal fibroblast nuclei were detected in 80% of the nuclei (n = 300) at P2 and were increased to 90% at P15. Only a few abnormal nuclei (~20%) at P2 and 30% at P15 were detected in 300 nuclei of the age-matched control (**Figure 2E**).

To investigate a potential mislocalization of mutant LEMD2, immunohistochemistry experiments were conducted of affected cardiac tissue, affected fibroblasts, and *in vitro* cellular expression studies of recombinant wild-type and mutant LEMD2 proteins. We detected LEMD2 at the expected localization at the nuclear membrane in cardiac tissue from patient 600, II-16 and fibroblasts from patient 600, II-18 by using a C-terminal LEMD2-specific antibody. There was no difference compared with the control subjects in either experiment. Furthermore, staining of cardiac tissue and fibroblast cells showed co-localization of both LMNA and LEMD2 in patients and control subjects (**Figures 3A and 3B**, Supplemental Figure 1). We measured the expression of LEMD2 and LMNA by Western blot analysis using whole protein lysates from fibroblasts; no significant difference was noted between the patient and control subjects (**Figure 3C**).

We subsequently introduced the c.38T>G mutation into a full-length human *LEMD2* complementary DNA clone and expressed either mutant or wild-type eGFP-tagged LEMD2 in C2C12 cells. The wild-type (p.L13) as well as the mutant (p.R13) protein showed normal localization at the nuclear membrane (**Figure 3D**), consistent with the finding in cardiac tissue and fibroblast cells. Furthermore, co-transfection with *LMNA* complementary DNA clone showed co-localization of both proteins in vitro. In addition, HEK293 cells expressing wild-type or mutant eGFP-LEMD2 demonstrated similar expression levels, indicating a stable mutant protein (**Figure 3E**).

THE LEMD2 MUTATION INDUCES A PROLIFERATION DEFECT AND CELL SENESCENCE IN PATIENT FIBROBLASTS. To test the effect of mutant LEMD2 on cell proliferation, fibroblast cells from patient and

FIGURE 2 The Mutation p.L13R in LEMD2 Causes Interstitial Fibrosis and Abnormal Nuclei in Affected Myocardial Tissue and Fibroblasts

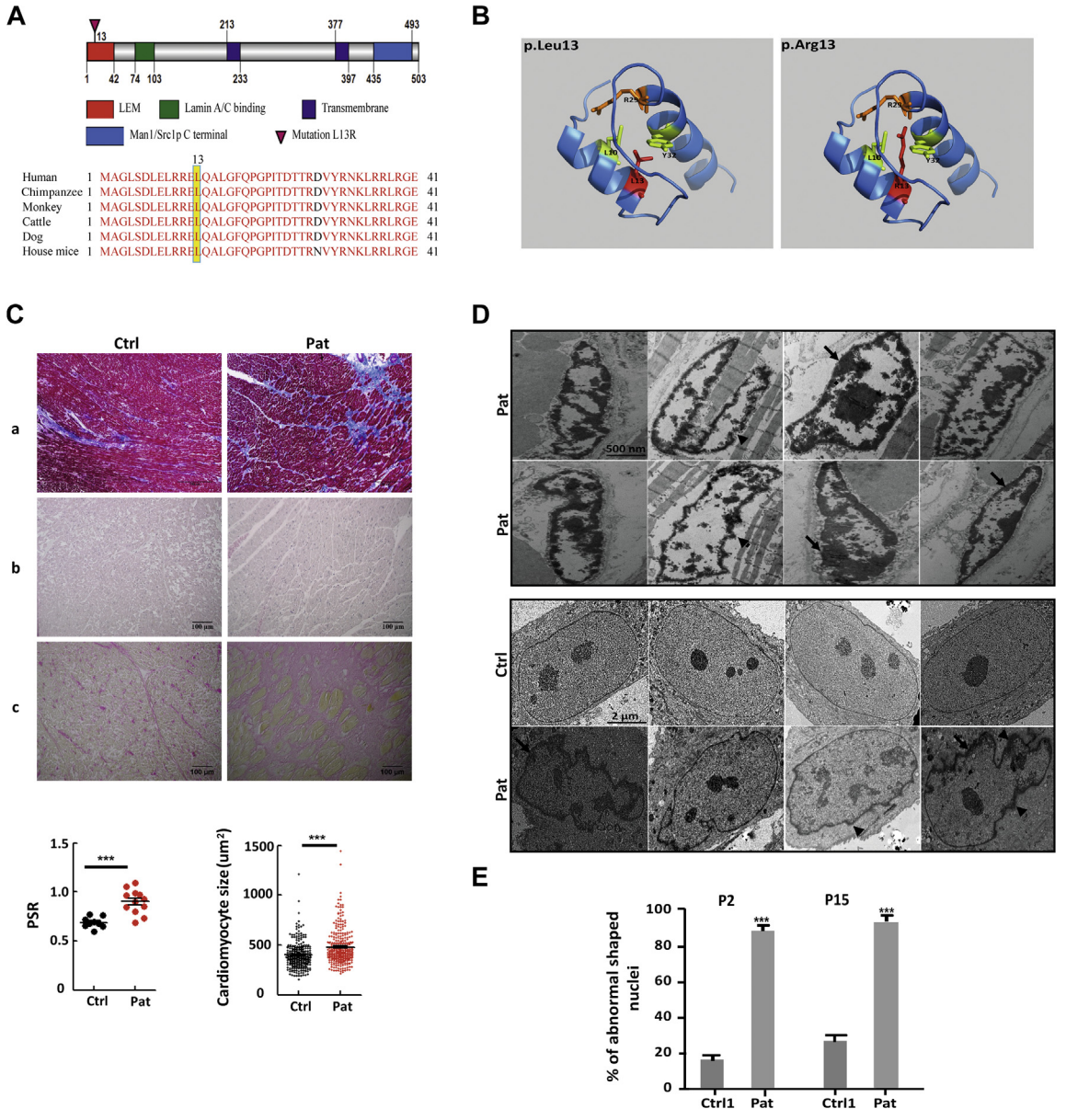

(A) Protein domain structure of human LEM domain containing protein 2 (LEMD2) and conserved motifs. **(Top)** the LEMD2 protein consists of an LEM domain, lamin A/C–binding domain, 2 transmembrane domains, and a Man1/Src1p C-terminal domain. Domain information was obtained from UniProt (63) and Brachner et al. (10). The **red arrow** indicates the location of the human mutation. **(Bottom)** The leucine residue at position 13 **(yellow shadow)** of LEMD2 is conserved across species. **(B)** Predicted 3-dimensional structure of the N-terminal domain of LEMD2 with wild-type leucine (Leu) in the **left panel** and the replaced arginine (Arg) at position 13 in the **right**. **(C)** Histology of cardiac tissue from patient 600, II-16 (Pat) showing extensive interstitial fibrosis and myocyte hypertrophy compared with the control (Ctrl). **a,** Masson's trichrome (scale bar: 500 μm) staining shows fibrotic tissue in **blue**; **b**, hematoxylin and eosin staining (scale bar: 100 μm) and **(c)** picro sirius red (PSR) demonstrate collagen deposits (scale bar: 100 μm). Myocyte size in hematoxylin and eosin and collagen deposits in PSR were significantly increased in Pat vs. Ctrl; ***$p < 0.001$. **(D)** Representative images of affected myocardial tissue **(upper panel)** recorded by transmission electron microscopy revealed elongation and bizarre shapes/invagination of the membrane **(arrowheads)** of nuclei with clumping of peripheral heterochromatin **(arrows)**. Transmission electron microscope images of fibroblasts **(lower panel)** from patient 600, II-18 (Pat) and age-matched control (Ctrl1). Note the abnormal morphology **(arrowhead)** of the nuclei and the condensed heterochromatin **(arrows)**. **(E)** Quantification of abnormal nuclei in patient and age-matched control fibroblasts at passage 2 (P2) and passage 15 (P15); $n = 300$ nuclei, respectively. There is a significant increase of abnormal nuclei in the patient cells (Pat) compared with the control (Ctrl1); $n = 300$ nuclei; ***$p < 0.001$.

FIGURE 3 Unchanged LEMD2 Localization and Expression in Patient Cells, Cardiac Tissue, and Transfected C2C12 Cells

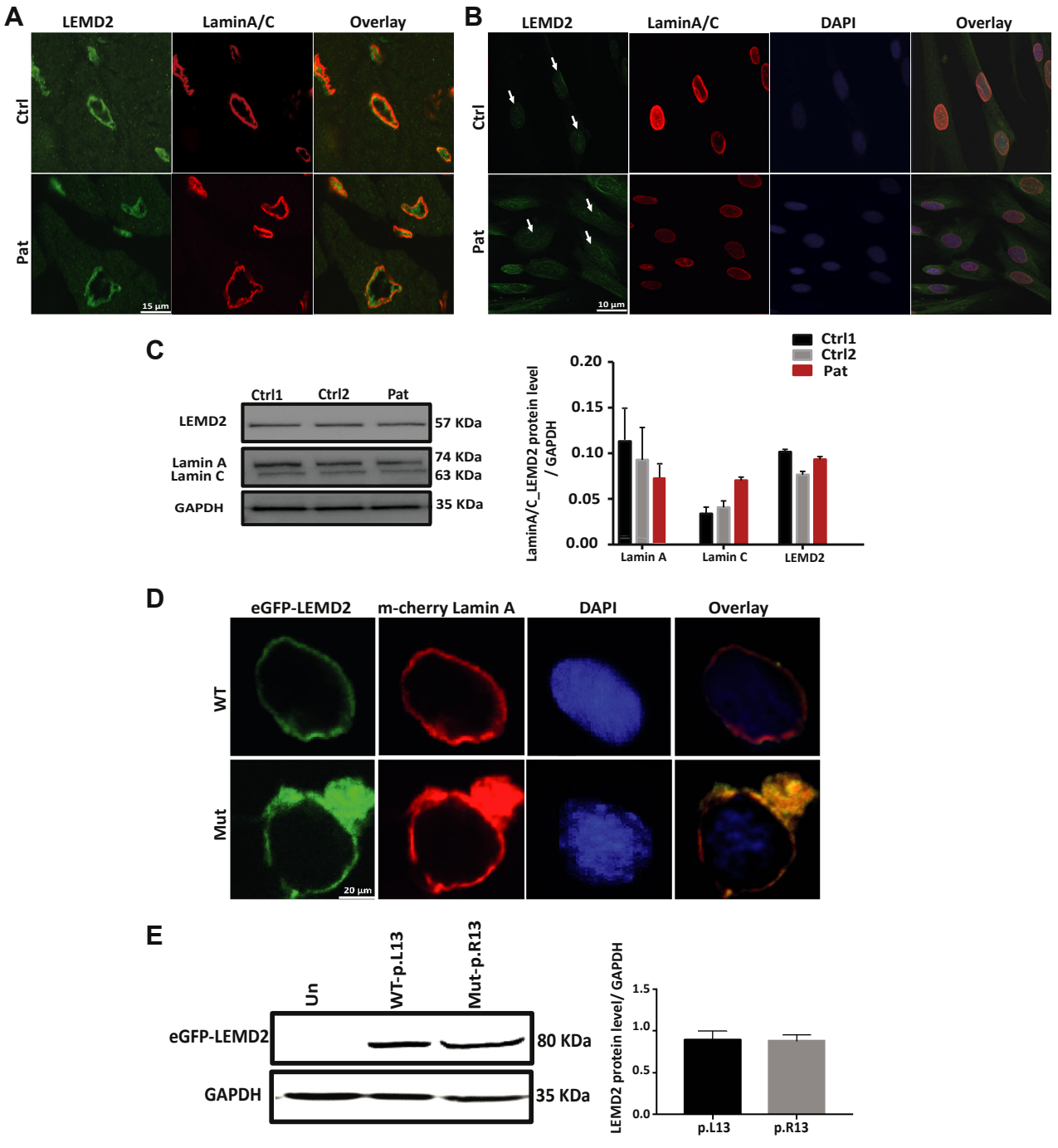

(A and B) Representative confocal images of patient and control myocardial tissue as well as fibroblasts showing normal localization of LEMD2 **(green, arrow)** co-localizing with lamin A/C **(red)** at the nuclear membrane; 4′,6′-diamidino-2-phenylindole (DAPI) **(blue)** indicates nuclei. Scale bars represent 20 μm. **(C)** Western blot showing LEMD2 and lamin A/C protein expression in fibroblasts in the **left panel**. Glyceraldehyde-3-phosphate dehydrogenase (GAPDH) was used as loading control. Quantification by densitometry (n = 3 experiments with 2 to 3 replicates) of LEMD2; quantification of lamin A and C and LEMD2 protein expression in the **right panel** shows no difference. **(D)** Representative confocal images of transfected C2C12 cells with recombinant enhanced green fluorescent protein (eGFP)-tagged wild-type (WT) (p.L13) or mutant (p.R13) LEMD2 **(green)** co-transfected with mCherry-lamin A/C (LMNA) **(red)** demonstrated co-localization. Scale bar represents 20 μm. **(E)** Western blot analysis of eGFP-LEMD2 proteins after transfection into HEK293 cells. GAPDH was used for loading control. Quantification by densitometry (n = 3) reveals no difference in the protein level between mutant (p.R13) and WT (p.L13) LEMD2. Un = un-transfected; other abbreviations as in Figure 2.

2 control subjects (age matched, younger control) underwent live cell counting using the IncuCyte microscope at different passage numbers (P2 and P15). We found that patient fibroblasts demonstrated a significantly diminished proliferation rate at P2 compared with both control subjects; however, the age-matched fibroblasts also showed slower rates of proliferation compared with the younger-aged control. At P15, patient cells did not proliferate but remained viable in culture, whereas both controls still proliferated (**Figure 4A**). Because this finding is a feature of premature senescence, we stained for β-galactosidase activity as a marker for cell senescence and found a significant increase in the number of cells positive for β-galactosidase at P6 and P15 in patient cells compared with both control subjects (**Figure 4B**). Remarkably, even fibroblasts from an individual 20 years older (Ctrl3) exhibited fewer β-galactosidase–positive cells compared with patient fibroblasts. We concluded that cells expressing mutant LEMD2 undergo premature senescence.

LEMD2 has been shown to be involved in DNA replication and mitosis. To understand the effects of mutant LEMD2 on cell cycle progression, we stained fibroblasts from the patient and 2 control subjects by using propidium iodide and examined cell cycle phase distribution. A larger portion of patient cells and the older age control cells were unable to progress from the G1 phase to the S phase and resulted in a prolonged G1 phase, which was even more significant at higher passage numbers. These data indicate that mutant LEMD2 may induce a G1 arrest (**Figure 4C**). Furthermore, we examined levels of cell cycle regulatory protein (Aurora B), a well-established G2/M phase marker. Whole protein lysates from patient cells exhibited decreased levels of Aurora B expression compared with both control subjects, consistent with the result from the cell cycle experiment (**Figure 4D**).

The abnormal proliferation profile seen in mutant fibroblasts could be a consequence of the imbalance between proliferation and apoptosis. We therefore assessed increased apoptosis in patient tissue and fibroblasts. First, affected heart and liver tissue were stained with 5-bromo-2′-deoxyuridine 5′-triphosphate, and the number of brown apoptotic bodies was counted. No obvious apoptotic bodies were detected in the patient and 2 control tissues (**Figure 5A**). We used the same assay in the patient and control fibroblasts and measured broken DNA ends by using flow cytometry. No significant difference in the apoptotic signals between the patient and the 2 control subjects were detected (**Figure 5B**). Finally, we tested the expression of caspase 3 and annexin V in whole protein lysates from fibroblasts and found no difference between the patient and control cells (**Figure 5C**). These data suggest that the mutation in LEMD2 does not affect the apoptotic pathway.

DISCUSSION

Genes-encoding INM proteins, most importantly *LMNA* and *EMD*, have been shown to be involved in the pathogenesis of human inherited DCMs. Here, we report a new homozygous missense mutation in the INM protein LEMD2 that leads to juvenile cataract and a severe form of arrhythmic cardiomyopathy with variable onset in people of the Hutterite founder population. We clinically and genetically characterized a cohort of 18 individuals from 2 different branches of the Hutterite population and found a primarily arrhythmic phenotype. Importantly, frequent ventricular arrhythmias and focal LV fibrosis preceded LV dilation and depressed myocardial performance, which are the classic hallmarks of DCM (30). However, the progression of LEMD2-associated disease may also lead to the common features of DCM: a hypokinetic left ventricle with decreased LV function as seen in one of the patients who required heart transplantation (family 290, II-5). However, our data support the requirement to recognize a broader phenotypic spectrum of DCM as recently outlined by Pinto et al. (31), in particular for early stages of genetically determined cardiomyopathies. Because ventricular arrhythmias are often life-threatening before other clinical symptoms occur and precede LV dysfunction in most of our cases, we decided to call it “arrhythmic cardiomyopathy,” which should also be distinguished from arrhythmogenic cardiomyopathy (ACM). In ACM, myocardium of the right, and often of both, ventricles are replaced by fibrotic and fatty tissue. Our patients did not exhibit any right ventricular involvement by cardiac imaging, we observed no fat tissue replacement in the histology of autopsy tissue, and none of the patients fulfilled the diagnostic Task Force Criteria for ACM (32).

Interestingly, the delayed enhancement by CMR imaging detected subepicardial, subendocardial, and at later stages transmural patchy fibrosis affecting mainly the inferior and inferolateral wall segments. Although the LGE pattern was suggestive of an ischemic etiology, there was no evidence of obstructive coronary artery disease on cardiac computed tomography imaging or coronary angiography.

FIGURE 4 The LEMD2 p.L13R Mutation Inhibits Proliferation, Induces Cell Senescence, and Cell Cycle Arrest in Fibroblasts

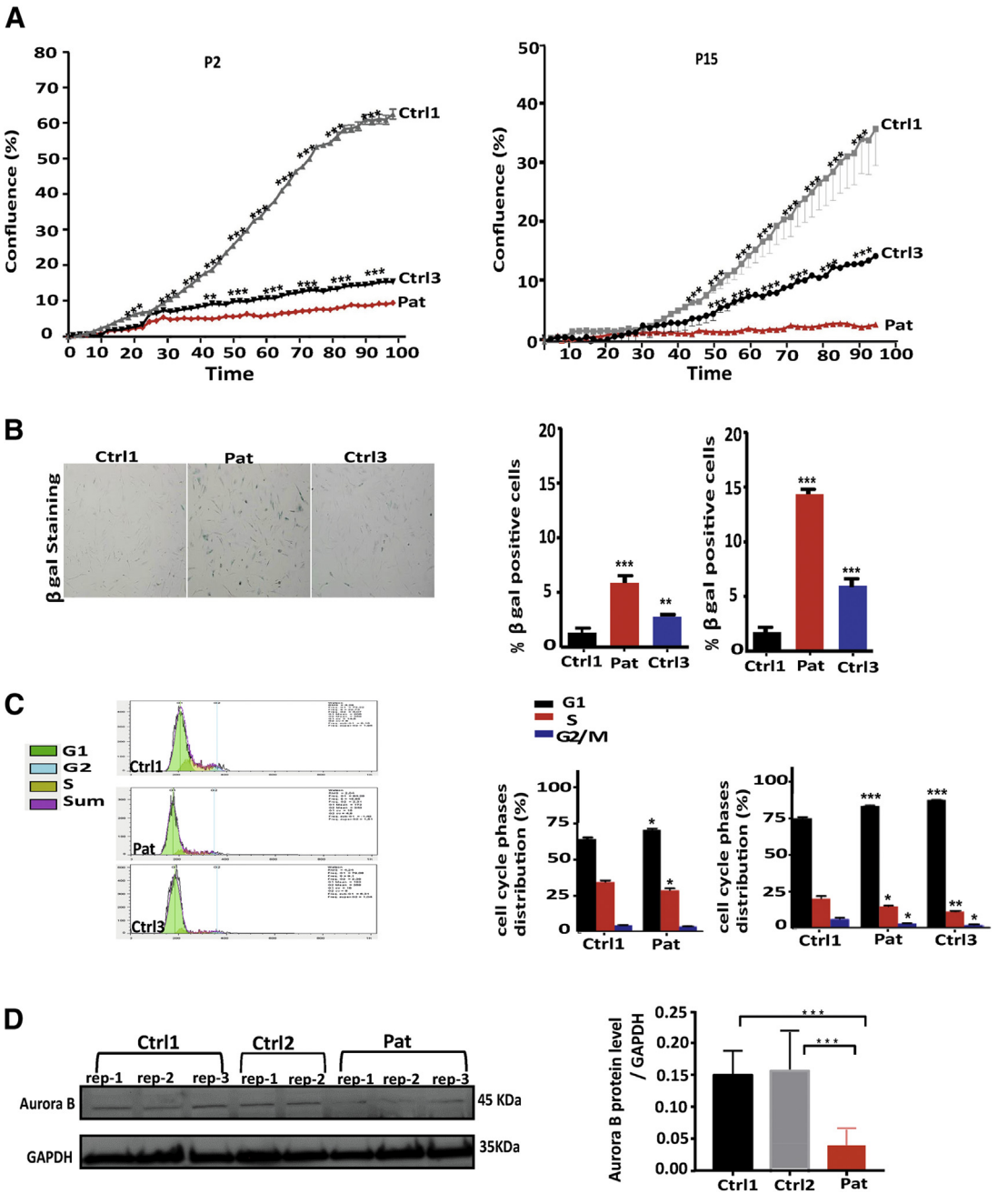

(A) Cell proliferation assay based on confluence from passage 2 (P2) in the **left panel** and P15 in the **right panel** in patient (Pat) fibroblasts, Ctrl1, and an older age ("high-senescence") control (Ctrl3). There was a significant difference in the rate of proliferation detected between both control subjects and patient at P2 and P15. The cells were imaged every 2 h for 90 h. n = 8 wells, mean ± SD, ***$p < 0.001$. **(B)** Images of β-galactosidase (β gal)-stained fibroblasts from patient and Ctrl1 as well as Ctrl3 at passage 6 (P6) and P15 in the **left panel**. Note that the amount of blue-stained cells is visibly higher in patient cells. **(Right)** Quantification of β gal-stained cells revealed increased cell senescence in patient cells compared with both control subjects at passages as indicated (n = 3; **$p < 0.01$; ***$p < 0.001$). **(C)** Fibroblasts stained with propidium iodide and measurements of the deoxyribonucleic acid content for each phase of the cell cycle by flow cytometry. Cells were taken from Ctrl1 at P6 and 9, from the patient (Pat) at passage 8 and passage 11, and from Ctrl3 at passage 12. Representative diagrams of each phase of the cell cycle are shown in the **left panel**. **(Right)** Quantification of the deoxyribonucleic acid content showed a potential arrest in the G1 phase in patient fibroblasts compared with Ctrl1 and similar to Ctrl3 at later passage. n = 3; **$p < 0.01$; *$p < 0.05$; ***$p < 0.001$. **(D)** Western blot of Aurora B protein expression in patient and control cells on the left panel. GAPDH was used as loading control. **(Right)** Quantification by densitometry of Aurora B protein expression revealed a significant difference between both control subjects and patient fibroblasts. n = 3 experiments with each 2 to 3 replicates; ***$p < 0.001$. Abbreviations as in Figures 2 and 3.

FIGURE 5 The Mutation in LEMD2 Does Not Induce Significant Apoptosis

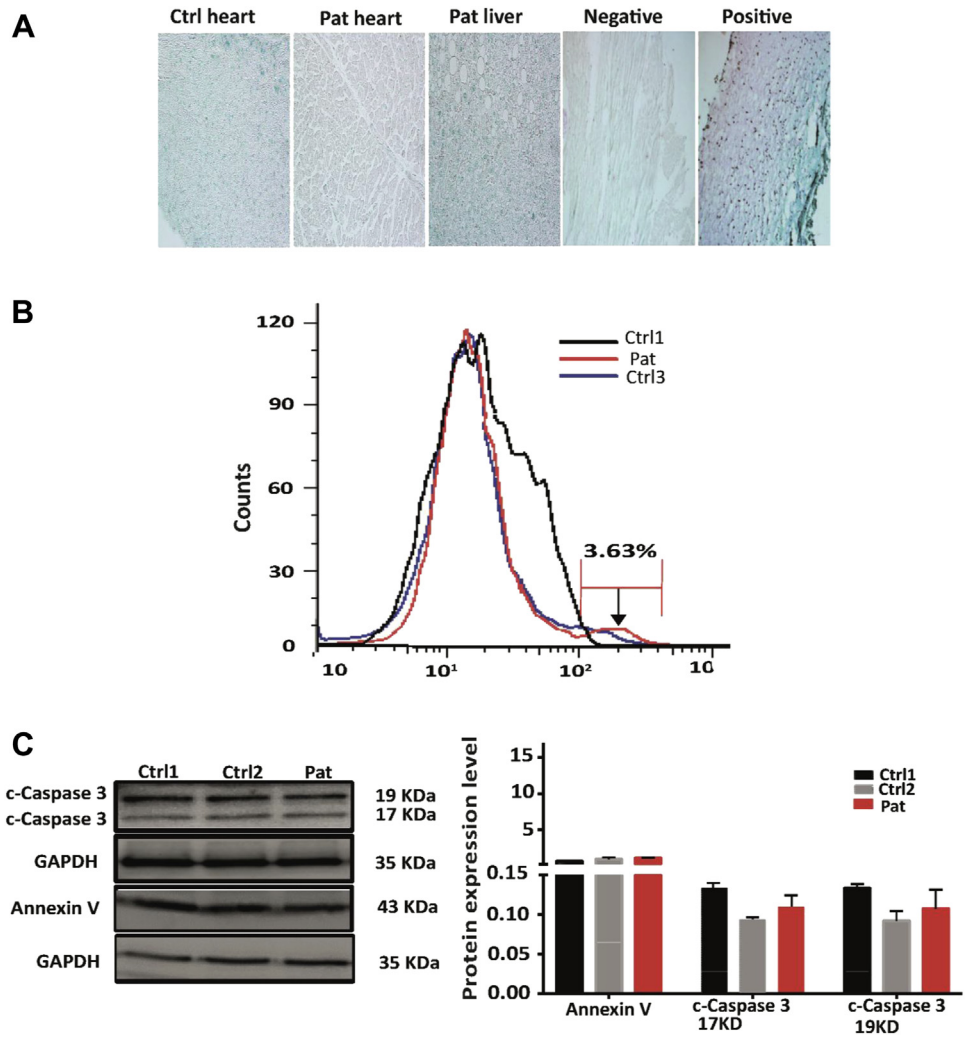

(A) Apoptosis assays were conducted by labeling the deoxyribonucleic acid with 5-bromo-2′-deoxyuridine 5′-triphosphate) in heart and liver tissue from the affected patient (family 600, II-16) and control heart samples. A positive control was created by adding 1 μg/μl deoxyribonucleic acids. Apoptotic cells were detected as brown dots. No signs of apoptosis were detected in all tested tissue. **(B)** Terminal deoxynucleotidyltransferase-mediated dUTP nick end labeling staining of fibroblasts and flow cytometry from patient and Ctrl1 and Ctrl3. The histograms of the fluorescein signal collected by using the terminal deoxynucleotidyltransferase-mediated dUTP nick end labeling method are shown. There is no difference in the apoptotic signals between the 2 control subjects and patient cells. **(C)** Western blot analysis of apoptotic markers (annexin V, caspase 3 [2 subunits: 17 and 19 KD]) in patient and control fibroblasts on the left panel. GAPDH was used as loading control. Quantification of apoptotic markers by densitometry does not show a significant difference in expression levels ($n = 3$ experiments with each 2 to 3 replicates). Abbreviations as in Figures 2 to 4.

Localized fibrotic patterns have also been shown in other forms of cardiomyopathy; for example, storage diseases such as Fabry and Danon disease exhibiting predominantly inferolateral scarring (33,34). Scar formation in DCM is often a sign of poor prognosis due to malignant arrhythmias and sudden death, which is common in our LEMD2 population. More than one-third (7 of 18) of patients died suddenly or required resuscitation and/or an ICD shock for malignant arrhythmias, indicating that clinical risk assessment should be attentive to arrhythmias and late enhancement in the CMR images rather than focus on the LV function, which was either normal or mildly reduced in most cases.

Even if not directly comparable, the outcome of *LMNA*-related DCM is known as less favorable compared with other forms of DCM (35-37) . Myocardial fibrosis with minor systolic dysfunction and dilatation, but significant atrioventricular conduction disease, is a common feature of *LMNA* mutation carriers, particularly in early disease (38). In addition, EMD-related cardiomyopathy often starts with sinus bradycardia and conduction disease (39). Similar to *LEMD2* disease, in *LMNA* and *EMD* cardiomyopathy, fibrosis and arrhythmias usually preceded the DCM phenotype, but in contrast, *LEMD2* cardiomyopathy did not present with major conduction defects, at least not in our patients. Further clinical characterization of a bigger patient cohort and longer follow-ups will help to define the phenotype and outcome of *LEMD2* cardiomyopathy more precisely.

LEMD2 is one of the Group II LEM domain proteins that contain an amino-terminal LEM domain in the nucleoplasm and 2 interior transmembrane domains. It interacts with LMNA by its N-terminal and transmembrane domains. The localization of LEMD2 in a lamin-dependent manner is mediated by the retention domain inside the N-terminal of LEMD2 (**Figure 1D**). Deficiency or loss of the A-type lamins (*LMNA*) causes mislocalization of the LEMD2 protein to the endoplasmic reticulum (10). If and how our missense mutation affects LMNA association was investigated by co-localization studies in cardiac tissue and fibroblast cells, as well as transfected C2C12 cells. Our results showed that the localization of both LEMD2 and LMNA at the NE was not altered, indicating that the mutation may not affect the retention signal and thus LMNA binding.

A remarkable finding was the bizarre nuclear morphology and the abnormally condensed peripheral chromatin in affected heart tissue and fibroblast cells. It is known that deficiency of LEMD2 disrupts the NE structure and causes a misshaped nucleus with invaginations and lobulations (40,41), resulting in lower nuclear circularity in the *Caenorhabditis elegans* mutant (42). LEMD2 has an important indirect role in chromatin organization because it is a binding component of the peripheral heterochromatin A-tether through formation of a complex with the N-terminus of LMNA (43). It also binds the DNA-binding protein BANF, which can influence histone post-translational modifications (44). BANF plays important structural roles in nuclear assembly and chromatin architecture during interphase, and undefined roles in gene regulation. It regulates specific gene expression through its interaction with LEM proteins. It is a common feature of many LEM proteins to interact directly with transcriptional regulators (45). We hypothesize that the L13R mutation may disrupt the interaction of BANF and LEMD2, which in turn leads to abnormal downstream transcriptional regulation. Interestingly, in *Schizosaccharomyces pombe*, the chromatin association and tethering of centromeres to the periphery are mediated by the LEM domain of yeast LEMD2, whereas the C-terminal MSC domain is required and sufficient to mediate the proper localization of telomeres (46) and contributes to heterochromatin silencing (47). We speculate that the abnormal chromatin condensation was either caused by a binding defect to BANF or an increased affinity for the LEM domain to bind with centromeres because of the mutated positive charged "arginine," which may lead to heterochromatin augmentation.

We investigated cell proliferation, cell cycle arrest, and β-galactosidase activity in patient fibroblasts. Mutated fibroblasts showed a trend toward disturbed cell proliferation, cell cycle arrest in G1 phase, and increased β-galactosidase activity, which is a consequence of an increased number of lysosomes (48). In combination with the abnormally condensed peripheral chromatin, these affected cells enter into senescence. The condensed punctate foci of peripheral chromatin are termed senescence-associated heterochromatin foci (SAHF) (49,50). SAHF formation occurs relatively late during the onset of senescence (51) and is prominent in acute senescence models, such as oncogene-induced senescent cells, and infrequently detected in replicative senescent cells (52,53). SAHFs are generated by a spatial rearrangement of pre-existing heterochromatin involving a clustering of regions that share specific histone modifications (54-56). They appear to maintain senescence through repression of growth-promoting genes (57), a process that might be important in the pathogenesis of LEMD2-associated cardiac disease.

We observed that a high percentage of patient fibroblasts exhibited premature cell senescence compared with control subjects, whereas apoptosis did not play a major role. Recently, several studies have shown that senescent cells actively suppress apoptosis (58,59); Chang et al. (60) and Zhu et al. (61) used the antiapoptotic protein inhibitors to trigger the senescent cells into apoptotic death. Apoptotic cells are eliminated by phagocytes in a manner that does not stimulate inflammation (62); senescent cells are viable, however, and have the potential to influence neighboring cells through pro-inflammatory secretion of growth factors and cytokines, which are well known as the senescence-associated secretory

phenotype. These phenotypes may influence the development of cardiomyopathy due to inflammation followed by fibrosis.

There are number of unanswered questions in this disease, including: Why is there a phenotype restricted to the heart and lens despite ubiquitous LEMD2 expression? How does the mutation disturb the interaction to potential binding partners? How does the abnormal nuclear morphology affect gene transcription and signal transduction? More mechanistic research needs to be conducted to understand the complex mechanisms involved in the pathogenesis of the p.L13R LEMD2 mutation in the development of cardiomyopathy.

CONCLUSIONS

Mutation in LEMD2 leads to a syndromic form of early-onset cataract and an arrhythmic DCM in which ventricular arrhythmias often precede dilatation and LV dysfunction. Mutant LEMD2 leads to remarkable changes in the shape of nuclei with condensed heterochromatin formation, reduced proliferation capacity, and cell senescence in fibroblasts suggesting the involvement of LEMD2 in chromatin remodeling and premature aging.

ACKNOWLEDGMENTS The authors thank the family members for their help and participation in this study. They also thank Dr. Yong Xiang Chen (University of Calgary) for his help with the histology and Kristina Martens (University of Calgary) for her technical help in the laboratory. They are also thankful to Dr. Wei-Xiang Dong (University of Calgary) for his help performing the transmission electron microscopy, as well as Dr. Rima-Marie Wazen and Dr. Pina Colarusso (University of Calgary) for helping with the IncuCyte ZOOM system. The IncuCyte ZOOM system has been purchased by the International Microbiome Centre, which is supported by the Cumming School of Medicine, University of Calgary, Western Economic Diversification, and Alberta Economic Development and Trade, Canada.

The authors thank the Genome Aggregation Database and the groups that provided exome and genome variant data to this resource. A full list of contributing groups can be found at http://gnomad.broadinstitute.org/about.

ADDRESS FOR CORRESPONDENCE: Dr. Brenda Gerull, Comprehensive Heart Failure Center and Department of Internal Medicine I, University Hospital Würzburg, Am Schwarzenberg 15, 97078 Würzburg, Germany. E-mail: gerull_b@ukw.de.

PERSPECTIVES

COMPETENCY IN MEDICAL KNOWLEDGE: Familial DCM can be caused by mutated proteins involved in many subcellular systems, but the NE and its interacting proteins play an emerging role in the pathogenesis of DCM. *LEMD2* is a novel disease gene for DCM with an arrhythmic phenotype preceding LV dysfunction similar to *LMNA*- and *EMD*-related cardiomyopathies. Our analysis presents for the first time a detailed description of the cardiac phenotype associated with LEMD2 disease, as well as pathogenetic and molecular findings observed in patient cells and cardiac tissue indicating chromatin remodeling, reduced proliferation capacity, and cell senescence. LEMD2 disease expands the spectrum of clinical laminopathies and may account for a proportion of cardiomyopathy of undetermined cause in populations outside the Hutterites.

TRANSLATIONAL OUTLOOK: Despite decades of discovery, the complex mechanisms of laminopathies leading to cardiac disease and premature aging (progeria) are still not fully understood. LEMD2 as a new player, and its role in cardiomyopathy, may help to further unravel the interactions of INM proteins of the INM, nucleoplasm, and cytoplasm. It may also aid in determining the roles of INM proteins in the maintenance of cellular integrity, in regulation of signaling pathways, and in chromatin organization and regulation of gene expression. Future research should focus on the role of LEMD2 in health and disease and may add a piece to the puzzle of understanding the complex network involved in laminopathies.

REFERENCES

1. Dellefave L, McNally EM. The genetics of dilated cardiomyopathy. Curr Opin Cardiol 2010;25:198–204.

2. Haas J, Frese KS, Peil B, et al. Atlas of the clinical genetics of human dilated cardiomyopathy. Eur Heart J 2015;36:1123–35.

3. Schreiber KH, Kennedy BK. When lamins go bad: nuclear structure and disease. Cell 2013;152:1365–75.

4. Fatkin D, MacRae C, Sasaki T, et al. Missense mutations in the rod domain of the lamin A/C gene as causes of dilated cardiomyopathy and conduction-system disease. N Engl J Med 1999;341:1715–24.

5. Bione S, Maestrini E, Rivella S, et al. Identification of a novel X-linked gene responsible for Emery-Dreifuss muscular dystrophy. Nat Genet 1994;8:323–7.

6. Cai M, Huang Y, Ghirlando R, et al. Solution structure of the constant region of nuclear envelope protein LAP2 reveals two LEM-domain structures: one binds BAF and the other binds DNA. EMBO J 2001;20:4399–407.

7. Lee KK, Haraguchi T, Lee RS, et al. Distinct functional domains in emerin bind lamin A and DNA-bridging protein BAF. J Cell Sci 2001;114:4567–73.

8. Shumaker DK, Lee KK, Tanhehco YC, et al. LAP2 binds to BAF.DNA complexes: requirement for the LEM domain and modulation by variable regions. EMBO J 2001;20:1754–64.

9. Mansharamani M, Wilson KL. Direct binding of nuclear membrane protein MAN1 to emerin in vitro and two modes of binding to barrier-to-autointegration factor. J Biol Chem 2005;280:13863–70.

10. Brachner A, Reipert S, Foisner R, et al. LEM2 is a novel MAN1-related inner nuclear membrane protein associated with A-type lamins. J Cell Sci 2005;118:5797–810.

11. Ikegami K, Egelhofer TA, Strome S, et al. Caenorhabditis elegans chromosome arms are anchored to the nuclear membrane via discontinuous association with LEM-2. Genome Biol 2010;11:R120.

12. Gruenbaum Y, Lee KK, Liu J, et al. The expression, lamin-dependent localization and RNAi depletion phenotype for emerin in C. elegans. J Cell Sci 2002;115:923–9.

13. Tapia O, Fong LG, Huber MD, et al. Nuclear envelope protein Lem2 is required for mouse development and regulates MAP and AKT kinases. PloS One 2015;10:e0116196.

14. Segura-Totten M, Wilson KL. BAF: roles in chromatin, nuclear structure and retrovirus integration. Trends Cell Biol 2004;14:261–6.

15. Huber MD, Guan T, Gerace L. Overlapping functions of nuclear envelope proteins NET25 (Lem2) and emerin in regulation of extracellular signal-regulated kinase signaling in myoblast differentiation. Mol Cell Biol 2009;29:5718–28.

16. Boone PM, Yuan B, Gu S, et al. Hutterite-type cataract maps to chromosome 6p21.32-p21.31, cosegregates with a homozygous mutation in LEMD2, and is associated with sudden cardiac death. Mol Genet Genomic Med 2016;4:77–94.

17. Hostetler JA. History and relevance of the Hutterite population for genetic studies. Am J Med Genet 1985;22:453–62.

18. Martin AO. The founder effect in a human isolate: evolutionary implications. Am J Phys Anthropol 1970;32:351–67.

19. UCSC Gene Bioinformatics. Available at: http://genome.ucs.edu/FAQ.FAQreleases.html. Accessed February 1, 2019.

20. Genome Aggregate Database. Available at: http://gnomad.broadinstitute.org/. Accessed February 1, 2019.

21. Lek M, Karczewski KJ, Minikel EV, et al. Analysis of protein-coding genetic variation in 60,706 humans. Nature 2016;536:285–91.

22. Berman HM, Westbrook J, Feng Z, et al. The Protein Data Bank. Nucleic Acids Res 2000;28:235–42.

23. IHC WORLD. Available at: http://www.ihcworld.com. Accessed February 1, 2019.

24. APO-BRDU-IHC Colorimetric kit. Phoenix Flow Systems. Available at: http://www.phnxflow.com/APO-BrdU-IHC.protocol.pdf. Accessed February 1, 2019.

25. Shokeir MH, Lowry RB. Juvenile cataract in Hutterites. Am J Med Genet 1985;22:495–500.

26. Pearce WG, Mackay JA, Holmes TM, et al. Autosomal recessive juvenile cataract in Hutterites. Ophthalmic Paediatr Genet 1987;8:119–24.

27. Uricchio LH, Chong JX, Ross KD, et al. Accurate imputation of rare and common variants in a founder population from a small number of sequenced individuals. Genetic Epidemiol 2012;36:312–9.

28. Livne OE, Han L, Alkorta-Aranburu G, et al. PRIMAL: fast and accurate pedigree-based imputation from sequence data in a founder population. PLoS Comput Biol 2015;11:e1004139.

29. Cattin ME, Bertrand AT, Schlossarek S, et al. Heterozygous LmnadelK32 mice develop dilated cardiomyopathy through a combined pathomechanism of haploinsufficiency and peptide toxicity. Hum Mol Genet 2013;22:3152–64.

30. Bozkurt B, Colvin M, Cook J, et al. Current diagnostic and treatment strategies for specific dilated cardiomyopathies: a scientific statement from the American Heart Association. Circulation 2016;134:e579–646.

31. Pinto YM, Elliott PM, Arbustini E, et al. Proposal for a revised definition of dilated cardiomyopathy, hypokinetic non-dilated cardiomyopathy, and its implications for clinical practice: a position statement of the ESC working group on myocardial and pericardial diseases. Eur Heart J 2016;37:1850–8.

32. Marcus FI, McKenna WJ, Sherrill D, et al. Diagnosis of arrhythmogenic right ventricular cardiomyopathy/dysplasia: proposed modification of the Task Force criteria. Circulation 2010;121:1533–41.

33. Deva DP, Hanneman K, Li Q, et al. Cardiovascular magnetic resonance demonstration of the spectrum of morphological phenotypes and patterns of myocardial scarring in Anderson-Fabry disease. J Cardiovasc Magn Reson 2016;18:14.

34. Etesami M, Gilkeson RC, Rajiah P. Utility of late gadolinium enhancement in pediatric cardiac MRI. Pediatr Radiol 2016;46:1096–113.

35. van Spaendonck-Zwarts KY, van Rijsingen IA, van den Berg MP, et al. Genetic analysis in 418 index patients with idiopathic dilated cardiomyopathy: overview of 10 years' experience. Eur J Heart Fail 2013;15:628–36.

36. Jansweijer JA, Nieuwhof K, Russo F, et al. Truncating titin mutations are associated with a mild and treatable form of dilated cardiomyopathy. Eur J Heart Fail 2017;19:512–21.

37. van Tintelen JP, Tio RA, Kerstjens-Frederikse WS, et al. Severe myocardial fibrosis caused by a deletion of the 5' end of the lamin A/C gene. J Am Coll Cardiol 2007;49:2430–9.

38. Holmstrom M, Kivisto S, Helio T, et al. Late gadolinium enhanced cardiovascular magnetic resonance of lamin A/C gene mutation related dilated cardiomyopathy. J Cardiovasc Magn Reson 2011;13:30.

39. Sanna T, Dello Russo A, Toniolo D, et al. Cardiac features of Emery-Dreifuss muscular dystrophy caused by lamin A/C gene mutations. Eur Heart J 2003;24:2227–36.

40. Liu J, Lee KK, Segura-Totten M, et al. MAN1 and emerin have overlapping function(s) essential for chromosome segregation and cell division in Caenorhabditis elegans. Proc Natl Acad Sci U S A 2003;100:4598–603.

41. Gonzalez Y, Saito A, Sazer S. Fission yeast Lem2 and Man1 perform fundamental functions of the animal cell nuclear lamina. Nucleus 2012;3:60–76.

42. Morales-Martinez A, Dobrzynska A, Askjaer P. Inner nuclear membrane protein LEM-2 is required for correct nuclear separation and morphology in C. elegans. J Cell Sci 2015;128:1090–6.

43. Thanisch K, Song C, Engelkamp D, et al. Nuclear envelope localization of LEMD2 is developmentally dynamic and lamin A/C dependent yet insufficient for heterochromatin tethering. Differentiation 2017;94:58–70.

44. de Montes Oca R, Andreassen PR, Wilson KL. Barrier-to-autointegration factor influences specific histone modifications. Nucleus 2011;2:580–90.

45. Berk JM, Tifft KE, Wilson KL. The nuclear envelope LEM-domain protein emerin. Nucleus 2013;4:298–314.

46. Barrales RR, Forn M, Georgescu PR, et al. Control of heterochromatin localization and silencing by the nuclear membrane protein Lem2. Genes Develop 2016;30:133–48.

47. Braun S, Barrales RR. Beyond tethering and the LEM domain: MSCellaneous functions of the inner nuclear membrane Lem2. Nucleus 2016;7:523–31.

48. Dimri GP, Lee X, Basile G, et al. A biomarker that identifies senescent human-cells in culture and in aging skin in-vivo. Proc Natl Acad Sci U S A 1995;92:9363–7.

49. Narita M, Nunez S, Heard E, et al. Rb-mediated heterochromatin formation and silencing of E2F target genes during cellular senescence. Cell 2003;113:703–16.

50. Zhang R, Zhang RG, Poustovoitov MV, et al. Formation of macroH2A-containing senescence associated heterochromatin foci (SAHF) and senescence driven by ASF1A and HIRA. Gerontologist 2005;45:46.

51. Swanson EC, Rapkin LM, Bazett-Jones DP, et al. Unfolding the story of chromatin organization in senescent cells. Nucleus 2015;6:254–60.

52. Sun L, Yu R, Dang W. Chromatin architectural changes during cellular senescence and aging. Genes 2018;9.

53. Kosar M, Bartkova J, Hubackova S, et al. Senescence-associated heterochromatin foci are dispensable for cellular senescence, occur in a cell type- and insult-dependent manner and follow expression of p16(ink4a). Cell Cycle 2011;10:457–68.

54. Parry AJ, Narita M. Old cells, new tricks: chromatin structure in senescence. Mamm Genome 2016;27:320–31.

55. Chandra T, Kirschner K, Thuret JY, et al. Independence of repressive histone marks and chromatin compaction during senescent heterochromatic layer formation. Molecular Cell 2012;47:203–14.

56. Chandra T, Ewels PA, Schoenfelder S, et al. Global reorganization of the nuclear landscape in senescent cells. Cell Reports 2015;10:471–83.

57. Corpet A, Stucki M. Chromatin maintenance and dynamics in senescence:a spotlight on SAHF formation and the epigenome of senescent cells. Chromosoma 2014;123:423–36.

58. Childs BG, Baker DJ, Kirkland JL, et al. Senescence and apoptosis:dueling or complementary cell fates? EMBO Reports 2014;15:1139–53.

59. He S, Sharpless NE. Senescence in health and disease. Cell 2017;169:1000–11.

60. Chang J, Wang Y, Shao L, et al. Clearance of senescent cells by ABT263 rejuvenates aged hematopoietic stem cells in mice. Nature Med 2016;22:78–83.

61. Zhu Y, Tchkonia T, Fuhrmann-Stroissnigg H, et al. Identification of a novel senolytic agent, navitoclax, targeting the Bcl-2 family of anti-apoptotic factors. Aging Cell 2016;15:428–35.

62. Erwig LP, Henson PM. Clearance of apoptotic cells by phagocytes. Cell Death Differentiation 2008;15:243–50.

63. UniProt. Available at: http://www.uniprot.org/uniprot/Q8NC56. Accessed February 1, 2019.

KEY WORDS chromatin remodeling, dilated cardiomyopathy, inner nuclear membrane, LEMD2, sudden death

APPENDIX For supplemental tables and a figure, please see the online version of this paper.

JACC: BASIC TO TRANSLATIONAL SCIENCE VOL. 4, NO. 2, 2019
© 2019 THE AUTHORS. PUBLISHED BY ELSEVIER ON BEHALF OF THE AMERICAN COLLEGE OF CARDIOLOGY FOUNDATION. THIS IS AN OPEN ACCESS ARTICLE UNDER THE CC BY-NC-ND LICENSE (http://creativecommons.org/licenses/by-nc-nd/4.0/).

PRECLINICAL RESEARCH

Glucagon-Like Peptide-1–Mediated Cardioprotection Does Not Reduce Right Ventricular Stunning and Cumulative Ischemic Dysfunction After Coronary Balloon Occlusion

Joel P. Giblett, MD,[a,b] Richard G. Axell, PhD,[c] Paul A. White, PhD,[c] Muhammad Aetesam-Ur-Rahman, MBBS,[a,b] Sophie J. Clarke, PhD,[b] Nicola Figg, BSc,[b] Martin R. Bennett, PhD,[b] Nick E.J. West, MD,[a] Stephen P. Hoole, MA, DM[a,b]

VISUAL ABSTRACT

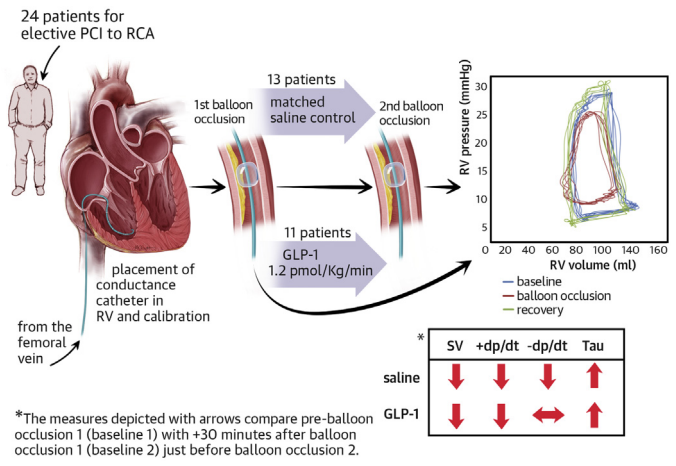

Giblett, J.P. et al. J Am Coll Cardiol Basic Trans Science. 2019;4(2):222–33.

HIGHLIGHTS

- **GLP-1 protects against ischemic left ventricular dysfunction after serial coronary balloon occlusion of the left anterior descending artery**
- **This study assessed whether serial right coronary artery balloon occlusion affected the right ventricle in a similar fashion using a conductance catheter method**
- **Serial balloon occlusion of the right coronary artery causes stunning and cumulative ischemic dysfunction in the right ventricle**
- **GLP-1 did not protect against stunning and cumulative ischemic dysfunction in the right ventricle**

From the [a]Department of Interventional Cardiology, Royal Papworth Hospital, Cambridge, United Kingdom; [b]Division of Cardiovascular Medicine, University of Cambridge, Cambridge, United Kingdom; and the [c]Medical Physics and Clinical Engineering, Cambridge University Hospital NHS Foundation Trust, Cambridge, United Kingdom. This study was supported by a National Institute for Health Research Healthcare Scientist Doctoral Fellowship Grant (NIHR-HCS-D12-14). Ms. Clarke is an employee of Merck Sharp & Dohme. The authors have reported that they have no relationships relevant to the contents of this paper to disclose.

All authors attest they are in compliance with human studies committees and animal welfare regulations of the authors' institutions and Food and Drug Administration guidelines, including patient consent where appropriate. For more information, visit the *JACC: Basic to Translational Science* author instructions page.

Manuscript received September 10, 2018; revised manuscript received December 7, 2018, accepted December 10, 2018.

ISSN 2452-302X https://doi.org/10.1016/j.jacbts.2018.12.002

SUMMARY

Stunning and cumulative ischemic dysfunction occur in the left ventricle with coronary balloon occlusion. Glucagon-like peptide (GLP)-1 protects the left ventricle against this dysfunction. This study used a conductance catheter method to evaluate whether the right ventricle (RV) developed similar dysfunction during right coronary artery balloon occlusion and whether GLP-1 was protective. In this study, the RV underwent significant stunning and cumulative ischemic dysfunction with right coronary artery balloon occlusion. However, GLP-1 did not protect the RV against this dysfunction when infused after balloon occlusion.
(J Am Coll Cardiol Basic Trans Science 2019;4:222–33) © 2019 The Authors. Published by Elsevier on behalf of the American College of Cardiology Foundation. This is an open access article under the CC BY-NC-ND license (http://creativecommons.org/licenses/by-nc-nd/4.0/).

ABBREVIATIONS AND ACRONYMS

BL = baseline

BO1 = first balloon occlusion

BO2 = second balloon occlusion

dP/dt_{max} = maximal rate of isovolumetric contraction

dP/dt_{min} = maximal rate of isovolumetric relaxation

DSHB = Developmental Studies Hybridoma Bank

EDP = end-diastolic pressure

GLP = glucagon-like peptide

GLP-1R = glucagon-like peptide 1 receptor

LV = left ventricular

PCI = percutaneous coronary intervention

PV = pressure–volume

RCA = right coronary artery

RV = right ventricular

Tau = time constant of diastolic relaxation

The importance of the right ventricle in the pathophysiology of heart disease is of increasing clinical relevance (1). Involvement of the right ventricle in myocardial infarction raises the risk of cardiogenic shock and increases mortality, even when treated with primary percutaneous coronary intervention (PCI) (2). Pre-existing right ventricular (RV) failure portends poor prognosis in several conditions (3), and acute deterioration in RV function often has important hemodynamic and clinical consequences.

The blood supply to the right ventricle depends on the coronary anatomy. In a right-dominant system (80%), the right coronary artery (RCA) supplies most of the right ventricle (4). The right ventricle is believed to be relatively resistant to ischemia compared with the left ventricle, as propelling blood into a low-resistance pulmonary circulation requires less work. The right ventricle has thinner, less muscular walls with a lower energetic demand and a lower nutrient/oxygen requirement as a result (5). Coronary balloon inflation during PCI provides a model of supply ischemia. Brief coronary balloon occlusion of the RCA reduces RV stroke volume and stroke work, while there is persistent deterioration of both systolic and diastolic function at 15 min after reperfusion (6,7). Studies of brief coronary occlusion on left ventricular (LV) function suggest that, after transient improvement resulting from reactive hyperemia, residual ventricular dysfunction is revealed (stunning) when coronary flow normalizes at some point after reperfusion (8).

Glucagon-like peptide (GLP)-1is an incretin hormone, produced from L cells in response to food bolus. GLP-1 receptor (GLP-1R) agonists such as exenatide and liraglutide are used in the management of diabetes mellitus. Data from large trials have shown that these agents have cardiovascular benefits (9,10). Native GLP-1 has been shown to protect against stunning and cumulative ischemic dysfunction in the left ventricle, whether administered before or after balloon occlusion (11–13).

Animal studies have found that GLP-1 protection against lethal ischemia-reperfusion in the left ventricle is dependent on intracellular signaling pathways involving p70s6K and the phosphoinositol-3-kinase-Akt complex (14–16). These signal cascades are important in the transduction of ischemic preconditioning, and the final effector is the mitochondrial potassium-adenosine triphosphate channel (m-KATP channel). However, blockade of the m-KATP channel, a final effector of ischemic preconditioning, did not abrogate GLP-1 protection in humans (13). Similarly, animal models have implicated changes in myocardial metabolism in GLP-1 cardioprotection (17–21), but a series of human studies have cast doubt on altered substrate use as the cause (12,22,23). A recent study found that GLP-1 is a coronary-specific vasodilator in humans but does not exert its ventricular effect by reducing systemic vascular tone. This study also confirmed that the GLP-1R was present on LV cardiomyocytes but was not expressed on vascular tissue, and thus GLP-1 is likely to have a direct ventricular effect, with secondary vasodilator effects mediated by ventricular-arterial cross-talk (24).

The present study investigated whether RV dysfunction occurs during serial coronary balloon occlusion, assessed by using the gold standard conductance catheter technique (25–28), and whether it is ameliorated by GLP-1. These data will confirm whether GLP-1 cardioprotection is confined to the left ventricle or whether it offers protection from RV ischemia.

METHODS

STUDY POPULATION. Patients with severe, dominant (providing the posterior descending artery) RCA

FIGURE 1 Study Time Line

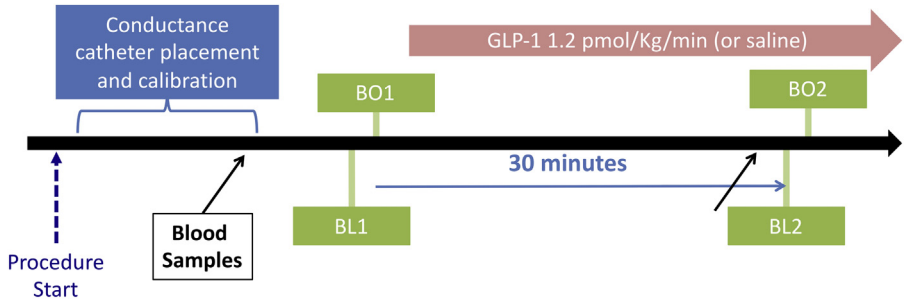

Blood samples taken before baseline (BL1) and at 30-min recovery (BL2). BO1 = first balloon occlusion; BO2 = second balloon occlusion; GLP-1 = glucagon-like peptide 1.

disease awaiting single-vessel elective PCI, and with normal RV function assessed by echocardiography, were recruited. Patients were excluded if they had experienced a myocardial infarction in the preceding 3 months, had a pacemaker or significant valvular heart disease, or were not in sinus rhythm. All patients provided written informed consent before study inclusion.

Patients were recruited in 2 blocks (control followed by GLP-1) to test the first hypothesis that serial balloon occlusion caused ischemic dysfunction, before testing whether GLP-1 infusion ameliorated the dysfunction. The study protocol was designed to match that used by Read et al. (11) to assess the effect of GLP-1 on the left ventricle. The study was approved by the local ethics committee (REC 14/EE/0141) and complied with the Declaration of Helsinki. The study was registered on clinicaltrials.gov (NCT02236299); the trial identification number was UKCRN14028.

PRE-STUDY PROTOCOL. Variables that could alter coronary or ventricular hemodynamic variables were minimized. Patients were asked to abstain from consuming caffeine, alcohol, and nicotine, as well as nicorandil and oral/sublingual nitrates, in the 24 h before the procedure. Patients were fasted for 6 h, received aspirin 300 mg and clopidogrel 300 mg before the procedure, and were anticoagulated with unfractionated heparin (70 to 100 IU/kg). An activated clotting time was maintained >250 s throughout the procedure.

CARDIAC CATHETERIZATION. Figure 1 depicts the study time line. A 6-F sheath was placed in the right radial artery and a 7-F sheath was placed in the right femoral vein under local anesthetic. Glyceryl trinitrate 100 μg was administered into the radial artery at the beginning of the procedure as standard to prevent radial spasm but not into the coronary arteries. Patients received 500 ml 0.9% saline administered intravenously before the procedure. No other infusions were administered during the procedure. A 6-F multipurpose catheter was positioned in the pulmonary artery and then the right atrium to measure mean pressures and obtain mixed venous blood gas saturations for determination of indirect Fick cardiac output. Blood was sampled to measure blood resistivity. A 7-F eight-electrode conductance catheter (Millar, Inc., Houston, Texas) was connected to an MPVS Ultra (Millar, Inc.) signal-conditioning unit in series with the PowerLab 16/30 (ADInstruments, New South Wales, Australia) 16-channel amplifier. The conductance catheter was submersed in a saline bath and the pressure transducer zeroed before insertion through the venous sheath and positioning it apically along the long axis of the right ventricle under fluoroscopic guidance (Figure 2A). The conductance catheter was calibrated by using the technique first described in the left ventricle by Baan et al. (29) that has subsequently been used for the right ventricle (30,31).

PRESSURE-VOLUME LOOP DATA ACQUISITION. The conductance technique was used to measure the pressure-volume (PV) loop relationship during mid-expiration breath hold, providing beat-to-beat assessment of RV function at steady state for at least 5 cardiac cycles. PV loop data were recorded at baseline (BL1), the end of a 1-min low-pressure (<4 atm) balloon occlusion (BO1), and at 1-min recovery. The study infusion was then immediately commenced. PV loop data were acquired after

30-min recovery and at the end of a further 1-min balloon occlusion (BO2). Once data collection was completed, PCI was performed at operator discretion. An example of PV loops generated from the right ventricle during balloon occlusion is shown in Figure 2B.

OFFLINE RV HEMODYNAMIC MEASUREMENTS. Conductance catheter data were analyzed offline by using LabChart software (LabChart 7.0, ADInstruments). Five steady-state PV loops were recorded at each time point, generating load-dependent parameters of systolic and diastolic function. Systolic parameters of ventricular function were cardiac output, stroke volume, stroke work, ejection fraction, end-systolic pressure, and the maximum rate of isovolumic contraction (dP/dt_{max}). Effective arterial elastance to assess afterload was also assessed. Diastolic parameters of ventricular function were end-diastolic pressure (EDP), the maximum rate of isovolumic relaxation (dP/dt_{min}), and the time constant of diastolic relaxation (Tau) (32-34). Tau represents the exponential decay of the RV pressure during isovolumic relaxation and was determined by using the Weiss method. Tau is considered load dependent but is predominantly affected by heart rate.

STUDY INFUSIONS. Infusion of GLP-1 (7 to 36) amide acetate (or 0.9% saline solution at matched rate) at 1.2 pmol/kg/min was administered after the first balloon occlusion (BO1) until completion of the PV loop measurement (after BO2). This infusion was at the same dose as that administered in previous studies which reduced ischemic dysfunction in the left ventricle (11-13).

BIOCHEMISTRY. Baseline peripheral venous blood samples to measure glucose, insulin, GLP-1 (7 to 36) amide, and free fatty acids were obtained at the beginning of the case. Additional peripheral venous blood samples were drawn before the second balloon occlusion. Blood for GLP-1 assays was drawn up into pre-prepared 2-ml syringes containing 20 μl of dipeptidyl peptidase-4 inhibitor (Merck Millipore, Nottingham, United Kingdom). These syringes were chilled before collection, and the blood sample was immediately transferred to 2.5-ml ethylenediaminetetraacetic acid tubes, which had also been prepared, containing the protease inhibitor aprotinin (Trasylol, Nordic Group, Trondheim, Norway). These samples were kept in crushed ice until they were spun and stored at −20°C. Samples for

FIGURE 2 Example of Data Acquisition

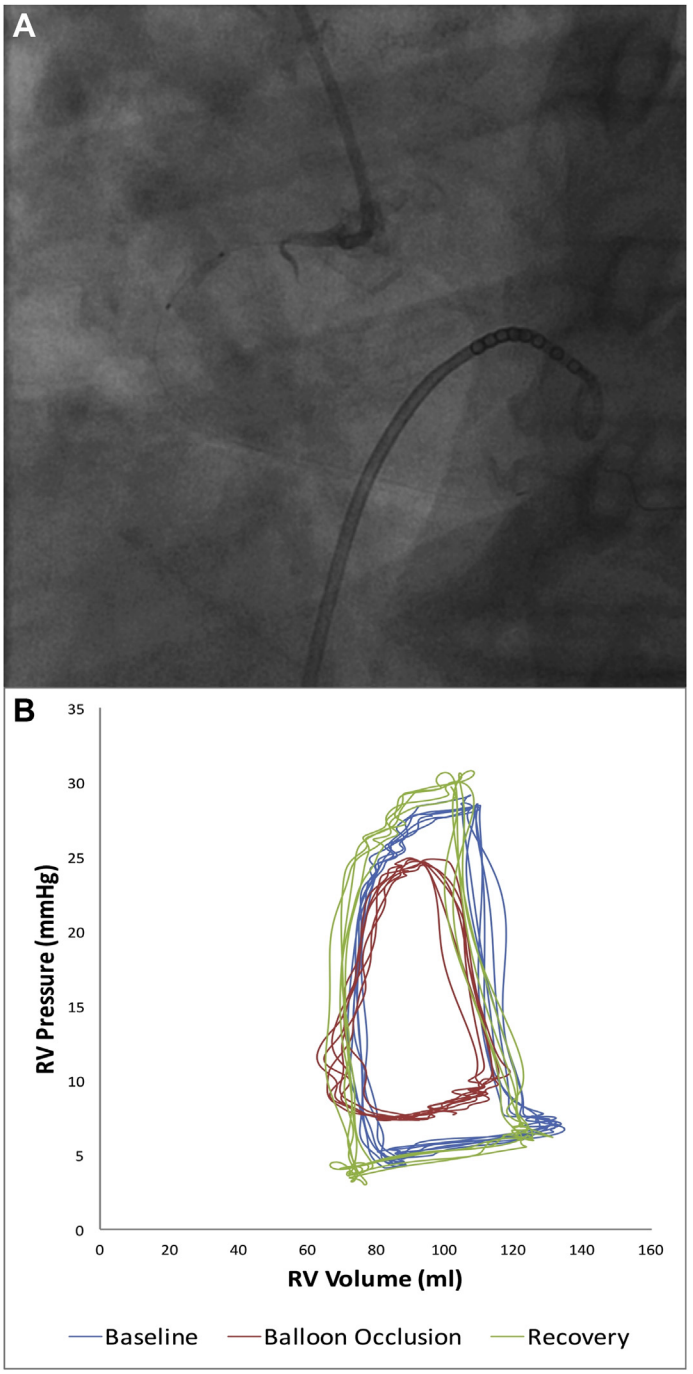

(A) Fluoroscopic image of the conductance catheter located in the right ventricle during low-pressure balloon occlusion of the right coronary artery. **(B)** Right ventricular (RV) pressure-volume loops recorded at baseline **(blue)**, at the end of the low-pressure balloon occlusion **(red)**, and at 15-min recovery **(green)**.

JACC: BASIC TO TRANSLATIONAL SCIENCE VOL. 4, NO. 2, 2019
APRIL 2019:222–33

TABLE 1 Demographic and Hemodynamic Data

	Control (n = 13)	GLP-1 (n = 11)	p Value
Demographic characteristics			
Age, yrs	72 (62–75)	66 (58–72)	0.25
Male	11 (84.6)	7 (63.6)	0.24
Body mass index, kg/m^2	28.0 ± 4.0	31.3 ± 5.3	0.10
Smoking history	8 (61.5)	5 (45.4)	0.43
CCS class (II+)	11 (84.6)	7 (63.6)	0.24
NYHA functional class (II or higher)	4 (30.7)	6 (54.5)	0.24
Previous PCI	6 (46.2)	4 (36.3)	0.63
Hypertension	4 (30.7)	3 (27.3)	0.85
Diabetes	1 (7.6)	3 (27.3)	0.20
Previous MI	3 (23.1)	2 (18.1)	0.77
Hemoglobin, g/dl	13.7 ± 1.7	13.7 ± 1.2	0.99
Creatinine, mg/dl	1.0 ± 0.3	1.0 ± 0.2	0.36
Baseline hemodynamic variables			
Systolic blood pressure, mm Hg	136 ± 21	140 ± 27	0.69
Diastolic blood pressure, mm Hg	68 ± 12	69 ± 10	0.98
Systemic MAP, mm Hg	91 ± 13	93 ± 13	0.79
Mean RA pressure, mm Hg	6 (4–8)	4 (3–6)	0.12
Mean PA pressure, mm Hg	18 (17–21)	13 (12–19)	0.07
PA saturations, %	71.6 ± 7.0	71.2 ± 3.6	0.86
Aortic saturations, %	94.6 ± 2.2	96.0 ± 1.4	0.11
Cardiac output, l/min	5.27 ± 1.05	4.88 ± 0.79	0.14
Cardiac index, l/min/kg	2.67 ± 0.51	2.45 ± 0.29	0.07
Baseline hemodynamic variables–RV conductance catheter data			
Stroke work, mm Hg/ml	1,377 ± 575	1,001 ± 382	0.06
Stroke volume, mm Hg/ml	85.9 ± 17.7	81.5 ± 18.6	0.26
End-systolic pressure, mm Hg	28.5 ± 8.7	24.5 ± 7.2	0.26
End diastolic pressure, mm Hg	7.6 ± 3.9	8.6 ± 3.6	0.37
End systolic volume, ml	104 ± 41	81 ± 43	0.19
End diastolic volume, ml	147 ± 40	118 ± 50	0.19
Ejection fraction, %	57.7 ± 9.4	61.7 ± 13.1	0.41
dP/dt_{max}, mm Hg/s	360 ± 78	368 ± 116	0.97
dP/dt_{min}, mm Hg/s	−259 ± 91	−246 ± 49	0.80
Tau, ms	56 ± 13	68 ± 21	0.06
Ea, mm Hg/ml	0.34 ± 0.09	0.33 ± 0.15	0.98

Values are median (interquartile range), n (%), or mean ± SD.

CCS = Canadian Cardiovascular Society functional classification of angina; dP/dt_{max} = maximum rate of isovolumic contraction; dP/dt_{min} = maximum rate of isovolumic relaxation; Ea = effective arterial elastance; GLP-1 = glucagon-like peptide 1; NYHA = New York Heart Association; MI = myocardial infarction; MAP = mean arterial pressure; PA = pulmonary artery; PCI = percutaneous coronary intervention; RA = right atrial; Tau = time constant of diastolic relaxation.

insulin and free fatty acids were also collected. Blood samples were collected into lithium-heparin tubes, which were also stored on crushed ice before centrifugation and storage at −20°C. All samples were spun within 1 h of collection.

IMMUNOHISTOCHEMISTRY. Human tissue samples from anonymous donors were stained for the GLP-1R to correlate our clinical findings with immunohistochemistry. LV and RV samples from nondiabetic patients with ischemic heart disease were stained. Tissue samples from the Royal Papworth Hospital Tissue Bank were stained for the presence of the GLP-1R. Tissue samples were fixed in 4% paraformaldehyde in 0.1 M phosphate buffer for a minimum of 24 h before dehydration and paraffin embedding. Pancreas was used as a positive control and also stained with hematoxylin-eosin to identify the beta cells. Matched tissue samples from left and right ventricles underwent immunohistochemical analysis using the mAb 3F52 GLP-1R antibody. This receptor was sourced from the University of Iowa Developmental Studies Hybridoma Bank (DSHB); monoclonal antibody (mAb) 3F52 was deposited to the DSHB by Knudsen, L.B. (DSHB Hybridoma Product mAb 3F52). It has previously been validated as specific for the GLP-1R to map GLP-1R expression (35).

STATISTICAL ANALYSIS. Data are expressed as mean ± SD unless otherwise stated. Analysis was performed by using SPSS version 25 (IBM SPSS Statistics, IBM Corporation, Armonk, New York). The sample sizes used in the present analysis had the power to detect differences between treatment and placebo groups as estimated by previous research (11). A minimum of 11 patients per group was needed to achieve 80% power. Permission to recruit 15 patients in each group was obtained, ensuring that the study could be completed if datasets were incomplete. Comparison within the groups used a paired Student's *t*-test. For comparisons between groups, nonparametric data were compared by using a Mann-Whitney *U* test, whereas normally distributed data used an unpaired Student's *t*-test. Categorical data were compared with the Fisher exact test. The p values <0.05 were considered statistically significant.

RESULTS

A total of 27 patients were recruited to the study. Three patients were withdrawn from subsequent analysis for technical reasons. Patient demographic data are summarized in Table 1. There were no statistically significant differences between the groups, although patients in the GLP-1 group trended toward having increased mean pulmonary artery pressure compared with the control group. Baseline hemodynamic data were broadly similar between groups. However, there was a trend toward increased Tau ($p = 0.06$) and reduced stroke work ($p = 0.06$) in the GLP-1 group.

TABLE 2 RV Hemodynamic Data at All Study Time Points

	BL1	BO1	p Value (vs. BL1)	1-min	p Value (vs. BL1)	BL2	p Value (vs. BL1)	BO2	p Value (vs. BO1)
Control group									
Heart rate, beats/min	62 ± 12	58 ± 11	0.17	61 ± 12	0.08	62 ± 10	0.47	59 ± 10	0.28
Stroke work, mm Hg/ml	1,377 ± 575	742 ± 355	<0.01	1,351 ± 688	0.29	954 ± 381	<0.01	745 ± 216	0.94
Cardiac output, l/min	5.3 ± 1.0	3.6 ± 0.8	<0.01	5.0 ± 1.1	0.06	4.6 ± 1.2	0.03	4.1 ± 0.9	0.42
Stroke volume, ml	85.9 ± 17.7	62.6 ± 13.1	<0.001	82.1 ± 17.8	0.28	75.8 ± 17.2	0.06	67.0 ± 16.5	0.48
ESP, mm Hg	28.5 ± 8.7	28.0 ± 9.3	0.58	27.2 ± 12.3	0.57	29.2 ± 11.7	0.54	29.5 ± 9.5	0.03
EDP, mm Hg	7.6 ± 3.9	9.6 ± 4.0	<0.001	7.5 ± 4.2	0.03	9.0 ± 3.3	<0.01	10.8 ± 4.1	0.06
ESV, ml	104.7 ± 40.8	116.6 ± 31.7	0.18	87.5 ± 39.9	0.14	123.9 ± 43.5	0.05	130.8 ± 43.2	0.01
EDV, ml	146.8 ± 40.2	145.8 ± 27.3	0.80	130.3 ± 33.2	0.19	161.0 ± 37.9	0.25	163.6 ± 42.5	0.03
Ejection fraction, %	57.7 ± 11.5	44.3 ± 13.0	<0.01	59.8 ± 18.9	0.08	48.5 ± 10.2	<0.01	43.9 ± 13.6	0.30
dP/dt_{max}, mm Hg/s	360 ± 78	297 ± 90	<0.01	411 ± 144	<0.01	326 ± 85	<0.01	276 ± 86	0.01
dP/dt_{min}, mm Hg/s	−260 ± 91	−192 ± 76	<0.01	−235 ± 105	0.44	−230 ± 97	<0.01	−192 ± 87	0.99
Tau, ms	55.8 ± 13.4	108.2 ± 43.3	<0.001	69.3 ± 27.5	0.02	72.9 ± 14.0	<0.001	106.0 ± 29.6	0.77
Ea, mm Hg/ml	0.34 ± 0.10	0.50 ± 0.19	0.01	0.32 ± 0.14	0.85	0.41 ± 0.20	0.10	0.47 ± 0.19	0.74
GLP-1 group									
Heart rate, beats/min	62 ± 10	60 ± 8	0.41	63 ± 8	0.71	60 ± 9	0.19	60 ± 7	0.77
Stroke work, mm Hg/ml	1,001 ± 381	878 ± 378	0.14	852 ± 406	0.12	860 ± 374	0.31	787 ± 369	0.18
Cardiac output, l/min	4.9 ± 0.6	4.1 ± 0.8	<0.01	4.4 ± 0.9	0.26	4.3 ± 1.3	0.16	4.1 ± 1.0	0.52
Stroke volume, ml	81.5 ± 18.5	68.3 ± 16.4	0.04	72.2 ± 20.7	0.28	73.9 ± 24.8	0.22	69.1 ± 19.5	0.54
ESP, mm Hg	24.5 ± 7.2	25.7 ± 8.8	0.26	26.5 ± 8.1	0.06	26.3 ± 5.4	0.05	27.1 ± 6.9	0.24
EDP, mm Hg	8.6 ± 3.6	10.2 ± 4.3	0.04	9.8 ± 3.9	0.04	9.7 ± 3.4	0.08	10.4 ± 3.9	0.34
ESV, ml	81.1 ± 43.4	83.9 ± 41.1	0.41	77.0 ± 46.1	0.59	83.2 ± 30.8	0.08	91.6 ± 42.1	0.04
EDV, ml	118.8 ± 50.3	120.7 ± 48.8	0.74	120.9 ± 44.5	0.79	136.3 ± 54.6	0.15	132.0 ± 48.4	0.11
Ejection fraction, %	61.7 ± 13.1	53.4 ± 10.4	0.01	60.8 ± 16.5	0.92	55.9 ± 12.3	0.04	54.9 ± 13.8	0.87
dP/dt_{max}, mm Hg/s	368 ± 115	307 ± 86	0.05	346 ± 89	0.50	313 ± 76	0.02	295 ± 73	0.59
dP/dt_{min}, mm Hg/s	−246 ± 49	−219 ± 67	0.05	−238 ± 57	0.25	−240 ± 39	0.84	−216 ± 59	0.92
Tau, ms	67.8 ± 21.0	96.5 ± 41.3	0.01	87.4 ± 31.8	<0.01	79.6 ± 22.3	<0.01	99.5 ± 33.9	0.32
Ea, mm Hg/ml	0.33 ± 0.15	0.39 ± 0.23	0.06	0.41 ± 0.24	0.07	0.41 ± 0.21	0.01	0.45 ± 0.29	0.05

Values are mean ± SD.

1-min = 1-minute recovery; BL1 = baseline; BL2 = 30-min recovery; BO1 = first balloon occlusion; BO2 = second balloon occlusion; ESP = end-systolic pressure; EDP = end-diastolic pressure; ESV = end-systolic volume; EDV = end-diastolic volume; other abbreviations as in Table 1.

EFFECT OF REPEATED CORONARY BALLOON OCCLUSION ON RV FUNCTION. Occlusion of the RCA was associated with deterioration of systolic and diastolic function compared with baseline (BL1). At the end of the first balloon occlusion (BO1), stroke volume, ejection fraction, and dP/dt_{max} were significantly reduced, with Tau and EDP increased (Table 2). Systolic function improved modestly after 1 min of reperfusion, and only dP/dt_{max} improved to above baseline function. Similarly, there were modest improvements in diastolic function at the 1-min recovery, but Tau was still significantly impaired compared with baseline. At 30-min recovery (BL2), there was numerical improvement compared with BO1 in most measures of systolic and diastolic function, with stroke volume ($p = 0.08$), dP/dt_{max} ($p = 0.07$), and dP/dt_{min} ($p = 0.09$) trending toward improvement, and a statistically significant improvement in Tau ($p < 0.01$). Nonetheless, most measures remained impaired compared with BL1 (cardiac output, stroke work, ejection fraction, dP/dt_{max}, dP/dt_{min}, EDP, and Tau), suggesting that there was stunning of the right ventricle at the 30-min recovery. Further balloon occlusion (BO2) was associated with impairment of the right ventricle, but only dP/dt_{max} ($p = 0.01$) showed significant impairment of function compared with BO1, consistent with cumulative ischemic RV dysfunction.

EFFECT OF GLP-1 ON RV FUNCTION DURING BALLOON OCCLUSION. The change in parameters of RV function in the GLP-1 group was similar to those of the saline control group, with systolic and diastolic dysfunction after BO1 (before starting the GLP-1 infusion), stunning, and cumulative ischemic RV dysfunction observed (Table 2). There was no significant difference in any marker of systolic or diastolic function between the saline and GLP-1 groups at

FIGURE 3 Serial RV Hemodynamic Data

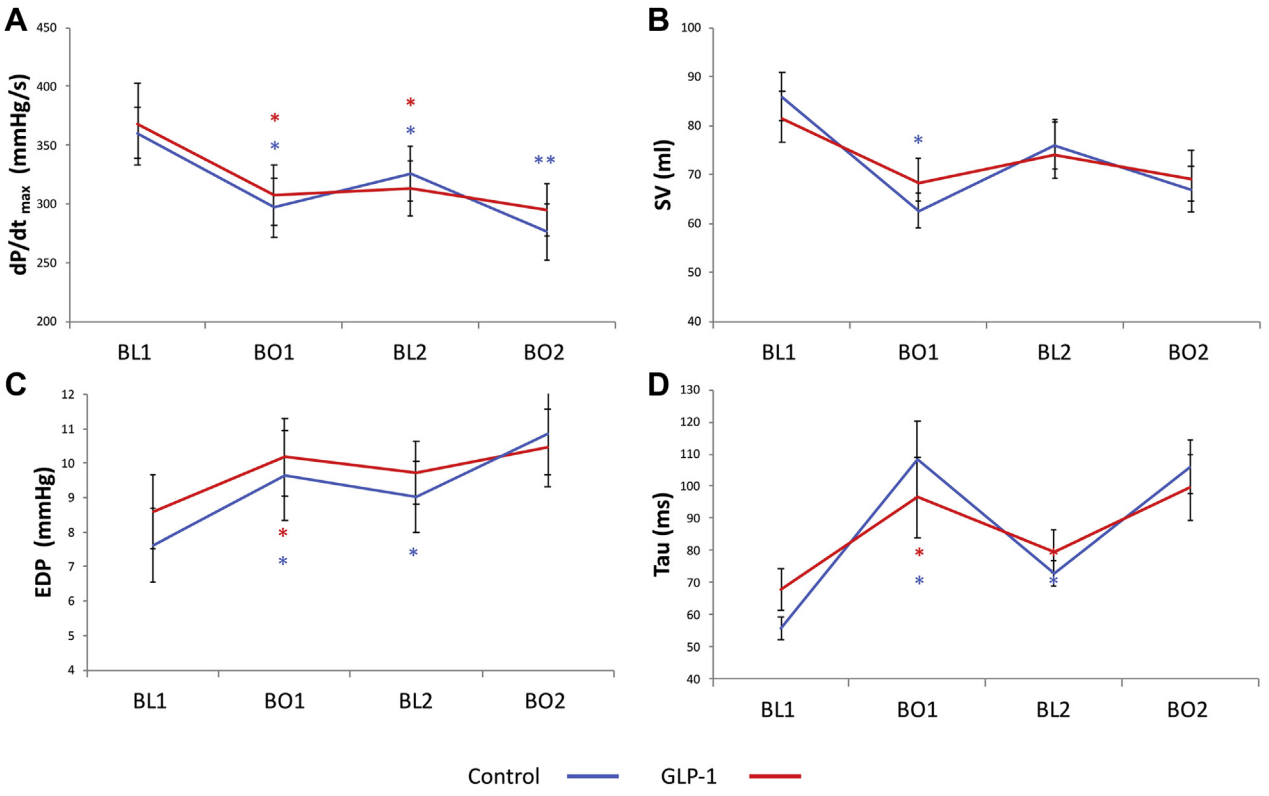

BO1 caused significant reduction in the **(A)** maximum rate of isovolumic contraction (dP/dt_{max}) and **(B)** stroke volume (SV) and **(C)** increases in end-diastolic pressure (EDP) and **(D)** the time constant of diastolic relaxation (Tau). *$p < 0.05$ versus BL1. Cumulative ischemic dysfunction measured according to dP/dt_{max} after a second balloon occlusion was observed. **$p < 0.05$ versus BO1. There was no significant difference in any right ventricular index between GLP-1 and control saline. Mean ± SEM. Compared by using Student's *t*-test. GLP-1, n = 11; control, n = 13. Abbreviations as in Figure 1.

either 30-min recovery or the second balloon occlusion (Figure 3).

BIOCHEMISTRY. Figure 4 shows that GLP-1 levels rose in the GLP-1–infused arm while remaining unchanged in the control arm. GLP-1 was metabolically active, causing a significant rise in insulin levels and a fall in plasma glucose levels. There was a small, but significant, drop in insulin levels in the control group. This reduction may represent the fasted nature of the cohort. However, there were no hypoglycemic episodes recorded during the study. Plasma free fatty acids rose in both groups as a result of the administration of unfractionated heparin required for the procedure (36), but there were no significant differences in free fatty acid levels between the groups.

IMMUNOHISTOCHEMISTRY. Antibody staining of human RV and LV tissue confirmed patchy mAb 3F52 binding to cardiomyocytes, indicating the presence of the GLP-1R in both ventricles (Figure 5).

DISCUSSION

To the best of our knowledge this study is the first, to assess the effect of GLP-1 on RV function using the conductance technique in humans during supply ischemia precipitated by repeat coronary balloon occlusion. RCA occlusion was associated with marked deterioration in systolic and diastolic measures of RV function. There was rapid RV recovery of some indices at 1 min, although residual stunning was observed at 30 min. Further occlusion was associated with cumulative RV dysfunction in some indices. GLP-1 did not abrogate myocardial stunning or ischemic RV dysfunction.

Ischemic LV dysfunction and stunning after transient coronary balloon occlusion have been reported

FIGURE 4 Serial Biochemical Data

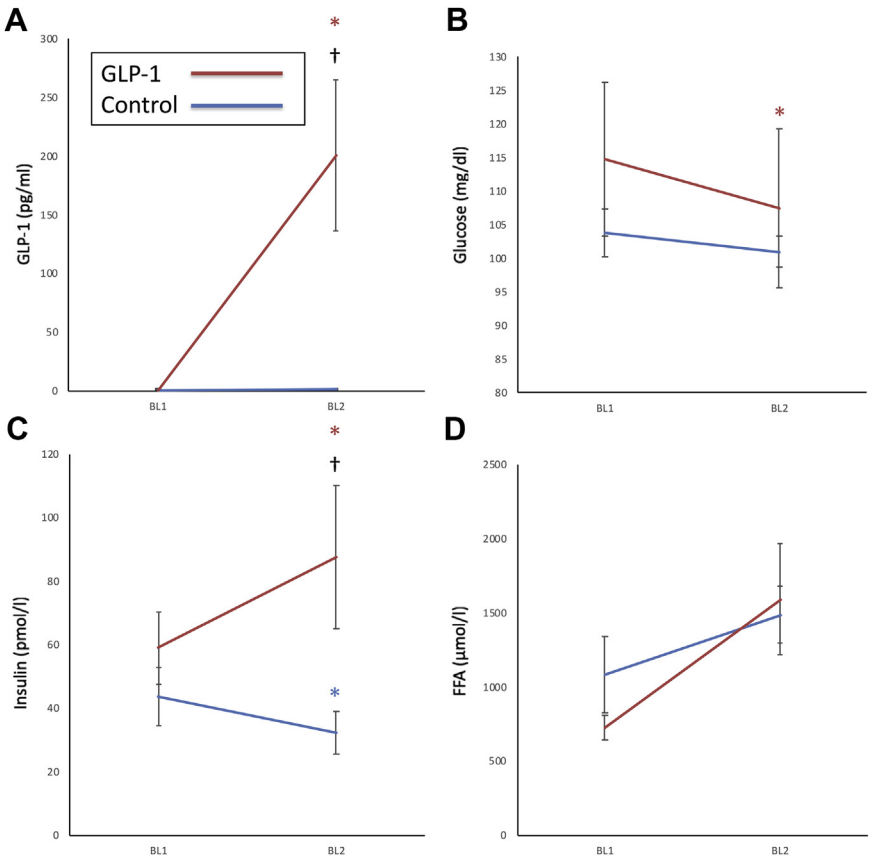

Comparison of change in plasma levels of **(A)** GLP-1 (7 to 36) amide, **(B)** glucose, **(C)** insulin, and **(D)** free fatty acids (FFA). Mean ± SEM. Compared by using Student's *t*-test. GLP-1, n = 11; control, n = 13. *p < 0.05 versus, BL1, †p < 0.05 versus control. Abbreviations as in Figure 1.

previously by our group (11-13). Transient supra-baseline improvement in systolic performance occurs during early reperfusion due to reactive hyperemia, causing increased coronary flow that augments LV function through a phenomenon known as the Gregg effect (37). Increased volume of the microvasculature after reperfusion causes stretch-activated calcium channels to open. The resultant influx of calcium increases myocyte contractility and briefly masks the effect of ischemic LV dysfunction, despite the presence of stunning (38). Stunning is revealed when the reactive hyperemia subsides.

In the present study, the magnitude of the effect of coronary balloon occlusion and reperfusion on RV function was blunted compared with studies investigating the left ventricle. This difference may be explained by: 1) the comparatively low myocardial mass of the right ventricle; 2) reduced ischemic burden during RCA occlusion; 3) the conduit nature of the right ventricle as a volume pump; and 4) because up to 50% of RV function is derived from the left ventricle, through a shared septum and ventricular interdependence. Nevertheless, in contrast to previous studies (6), we assessed the prolonged recovery of the right ventricle from transient supply ischemia. We confirmed that, like the left ventricle, when reactive hyperemia subsides, RV stunning is discernible and cumulative RV dysfunction can be observed.

GLP-1 abrogates LV stunning and cumulative ischemic dysfunction during both supply (coronary artery occlusion) and demand (dobutamine stress) ischemia, in a consistent manner (11,13,39). The absence of a cardioprotective effect in the right

FIGURE 5 Immunohistochemistry Sections Labeling the GLP-1R With and Without mAb 3F52 Antibody

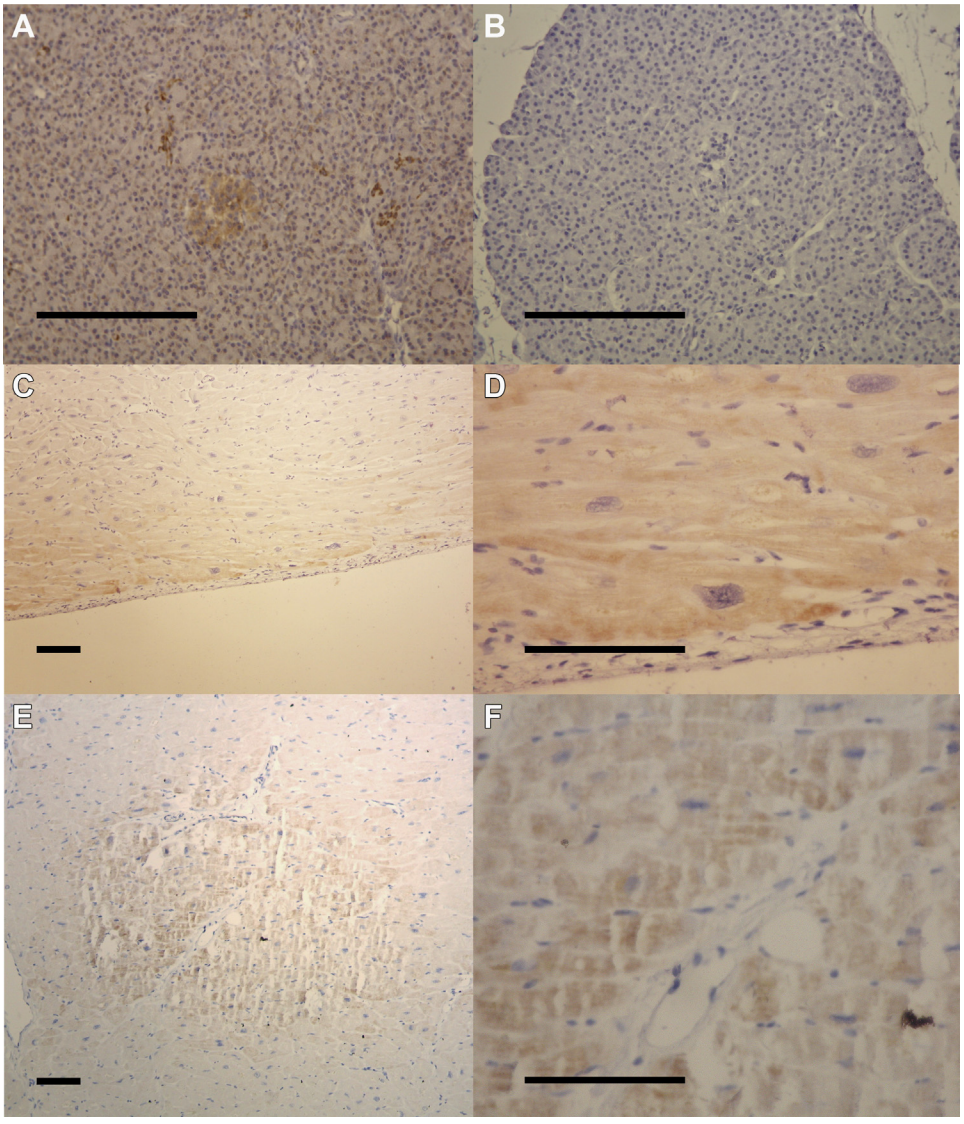

(A) Pancreatic tissue, high-power (60×), positive control with monoclonal 3F52 antibody, showing moderate widespread staining for glucagon-like peptide 1 receptor (GLP-1R) with high staining in beta cells. **(B)** Pancreatic tissue, negative control without mAb 3F52 antibody, high power (60×), confirming no staining. Right ventricular sections from an explanted heart with ischemic heart disease, **(C)** low power and **(D)** high power (60×), confirming staining with mAb 3F52 for GLP-1R in right ventricular tissue. Matched left ventricular sections, **(E)** low power and **(F)** high power (60×), confirming staining with mAb 3F52 for GLP-1R in the left ventricle. Scale is 100 μm in all images.

ventricle is surprising, particularly as we have confirmed that GLP-1 levels were significantly augmented in our study and that the GLP-1R is expressed on RV myocytes. This finding is consistent with other recently published data showing the presence of GLP-1R messenger ribonucleic acid in all 4 chambers of the heart (40). The absence of protective effect may again be explained by the reduced mass of the right ventricle. Although GLP-1 still binds to cardiomyocytes in the right ventricle, the effect size could be too small to be detected clinically by the conductance catheter. Furthermore, the reduced myocardial mass of the right ventricle may prevent the detection of cardioprotection by GLP-1 in this thinner walled ventricle. The GLP-1R appears to be expressed in the same density as in the left ventricle,

although we have not been able to accurately quantify receptor density for comparison in this study. It is possible that although GLP-1 binds the receptor in the right ventricle, this action does not affect the RV cardiomyocytes in the same fashion as in the left ventricle. The presence of persistent RV impairment after PCI to the RCA is pertinent to clinical practice.

Our findings may be especially relevant in patients with limited RV functional reserve, in whom hemodynamic instability after PCI is a particular risk. Minimizing the duration of coronary balloon occlusion during PCI in this subset of patients could reduce the risk of hemodynamic compromise. From a translational perspective, GLP-1 and GLP-1R agonists remain potential therapeutic agents for those with acute hemodynamic disturbance related to myocardial ischemia. Pilot studies have shown that GLP-1R agonists reduce the need for inotropic support for critically ill patients (41,42). However, our data suggest that, although GLP-1 may be a possible therapy for ischemic LV dysfunction, GLP-1 is not likely to be a useful therapy for reducing ischemic RV dysfunction.

STUDY LIMITATIONS. The 30-min recovery period was chosen for ethical and practical reasons. Longer follow-up to show that parameters eventually returned to baseline values would be desirable to confirm the reversible nature of RV stunning. Similarly, we did not directly confirm coronary flow normalization required to fulfill the definition of stunning. However, we and others have confirmed recovery of basal flow velocity within this time frame in the left coronary artery (8). The myocardial bed subtended by the RCA is smaller, and therefore, a priori, the ischemic insult after RCA occlusion is less and subsequent reactive hyperemia in response shorter than that seen after left coronary artery occlusion. Despite recruiting patients with proximal stenoses in dominant RCAs, we did not confirm the degree of ischemic insult by using another modality (e.g., serum lactate). It is possible that the 2 groups had different ischemic burdens that masked any difference being observed in the GLP-1 group.

The right ventricle is a challenging chamber to assess in all imaging modalities. For RV conductance studies, its thin wall increases parallel conductance, whereas its eccentric shape means that volume assessment is less amenable to simple geometric modeling than the conical left ventricle. Nonetheless, a number of studies have shown that RV conductance studies provide accurate assessment of the right ventricle (6,26,27).

Patients in the present study were not randomized to treatment. However, all eligible patients were consecutively recruited into the study from the elective PCI waiting list compiled independently from the clinicians involved in the study. The endpoint data were objective empiric hemodynamic data and not influenced by knowledge of the allocation and techniques employed were familiar to the operators, minimizing the risk of a "learning curve" on the results. GLP-1 protects against ischemic left ventricular dysfunction. There was a nonsignificant difference in the baseline characteristics of the 2 groups that was unexpected and may have disadvantaged the GLP-1 group and prevented small improvements in RV dysfunction being observed after GLP-1 compared with control subjects. However, patients also acted as their own control with serial BO, and we believe a neutral effect of GLP-1 on the right ventricle is likely.

CONCLUSIONS

Stunning and cumulative ischemic RV dysfunction was observed after RCA balloon occlusion in human subjects. This scenario may contribute to hemodynamic instability in patients with limited RV reserve. GLP-1 infusion did not attenuate this ischemic RV dysfunction.

ACKNOWLEDGMENTS The authors thank the staff in the cardiac catheter laboratory at Royal Papworth Hospital for their assistance and thank the patients for participating in this study.

ADDRESS FOR CORRESPONDENCE: Dr. Stephen P. Hoole, Department of Interventional Cardiology, Royal Papworth Hospital, Lakeside Cres, Papworth Everard, Cambridge CB23 3RE, United Kingdom. E-mail: s.hoole@nhs.net.

PERSPECTIVES

COMPETENCY IN MEDICAL KNOWLEDGE: Animal studies have shown that GLP-1 protects against lethal ischemia-reperfusion injury. Human studies have shown that GLP-1 protects against ischemic left ventricular dysfunction. This translational study found that stunning and cumulative dysfunction occur in the right ventricle but that GLP-1 does not abrogate this action. These findings may be of clinical relevance to a subset of patients with limited RV reserve during PCI.

TRANSLATIONAL OUTLOOK: Additional research is needed to address the mechanisms behind GLP-1 cardioprotection in the left ventricle and whether GLP-1 also protects against lethal ischemia-reperfusion injury in humans.

REFERENCES

1. Haddad F, Hunt SA, Rosenthal DN, Murphy DJ. Right ventricular function in cardiovascular disease, part I: anatomy, physiology, aging, and functional assessment of the right ventricle. Circulation 2008;117:1436–48.

2. O'Rourke RA, Dell'Italia LJ. Diagnosis and management of right ventricular myocardial infarction. Curr Probl Cardiol 2004;29:6–47.

3. de Groote P, Millaire A, Foucher-Hossein C, et al. Right ventricular ejection fraction is an independent predictor of survival in patients with moderate heart failure. J Am Coll Cardiol 1998;32:948–54.

4. Farrer-Brown G. Vascular pattern of myocardium of right ventricle of human heart. Br Heart J 1968;30:679–86.

5. Haupt HM, Hutchins GM, Moore GW. Right ventricular infarction: role of the moderator band artery in determining infarct size. Circulation 1983;67:1268–72.

6. Bishop A, White P, Groves P, et al. Right ventricular dysfunction during coronary artery occlusion: pressure-volume analysis using conductance catheters during coronary angioplasty. Heart 1997;78:480–7.

7. Axell RG, Giblett JP, White PA, et al. Stunning and right ventricular dysfunction is induced by coronary balloon occlusion and rapid pacing in humans: insights from right ventricular conductance catheter studies. J Am Heart Assoc 2017;6.

8. Hoole SP, Heck PM, White PA, et al. Stunning and cumulative left ventricular dysfunction occurs late after coronary balloon occlusion in humans insights from simultaneous coronary and left ventricular hemodynamic assessment. J Am Coll Cardiol Intv 2010;3:412–8.

9. Marso SP, Daniels GH, Brown-Frandsen K, et al. Liraglutide and cardiovascular outcomes in type 2 diabetes. N Engl J Med 2016;375:311–22.

10. Marso SP, Bain SC, Consoli A, et al. Semaglutide and cardiovascular outcomes in patients with type 2 diabetes. N Engl J Med 2016;375:1834–44.

11. Read PA, Hoole SP, White PA, et al. A pilot study to assess whether glucagon-like peptide-1 protects the heart from ischemic dysfunction and attenuates stunning after coronary balloon occlusion in humans. Circ Cardiovasc Interv 2011;4:266–72.

12. McCormick LM, Hoole SP, White PA, et al. Pretreatment with glucagon-like peptide-1 protects against ischemic left ventricular dysfunction and stunning without a detected difference in myocardial substrate utilization. J Am Coll Cardiol Intv 2015;8:292–301.

13. Giblett JP, Axell RG, White PA, et al. Glucagon-like peptide-1 derived cardioprotection does not utilize a KATP-channel dependent pathway: mechanistic insights from human supply and demand ischemia studies. Cardiovasc Diabetol 2016;15:99.

14. Bose AK, Mocanu MM, Carr RD, Brand CL, Yellon DM. Glucagon-like peptide 1 can directly protect the heart against ischemia/reperfusion injury. Diabetes 2005;54:146–51.

15. Bose AK, Mocanu MM, Carr RD, Yellon DM. Glucagon like peptide-1 is protective against myocardial ischemia/reperfusion injury when given either as a preconditioning mimetic or at reperfusion in an isolated rat heart model. Cardiovasc Drugs Ther 2005;19:9–11.

16. Bose AK, Mocanu MM, Carr RD, Yellon DM. Myocardial ischaemia-reperfusion injury is attenuated by intact glucagon like peptide-1 (GLP-1) in the in vitro rat heart and may involve the p70s6K pathway. Cardiovasc Drugs Ther 2007;21:253–6.

17. Nikolaidis LA, Elahi D, Shen YT, Shannon RP. Active metabolite of GLP-1 mediates myocardial glucose uptake and improves left ventricular performance in conscious dogs with dilated cardiomyopathy. Am J Physiol Heart Circ Physiol 2005;289:H2401–8.

18. Kavianipour M, Ehlers MR, Malmberg K, et al. Glucagon-like peptide-1 (7-36) amide prevents the accumulation of pyruvate and lactate in the ischemic and non-ischemic porcine myocardium. Peptides 2003;24:569–78.

19. Hausenloy DJ, Whittington HJ, Wynne AM, et al. Dipeptidyl peptidase-4 inhibitors and GLP-1 reduce myocardial infarct size in a glucose-dependent manner. Cardiovasc Diabetol 2013;12:154.

20. Bao W, Aravindhan K, Alsaid H, et al. Albiglutide, a long lasting glucagon-like peptide-1 analog, protects the rat heart against ischemia/reperfusion injury: evidence for improving cardiac metabolic efficiency. PLoS One 2011;6:e23570.

21. Aravindhan K, Bao W, Harpel MR, Willette RN, Lepore JJ, Jucker BM. Cardioprotection resulting from glucagon-like peptide-1 administration involves shifting metabolic substrate utilization to increase energy efficiency in the rat heart. PLoS One 2015;10:e0130894.

22. Halbirk M, Norrelund H, Moller N, et al. Cardiovascular and metabolic effects of 48-h glucagon-like peptide-1 infusion in compensated chronic patients with heart failure. Am J Physiol Heart Circ Physiol 2010;298:H1096–102.

23. Gejl M, Lerche S, Mengel A, et al. Influence of GLP-1 on myocardial glucose metabolism in healthy men during normo- or hypoglycemia. PLoS One 2014;9:e83758.

24. Clarke SJ, Giblett JP, Yang LL, et al. GLP-1 is a coronary artery vasodilator in humans. J Am Heart Assoc 2018;7:e010321.

25. Axell RG, Hoole SP, Hampton-Till J, White PA. RV diastolic dysfunction: time to re-evaluate its importance in heart failure. Heart Fail Rev 2015;20:363–73.

26. Bishop A, White P, Chaturvedi R, Brookes C, Redington A, Oldershaw P. Resting right ventricular function in patients with coronary artery disease: pressure volume analysis using conductance catheters. Int J Cardiol 1997;58:223–8.

27. White PA, Bishop AJ, Conroy B, Oldershaw PJ, Redington AN. The determination of volume of right ventricular casts using a conductance catheter. Eur Heart J 1995;16:1425–9.

28. Aguero J, Ishikawa K, Hadri L, et al. Intratracheal gene delivery of SERCA2a ameliorates chronic post-capillary pulmonary hypertension: a large animal model. J Am Coll Cardiol 2016;67:2032–46.

29. Baan J, van der Velde ET, de Bruin HG, et al. Continuous measurement of left ventricular volume in animals and humans by conductance catheter. Circulation 1984;70:812–23.

30. McKay RG, Spears JR, Aroesty JM, et al. Instantaneous measurement of left and right ventricular stroke volume and pressure-volume relationships with an impedance catheter. Circulation 1984;69:703–10.

31. McCabe C, White PA, Hoole SP, et al. Right ventricular dysfunction in chronic thromboembolic obstruction of the pulmonary artery: a pressure-volume study using the conductance catheter. J Applied Physiol 2014;116:355–63.

32. Weiss JL, Frederiksen JW, Weisfeldt ML. Hemodynamic determinants of the time-course of fall in canine left ventricular pressure. J Clin Invest 1976;58:751–60.

33. Raff GL, Glantz SA. Volume loading slows left ventricular isovolumic relaxation rate. Evidence of load-dependent relaxation in the intact dog heart. Circulation Res 1981;48:813–24.

34. Matsubara H, Takaki M, Yasuhara S, Araki J, Suga H. Logistic time constant of isovolumic relaxation pressure-time curve in the canine left ventricle. Better alternative to exponential time constant. Circulation 1995;92:2318–26.

35. Pyke C, Heller RS, Kirk RK, et al. GLP-1 receptor localization in monkey and human tissue: novel distribution revealed with extensively validated monoclonal antibody. Endocrinology 2014;155:1280–90.

36. Nelson PG. Effect of heparin on serum free-fatty-acids, plasma catecholamines, and the incidence of arrhythmias following acute myocardial infarction. Br Med J 1970;3:735–7.

37. Gregg DE. Effect of coronary perfusion pressure or coronary flow on oxygen usage of the myocardium. Circ Res 1963;13:497–500.

38. Stahl LD, Aversano TR, Becker LC. Selective enhancement of function of stunned myocardium by increased flow. Circulation 1986;74:843–51.

39. Read PA, Khan FZ, Heck PM, Hoole SP, Dutka DP. DPP-4 inhibition by sitagliptin improves the myocardial response to dobutamine stress and mitigates stunning in a pilot study of patients with

coronary artery disease. Circ Cardiovasc Imaging 2010;3:195–201.

40. Baggio LL, Yusta B, Mulvihill EE, et al. GLP-1 receptor expression within the human heart. Endocrinology 2018;159:1570–84.

41. Galiatsatos P, Gibson BR, Rabiee A, et al. The glucoregulatory benefits of glucagon-like peptide-1 (7-36) amide infusion during intensive insulin therapy in critically ill surgical patients: a pilot study. Crit Care Med 2014;42:638–45.

42. Sokos GG, Bolukoglu H, German J, et al. Effect of glucagon-like peptide-1 (GLP-1) on glycemic control and left ventricular function in patients undergoing coronary artery bypass grafting. Am J Cardiol 2007;100:824–9.

KEY WORDS cardioprotection, glucagon-like peptide-1, ischemia-reperfusion injury, right ventricle

JACC: BASIC TO TRANSLATIONAL SCIENCE VOL. 4, NO. 2, 2019
© 2019 THE AUTHORS. PUBLISHED BY ELSEVIER ON BEHALF OF THE AMERICAN COLLEGE OF CARDIOLOGY FOUNDATION. THIS IS AN OPEN ACCESS ARTICLE UNDER THE CC BY-NC-ND LICENSE (http://creativecommons.org/licenses/by-nc-nd/4.0/).

PRECLINICAL RESEARCH

Cardiac Nuclear High-Mobility Group Box 1 Ameliorates Pathological Cardiac Hypertrophy by Inhibiting DNA Damage Response

Tetsuya Takahashi, MD,[a] Tetsuro Shishido, MD, PHD,[a] Daisuke Kinoshita, MD, PHD,[a] Ken Watanabe, MD,[a] Taku Toshima, MD,[a] Takayuki Sugai, MD,[a] Taro Narumi, MD, PHD,[a] Yoichiro Otaki, MD, PHD,[a] Harutoshi Tamura, MD, PHD,[a] Satoshi Nishiyama, MD, PHD,[a] Takanori Arimoto, MD, PHD,[a] Hiroki Takahashi, MD, PHD,[a] Takuya Miyamoto, MD, PHD,[a] Tetsu Watanabe, MD, PHD,[a] Chang-Hoon Woo, DVM, PHD,[b] Jun-ichi Abe, MD, PHD,[c] Yasuchika Takeishi, MD, PHD,[d] Isao Kubota, MD, PHD,[a] Masafumi Watanabe, MD, PHD[a]

VISUAL ABSTRACT

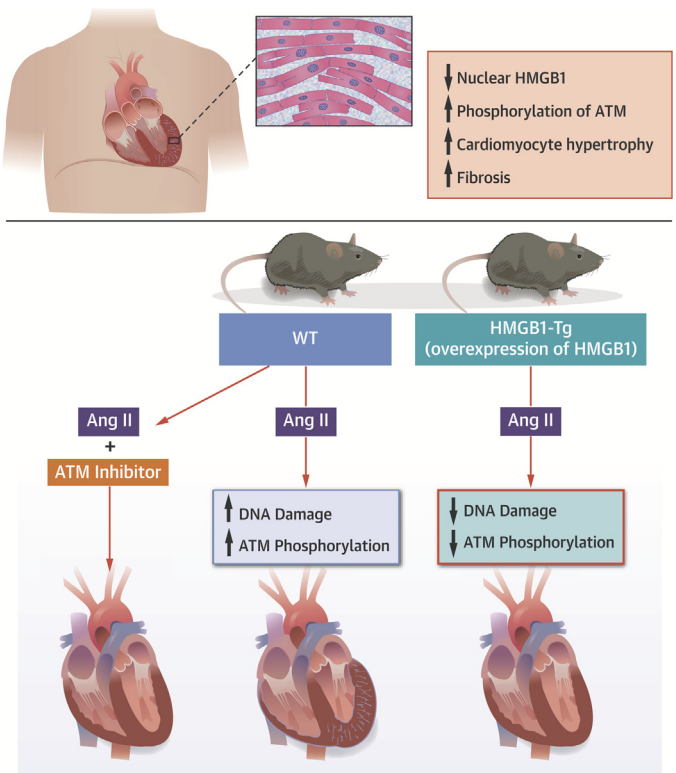

Takahashi, T. et al. J Am Coll Cardiol Basic Trans Science. 2019;4(2):234–47.

HIGHLIGHTS

- **HMGB1 is a DNA-binding protein associated with nuclear homeostasis and DNA repair.**
- **Decreased nuclear HMGB1 expression is observed in human failing hearts, which is associated with cardiomyocyte hypertrophy and fibrosis.**
- **Cardiac nuclear HMGB1 overexpression ameliorates Ang II–induced pathological cardiac remodeling by inhibiting cardiomyocyte DNA damage and following ataxia telangiectasia mutated activation in mice.**
- **Ataxia telangiectasia mutated inhibitor treatment provided a cardioprotective effect on Ang II–induced cardiac remodeling in mice.**

From the [a]Department of Cardiology, Pulmonology, and Nephrology, Yamagata University School of Medicine, Yamagata, Japan; [b]Department of Pharmacology, College of Medicine, Yeungnam University, Daegu, Republic of Korea; [c]Department of Cardiology - Research, Division of Internal Medicine, University of Texas MD Anderson Cancer Center, Houston, Texas; and the [d]Department of Cardiology and Hematology, Fukushima Medical University, Fukushima, Japan. This study was supported in part by a Grant-in-Aid

ISSN 2452-302X https://doi.org/10.1016/j.jacbts.2018.11.011

SUMMARY

High-mobility group box 1 (HMGB1) is a deoxyribonucleic acid (DNA)–binding protein associated with DNA repair. Decreased nuclear HMGB1 expression and increased DNA damage response (DDR) were observed in human failing hearts. DNA damage and DDR as well as cardiac remodeling were suppressed in cardiac-specific HMGB1 overexpression transgenic mice after angiotensin II stimulation as compared with wild-type mice. In vitro, inhibition of HMGB1 increased phosphorylation of extracellular signal-related kinase 1/2 and nuclear factor kappa B, which was rescued by DDR inhibitor treatment. DDR inhibitor treatment provided a cardioprotective effect on angiotensin II–induced cardiac remodeling in mice. (J Am Coll Cardiol Basic Trans Science 2019;4:234–47) © 2019 The Authors. Published by Elsevier on behalf of the American College of Cardiology Foundation. This is an open access article under the CC BY-NC-ND license (http://creativecommons.org/licenses/by-nc-nd/4.0/).

Heart failure is a common disease and has been increasing worldwide (1,2). Despite advances in the treatment of heart failure, patients with heart failure are faced with a poor prognosis (3). Cardiac remodeling, characterized by cardiac hypertrophy and fibrosis, is closely associated with the development of heart failure and death (4,5). It is well known that neurohumoral activation such as angiotensin II (Ang II) is one of the major risk factors for pathological cardiac remodeling and subsequent heart failure (6). However, treatment that is able to sufficiently suppress pathological cardiac remodeling has not been established yet.

SEE PAGE 248

High-mobility group box 1 (HMGB1) is an abundant chromatin-associated nuclear nonhistone binding protein, which has various functions in maintaining cellular homeostasis (7,8). HMGB1 translocates to extracellular from intracellular under various stress situations, and acts as a damage-associated molecular pattern (DAMP) that triggers several inflammatory responses (9,10). Extracellular HMGB1 was reported to cause cardiac hypertrophy and promote myocardial ischemia or reperfusion injury and inflammation (11–13). In contrast, intracellular HMGB1 plays roles in maintaining nucleosome structure, regulating gene transcription, replication, and DNA repair (7,8). Recently, it was reported that intracellular HMGB1 has a more important role in cell fate than extracellular HMGB1 during some inflammatory diseases since ablation of nuclear HMGB1 worsens disease condition (14–16). We previously reported that cardiac nuclear HMGB1 prevents cardiomyocyte deoxyribonucleic acid (DNA) damage in a pressure overload heart failure mouse model (17). However, the molecular mechanism underlying the antihypertrophic effect of cardiac nuclear HMGB1 has not been fully elucidated.

Various types of stress cause cellular DNA damage, and the DNA damage response (DDR) is induced immediately after DNA damage to repair it (18). Activation of the DDR occurs after excessive DNA damage and is reported to be observed in end-stage failing human hearts (19). Moreover, previous studies have revealed that DDR activation plays a crucial role in development of cardiac remodeling after myocardial infarction and cardiac hypertrophy (20,21).

We hypothesized that cardiac nuclear HMGB1 suppresses pathological cardiac remodeling through inhibition of DDR activation.

METHODS

A detailed description of all experimental procedures is provided in the Supplemental Appendix.

ABBREVIATIONS AND ACRONYMS

Ang II = angiotensin II
ANP = atrial natriuretic peptide
ATM = ataxia telangiectasia mutated
BNP = brain natriuretic peptide
CVF = collagen volume fraction
DAMP = damage-associated molecular pattern
DDR = deoxyribonucleic acid damage response
DNA = deoxyribonucleic acid
E/A ratio = ratio of early to atrial wave
ERK1/2 = extracellular signal-related kinase 1/2
HMGB1 = high-mobility group box 1
HMGB1-Tg = high-mobility group box 1 transgenic
HW/TL = heart weight to tibial length
IVSd = interventricular septum diameter
LVDd = left ventricular diastolic dimension
LVDs = left ventricular systolic dimension
MyD = cardiomyocyte diameter
NF-κB = nuclear factor kappa B
NRCM = neonatal rat cardiomyocyte
p-ATM = phosphorylation of ataxia telangiectasia mutated
PWd = posterior wall diameter
WT = wild-type

from the 21st Century of Excellence (COE) and Global COE program of the Japan Society for the Promotion of Science (No. F03), and a grant-in-aid for Scientific Research (18K08025, 18K08059, and 16K09490) from the Ministry of Education, Culture, Sports, Science, and Technology, Japan. The authors have reported that they have no relationships relevant to the contents of this paper to disclose.

All authors attest they are in compliance with human studies committees and animal welfare regulations of the authors' institutions and Food and Drug Administration guidelines, including patient consent where appropriate. For more information, visit the *JACC: Basic to Translational Science* author instructions page.

Manuscript received July 9, 2018; revised manuscript received October 19, 2018, accepted November 19, 2018.

HUMAN STUDIES. This study included 27 patients with heart failure and 5 control patients who were assessed to rule out cardiomyopathy and had normal cardiac function. Written informed consent was obtained from all patients before entry into the study. The protocol was performed in accordance to the Helsinki Declaration and was approved by the human investigations committee of our institution. Biopsy samples were immediately washed in phosphate-buffered saline before being snap-frozen in liquid nitrogen for immunofluorescent co-staining and biochemical measurements. Immunofluorescence was performed to evaluated the expressions of cardiac nuclear HMGB1, phosphorylation of ataxia telangiectasia mutated (p-ATM), and γ-H2AX in failing (n = 5) and normal human hearts (n = 5). The heart sections were stained with hematoxylin and eosin to assess cardiomyocyte diameter (MyD). The degree of collagen volume fraction (CVF) was assessed by Masson's trichrome staining as previously described (22). Blood samples were obtained to measure brain natriuretic peptide (BNP) levels. Correlations between nuclear HMGB1 levels and MyD, CVF, and serum BNP levels were assessed (n = 32).

ANIMAL MODELS. Cardiac hypertrophy was induced in 10- to 12-week-old mice with cardiac-specific overexpression of HMGB1 (HMGB1-Tg) and their wild-type (WT) littermates by chronic infusion of Ang II (1.5 mg/kg/day) or saline as previously described (23). For ATM inhibitor experiments, KU55933 (5 mg/kg) or vehicle was injected intraperitoneally to HMGB1-Tg mice at 2, 5, 8, and 11 days after Ang II infusion. After 2 weeks, blood pressure, cardiac function, and dimension were measured. The hearts were removed for examination of histological changes and biochemical analysis of various protein expression levels.

ECHOCARDIOGRAPHY DETERMINATION. Transthoracic echocardiography was performed before and after Ang II infusion under anesthesia as previously described (24). Left ventricular diastolic dimension (LVDd), left ventricular systolic dimension (LVDs), interventricular septum diameter (IVSd), posterior wall diameter (PWd), left ventricular fractional shortening (FS), and the transmitral Doppler velocity ratio of early to atrial wave (E/A ratio) were measured (n = 10 in WT saline group; n = 10 in WT Ang II group; n = 6 in HMGB1-Tg saline group; n = 6 in HMGB1-Tg Ang II group). As for ATM inhibitor experiments, the same parameters were also measured (n = 9 in WT vehicle group; n = 10 in WT Ang II + vehicle group; n = 6 in HMGB1-Tg Ang II + vehicle group; n = 6 in WT Ang II + KU55933 group; n = 6 in HMGB1-Tg Ang II + KU55933 group).

CELL CULTURE AND TREATMENT. Primary culture of neonatal rat cardiomyocytes (NRCMs) was performed as previously described (25,26). HMGB1 small interfering ribonucleic acid (siHMGB1), pcDNA-HMGB1 were transfected into NRCMs by using Lipofectamine 3000 Reagent (Invitrogen, Carlsbad, California) according to the manufacturer's instructions. After serum starvation for 24 h, cardiomyocytes were stimulated with 1-μM Ang II for 24 h to induce cardiac hypertrophy, and samples were collected to perform each experiment. For ATM inhibitor experiments, cardiomyocytes were pretreated with KU55933 (10 μM) for 1 h before Ang II stimulation.

STATISTICAL ANALYSIS. Data are presented as the mean ± SE. Statistical significance was evaluated using unpaired Student *t* test with Welch correction for comparing 2 groups. Comparing ≥3 groups were done using 1-way analysis of variance. Post hoc pairwise comparisons were done using the Tukey-Kramer method. Correlation between 2 variables was examined by using Pearson's product moment correlation coefficient. Because CVF and BNP were not normally distributed, we used $\log_{10}$ CVF and $\log_{10}$ BNP values in the Pearson correlation analysis. A value of $p < 0.05$ was considered statistically significant. All statistical analyses were performed using a standard statistical program package (JMP version 11, SAS Institute Inc., Cary, North Carolina).

RESULTS

EXPRESSION OF HMGB1 IN FAILING HUMAN HEARTS. We investigated the expression of nuclear HMGB1, DNA damage, and DDR in failing and normal human hearts. Immunofluorescence demonstrated that nuclear HMGB1 expression was significantly decreased and p-ATM expression was significantly increased in failing hearts compared with that of normal hearts (**Figures 1A to 1C**). γ-H2AX is known as an early and sensitive marker of DNA damage (27). The expression of γ-H2AX was also significantly increased in failing hearts compared with those of normal hearts (Supplemental Figures 1A to 1C). We evaluated the relationship among cardiomyocyte diameter, collagen volume fraction, serum BNP levels, and nuclear HMGB1 expression levels. A significant negative correlation was observed between nuclear HMGB1 levels and MyD, CVF, and BNP levels (**Figures 1D to 1F**).

THE PROTECTIVE EFFECT OF NUCLEAR HMGB1 ON PATHOLOGICAL CARDIAC REMODELING INDUCED BY ANG II. To investigate the potential role of nuclear HMGB1 in pathological cardiac remodeling, we subjected WT and HMGB1-Tg mice to Ang II

FIGURE 1 **Nuclear HMGB1 and p-ATM Expression in Failing Human Heart**

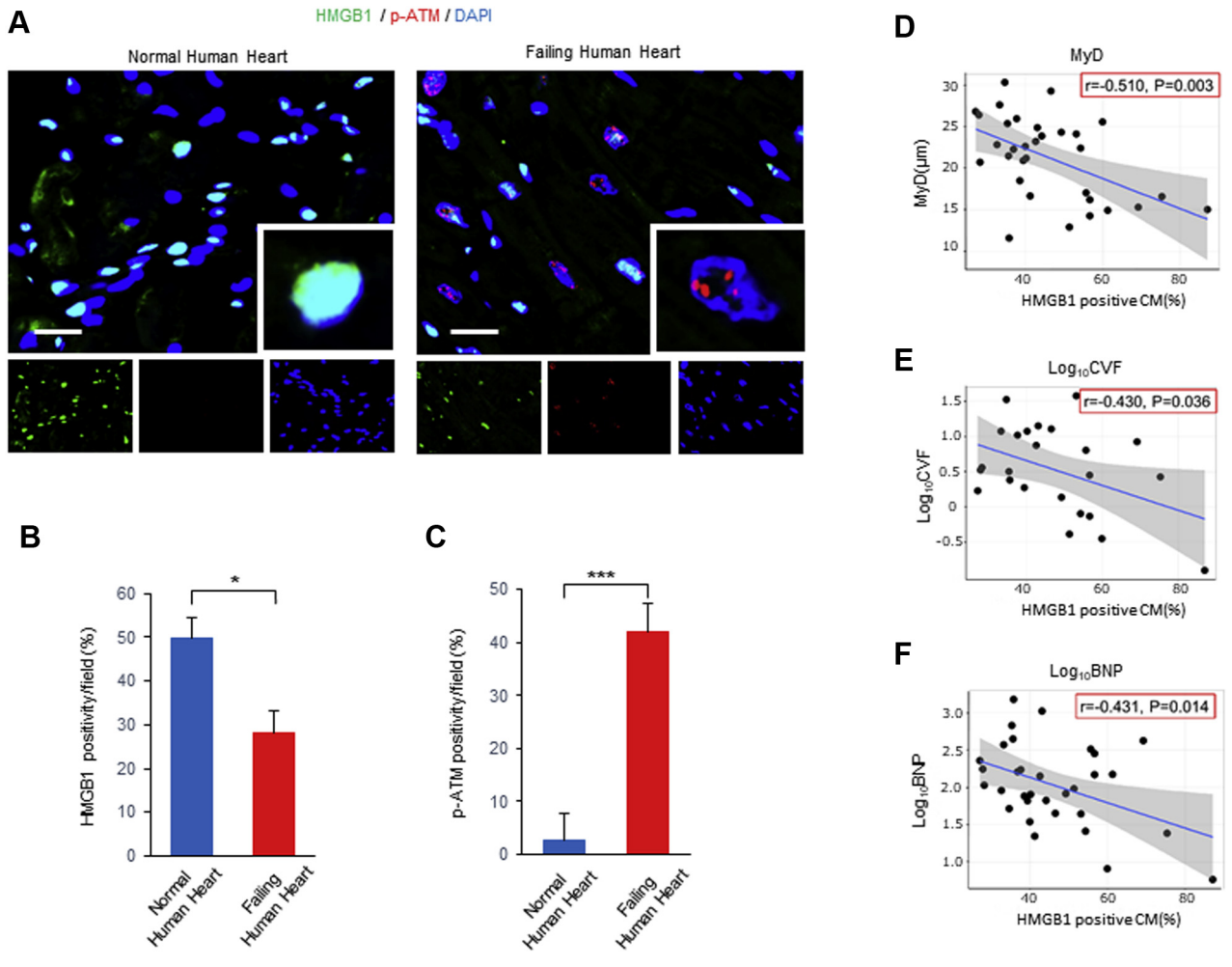

(A to C) Representative images and analysis of immunostaining of high-mobility group box 1 (HMGB1) **(green)**, phosphorylation of ataxia telangiectasia mutated (p-ATM) **(red)**, and DAPI **(blue)** in normal human hearts and failing human hearts. The number of HMGB1- and p-ATM-positive cardiomyocytes (CMs) per field was counted. Scale bars = 20 μm. Results are presented as the mean ± SE. (n = 5 per group). *$p < 0.05$; ***$p < 0.001$. **(D to F)** Negative correlation between nuclear HMGB1-positive CM and cardiomyocyte diameter (MyD), collagen volume fraction (CVF), or serum brain natriuretic peptide (BNP) levels (n = 32).

infusion for 2 weeks. After Ang II infusion, WT mice exhibited significant increases in the IVSd and PWd, whereas HMGB1-Tg mice showed a reduction in hypertrophic changes. There were no significant differences in the LVDd, LVDs, and FS between WT and HMGB1-Tg mice. The E/A ratio was significantly decreased in WT mice after Ang II infusion whereas the E/A ratio of HMGB1-Tg mice was attenuated (**Table 1**, Supplemental Figure 2).

There was no significant difference in blood pressure after Ang II infusion between WT and HMGB1-Tg mice (**Table 2**). Histological analysis with hematoxylin and eosin staining revealed that the cardiomyocyte hypertrophy induced by Ang II was significantly attenuated in the HMGB1-Tg mice compared with that of the WT mice (**Figures 2A and 2B**). Ang II infusion also resulted in an increase in the heart weight to tibial length (HW/TL) ratio in WT mice, whereas the increase in the HW/TL ratio was suppressed in HMGB1-Tg mice (**Figure 2C**). Masson's trichrome staining also demonstrated that HMGB1-Tg mice showed less fibrosis after Ang II infusion compared with that of WT mice (**Figures 2D and 2E**). These results suggest that cardiac nuclear HMGB1 protects against Ang II-induced pathological cardiac remodeling.

TABLE 1 Echocardiographic Data of WT and HMGB1-Tg Mice Following Saline or Ang II Infusion

	WT Saline (n = 10)	WT Ang II (n = 10)	HMGB1-Tg Saline (n = 6)	HMGB1-Tg Ang II (n = 6)
LVDd, mm	3.43 ± 0.11	3.35 ± 0.11	3.43 ± 0.11	3.47 ± 0.11
LVDs, mm	1.82 ± 0.08	1.86 ± 0.08	1.86 ± 0.08	1.89 ± 0.08
IVSd, mm	0.61 ± 0.03	1.03 ± 0.03*	0.66 ± 0.03	0.72 ± 0.03†
PWd, mm	0.71 ± 0.03	1.02 ± 0.03*	0.71 ± 0.03	0.77 ± 0.03†
FS, %	47.0 ± 1.4	43.7 ± 1.4	45.8 ± 1.4	45.8 ± 1.4
E/A ratio	1.85 ± 0.05	1.11 ± 0.05*	1.80 ± 0.06	1.47 ± 0.06†‡

Values are mean ± SE. *p < 0.001 versus WT saline mice. †p < 0.001 versus WT Ang II mice. ‡p < 0.01 versus HMGB1-Tg saline mice.

Ang II = angiotensin II; E/A ratio = ratio of early to atrial wave; FS = fractional shortening; MGB1-Tg = cardiac-specific high-mobility group box 1 overexpression transgenic mice; IVSd = interventricular septum diameter; LVDd = left ventricular diastolic dimension; LVDs = left ventricular systolic dimension; PWd = posterior wall diameter; HWT = wild-type mice.

THE PROTECTIVE EFFECT OF CARDIAC NUCLEAR HMGB1 ON DNA DAMAGE AND DDR IN VIVO. We next examined whether cardiac nuclear HMGB1 overexpression prevents DNA damage and DDR in vivo. Immunofluorescence revealed that nuclear γ-H2AX-positive cardiomyocytes was increased in WT mice, whereas HMGB1-Tg mice showed attenuated γ-H2AX expression after Ang II infusion (**Figures 3A and 3B**). Western blot analysis also showed that decreased γ-H2AX expression was observed in HMGB1-Tg mice compared with that of WT mice after Ang II infusion (**Figures 3C and 3D**). Ang II infusion resulted in a significant increase in the p-ATM positive cardiomyocytes in WT mice, whereas HMGB1-Tg mice showed less p-ATM positive cardiomyocytes (**Figures 3E and 3F**). Western blot analysis showed that p-ATM was significantly lower in HMGB1-Tg mice compared with that of WT mice after Ang II infusion (**Figures 3G and 3H**). These data suggest that cardiac nuclear HMGB1 protects against Ang II-induced DNA damage and DDR.

TABLE 2 Hemodynamic Data of WT and HMGB1-Tg Mice Following Saline or Ang II Infusion

	WT Saline (n = 14)	WT Ang II (n = 10)	HMGB1-Tg Saline (n = 15)	HMGB1-Tg Ang II (n = 10)
BW, g	25.7 ± 0.6	27.1 ± 0.6	26.3 ± 0.6	26.8 ± 0.6
Hemodynamic parameter				
HR, beats/min	608 ± 17	612 ± 20	586 ± 16	615 ± 20
SBP, mm Hg	92 ± 3.3	142 ± 3.9*	95 ± 3.2	138 ± 3.9†
DBP, mm Hg	36 ± 5.7	95 ± 6.8‡	32 ± 5.5	69 ± 6.7†
MBP, mm Hg	55 ± 4.6	111 ± 5.5*	51 ± 4.5	92 ± 5.5†

Values are mean ± SE. *p < 0.001 versus WT saline mice. †p < 0.001 versus HMGB1-Tg saline mice. ‡p < 0.01versus WT saline mice.

BW = body weight; DBP = diastolic blood pressure; HR = heart rate; MBP = mean blood pressure; SBP = systolic blood pressure; other abbreviations as in Table 1.

IMPACT OF NUCLEAR HMGB1 ON HYPERTROPHIC RESPONSE INDUCED BY ANG II IN VITRO. We examined the effect of HMGB1 on the hypertrophic response in cultured NRCMs. Immunostaining of NRCMs for α-actinin indicated that HMGB1 overexpression significantly attenuated the increase in cardiomyocyte hypertrophy induced by Ang II (Supplemental Figures 3A and 3B). In contrast, HMGB1 knockdown promoted the hypertrophic growth of cardiomyocytes in response to Ang II (Supplemental Figures 3C and 3D). These data indicated that cardiac nuclear HMGB1 prevents cardiomyocyte hypertrophy in response to Ang II stimulation.

THE PROTECTIVE EFFECT OF CARDIAC NUCLEAR HMGB1 ON DNA DAMAGE AND DDR IN VITRO. We determined whether HMGB1 regulates DNA damage and the DDR in NRCMs after Ang II stimulation. Bimodal upregulation of p-ATM and γ-H2AX were observed 2 and 24 h after Ang II stimulation in NRCMs. In contrast, nuclear HMGB1 expression was decreased 1 and 24 h after Ang II stimulation in NRCMs (Supplemental Figure 4). HMGB1 overexpression resulted in a significant decrease in the number of nuclear γ-H2AX foci (**Figures 4A and 4B**). Western blot analysis showed that γ-H2AX expression was attenuated in HMGB1 overexpression NRCMs (**Figures 4C and 4D**). HMGB1 overexpression also decreased the number of nuclear p-ATM foci induced by Ang II stimulation (**Figures 4E and 4F**). Western blot analysis demonstrated that p-ATM was also attenuated in HMGB1 overexpression NRCMs (**Figures 4G and 4H**).

In contrast, HMGB1 knockdown significantly increased the number of nuclear γ-H2AX foci in NRCMs after Ang II stimulation (**Figures 5A and 5B**). Western blot analysis also revealed that γ-H2AX expression was further enhanced in HMGB1 knockdown NRCMs after Ang II stimulation (**Figures 5C and 5D**). HMGB1 knockdown significantly increased the number of nuclear p-ATM foci in NRCMs (**Figures 5E and 5F**), and p-ATM expression was enhanced in HMGB1 knockdown NRCMs after Ang II stimulation (**Figures 5G and 5H**). These data suggested that nuclear HMGB1 regulates Ang II-induced DNA damage and the DDR in vitro.

THE IMPACT OF HMGB1 AND ATM ON ANG II–INDUCED CARDIAC HYPERTROPHIC RESPONSE. To investigate further mechanisms by which HMGB1 and DDR are involved in Ang II-induced hypertrophic response, the association between HMGB1 and ATM was examined by immunoprecipitation experiments. Immunoprecipitation revealed a potential interaction between HMGB1 and ATM in NRCMs (Supplemental Figures 5A and 5B). In addition, Ang II

FIGURE 2 **Cardiac Nuclear HMGB1 Protects Mice Against Ang II–Induced Cardiac Remodeling**

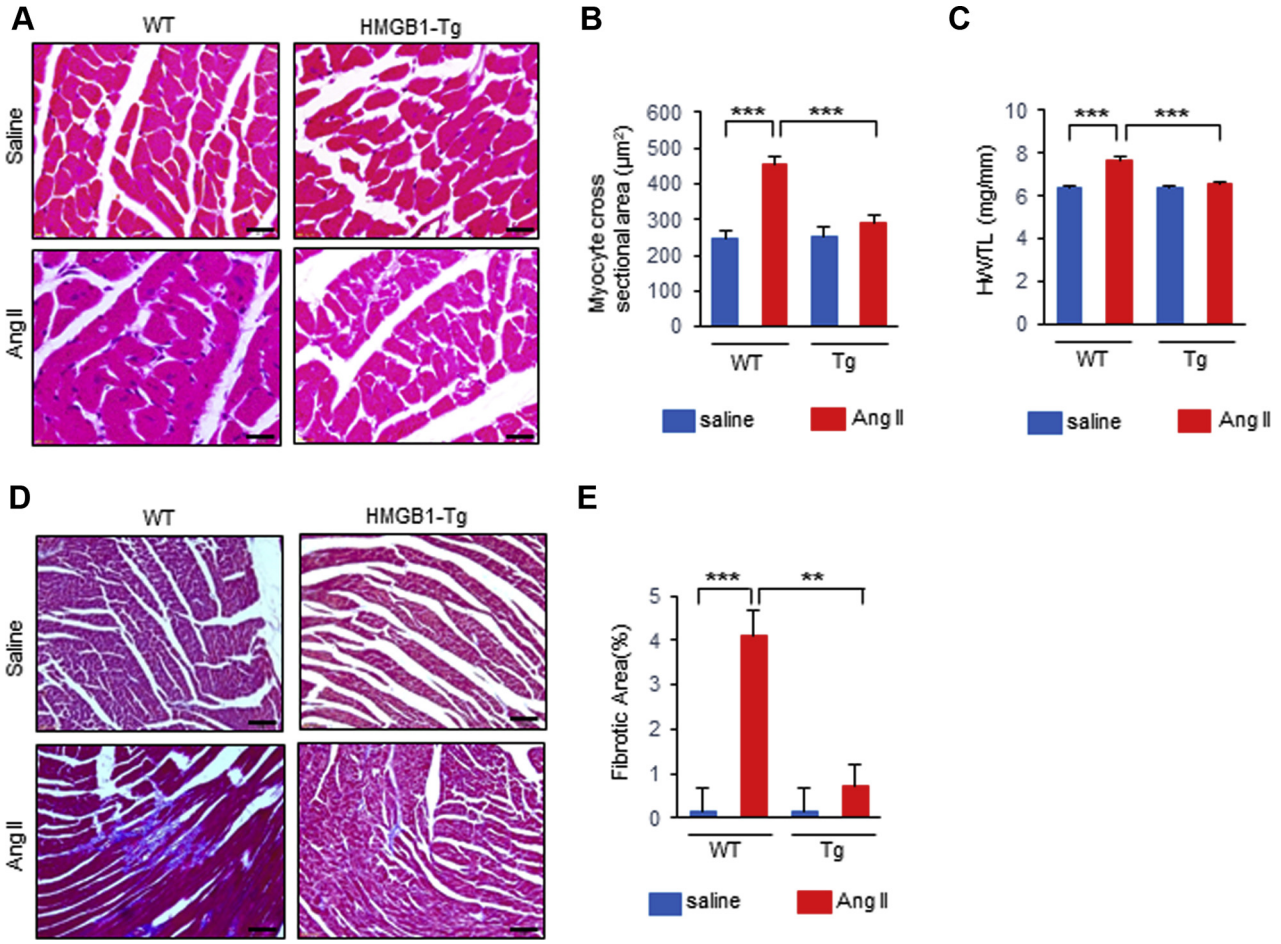

(A, B) Representative images and analysis of CM cross-sectional area from hematoxylin and eosin (H&E)–stained left ventricular sections in wild-type (WT) and HMGB1 transgenic (HMGB1-Tg) mice following saline or angiotensin II (Ang II) infusion. Scale bars = 20 μm. (n = 6 per group). **(C)** The ratio of heart weight to tibial length (HW/TL) in WT and HMGB1-Tg mice following saline or Ang II infusion (n = 10 per group). **(D, E)** Representative images and analysis of cardiac fibrosis area by Masson's trichrome staining in left ventricular sections in WT and HMGB1-Tg mice following saline or Ang II infusion. Scale bars = 50 μm. n = 5 in WT saline group; n = 4 in WT Ang II group; n = 5 in HMGB1-Tg saline group; n = 5 in HMGB1-Tg Ang II group. Results are presented as the mean ± SE. **$p < 0.01$; ***$p < 0.001$. Abbreviations as in Figure 1.

stimulation decreased the interaction between HMGB1 and ATM (Supplemental Figure 5C).

Next, we analyzed the effect of HMGB1 on activation of the hypertrophic signaling pathway. HMGB1 overexpression significantly attenuated the phosphorylation of ERK1/2 and nuclear factor kappa B (NF-κB) induced by Ang II in NRCMs (**Figures 6A and 6B**). HMGB1 knockdown exhibited enhanced Ang II mediated activation of the ERK1/2 and NF-κB pathway (**Figures 6C and 6D**). We examined the effect of ATM on hypertrophic signaling kinases in NRCMs using a specific ATM inhibitor KU55933. Ang II–induced phosphorylation of ERK1/2 and NF-κB was reduced by treatment with an ATM inhibitor in NRCMs (Supplemental Figures 6A and 6B). Furthermore, the enhanced phosphorylation of ERK1/2 and NF-κB by Ang II stimulation in HMGB1 knockdown NRCMs was suppressed by treatment with an ATM inhibitor (**Figure 6E**). We also evaluated the impact of nuclear HMGB1 and ATM on fetal cardiac gene expression. Atrial natriuretic peptide (ANP) and BNP promoter activities were increased by Ang II stimulation in vitro (Supplemental Figures 7A and 7B). HMGB1 knockdown exhibited enhanced ANP and BNP promoter activities induced by Ang II, which was abolished after pretreatment with ATM inhibitor (**Figures 6F and 6G**).

FIGURE 3 Cardiac Nuclear HMGB1 Prevents Ang II–Induced DNA Damage and the DDR in Mice

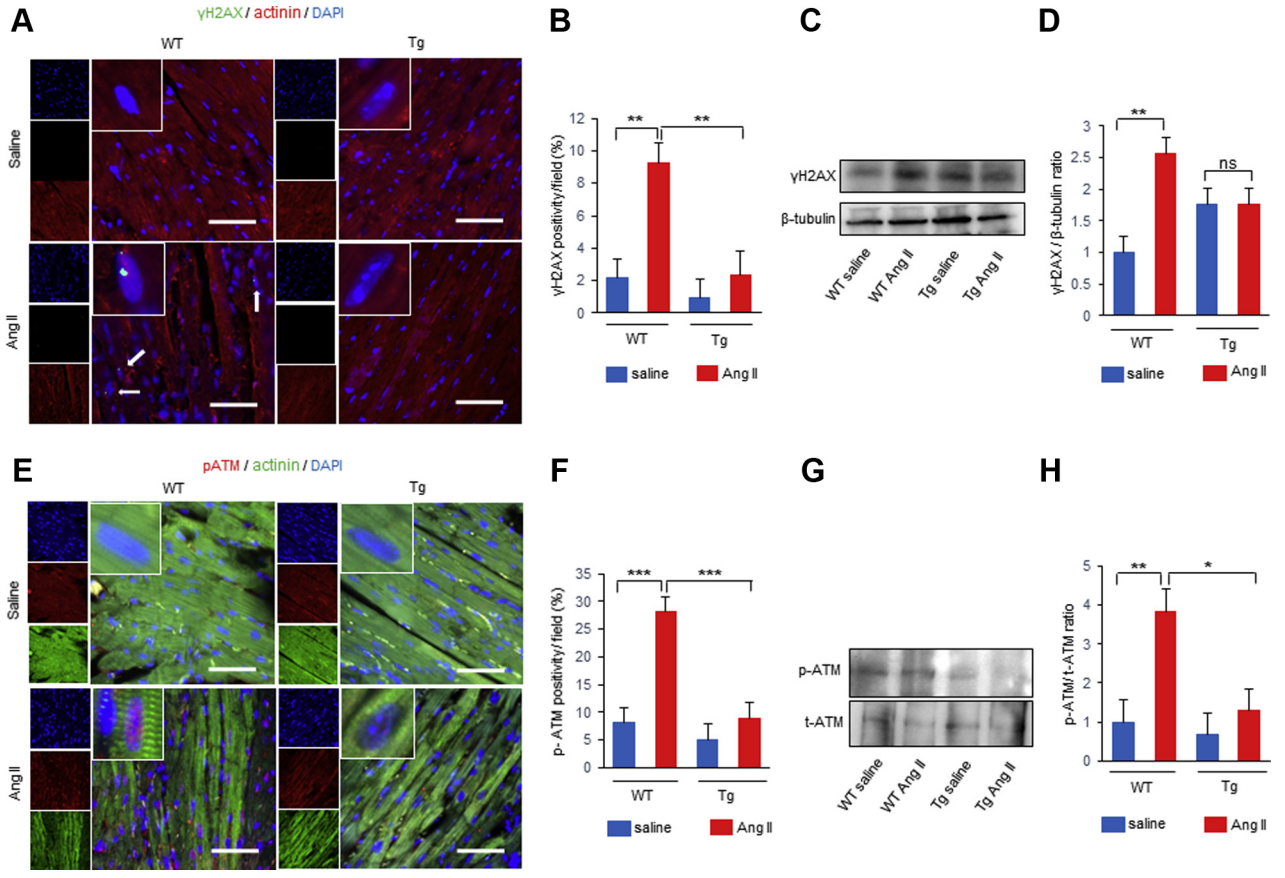

(A, B) Representative images and analysis of immunostaining of γ-H2AX **(green)**, α-actinin **(red)**, and DAPI **(blue)** in saline- or Ang II–treated WT and HMGB1-Tg mice. The number of γ-H2AX–positive CMs per field was counted. Scale bars = 50 μm. n = 6 in WT saline group; n = 6 in WT Ang II group; n = 6 in HMGB1-Tg saline group; n = 4 in HMGB1-Tg Ang II group. **(C, D)** Representative images and analysis of Western blots of γ-H2AX and β-tubulin from hearts of WT and HMGB1-Tg mice following saline or Ang II infusion (n = 5 per group). **(E, F)** Representative images and analysis of immunostaining of p-ATM **(red)**, α-actinin **(green)**, and DAPI **(blue)** in saline- or Ang II–treated WT and HMGB1-Tg mice. The number of p-ATM–positive CMs per field was counted. Scale bars = 50 μm. n = 6 in WT saline group; n = 7 in WT Ang II group; n = 5 in HMGB1-Tg saline group; n = 6 in HMGB1-Tg Ang II group. **(G, H)** Representative images and analysis of Western blots of p-ATM and total ATM from hearts of WT and HMGB1-Tg mice following saline or Ang II infusion (n = 6 per group). Results are presented as the mean ± SE. *$p < 0.05$; **$p < 0.01$; ***$p < 0.001$. DDR = deoxyribonucleic acid damage response; DNA = deoxyribonucleic acid; Other abbreviations as in Figures 1 and 2.

These results suggest that HMGB1 regulates Ang II–induced cardiac hypertrophy through inhibiting ATM activity.

THE CARDIOPROTECTIVE EFFECT OF PHARMACOLOGICAL ATM INHIBITION FOR ANG II–INDUCED PATHOLOGICAL CARDIAC REMODELING. To evaluate the therapeutic potential of ATM inhibitor, we treated WT and HMGB1-Tg mice with either ATM inhibitor or vehicle after Ang II infusion for 2 weeks (Figure 7A). Pharmacological ATM inhibition demonstrated cardioprotective effect in WT mice and also provided synergic cardioprotective effect in HMGB1-Tg mice for Ang II–induced pathological cardiac remodeling. WT and HMGB1 mice treated with the ATM inhibitor exhibited significant decrease in the IVSd and PWd compared with that of WT and HMGB1-Tg mice treated with vehicle after Ang II infusion. Pharmacological ATM inhibition did not alter the LVDd, whereas the FS was slightly improved in WT mice with ATM inhibitor. The E/A ratio was significantly improved when WT and HMGB1-Tg mice were treated with the ATM inhibitor after Ang II infusion compared with that of WT and HMGB1-Tg mice treated with vehicle after Ang II infusion (Table 3, Supplemental

FIGURE 4 Effect of HMGB1 Overexpression on DNA Damage and DDR After Ang II Stimulation

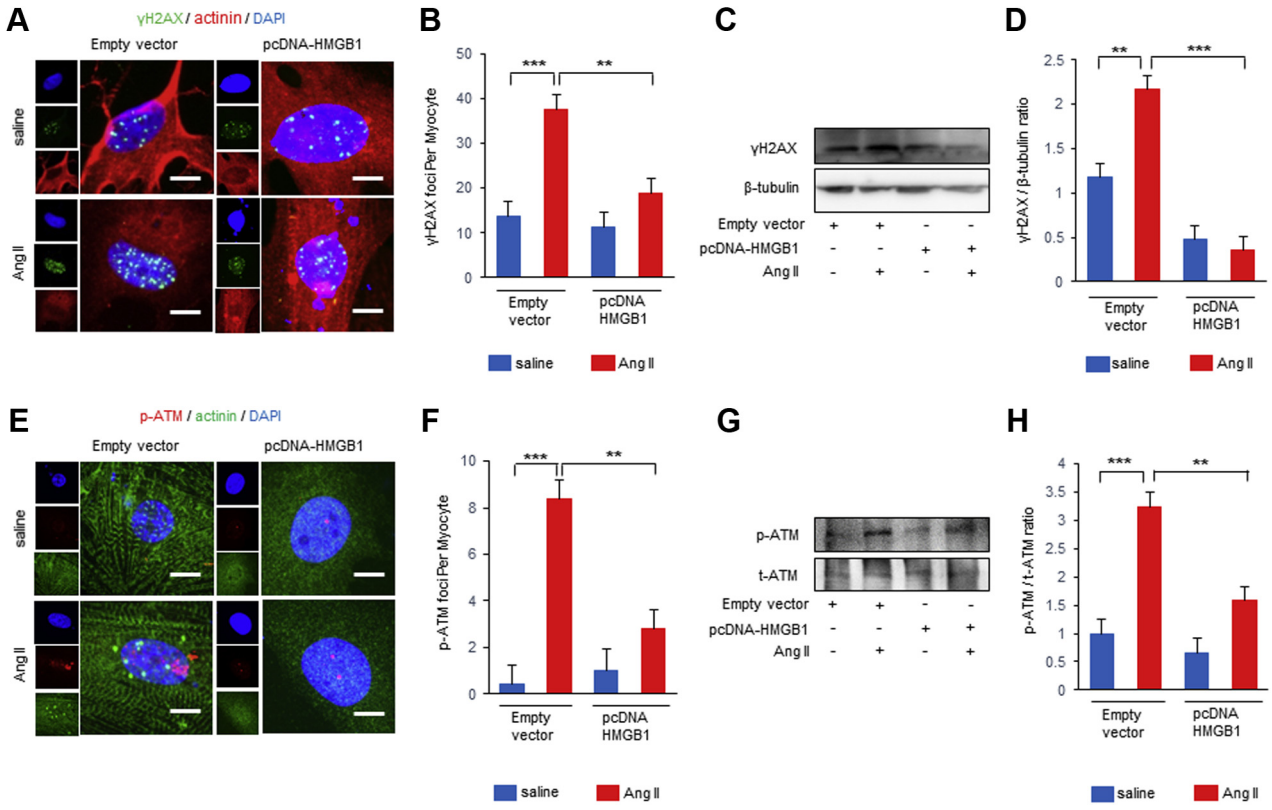

(A, B) Representative images and analysis of immunostaining of nuclear foci of γ-H2AX **(green)**, α-actinin **(red)**, and DAPI **(blue)** of neonatal rat CMs (NRCMs) transfected with pcDNA-HMGB1 or control vector and then treated with saline or Ang II for 24 h. The foci number of γ-H2AX per NRCM was counted. Scale bars = 20 μm. n = 6 per group. **(C, D)** Representative images and analysis of Western blots of γ-H2AX. NRCMs transfected with pcDNA-HMGB1 or control saline and then treated with vehicle or Ang II for 24 h (n = 5 per group). **(E, F)** Representative images and analysis of immunostaining of nuclear foci of p-ATM **(red)**, α-actinin **(green)**, and DAPI **(blue)** of NRCMs transfected with pcDNA-HMGB1 or control vector and then treated with saline or Ang II for 24 h. The foci number of p-ATM per NRCM was counted. Scale bars = 20 μm. n = 5 in control vector saline group; n = 5 in control vector Ang II group; n = 4 in pcDNA-HMGB1 saline group; n = 5 in pcDNA-HMGB1 Ang II group. **(G, H)** Representative images and analysis of Western blots of p-ATM and total ATM. NRCMs transfected with pcDNA-HMGB1 or control vector and then treated with saline or Ang II for 24 h (n = 4 per group). **p < 0.01; ***p < 0.001. Abbreviations as in Figures 1–3.

Figure 8). WT and HMGB1-Tg mice treated with the ATM inhibitor showed a lower HW/TL ratio than WT and HMGB1-Tg mice treated with vehicle after Ang II infusion (Figure 7B). ATM inhibitor treatment provided no significant effect on blood pressure (Table 4). Histological analysis demonstrated that both Ang II–induced cardiomyocyte hypertrophy and fibrosis were significantly attenuated when WT and HMGB1-Tg mice were treated with the ATM inhibitor after Ang II infusion compared with that of WT and HMGB1-Tg mice treated with vehicle after Ang II infusion (Figures 7C to 7E). These results suggest that pharmacological ATM inhibition preserves cardiac function and reduces cardiac hypertrophy and fibrosis after Ang II infusion.

DISCUSSION

Our study shows that nuclear HMGB1 expression was decreased and phosphorylation of ATM was increased in the failing human heart. Decreased nuclear HMGB1 expression in failing human hearts was associated with cardiomyocyte hypertrophy, fibrosis, and high serum BNP levels. Both in vivo and in vitro studies revealed that cardiac nuclear HMGB1 prevented Ang II–induced pathological cardiac hypertrophy through inhibition of the DDR pathway. Mechanistically, cardiac nuclear HMGB1 inhibited phosphorylation of ATM and subsequent activation of ERK 1/2 and NF-κB signaling. Moreover, a specific ATM inhibitor, KU55933, prevented Ang II–induced

FIGURE 5 Effect of HMGB1 Suppression on DNA Damage and DDR After Ang II Stimulation

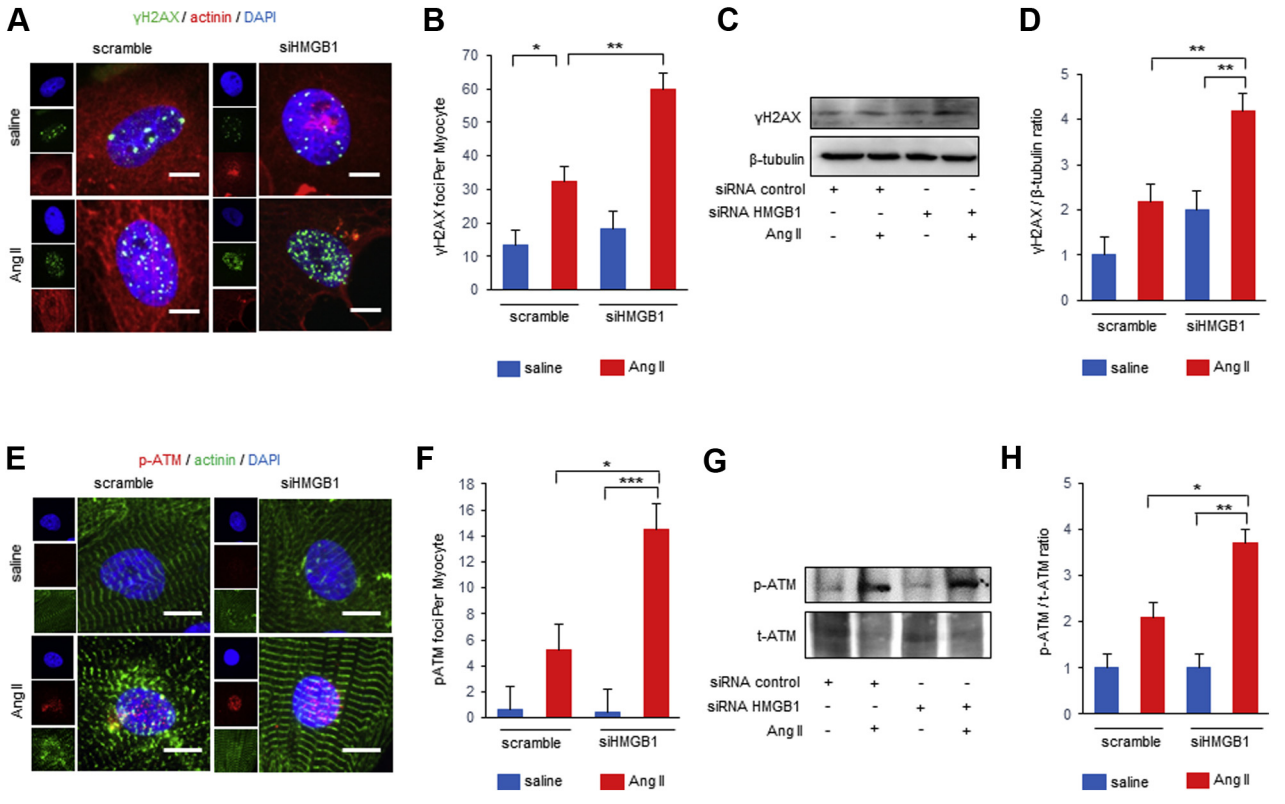

(A, B) Representative images and analysis of immunostaining of nuclear foci of γ-H2AX **(green)**, α-actinin **(red)**, and DAPI **(blue)** of NRCMs transfected with small interfering HMGB1 (siHMGB1) or nonspecific control small interfering ribonucleic acid (siRNA) and then treated with saline or Ang II for 24 h. The foci number of γ-H2AX per NRCM was counted. Scale bars = 20 μm. n = 6 in scramble saline group; n = 6 in scramble Ang II group; n = 5 in siHMGB1 saline group; n = 6 in siHMGB1 Ang II group. **(C, D)** Representative images and analysis of Western blots of γ-H2AX. NRCMs transfected with siHMGB1 or nonspecific control siRNA and then treated with saline or Ang II for 24 h (n = 6 per group). **(E, F)** Representative images and analysis of immunostaining of nuclear foci of p-ATM **(red)**, α-actinin **(green)**, and DAPI **(blue)** of NRCMs transfected with siHMGB1 or nonspecific control siRNA and then treated with saline or Ang II for 24 h. The foci number of p-ATM per NRCM was counted. Scale bars = 20 μm. n = 5 in scramble saline group; n = 4 in scramble Ang II group; n = 5 in siHMGB1 saline group; n = 4 in siHMGB1 Ang II group. **(G, H)** Representative images and analysis of Western blots of p-ATM and total ATM. NRCMs transfected with siHMGB1 or nonspecific control siRNA and then treated with saline or Ang II for 24 h (n = 3 per group). Results are presented as the mean ± SE. *p < 0.05; **p < 0.01; ***p < 0.001. Abbreviations as in Figures 1–4.

pathological cardiac remodeling. These results provide new insight into the pathogenesis of cardiac remodeling and therapeutic potential of HMGB1-DDR axis.

In the present study, we showed that cardiac nuclear HMGB1 plays a protective role in Ang II–induced cardiac hypertrophy, suggesting that cardiac nuclear HMGB1 is one of the key regulator of pathological cardiac remodeling. HMGB1 is a nonhistone nuclear protein and a member of the HMG protein superfamilies. HMGB1 is the most abundant HMG protein and has multiple functions both inside and outside of the cell. Extracellular HMGB1 acts as a DAMP, which causes various inflammatory and immune responses (28). Extracellular HMGB1 causes cardiac hypertrophy and worsens ischemia or reperfusion injury, myocardial inflammation, and fibrosis (11–13). Thus, several studies have demonstrated the role of extracellular HMGB1 in cardiac remodeling. However, the role of intracellular HMGB1, especially nuclear HMGB1, in cardiac remodeling is poorly defined. We previously reported that cardiac nuclear HMGB1 protected against pressure overload induced heart failure and doxorubicin-induced cardiomyopathy (17,25). The protective roles of nuclear HMGB1 are further supported by the findings that ablation of nuclear HMGB1 worsens acute pancreatitis, liver ischemia and reperfusion injury, and bacterial infection (14,15,29). Consistent with these studies, our results show the cardioprotective role of cardiac nuclear HMGB1 on pathological cardiac hypertrophy and fibrosis.

FIGURE 6 Effect of HMGB1 and ATM on Cardiac Hypertrophic Signaling

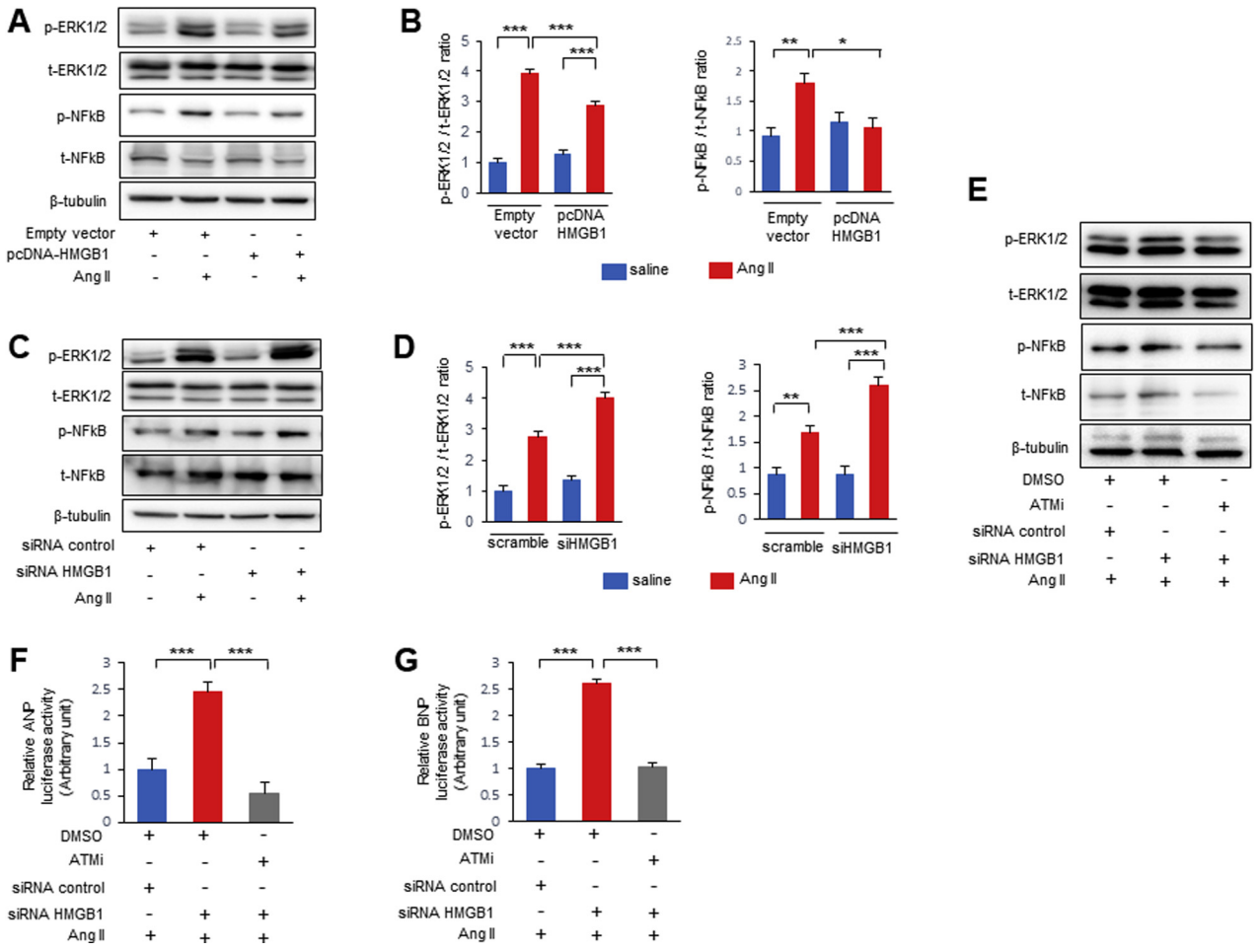

(A, B) Representative images and analysis Western blots of phospho-extracellular signal-related kinase 1/2 (p-ERK1/2), total ERK1/2 (t-ERK1/2), phospho-nuclear factor kappa B (p-NF-κB), and total NF-κB (t-NF-κB) from NRCMs transfected with pcDNA-HMGB1 or control vector and then treated with saline or Ang II for 4 h (n = 6 per group). **(C, D)** Representative images and analysis of Western blots of p-ERK1/2, t-ERK1/2, p-NF-κB, and t-NF-κB from NRCMs transfected with siHMGB1 or nonspecific control siRNA and then treated with saline or Ang II for 4 h (n = 6 per group). **(E)** Representative Western blots of p-ERK1/2, t-ERK1/2, p-NF-κB, and t-NF-κB. NRCMs transfected with siHMGB1 or nonspecific control siRNA were pretreated with an ATM inhibitor (KU55933) or dimethyl sulfoxide (DMSO) for 1 h before Ang II stimulation, and then stimulated with saline or Ang II for 4 h. **(F, G)** Quantification of atrial natriuretic peptide (ANP) and BNP promoter activities. Rat H9C2 cells were pretreated with an ATM inhibitor (KU55933) or DMSO for 1 h before Ang II stimulation, and then stimulated with saline or Ang II for 24 h (n = 6 per group). Results are presented as the mean ± SE. *p < 0.05; **p < 0.01; ***p < 0.001. Abbreviations as in Figures 1 to 5.

The present study showed that cardiac nuclear HMGB1 prevented cardiomyocytes against DNA damage and following DDR activation because HMGB1 prevented upregulation of γ-H2AX, a specific marker of DNA damage, and p-ATM. Intracellular HMGB1 has various functions such as DNA chaperone, DNA repair, chromosome guardian, autophagy sustainer, and protector from apoptotic cell death. Loss of nuclear HMGB1 caused decreased chromatin accessibility to repair DNA damage, resulted in nuclear catastrophe, and subsequent cell death (14,15). These studies indicate the role of nuclear HMGB1 as a defender against cellular DNA damage in several disease conditions. In the heart, significantly more DNA damage was observed in heart failure patients compared with that of normal-health control subjects (19). In the experimental model, DNA damage was also observed in a mouse model of myocardial infarction, which was associated with cell apoptosis (30). Excessive DNA damage causes phosphorylation of ATM, a key regulator of DDR, and contributes to several disease conditions, including heart failure.

FIGURE 7 Cardioprotective Effect of the ATM Inhibitor on Ang II-Induced Pathological Cardiac Remodeling

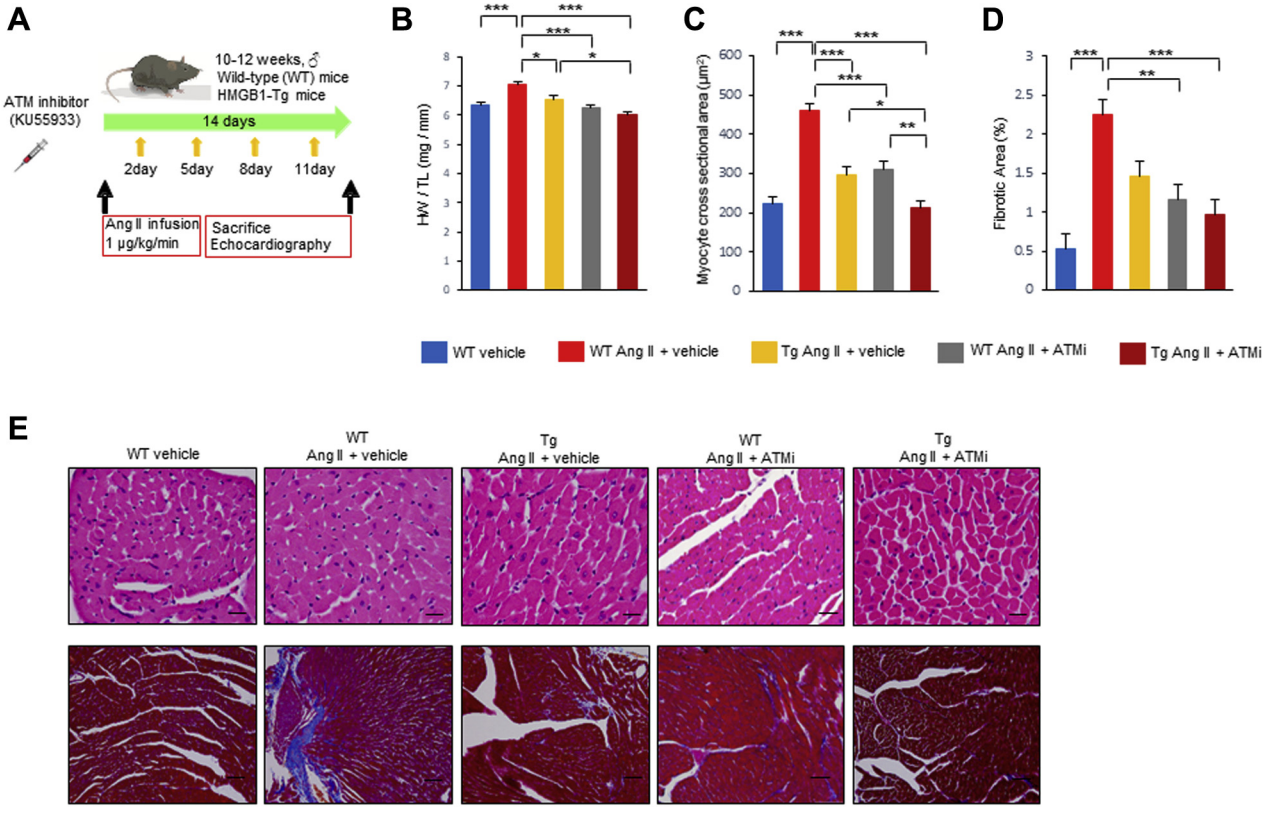

(A) Timeline of Ang II infusion and ATM inhibitor (KU55933) or vehicle administration in mice. **(B)** The ratio of HW/TL in WT and HMGB1-Tg mice subjected to Ang II infusion and vehicle or ATM inhibitor (KU55933) treatment (n = 8 in WT vehicle group; n = 8 in WT Ang II + vehicle group; n = 6 in HMGB1-Tg Ang II + vehicle group; n = 6 in WT Ang II + KU55933 group; n = 6 in HMGB1-Tg Ang II + KU55933 group). **(C)** Analysis of CM cross-sectional area by H&E staining in left ventricular sections in WT and HMGB1-Tg mice subjected to Ang II infusion and vehicle or ATM inhibitor (KU55933) treatment (n = 10 in WT vehicle group; n = 10 in WT Ang II + vehicle group; n = 9 in HMGB1-Tg Ang II + vehicle group; n = 7 in WT Ang II + KU55933 group; n = 9 in HMGB1-Tg Ang II + KU55933 group). **(D)** Analysis of cardiac fibrosis by Masson's trichrome staining in left ventricular sections in WT and HMGB1-Tg mice subjected to Ang II infusion and vehicle or ATM inhibitor (KU55933) treatment (n = 6 per group). **(E)** Representative images of CM cross-sectional area by H&E staining (Scale bars = 20 μm) and cardiac fibrosis by Masson's trichrome staining (Scale bars = 50 μm) in left ventricular sections in WT and HMGB1-Tg mice subjected to Ang II infusion and vehicle or ATM inhibitor (KU55933) treatment. Results are presented as the mean ± SE. *p < 0.05; **p < 0.01; ***p < 0.001. Abbreviations as in Figures 1 to 6.

TABLE 3 Echocardiographic Data of WT and HMGB1-Tg Mice Subjected to Ang II Infusion and Vehicle or ATMi Treatment

	WT Vehicle (n = 9)	WT Ang II + Vehicle (n = 10)	HMGB1-Tg Ang II + Vehicle (n = 6)	WT Ang II + ATMi (n = 6)	HMGB1-Tg Ang II + ATMi (n = 6)
LVDd, mm	3.15 ± 0.15	3.04 ± 0.14	3.36 ± 0.18	2.96 ± 0.18	3.32 ± 0.18
LVDs, mm	1.63 ± 0.11	1.76 ± 0.10	1.89 ± 0.13	1.40 ± 0.13	1.72 ± 0.13
IVSd, mm	0.74 ± 0.03	1.04 ± 0.03*	0.85 ± 0.04†	0.80 ± 0.04‡	0.70 ± 0.05‡
PWd, mm	0.76 ± 0.03	1.00 ± 0.03*	0.88 ± 0.04	0.80 ± 0.04†	0.75 ± 0.04‡
FS, %	48.6 ± 1.6	42.5 ± 1.5	43.2 ± 2.0	52.3 ± 2.0†	48.6 ± 2.0
E/A ratio	1.84 ± 0.06	1.13 ± 0.06*	1.41 ± 0.07§	1.68 ± 0.07‡	2.02 ± 0.07‡

Values are mean ± SE. *p < 0.001 versus WT vehicle mice. †p < 0.01versus WT Ang II mice. ‡p < 0.001 versus WT Ang II mice. §p < 0.05versus WT Ang II mice.
ATMi = ataxia telangiectasia mutated inhibitor; other abbreviations as in Table 1.

Phosphorylation of ATM was increased in end-stage failing human hearts, and prolonged mechanical unload by left ventricular assist device implantation decreased the expression of p-ATM in cardiomyocytes, which was associated with a reduction of cardiomyocyte cell size (31). In addition, a recent study demonstrated that DNA damage-induced ATM activation caused pressure overload induced heart failure in mice. Activation of ATM caused increases in inflammatory cytokines thorough NF-κB signaling. Those effects were rescued by ATM deletion, and the ATM deletion prevented heart failure progression in mice, suggesting a causative role for ATM in heart failure (32). These studies support the crucial role of

ATM in cardiac hypertrophy. Our study also demonstrated that HMGB1 interacts with ATM, and Ang II stimulation weakened the interaction and subsequent ATM activation. These results suggest that ATM activation was mediated, at least in part, by HMGB1. Thus, ATM is one of the important target molecules of HMGB1 in pathological cardiac hypertrophy.

ATM has crucial roles in the development of pathological cardiac remodeling. However, it remains unclear whether pharmacological ATM inhibition protects against pathological cardiac remodeling. In the present study, we demonstrated for the first time that ATM inhibitor treatment offered a synergic cardioprotective effect in WT and HMGB1-Tg mice against Ang II–induced cardiac hypertrophy and fibrosis. In addition, ATM inhibitor treatment suppressed Ang II–induced ANP and BNP activation and phosphorylation of ERK1/2 and NF-κB in vitro. KU55933 is a potent and selective inhibitor of ATM and is developed as an anticancer therapy (33). In addition to being an anticancer therapy, KU55933 provided protective effect against oxidative damage, inflammation, and senescence (34,35). Furthermore, KU55933 attenuated doxorubicin-induced cardiac dysfunction (36). Several studies demonstrated that ERK1/2 is involved in pathological cardiomyocyte hypertrophy (37,38). DNA damage causes ATM dependent NF-κB activation, and NF-κB activation is reported to be associated with pathological cardiac remodeling (39,40). Our results indicate that ATM inhibition prevented Ang II–induced pathological cardiac remodeling by targeting ERK1/2 and NF-κB pathways. In the present study, KU55933 provides the synergistic cardioprotective effect for Ang II–induced pathological cardiac remodeling in HMGB1-Tg mice. This cardioprotective effect of KU55933 in HMGB1-Tg mice might be contributed to that DNA damage was also mediated by other mechanisms in addition to nuclear HMGB1 (30,41–44). The present study demonstrated for the first time, the involvement of the HMGB1-ATM axis in pathological cardiac remodeling, and provided potential therapeutic efficacy of targeting DDR inhibition.

STUDY LIMITATIONS. First, we did not evaluate the effect of loss of cardiac nuclear HMGB1 on pathological cardiac remodeling in vivo, although we evaluated those effect in vitro using siHMGB1. A previous study showed that specific deletion of HMGB1 in cardiomyocytes did not affect cardiac function at baseline (45). However, the effect of cardiomyocyte specific HMGB1 deletion under stress conditions is still unclear. Second, our study could not rule out the possible protective effect of ATM inhibitor KU55933 on other cell types in vivo, although we confirmed the cardiomyocyte-specific protective effect of KU55933 in vitro. A previous study revealed that fibroblast-specific ATM knockout mice attenuated doxorubicin-induced cardiotoxicity (36). Third, we have not evaluated the effect of extracellular HMGB1 in both in vivo and in vitro studies. Because extracellular HMGB1 acts as DAMPs and affects reparative immune responses (9,10), extracellular HMGB1 may influence Ang II–induced pathological cardiac remodeling.

TABLE 4 Hemodynamic Data of WT and HMGB1-Tg Mice Subjected to Ang II Infusion and Vehicle or ATMi Treatment

	WT Vehicle (n = 15)	WT Ang II + Vehicle (n = 12)	HMGB1-Tg Ang II + Vehicle (n = 11)	WT Ang II + ATMi (n = 14)	HMGB1-Tg Ang II + ATMi (n = 9)
BW, g	26.4 ± 0.7	26.9 ± 0.7	25.9 ± 0.9	25.9 ± 0.7	24.8 ± 0.9
Hemodynamic parameter					
HR, beats/min	601 ± 20	582 ± 23	600 ± 24	619 ± 21	573 ± 26
SBP, mm Hg	93 ± 5	138 ± 6*	141 ± 6*	138 ± 5*	147 ± 6*
DBP, mm Hg	39 ± 7	87 ± 8*	71 ± 8†	71 ± 7‡	81 ± 9‡
MBP, mm Hg	57 ± 6	104 ± 7*	94 ± 7‡	93 ± 6‡	99 ± 8‡

Values are mean ± SE. *p < 0.001 versus WT vehicle mice. †p < 0.05 versus WT vehicle mice. ‡p < 0.01 versus WT vehicle mice.

Abbreviations as in Tables 1 to 3.

CONCLUSIONS

Our study documents a novel mechanism by which cardiac nuclear HMGB1 attenuates Ang II–induced pathological cardiac remodeling through inhibition of ATM activation. Furthermore, targeting DDR treatment by using a novel selective ATM inhibitor KU55933 prevents Ang II–induced pathological cardiac remodeling. This work provides further evidence of critical role of cardiac nuclear HMGB1 in the development of pathological cardiac remodeling, and possibly the development of novel therapeutics for heart failure treatment.

ACKNOWLEDGMENTS The authors thank Ms. Emiko Nishidate and Ms. Yuko Sasaki for their excellent technical assistance and comments. The authors thank Editage for the English language review.

ADDRESS FOR CORRESPONDENCE: Dr. Tetsuro Shishido, Department of Cardiology, Pulmonology, and Nephrology, Yamagata University School of Medicine, 2-2-2 Iida-nishi, Yamagata 990-9585, Japan. E-mail: tshishid@med.id.yamagata-u.ac.jp.

PERSPECTIVES

COMPETENCY IN MEDICAL KNOWLEDGE: Cardiac nuclear-specific HMGB1 overexpression in cardiomyocytes reduces left ventricular hypertrophy and remodeling after Ang II stimulation. Cardiac nuclear HMGB1 prevents cardiomyocyte DDR, which is associated with developing heart failure.

TRANSLATIONAL OUTLOOK: Further research is needed to explore the therapeutic potential of nuclear HMGB1 and DDR axis for patients with heart failure.

REFERENCES

1. Mozaffarian D, Benjamin EJ, Go AS, et al. Heart disease and stroke statistics–2015 update: a report from the American Heart Association. Circulation 2015;131:e29–322.

2. Ambrosy AP, Fonarow GC, Butler J, et al. The global health and economic burden of hospitalizations for heart failure: lessons learned from hospitalized heart failure registries. J Am Coll Cardiol 2014;63:1123–33.

3. Val-Blasco A, Piedras MJ, Ruiz-Hurtado G, et al. Role of NOD1 in heart failure progression via regulation of Ca2+ handling. J Am Coll Cardiol 2017;69:423–33.

4. Jessup M, Brozena S. Heart failure. N Engl J Med 2003;348:2007–18.

5. McMurray JJ, Pfeffer MA. Heart failure. Lancet 2005;365:1877–89.

6. Braunwald E. The war against heart failure: the Lancet lecture. Lancet 2015;385:812–24.

7. Nightingale K, Dimitrov S, Reeves R, Wolffe AP. Evidence for a shared structural role for HMG1 and linker histones B4 and H1 in organizing chromatin. EMBO J 1996;15:548–61.

8. Lange SS, Mitchell DL, Vasquez KM. High mobility group protein B1 enhances DNA repair and chromatin modification after DNA damage. Proc Natl Acad Sci U S A 2008;105:10320–5.

9. Lotze MT, Tracey KJ. High-mobility group box 1 protein (HMGB1): nuclear weapon in the immune arsenal. Nat Rev Immunol 2005;5:331–42.

10. Turner NA. Inflammatory and fibrotic responses of cardiac fibroblasts to myocardial damage associated molecular patterns (DAMPs). J Mol Cell Cardiol 2016;94:189–200.

11. Su FF, Shi MQ, Guo WG, et al. High-mobility group box 1 induces calcineurin-mediated cell hypertrophy in neonatal rat ventricular myocytes. Mediators Inflamm 2012;2012:805149.

12. Andrassy M, Volz HC, Igwe JC, et al. High-mobility group box-1 in ischemia-reperfusion injury of the heart. Circulation 2008;117:3216–26.

13. Zhang W, Lavine KJ, Epelman S, et al. Necrotic myocardial cells release damage-associated molecular patterns that provoke fibroblast activation in vitro and trigger myocardial inflammation and fibrosis in vivo. J Am Heart Assoc 2015;4:e001993.

14. Kang R, Zhang Q, Hou W, et al. Intracellular Hmgb1 inhibits inflammatory nucleosome release and limits acute pancreatitis in mice. Gastroenterology 2014;146:1097–107.

15. Huang H, Nace GW, McDonald KA, et al. Hepatocyte-specific high-mobility group box 1 deletion worsens the injury in liver ischemia/reperfusion: a role for intracellular high-mobility group box 1 in cellular protection. Hepatology 2014;59:1984–97.

16. Messer J, Chang E. Intracellular HMGB1: defender of client proteins and cell fate. Oncotarget 2015;6:8432–3.

17. Funayama A, Shishido T, Netsu S, et al. Cardiac nuclear high mobility group box 1 prevents the development of cardiac hypertrophy and heart failure. Cardiovasc Res 2013;99:657–64.

18. Sulli G, Di Micco R, d'Adda di Fagagna F. Crosstalk between chromatin state and DNA damage response in cellular senescence and cancer. Nat Rev Cancer 2012;12:709–20.

19. Siggens L, Figg N, Bennett M, Foo R. Nutrient deprivation regulates DNA damage repair in cardiomyocytes via loss of the base-excision repair enzyme OGG1. FASEB J 2012;26:2117–24.

20. Shukla PC, Singh KK, Quan A, et al. BRCA1 is an essential regulator of heart function and survival following myocardial infarction. Nat Commun 2011;2:593.

21. Sano M, Minamino T, Toko H, et al. p53-induced inhibition of Hif-1 causes cardiac dysfunction during pressure overload. Nature 2007;446:444–8.

22. Aoki T, Fukumoto Y, Sugimura K, et al. Prognostic impact of myocardial interstitial fibrosis in non-ischemic heart failure. Comparison between preserved and reduced ejection fraction heart failure. Circ J 2011;75:2605–13.

23. Lorenzen JM, Schauerte C, Hubner A, et al. Osteopontin is indispensible for AP1-mediated angiotensin II-related miR-21 transcription during cardiac fibrosis. Eur Heart J 2015;36:2184–96.

24. Shishido T, Nozaki N, Yamaguchi S, et al. Toll-like receptor-2 modulates ventricular remodeling after myocardial infarction. Circulation 2003;108:2905–10.

25. Narumi T, Shishido T, Otaki Y, et al. High-mobility group box 1-mediated heat shock protein beta 1 expression attenuates mitochondrial dysfunction and apoptosis. J Mol Cell Cardiol 2015;82:1–12.

26. Honda Y, Shishido T, Takahashi T, et al. Midkine deteriorates cardiac remodeling via epidermal growth factor receptor signaling in chronic kidney disease. Hypertension 2016;67:857–65.

27. Bonner WM, Redon CE, Dickey JS, et al. GammaH2AX and cancer. Nat Rev Cancer 2008;8:957–67.

28. Kang R, Chen R, Zhang Q, et al. HMGB1 in health and disease. Mol Aspects Med 2014;40:1–116.

29. Yanai H, Matsuda A, An J, et al. Conditional ablation of HMGB1 in mice reveals its protective function against endotoxemia and bacterial infection. Proc Natl Acad Sci U S A 2013;110:20699–704.

30. Wo D, Peng J, Ren DN, et al. Opposing roles of Wnt inhibitors IGFBP-4 and Dkk1 in cardiac ischemia by differential targeting of LRP5/6 and beta-catenin. Circulation 2016;134:1991–2007.

31. Canseco DC, Kimura W, Garg S, et al. Human ventricular unloading induces cardiomyocyte proliferation. J Am Coll Cardiol 2015;65:892–900.

32. Higo T, Naito AT, Sumida T, et al. DNA single-strand break-induced DNA damage response causes heart failure. Nat Commun 2017;8:15104.

33. Zhang T, Shen Y, Chen Y, Hsieh JT, Kong Z. The ATM inhibitor KU55933 sensitizes radioresistant bladder cancer cells with DAB2IP gene defect. Int J Rad Biol 2015;91:368–78.

34. Chwastek J, Jantas D, Lason W. The ATM kinase inhibitor KU-55933 provides neuroprotection against hydrogen peroxide-induced cell damage via a gammaH2AX/p-p53/caspase-3-independent mechanism: Inhibition of calpain and cathepsin D. Int J Biochem Cell Biol 2017;87:38–53.

35. Kang C, Xu Q, Martin TD, et al. The DNA damage response induces inflammation and senescence by inhibiting autophagy of GATA4. Science 2015;349:aaa5612.

36. Zhan H, Aizawa K, Sun J, et al. Ataxia telangiectasia mutated in cardiac fibroblasts regulates doxorubicin-induced cardiotoxicity. Cardiovasc Res 2016;110:85–95.

37. Yu CJ, Tang LL, Liang C, et al. Angiotensin-converting enzyme 3 (ACE3) protects against pressure overload-induced cardiac hypertrophy. J Am Heart Assoc 2016;5:e002680.

38. Bueno OF, Molkentin JD. Involvement of extracellular signal-regulated kinases 1/2 in cardiac hypertrophy and cell death. Circ Res 2002;91:776–81.

39. Barroso-Gonzalez J, Auclair S, Luan S, et al. PACS-2 mediates the ATM and NF-kappaB-dependent induction of anti-apoptotic Bcl-xL in response to DNA damage. Cell Death Differ 2016;23:1448–57.

40. Zhao QD, Viswanadhapalli S, Williams P, et al. NADPH oxidase 4 induces cardiac fibrosis and hypertrophy through activating Akt/mTOR and NFkappaB signaling pathways. Circulation 2015;131:643–55.

41. Gray K, Kumar S, Figg N, et al. Effects of DNA damage in smooth muscle cells in atherosclerosis. Circ Res 2015;116:816–26.

42. Zhou J, Ahmad F, Parikh S, et al. Loss of adult cardiac myocyte GSK-3 leads to mitotic catastrophe resulting in fatal dilated cardiomyopathy. Circ Res 2016;118:1208–22.

43. Tumurkhuu G, Shimada K, Dagvadorj J, et al. Ogg1-dependent DNA repair regulates NLRP3 inflammasome and prevents atherosclerosis. Circ Res 2016;119:e76–90.

44. Boon RA, Iekushi K, Lechner S, et al. MicroRNA-34a regulates cardiac ageing and function. Nature 2013;495:107–10.

45. Huebener P, Gwak GY, Pradere JP, et al. High-mobility group box 1 is dispensable for autophagy, mitochondrial quality control, and organ function in vivo. Cell Metab 2014;19:539–47.

KEY WORDS DNA damage response, HMGB1, pathological cardiac hypertrophy

APPENDIX For expanded Methods and References sections, please see the online version of this article.

JACC: BASIC TO TRANSLATIONAL SCIENCE VOL. 4, NO. 2, 2019
© 2019 PUBLISHED BY ELSEVIER ON BEHALF OF THE AMERICAN COLLEGE OF CARDIOLOGY FOUNDATION. THIS IS AN OPEN ACCESS ARTICLE UNDER THE CC BY-NC-ND LICENSE (http://creativecommons.org/licenses/by-nc-nd/4.0/).

EDITORIAL COMMENT

Nuclear Hmgb1

The Fix for the Failing Heart*

Angela Raucci, PhD,[a] Maurizio C. Capogrossi, MD[b,c]

Heart failure (HF) represents the final common pathway of different forms of heart disease, it affects patients across a broad age range, and its prevalence increases dramatically in the elderly population. Cardiomyocyte hypertrophy and cardiac fibrosis are hallmarks of HF (1). The mechanisms underlying the development and progression of different forms of HF remain an area of active investigation. The paper by Takahashi et al. (2) in this issue of *JACC: Basic to Translational Science* provides novel insights on the effect of high-mobility group box 1 protein (HMGB1) on deoxyribonucleic acid (DNA) damage response (DDR) in a mouse model of HF induced by chronic infusion of angiotensin II (Ang II).

SEE PAGE 234

DNA damage is induced by several insults, and DDR, which consists of a sophisticated network of signaling pathways involving cell cycle checkpoints, the DNA repair machinery, and transcriptional programs, is activated to restore the altered DNA and avoid genotoxic stress (3). The ataxia telangiectasia-mutated (ATM) kinase is 1 of the best-characterized DDR transducers, able to phosphorylate multiple DDR mediators, including the histone variant H2AX and the tumor suppressor p53, necessary to stop cell cycle and repair the DNA (4). If the repair fails, cells undergo apoptosis or cell cycle arrest and senescence (5).

DDR is observed also in post-mitotic cells such as cardiomyocytes, and its prolonged activation promotes apoptosis and detrimental cardiac remodeling after myocardial infarction (6,7). Persistent DDR plays a role in the pathogenesis of HF as well, and various types of damage, including oxidative DNA damage and DNA single- and double-strand breaks, have been found in cardiomyocytes of patients with end-stage HF and in the hearts of mice with cardiac hypertrophy induced by transverse aortic constriction or Ang II infusion (7–9). Genetic reduction of ATM attenuates left ventricular dysfunction and improves mortality in mice that underwent transverse aortic constriction by reducing nuclear factor-κB-mediated cardiac inflammation (8). Cardiomyocyte-specific genetic ablation or pharmacological inhibition of ATM reduces cardiac hypertrophy by preventing calcineurin expression and eukaryotic translation initiation factor 4E-binding protein 1 phosphorylation (9).

HMGB1 is a nonhistone chromatin protein involved in transcription regulation, DNA replication and repair, and nucleosome assembly (10–12). HMGB1 can be passively released by damaged cells or actively secreted by stressed immune cells and, once in the extracellular environment, it acts as an endogenous "alarmin" promoting inflammation or tissue repair and regeneration (13). Exogenous HMGB1 reduces cardiomyocyte contractility and induces hypertrophy and apoptosis, stimulates cardiac fibroblast activity, and cardiac stem cell proliferation and differentiation. Inhibitors of extracellular HMGB1 exert a protective function in experimental models of

*Editorials published in *JACC: Basic to Translational Science* reflect the views of the authors and do not necessarily represent the views of *JACC: Basic to Translational Science* or the American College of Cardiology.

From the [a]Unit of Experimental Cardio-Oncology and Cardiovascular Aging, Centro Cardiologico Monzino-IRCCS, Milan, Italy; [b]Division of Cardiology, Johns Hopkins Bayview Medical Center, Baltimore, Maryland; and the [c]Laboratory of Cardiovascular Science, National Institute on Aging, National Institutes of Health, Baltimore, Maryland.
This work was supported by Fondazione Cariplo (Research on Ageing diseases-2015) and Centro Cardiologico Monzino-IRCCS (Ricerca Corrente 2019) to Dr. Raucci. Dr. Capogrossib has reported that he has no relationships relevant to the contents of this paper to disclose.
All authors attest they are in compliance with human studies committees and animal welfare regulations of the authors' institutions and Food and Drug Administration guidelines, including patient consent where appropriate. For more information, visit the *JACC: Basic to Translational Science* author instructions page.

ISSN 2452-302X https://doi.org/10.1016/j.jacbts.2019.03.008

myocardial ischemia/reperfusion and in cardiomyopathies induced by mechanical stress, diabetes, infection, or chemotherapeutic drugs, mainly by reducing inflammation. In contrast, administration of recombinant HMGB1 after myocardial infarction induced by permanent coronary artery ligation promotes cardiac regeneration and preserves left ventricular function (14,15). Notably, mice overexpressing HMGB1 in cardiomyocytes (HMGB1-Tg) are protected from cardiac damage induced by myocardial infarction, genotoxic drugs, and hypertrophic stimuli, and maintenance of high levels of nuclear HMGB1 inhibits cardiomyocyte apoptosis (16–18). Thus, HMGB1 may play both beneficial and detrimental functions after a cardiac injury depending on the specific experimental model and its subcellular localization.

In the paper by Takahashi et al. (2), the authors identify a previously unknown mechanism by which nuclear HMGB1 prevents pathologic cardiac hypertrophy. The study starts with the intriguing observation that nuclear HMGB1 decreases and phosphorylation of ATM (p-ATM) and γ-H2AX expression increase in failing human hearts. Furthermore, nuclear HMGB1 levels in cardiomyocytes inversely correlate with cell hypertrophy, cardiac fibrosis, and brain natriuretic peptide serum levels. Lower HMGB1 content favors HF progression because preservation of high levels of nuclear HMGB1 in cardiomyocytes protects against pathologic cardiac remodeling. Indeed, HMGB1-Tg mice exhibit an attenuation of Ang II–mediated hypertrophy and fibrosis along with a reduction of the Ang II–induced increase in interventricular septum diameter and posterior wall diameter, and decrease of early to atrial wave ratio. Interestingly, the authors show that HMGB1 prevents detrimental DDR activation *in vivo* because Ang II–treated hearts of HMGB1-Tg mice exhibit lower levels of p-ATM and γ-H2AX compared with wild-type mice. Consistently, Ang II reduces the expression of HMGB1 before inducing p-ATM and γ-H2AX activation in isolated neonatal rat cardiomyocytes (NRCMs). In these cells, HMGB1 overexpression attenuates Ang II–mediated hypertrophic growth; in contrast, HMGB1 silencing enhances p-ATM and γ-H2AX activation.

The authors show (2) that HMGB1 interacts with ATM in NRCMs and suggest that this interaction is an important mechanism to prevent ATM phosphorylation in response to Ang II and subsequent activation of the hypertrophic pathways ERK1/2 and nuclear factor-κB. Future experiments will be required to address whether this interaction also occurs *in vivo*. Moreover, the study shows that ATM activation and activity is not exclusively dependent on HMGB1 because a synergistic cardioprotective effect is observed in HMGB1-Tg animals treated with both Ang II and the ATM inhibitor KU55933, confirming recently published evidence that pharmacologic inhibition of ATM prevents detrimental cardiac remodeling (9).

Overall, some open questions remain. First, persistent DDR promotes cardiac inflammation (8), and it needs to be addressed whether nuclear HMGB1 modulates Ang II–induced inflammatory cells recruitment and cytokines levels *in vivo* or NRCM acquisition of an inflammatory phenotype *in vitro*. Of note, previous studies have not characterized the inflammatory response of HMGB1-Tg animals to a cardiac insult (16–18). Second, the cross-talk between nuclear and extracellular activities of HMGB1 is still unexplored. Although Takahashi et al. (2) did not measure circulating HMGB1 in wild-type and HMGB1-Tg mice or in the supernatant of NRCMs after Ang II treatment, it is likely that the protein is present in the extracellular environment because hypertrophic stimuli are known to induce acetylation and nuclear translocation of HMGB1 in cardiomyocytes (16). Third, it will be important to assess whether extracellular HMGB1 induces DNA damage accumulation or DDR exacerbation, thereby contributing to heart remodeling. Last, nuclear HMGB1 affects the DNA damage repair machinery by modulating the interactions between repair enzymes and damaged DNA (12). Hence, it will be interesting to consider whether, in addition to targeting and inhibiting ATM, nuclear HMGB1 directly protects the DNA from the damage induced by detrimental hypertrophic stimuli.

Regardless of the aforementioned limitations, the study by Takahashi et al. (2) provides novel insights into the mechanism whereby nuclear HMGB1 safeguards the heart from pathological remodeling and supports recent findings that suppression of aberrant DDR may became a novel therapeutic strategy against HF development and progression. Thus, understanding how cardiomyocytes may preserve nuclear HMGB1 to sustain efficient DDR after a cardiac insult represents a potentially clinically relevant therapeutic challenge.

ADDRESS FOR CORRESPONDENCE: Dr. Maurizio C. Capogrossi, Division of Cardiology, Johns Hopkins Bayview Medical Center, 4940 Eastern Avenue, Baltimore, Maryland 21224. E-mail: mcapogr1@jhu.edu.

JACC: BASIC TO TRANSLATIONAL SCIENCE VOL. 4, NO. 2, 2019
APRIL 2019:248–50

REFERENCES

1. Strait JB, Lakatta EG. Aging-associated cardiovascular changes and their relationship to heart failure. Heart Fail Clin 2012;8:143–64.

2. Takahashi T, Shishido T, Kinoshita D, et al. Cardiac nuclear high-mobility group box 1 ameliorates pathological cardiac hypertrophy by inhibiting DNA damage response. J Am Coll Cardiol Basic Trans Science 2019;4:234–47.

3. Branzei D, Foiani M. Regulation of DNA repair throughout the cell cycle. Nat Rev Mol Cell Biol 2008;9:297–308.

4. Shiloh Y, Ziv Y. The ATM protein kinase: regulating the cellular response to genotoxic stress, and more. Nat Rev Mol Cell Biol 2013;14:197–210.

5. Sulli G, Di Micco R, d'Adda di Fagagna F. Crosstalk between chromatin state and DNA damage response in cellular senescence and cancer. Nat Rev Cancer 2012;12:709–20.

6. Shukla PC, Singh KK, Quan A, et al. BRCA1 is an essential regulator of heart function and survival following myocardial infarction. Nature Communications 2011;2:593.

7. Siggens L, Figg N, Bennett M, Foo R. Nutrient deprivation regulates DNA damage repair in cardiomyocytes via loss of the base-excision repair enzyme OGG1. FASEB J 2012;26:2117–24.

8. Higo T, Naito AT, Sumida T, et al. DNA single-strand break-induced DNA damage response causes heart failure. Nature Comm 2017;8:15104.

9. Nakada Y, Nhi Nguyen NU, Xiao F, et al. DNA damage response mediates pressure overload-induced cardiomyocyte hypertrophy. Circulation 2019;139:1237–9.

10. Bianchi ME, Agresti A. HMG proteins: dynamic players in gene regulation and differentiation. Curr Opin Genet Dev 2005;15:496–506.

11. Celona B, Weiner A, Di Felice F, et al. Substantial histone reduction modulates genomewide nucleosomal occupancy and global transcriptional output. PLoS Biol 2011;9:e1001086.

12. Liu Y, Prasad R, Wilson SH. HMGB1: roles in base excision repair and related function. Biochim Biophys Acta 2010;1799:119–30.

13. Raucci A, Di Maggio S, Scavello F, D'Ambrosio A, Bianchi ME, Capogrossi MC. The Janus face of HMGB1 in heart disease: a necessary update. Cell Mol Life Sci 2019;76:211–29.

14. Di Maggio S, Milano G, De Marchis F, et al. Non-oxidizable HMGB1 induces cardiac fibroblasts migration via CXCR4 in a CXCL12-independent manner and worsens tissue remodeling after myocardial infarction. Biochim Biophys Acta Mol Basis Dis 2017;1863:2693–704.

15. Limana F, Germani A, Zacheo A, et al. Exogenous high-mobility group box 1 protein induces myocardial regeneration after infarction via enhanced cardiac C-kit+ cell proliferation and differentiation. Circ Res 2005;97:e73–83.

16. Funayama A, Shishido T, Netsu S, et al. Cardiac nuclear high mobility group box 1 prevents the development of cardiac hypertrophy and heart failure. Cardiovasc Res 2013;99:657–64.

17. Kitahara T, Takeishi Y, Harada M, et al. High-mobility group box 1 restores cardiac function after myocardial infarction in transgenic mice. Cardiovasc Res 2008;80:40–6.

18. Narumi T, Shishido T, Otaki Y, et al. High-mobility group box 1-mediated heat shock protein beta 1 expression attenuates mitochondrial dysfunction and apoptosis. J Mol Cell Cardiol 2015;82:1–12.

KEY WORDS cardiac hypertrophy, DNA damage, heart failure, HMGB1

JACC: BASIC TO TRANSLATIONAL SCIENCE VOL. 4, NO. 2, 2019
© 2019 THE AUTHORS. PUBLISHED BY ELSEVIER ON BEHALF OF THE AMERICAN COLLEGE OF CARDIOLOGY FOUNDATION. THIS IS AN OPEN ACCESS ARTICLE UNDER THE CC BY-NC-ND LICENSE (http://creativecommons.org/licenses/by-nc-nd/4.0/).

PRECLINICAL RESEARCH

Deletion of Sulfonylurea Receptor 2 in the Adult Myocardium Enhances Cardiac Glucose Uptake and Is Cardioprotective

Gregory Aubert, MD, PhD,[a,*] David Y. Barefield, PhD,[a,*] Alexis R. Demonbreun, PhD,[a,*] Mohun Ramratnam, MD,[b,*] Katherine S. Fallon, BS,[a] James L. Warner, BA,[a] Ann E. Rossi, PhD,[c] Michele Hadhazy, BS,[a] Jonathan C. Makielski, MD,[b] Elizabeth M. McNally, MD, PhD[c]

VISUAL ABSTRACT

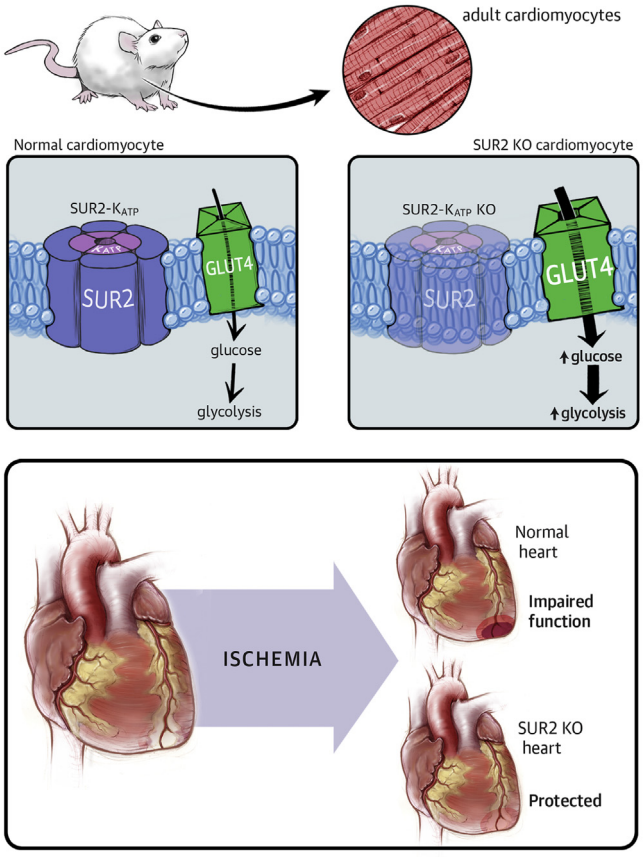

Aubert, G. et al. J Am Coll Cardiol Basic Trans Science. 2019;4(2):251–68.

HIGHLIGHTS

- **In the heart, SUR2 couples with a potassium channel to form an adenosine triphosphate-sensitive complex that responds to the energy state of the cell.**
- **The authors deleted SUR2 in adult cardiomyocytes and found a shift of the heart toward glycolytic metabolism, which is protective under cardiac stress.**
- **SUR2 was found to complex with glucose transporter type 4, the major glucose transporter.**
- **Drugs that antagonize the SUR2 receptor may be cardioprotective and useful for managing heart failure.**

From the [a]Center for Genetic Medicine, Northwestern University Feinberg School of Medicine, Chicago Illinois; [b]Division of Cardiology, Department of Medicine, University of Wisconsin-Madison, Madison, Wisconsin; and the [c]Section of Cardiology, University of Chicago, Chicago Illinois. *Drs. Aubert, Barefield, Demonbreun, and Ramratnam contributed equally to this work and are joint first authors. Supported by National Institutes of Health Grant No. HL 122109. The funders had no role in determining the experimental design or results interpretation. Dr. McNally has served as a consultant for Exonics, AstraZeneca, and Invitae;

ISSN 2452-302X https://doi.org/10.1016/j.jacbts.2018.11.012

JACC: BASIC TO TRANSLATIONAL SCIENCE VOL. 4, NO. 2, 2019
APRIL 2019:251–68

ABBREVIATIONS AND ACRONYMS

2DG = 2-deoxy-D-glucose

EDTA = ethylenediaminetetraacetic acid

FL Ex5 = LoxP sites flanking exon 5

GFP = green fluorescent protein

GLUT = glucose transporter

HEK293T = human embryonic kidney 293T

K_{ATP} = adenosine triphosphate–sensitive potassium

Kir = inward rectifying potassium channel

LVDP = left ventricular developed pressure

MCM = αMHC-MerCreMer

PCR = polymerase chain reaction

SUR = sulfonylurea receptor

SUMMARY

The adult myocardium relies on oxidative metabolism. In ischemic myocardium, such as the embryonic heart, glycolysis contributes more prominently as a fuel source. The sulfonylurea receptor 2 (SUR2) was previously implicated in the normal myocardial transition from glycolytic to oxidative metabolism that occurs during adaptation to postnatal life. This receptor was now selectively deleted in adult mouse myocardium resulting in protection from ischemia reperfusion injury. SUR2-deleted cardiomyocytes had enhanced glucose uptake, and SUR2 forms a complex with the major glucose transporter. These data identify the SUR2 receptor as a target to shift cardiac metabolism to protect against myocardial injury. (J Am Coll Cardiol Basic Trans Science 2019;4:251–68) © 2019 The Authors. Published by Elsevier on behalf of the American College of Cardiology Foundation. This is an open access article under the CC BY-NC-ND license (http://creativecommons.org/licenses/by-nc-nd/4.0/).

Adenosine triphosphate–sensitive potassium (K_{ATP}) channels respond to intracellular adenosine diphosphate–ATP ratio (1–4). In excitable cells and states where adenosine diphosphate is high, K_{ATP} channels open, allowing potassium efflux and cellular hyperpolarization. Correspondingly, high-ATP states promote K_{ATP} channel closure and cellular depolarization. Changes in membrane potential trigger a cascade of responses including the opening of voltage-sensitive calcium channels accompanied by an increase in intracellular calcium and shortening of the action potential to make the heart energetically more efficient (5,6). K_{ATP} channels contain 2 subunits, an inwardly rectifying potassium ion channel (Kir) (Kir6.1 or Kir6.2) and the sulfonylurea receptor (SUR1 or SUR2) (7–10). SUR2-contaning K_{ATP} channels are enriched in the heart, skeletal muscle, and vascular smooth muscle, where they regulate a range of physiological effects including cardiac stress response, blood pressure, and vascular tone (2). The major ventricular cardiomyocyte K_{ATP} channel is composed of SUR2 and Kir6.2, encoded by *ABCC9* and *KCNJ11,* respectively. In the mouse, genetic deletion of Kir6.2 leads to calcium overload and myocardial damage (5). Loss of Kir6.2 also leads to enhanced myocardial damage in the setting of hypertension and toxemia (11,12). Taken together, these studies describe enhanced susceptibility to stress in the cardiomyocyte lacking the Kir component of functional K_{ATP} channels.

We previously generated and characterized mice with 2 different deletions in SUR2. The first was a global deletion in which exons 14 to 18 of *Abcc9* were removed (13). These exons encode the first nucleotide-binding domain of SUR2 and with this deletion no full-length protein was detectable. This model, now referred to as SUR2-Ex14/18, developed hypertension, episodic coronary artery vascular spasm, bradycardia, and sudden death (13). Deleting *Kcnj8,* which encodes Kir6.1 and is the major component of vascular smooth muscle K_{ATP} channels, induced a similar phenotype (14). The similar phenotype between Kir6.1 and SUR2-deleted mice supported the notion that vascular spasm arises from loss of SUR2-Kir6.1 K_{ATP} channels in vascular smooth muscle.

The physiological role of SUR2-K_{ATP} channels is complex. Although loss of SUR2 results in vascular spasm and sudden death, it was also associated with protection from ischemic insult in surviving animals (15). SUR2 Ex14/18 mice were found to have reduced infarct size after global ischemia compared with normal mice, and therefore, protection from ischemia occurred in the absence of SUR2-K_{ATP} channels. We hypothesized that the continual vasospasm present in these animals was sufficient to trigger a preconditioned-like myocardium that was more resistant to stress. An alternative hypothesis implicated a smaller protein produced from the *Abcc9* gene, called SUR2-55, as responsible for mediating cardiac protection (16,17). SUR2-55 remained intact

and is a founder of Ikaika Therapeutics. All other authors have reported that they have no relationships relevant to the contents of this paper to disclose.

All authors attest they are in compliance with human studies committees and animal welfare regulations of the authors' institutions and Food and Drug Administration guidelines, including patient consent where appropriate. For more information, visit the *JACC: Basic to Translational Science* author instructions page.

Manuscript received October 19, 2018; revised manuscript received November 24, 2018, accepted November 26, 2018.

and readily detectable in SUR2-Ex14/18 mice. To assess this hypothesis, we generated a distinct deletion strategy for *Abcc9* to ablate both full-length SUR2 and SUR2-55. This mouse model, SUR2-Ex5, died in the neonatal window with cardiomyopathy, further suggesting a critical role for SUR2-55 in cardiac adaptation to postnatal life (18). We specifically found that SUR2-Ex5 mice failed to normally transition from glycolytic metabolism that is present in fetal myocardium to the postnatal oxidative metabolic state (18).

To address the role of SUR2 in the adult myocardium, we generated adult mice with a conditional ablation of *Abcc9*/SUR2 in the ventricular myocardium. These mice, referred to as cardiac-deleted SUR2 mice, survive with a mild reduction in left ventricular function. Cardiac-deleted SUR2 mice displayed protection from myocardial ischemia and augmented cardiomyocyte glucose handling. We found that SUR2 interacts with glucose transporter 4 (GLUT4), the major insulin-responsive glucose transporter in the adult cardiomyocyte. Correspondingly, SUR2-deleted cardiomyocytes had increased glycolysis. Taken together, these data present a model in which a myocardium favoring glucose metabolism may be better able to survive episodes of ischemic insult.

METHODS

ANIMALS. Mice with LoxP sites flanking exon 5 (Fl Ex5) of the *Abcc9* gene were generated by homologous recombination in mouse embryonic stem cells followed by transplantation into a pseudopregnant female. Fl Ex5 mice were crossed with the *αMHC-MerCreMer+* mouse line (Jackson B6.FVB(129)-*A1cf*$^{Tg(Myh6\text{-}cre/Esr1*)1Jmk}$/J) and maintained in a hemizygous state (19). These mice were bred and maintained on a C57BL/6J background. Animals were bred at Northwestern University and a subset was shipped to University of Wisconsin. Mice at both institutions were housed in environmentally controlled conditions in a specific pathogen free facility. All animals were housed and treated in accordance with the standards set by the Animal Care and Use Committees at Northwestern University and the University of Wisconsin-Madison.

TAMOXIFEN TREATMENT. Eight-week-old mice were treated via intraperitoneal injection with 50 μl of 50 mg/ml tamoxifen (T5648, Sigma-Aldrich, St. Louis, Missouri) diluted in sterile sunflower seed oil (S5007, Sigma-Aldrich) and passed through a 0.2-μm syringe filter. Tamoxifen was administered for 4 consecutive days to cause genomic recombination and deletion of *Abcc9* exon 5. Male and female mice were analyzed 2 to 4 weeks post-injection.

ECHOCARDIOGRAPHY. Cardiac function was assessed by echocardiography conducted under anesthesia (1% vaporized isoflurane in 100% O_2, 0.8 l/min). Echocardiography was performed using a Visual Sonics Vevo 2100 imaging system with an MS550D 22- to 55-MHz solid-state transducer (FujiFilm, Toronto, Canada). Short-axis M-mode images were acquired for analysis to provide heart chamber dimensions and calculate percent fractional shortening. Acquisition and analysis were conducted blinded to genotype.

TELEMETRY. Wireless cardiac TA11 ETA-F10 telemeters (Data Science International, Minneapolis, Minnesota) were surgically implanted subcutaneously in mice anesthetized with 3% vaporized isoflurane. The mice were allowed to recover for 3 days before data collection. Mice were housed individually and overnight electrocardiography recording were taken from 30 min of data when all animals showed clean traces. Mice were injected with 4 mg/kg isoproterenol intraperitoneally in phosphate-buffered saline and telemetric data was acquired for 30 min following the injection. Electrocardiography interval data were averaged for the duration of the recording with 1 average value reported per animal, as previously described (20).

ISOPROTERENOL CHALLENGE. To provide an alternate cardiac insult in vivo, we performed a chronic high-dose isoproterenol challenge (200 mg/kg intraperitoneally) twice daily for 6 days. This protocol has been shown to cause cardiomyocyte injury with minimal hypertrophic remodeling and regeneration (21). Animals were assessed for cardiac function with echocardiography 1 day before and 2 days after completion of the 6-day protocol, followed by sacrifice and tissue collection.

ISOLATED PERFUSED HEART ISCHEMIA AND REPERFUSION EXPERIMENTS. Male mice were anesthetized with inhaled 3% isoflurane and then euthanized with cervical dislocation. Hearts were rapidly excised and placed in chilled heparinized modified Krebs-Henseleit buffer (118-mM NaCl, 4.7-mM KCl, 1.2-mM $MgSO_4$, 1.2-mM KH_2PO_4, 25-mM $NaHCO_3$, 2.5-mM$CaCl_2$, 0.5-mM ethylenediaminetetraacetic acid [EDTA], and 5-mM glucose). Extracardiac tissue was dissected and discarded while the aorta was located. The aorta was then cannulated with the use of a 22-gauge cannula. The cannula was secured in place with 6-0 silk suture. Hearts were then perfused at a constant pressure of 80 mm Hg on a homemade Langendorff apparatus with modified Krebs-Henseleit

JACC: BASIC TO TRANSLATIONAL SCIENCE VOL. 4, NO. 2, 2019
APRIL 2019:251–68

buffer that was equilibrated with 95% O_2 and 5% CO_2 at 37°C. The left atrium was then excised and a fluid-filled balloon catheter constructed from a commercially available kit (Harvard Apparatus, Holliston, Massachusetts) was placed in the left ventricle. The balloon catheter was attached to an APT300 pressure transducer (Harvard Apparatus) and baseline left ventricular pressure was set between 5 and 10 mm Hg. Baseline cardiac function was recorded for 30 min. Mice were then subjected to 2 IR injury protocols. Protocol #1 subjected mice to 30 min of ischemia followed by 60 of reperfusion and protocol #2 subjected mice to 45 min of ischemia and 60 min of reperfusion. Hearts were paced at 360 beats/min via epicardial pacing leads with a Grass SD9 stimulator (Grass Instruments, West Warwick, Rhode Island). Left ventricular pressure was recorded throughout the experimental protocol and analyzed using LabChart Pro (ADInstruments, Colorado Springs, Colorado). Upon completion of reperfusion, hearts were rapidly removed from the Langendorff apparatus and perfused with 30 mM of KCl solution to arrest the hearts in diastole. Then the hearts were stained with 1% tetrazolium chloride solution for 10 min. The hearts were then sectioned into 7 to 8 slices. The sections were placed in 10% formalin and photographed the following day for the quantification of infarct size. Percent recovery was calculated by normalizing each time point against the baseline value. Hearts not meeting quality control (spontaneous beating, excessive baseline arrhythmias, or inability to develop a left ventricular (LV) pressure of >60 mm Hg when not paced) were removed (n = 1 heart).

CARDIOMYOCYTE ISOLATION. Mice were treated with 50 U heparin intraperitoneally 20 min before sacrifice. Mice were anesthetized under 5% vaporized isoflurane mixed with 100% oxygen. A thoracotomy was performed and the heart and lungs rapidly excised and submerged into ice-cold Tyrode solution without calcium (143-mM NaCl, 2.5-mM KCl, 16-mM $MgCl_2$, 11-mM glucose, 25-mM $NaHCO_3$, pH adjusted to 7.4). The ascending aorta was dissected out of the surrounding tissue and cannulated with an animal feeding needle (7900, Cadence Science, Staunton, Virginia) and secured with a 6-0 silk suture. The heart was initially perfused with 1 ml of ice-cold calcium-free Tyrode solution before being transferred to a Langendorff apparatus (Radnoti, Covina, California). Hearts were perfused with 37°C calcium-free Tyrode solution using a constant pressure (65-cm vertical distance between the buffer reservoir and cannula tip) for 1 to 2 min before perfusion for 5.5 min with digestion solution (0.15% collagenase type 2 [Worthington Biochemical, Lakewood, New Jersey], 0.1% 2,3-butanedione monoxime, 0.1% glucose, 100-U/ml penicillin/streptomycin, 112-mM NaCl, 4.7-mM KCl, 0.6-mM KH_2PO_4, 40-μM $CaCl_2$, 0.6-mM Na_2HPO_4, 1.2-mM $MgSO_4$, 30-μM phenol red, 21.4-mM $NaHCO_3$, 10-mM HEPES, and 30-mM taurine; pH adjusted to 7.4). The heart was removed from the cannula, triturated with a transfer pipette, and filtered through a 100-μm cell strainer. Cardiomyocytes were allowed to pellet by gravity for 7 min, followed by aspiration of digestion media and washing with stop buffer (formulated identically to digestion solution except with no collagenase and with 1% bovine serum albumin). Cells were again allowed to gravity pellet followed by a wash in stop buffer without bovine serum albumin. Cardiomyocytes were tolerated to calcium by adding Tyrode buffer with 0.3-mM $CaCl_2$ dropwise. Cell culture dishes were coated with 20 μg/ml laminin (23017-015; Gibco, Thermo Fisher Scientific, Waltham, Massachusetts) for 1 h at room temperature. Laminin solution was aspirated followed by plating of cardiomyocytes for 1 h to allow cell adhesion before experimentation.

POLYMERASE CHAIN REACTION AND GENOMIC DNA ANALYSIS. Genomic DNA was isolated from mouse tail tissues or total myocardial tissue samples. Polymerase chain reaction (PCR) was performed using primers flanking and within *Abcc9* exon 5 (forward primer: 5′-ATGTTGCTTCCTTGTGTTTAA TTCATGC-3′; reverse primer 1: 5′-GTTCTAGA-GAGTTCTCCATTCCGTTTG-3′; reverse primer 2: 5′-CGTTGCCAGTTAGAAAGTCAAAGTTAA-3′) and amplified using PCR with cycle conditions: 94°C, 30 s; 55°C, 60 s; 72°C, 60 s. Products were run on 2% agarose gel with ethidium bromide to visualize DNA recombination.

REVERSE TRANSCRIPTASE PCR AND QUANTITATIVE PCR ANALYSIS. Ribonucleic acid (RNA) was isolated from whole heart tissue and isolated cardiomyocytes. Samples were immediately placed in TRIzol (Ambion Diagnostics, Austin, Texas) and disrupted using a bead homogenizer (BioSpec, Bartlesville, Oklahoma), followed by centrifugation for 3 min at 12,000 × *g* at 4°C. Supernatant was mixed with one-fifth volume of chloroform and the tubes were incubated for 5 min at room temperature with periodic shaking, followed by centrifugation for 15 min at 12,000 × *g* at 4°C. RNA was extracted from the upper aqueous phase. RNA extraction was performed using the Aurum Total RNA Mini Kit (Bio-Rad Laboratories, Hercules, California) with DNAseI digestion, following the manufacturer's guidelines. Complementary DNA was synthesized using qScript cDNA SuperMix (Quanta Biosciences, Gaithersburg, Maryland) from 1 μg of RNA per sample, following the manufacturer's guidelines. Reverse

transcriptase PCR was performed on *Abcc9* to detect the removal of exon 5 from the messenger RNA using primers recognizing exon 4 and the exon 6/7 junction (forward: 5′- GTGCAAATTCATCATAACACGTG-3′; reverse: 5′-CATATCTTCTGACCCGGATGAC-3′). For all reactions, 35 cycles were performed with annealing at 63°C for 30 s and extension at 72°C for 1 min.

Quantitative PCR was performed using iTaq universal SYBR Green supermix (Bio-Rad) in a CFX96 Real-Time PCR Detection System (Bio-Rad). Control reactions were performed with RNA processed using the same method but without reverse transcriptase. Total *Abcc9* expression was assessed using primers designed against the exon 40/3′UTR junction (forward: 5′-TCATTCTCTGCATCGGGTTCAC-3′; reverse: 5′-GACGGTAGGCATTGAAGTACTTG). *Gapdh* was used as the reference gene for normalization (forward: 5′-TTGTGATGGGTGTGAACCACGA-3′; reverse: 5′-AGCCCTTCCACAATGCCAAAGT-3′). All quantitative PCR primer sequences are listed in Supplemental Table 1. For all reactions, 40 cycles were performed with annealing and extension at 60°C for 70 s total. Melt curves of the reaction products were obtained for each primer set using SybrGreen master mix. Quantitative PCR data were analyzed using the ΔΔCq method.

FASTING AND INSULIN CHALLENGE. Mice were fasted for 5 h, during which water was available. Mice were injected with sterile saline as control (minus insulin) or 2 mU/g insulin via intraperitoneal injection. Mice were sacrificed 30 or 60 min post-insulin injection and tissues were immediately harvested. For the 0-min time point, mice were only fasted.

CELL CULTURE. Human embryonic kidney 293T (HEK293T) cells were obtained from ATCC (CRL-11268, American Type Culture Collection, Manassas, Virginia). Cells were grown in Dulbecco's modified Eagle media supplemented with 10% fetal bovine serum and 1% penicillin/streptomycin (Thermo Fisher Scientific, Waltham, Massachusetts) in a 37°C incubator with 5% CO2.

TRANSFECTIONS. Cultured HEK293T cells were transfected with Glut4-myc (MR208202, OriGene, Rockville, Maryland) and either SUR2-green fluorescent protein (GFP), SUR55-GFP, or KIR6.2-GFP using FuGENE HD transfection reagent (Promega, Madison, Wisconsin). Cells were lysed 24 h post-transfection.

COIMMUNOPRECIPITATION. Cultured HEK293T cells were rinsed once with ice-cold phosphate buffered saline and lysed with radioimmunoprecipitation assay buffer (89900, Thermo Fisher Scientific, Rochester, New York) supplemented with polymethanesulfonyl fluoride- and EDTA-free protease inhibitor cocktail tablets (11836170001, Roche, Indianapolis, Indiana). Cells were scraped from the plate with a chilled cell-scraper (08-100-241, Thermo Fisher Scientific) and transferred to Eppendorf tubes on ice. Lysates were vortexed and triturated with an insulin syringe (14-829-1A, Thermo Fisher Scientific). Whole hearts were homogenized in radioimmunoprecipitation assay buffer supplemented with polymethanesulfonyl fluoride- and EDTA-free protease inhibitor cocktail tablets using a Dounce tissue grinder. Lysates were centrifuged at 10,000 × *g* for 5 min at 4°C and the supernatant was stored at -80°C until use; 500-μg protein (cells) or 1,000-μg protein (tissue) was cleared by nutating with 75-μl protein A/G beads (IP05, Millipore, Burlington, Massachusetts) and resuspended in lysis buffer for 1 h at 4°C. Cleared lysates were incubated with 3-μg anti-myc antibody (cells), 3-μg anti-Glut4 (tissue), or rabbit immunoglobulin G (31235, Thermo Fisher Scientific) for 3 h at 4°C on a nutator, followed by addition of 50-μl protein A/G beads and another 3-h incubation on a nutator at 4°C. Beads were washed 3 times with lysis buffer and centrifuged at 1000 × *g* for 1 min. Following the final wash, sample was eluted by addition of 25 μl of 2× Laemmli sample buffer (161-0737, Bio-Rad) with β-mercaptoethanol and incubated at room temperature for 30 min, 15 μl of urea buffer was then added before the sample was pipetted off the beads and stored at -20°C before being analyzed by sodium dodecyl sulfate polyacrylamide gel electrophoresis.

PROTEIN ISOLATION. Hearts were harvested and flash-frozen. TES buffer (20-mmol/l Tris, 250-mmol/l sucrose, 1-mmol/l EDTA, pH 7.4) with 1× complete protease (4693132001, Sigma-Aldrich) and phosphatase inhibitor tablets (4906837001, Sigma-Aldrich) was used for protein homogenization in a bead beater tissue homogenizer (BioSpec). Homogenized tissue samples were heated to 70°C in 2× Laemmli and ran on a 4% to 15% TGX gel (Bio-Rad).

MICROSOME PREPARATION. Total cardiac muscle membranes were prepared from age-matched mice using a protocol modified from (22,23). Hearts were excised, washed in phosphate buffered saline, and minced. Tissue was incubated in 1 ml high salt solution (2-mol/l NaCl, 20-mmol/l HEPES, pH 7.4, 5-mmol/l NaN_3) for 30 min at 4°C, centrifuged for 5 min at 1000 × *g* at 4°C, and the supernatant was discarded. The pellet was homogenized in 6 ml of TES buffer (20-mmol/l Tris, 250-mmol/l sucrose, 1-mmol/l EDTA, pH 7.4) using a Dounce homogenizer. The homogenate was centrifuged for 5 min at 1000 × *g* at 4°C. The pellet was rehomogenized in an additional 4 ml of TES buffer using a Dounce homogenizer. Both

supernatants were combined for a total of 10 ml. Homogenate was centrifuged for 10 min at 100 × *g* at 4°C. Supernatant was removed and the pellet was resuspended in 300-μl TES (input control). The supernatant was centrifuged again for 10 min at 5000 × *g* at 4°C. The supernatant was removed and the pellet was resuspended in 300-μl TES to yield a plasma membrane enriched fraction.

IMMUNOBLOTTING. Protein concentration was determined using Quick Start Bradford Dye Reagent (500-0205, Bio-Rad). Proteins were transferred to polyvinylidene difluoride membranes and blocked in StartingBlock T20 Blocking Buffer; antibodies were also diluted in StartingBlock T20 Blocking Buffer (Pierce, Rockford, Illinois). Primary antibodies used were: SUR2 TMD1 (24), Glut4 (07-1404, Millipore), Glut1 (ab15309, Abcam, Cambridge, Massachusetts), GFP (MBL598), insulin receptor β (3025, Cell Signaling, Danvers, Massachusetts), dystrophin (NCL-DYSB; Leica Biosystems, Buffalo Grove, Illinois), Phospho-FoxO1 (Thr24)/FoxO3a (Thr32) (9464, Cell Signaling), FoxO1 (2880, Cell Signaling), AKT (4685, Cell Signaling), phosphorylated AKT Thr308 (9275S, Cell Signaling) and phosphorylated AKT Ser473 (9271, Cell Signaling). Secondary antibodies conjugated to horseradish peroxidase were used at 1:5,000 (Jackson ImmunoResearch Laboratories, West Grove, Pennsylvania). SuperSignal West Pico Chemiluminescent Substrate (Thermo Fisher Scientific, Rochester, New York) and a Fluor Chem E FE0538 documentation system (Protein Simple, San Jose, California) were used for imaging. MemCode (Thermo Fisher Scientific) reversible stain was used as a loading control for total transferred protein. Images were quantified from at least 3 mice per genotype using Fiji software (National Institutes of Health, Bethesda, Maryland) normalized against loading controls.

CO-REGULATION DATABASE. Meta-analysis of gene expression was performed on CO-Regulation Database.

GLUCOSE UPTAKE ASSAY. 2-Deoxyglucose (2DG) uptake was measured using a colorimetric assay kit (ab136955, Abcam). Isolated adult cardiomyocytes were plated in a 96-well plate at a density of 1,500 cells/well in 100 μl of Krebs Ringers Phosphate HEPES buffer (20-mM HEPES, 5-mM KH_2PO_4, 1-mM $MgSO_4$, 1-mM $CaCl_2$, 136-mM NaCl, 4.7-mM KCl, pH 7.4) with 2% bovine serum albumin for 40 min. Cells were then treated with or without 1 mM of insulin for 20 min. Ten microliters of 10-mM 2DG were then added for 20 min. After 3 phosphate-buffered saline washes, the cells were harvested and 2DG was measured by colorimetric assay following the manufacturer's guidelines.

ISOLATED PERFUSED HEARTS FOR ^{13}C-GLUCOSE LABELING. Mice were anesthetized with inhaled 3% isoflurane and then euthanized with cervical dislocation, as described previously. Hearts were rapidly excised and placed in chilled heparinized modified Krebs-Henseleit buffer (118-mM NaCl, 4.7-mM KCl, 1.2-mM $MgSO_4$, 1.2-mM KH_2PO_4, 25-mM $NaHCO_3$, 2.5-mM$CaCl_2$, 0.5-mM EDTA, and 5-mM glucose). Extracardiac tissues were removed and discarded, and the aorta was cannulated with a 22-gauge cannula that was secured with 6-0 silk suture. Hearts were then perfused at a constant pressure of 80 mm Hg on a Langendorff apparatus with modified Krebs-Henseleit buffer equilibrated with 95% O_2 and 5% CO_2 at 37°C for 5 min. The media was then changed to ^{13}C-modified Krebs-Henseleit buffer containing 5 mM of ^{13}C-glucose in place of regular glucose. Hearts were perfused for 20 min followed by 5 min of washout with regular modified Krebs-Henseleit buffer. Hearts were then flash frozen.

METABOLITE ISOLATION. Flash frozen hearts from euthanized mice (metabolomic) or Langendorff apparatus (^{13}C-glucose labeling study) were powdered in a liquid nitrogen chilled mortar. One milliliter of methanol/water 80:20 (vol/vol) per sample was added. The homogenate was vortexed 1 min, and then centrifuge at ~20,160 x *g* for 15 min in a refrigerated centrifuge. Two hundred μl of supernatant was transferred into a tube with 800 μl of ice-cold methanol/water 80% (vol/vol). The protein pellet was used for protein quantitation using bicinchoninic acid assay. The metabolite-containing supernatant was then completely dried with a nitrogen gas N-EVAP (Organomation Associates, Inc. Berlin, Massachusetts). Dried metabolite pellets were conserved at -80°C until mass spectrometry processing.

MASS SPECTROMETRY. Services were performed by the Metabolomics Core Facility at Robert H. Lurie Comprehensive Cancer Center of Northwestern University. Fifty percent acetonitrile was added to the dried pellet tube for reconstitution, followed by centrifuged for 15 min at 20,000 *g*, 4°C. Supernatant was collected for liquid chromatography-mass spectrometry analysis. Samples were analyzed by high-performance liquid chromatography and high-resolution mass spectrometry and tandem mass spectrometry. The system uses a Thermo Q-Exactive in line with an electrospray source and an Ultimate3000 (Thermo Fisher Scientific) series high-performance liquid chromatography consisting of a binary pump, degasser, and auto-sampler outfitted with a Xbridge Amide column (Waters, Milford, Massachusetts) (dimensions of 4.6 mm × 100 mm and

a 3.5-μm particle size). The mobile phase A contained 95% (vol/vol) water, 5% (vol/vol) acetonitrile, 20-mM ammonium hydroxide, 20-mM ammonium acetate, pH 9.0; B was 100% acetonitrile. The gradient was as follows: 0 min, 15% acetonitrile; 2.5 min, 30% acetonitrile; 7 min, 43% acetonitrile; 16 min, 62% acetonitrile; 16.1 to 18 min, 75% acetonitrile; 18 to 25 min, 15% acetonitrile with a flow rate of 400 μl/min. The capillary of the ESI source was set to 275°C, with sheath gas at 45 arbitrary units, auxiliary gas at 5 arbitrary units and the spray voltage at 4.0 kV. In positive-negative polarity switching mode, an m/z scan range from 70 to 850 was chosen and MS1 data were collected at a resolution of 70,000. The automatic gain control target was set at 1×106 and the maximum injection time was 200 ms. The top 5 precursor ions were subsequently fragmented, in a data-dependent manner, using the higher energy collisional dissociation cell set to 30% normalized collision energy in MS2 at a resolution power of 17,500. Data acquisition and analysis were carried out by Xcalibur 4.1 software and Tracefinder 4.1 software, respectively (Thermo Fisher Scientific).

GLYCOGEN MEASUREMENT. Glycogen storage was measured using a colorimetric assay kit (ab169558, Abcam) using 100,000 isolated adult cardiomyocytes boiled in 200 μl of H_2O. The homogenate was processed following the manufacturer's guidelines.

STATISTICAL ANALYSIS. Statistical analyses were performed with Prism 6 (GraphPad Software, La Jolla, California). Data were tested for significance using a 2-tailed Student's *t* test or using 2-way analysis of variance. Significance was determined as $p \leq 0.05$. Data are presented as single values overlaid on graphs of the mean ± SEM. For the heart ischemia and reperfusion experiments, baseline data was compared using Prism and a Student's *t* test. Data was compared using a 2-way analysis of variance with Bonferroni's multiple comparisons test. The 2 cohorts that underwent ischemia protocols #1 and #2 were analyzed separately using a Student's *t* test.

RESULTS

TAMOXIFEN INDUCIBLE, CARDIAC-SPECIFIC DELETION OF *Abcc9*. Previously generated models of SUR2 mutations in mice resulted in distinct cardiovascular profiles. *Abcc9* mice engineered to lack exons 14 to 18, referred to as SUR2-Ex14/18 mice, survived but developed coronary artery spasm (13). This strategy resulted in global loss of full-length SUR2 but left intact the smaller splice form, SUR2-55 (**Figures 1A and 1B**). A second model, engineered to delete *Abcc9* exon 5 (SUR2-Ex5), ablated expression of both full-length SUR2 and the smaller SUR2-55 (**Figures 1A and 1B**) (18). This model displayed a more profound cardiovascular outcome with neonatal cardiomyopathy and lethality by 3 weeks of age (models are summarized in **Table 1**). To selectively ablate SUR2 expression in the adult myocardium, we now generated a conditional *Abcc9* floxed exon 5 allele in which LoxP sites flanked exon 5 of *Abcc9*. This mouse was then crossed to a tamoxifen-inducible αMHC-MerCreMer (MCM) transgenic mouse for cardiomyocyte-specific deletion (**Figure 1C**) (19). Adult mice 8 weeks of age received tamoxifen for 4 consecutive days (**Figure 1D**). Tamoxifen exposure resulted in recombination of genomic DNA only in the presence of Cre recombinase in cardiomyocytes but not in genomic DNA isolated from tail tissue (**Figure 1E**). Sequencing of reverse transcriptase PCR products showed the expected deletion of exon 5 in MCM Cre+ hearts, while exon 5 was retained in MCM Cre- hearts (**Figure 1F**). Quantitative PCR showed >75% reduction in total *Abcc9* transcript in tamoxifen exposed MCM Cre+ hearts (**Figure 1G**). We hypothesize non-*Myh6* expressing fibroblasts and endothelial cells found within the whole heart are the main source of the remaining *Abcc9* transcript in MCM Cre+ samples. SUR2 protein levels correlated with the quantitative PCR findings, demonstrating >75% reduction in SUR2 levels in MCM Cre+ hearts (**Figures 1H and 1I**). Transcript levels from the *Kcnj8* gene, which is localized 16 Kb from the *Abcc9* gene, was similar between MCM Cre- and MCM Cre+ hearts by quantitative PCR (**Figure 1J**). Thus, tamoxifen-induced cardiac-specific Cre expression induced deletion of *Abcc9* exon 5 resulting in decreased *Abcc9* messenger RNA and SUR2 protein expression.

REDUCED BASELINE HEART FUNCTION IN CARDIAC SUR2-DELETED MICE. To examine the role of SUR2 in the adult myocardium, we analyzed hearts from mice at 4 weeks following tamoxifen treatment. Body weight from both female and male mice, as well as heart weight to body weight ratios were not significantly different between the 2 groups (**Figures 2A and 2B**). Unlike the globally deleted exon 5 mice, which die in the neonatal period, mice with cardiac specific deletion of SUR2 survived (**Figure 2C**) (18). M-mode echocardiography showed abnormal cardiac function in tamoxifen-treated MCM Cre+ hearts (**Figure 2D**). Cardiac SUR2-deleted mice exhibited significantly reduced systolic function, with fractional shortening of 35.9 ± 1.8% in the MCM Cre- and 27.5 ± 1.9% in the MCM Cre+ hearts (**Figure 2E**). No significant difference in diastolic left ventricular internal diameter or left ventricular posterior wall thickness was noted between groups

FIGURE 1 Selective Ablation of *Abcc9* in the Adult CM

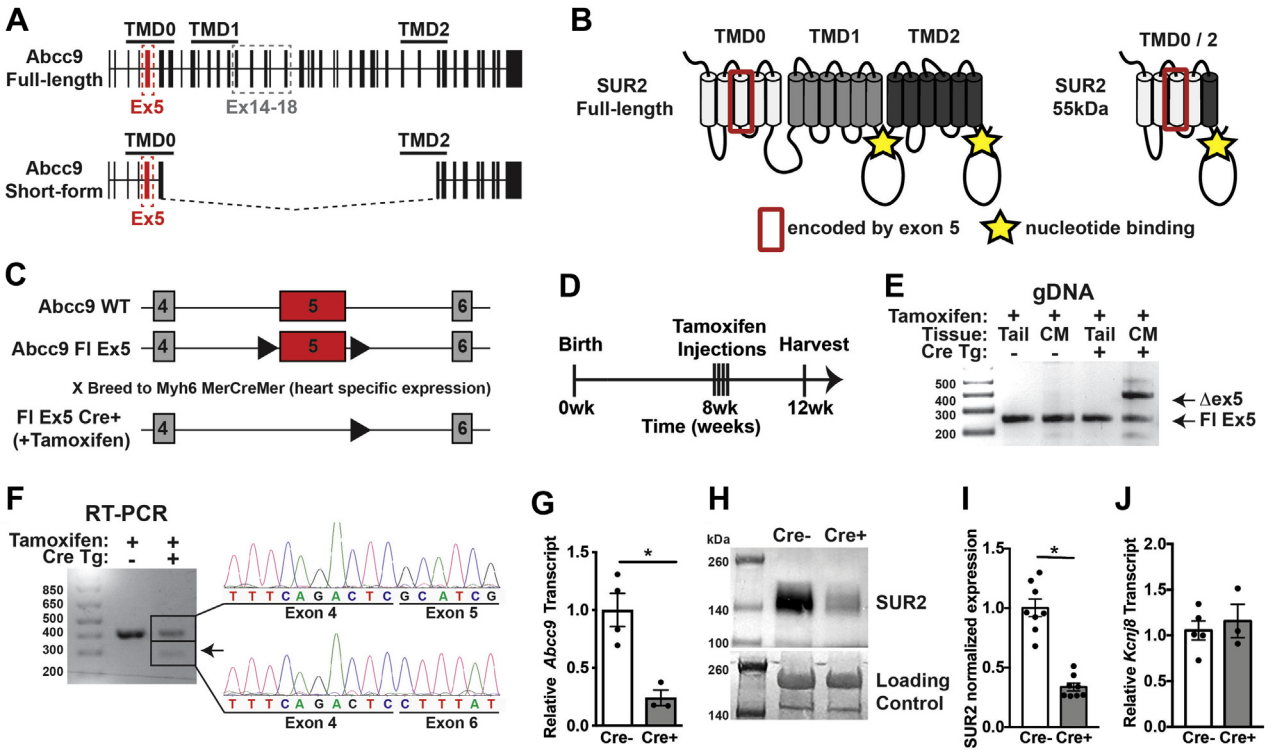

(A) *Abcc9* encodes sulfonylurea receptor 2 (SUR2), the major SUR expressed in the myocardium. Shown is a schematic of *Abcc9*-produced transcripts encoding SUR2 full-length and SUR2-55KDa forms. Exon 5 is shown in **red**. **(B)** Shown is a depiction of full-length SUR2 containing 3 transmembrane domains (TMDs): TMD0, TMD1, and TMD2. SUR2-55KDa protein contains TMD0 and a portion of TMD2. The position of the protein domains encoded by exon 5 is shown with a **red box**. **(C)** *Abcc9* gene targeting of exon 5 with LoxP sites **(black triangles)** flanking exon 5 **(red)**. These mice, referred to as Fl Ex5 (floxed exon 5), were bred to mice carrying a transgene which expresses Cre recombinase under the control of the *Myh6* promoter, MerCreMer (MCM), creating the cardiac Fl Ex 5 mouse model (19). **(D)** Tamoxifen dosing strategy for deletion of *Abcc9* exon 5. **(E)** Polymerase chain reaction (PCR) of genomic deoxyribonucleic acid (DNA) isolated from tail clip or cardiomyocytes (CMs) from MCM Cre– and MCM Cre+ Fl Ex5 mice using a 3-primer strategy to detect the deletion of exon 5 **(upper band)** or floxed exon 5 **(lower band)**. **(F)** Reverse transcriptase PCR (RT-PCR) from complementary DNA (cDNA) of tamoxifen-treated MCM Cre– and MCM Cre+ mice show the exon 5–including transcript **(upper band)** and the transcript generated from the exon 5 deletion **(lower band)**. Products confirmed by Sanger sequencing. **(G)** Quantitative PCR analysis of cDNA from ventricular myocardium from tamoxifen-treated MCM Cre– and MCM Cre+ mice show reduced total *Abcc9* transcript levels in Cre+ mice ($n = 4, 3$; $p = 0.008$). **(H, I)** Immunoblot analysis of hearts from tamoxifen-treated MCM Cre– and MCM Cre+ mice show reduction of full-length SUR2 protein ($n = 8$). *$p < 0.001$. **(J)** Quantitative PCR analysis of cDNA from isolated ventricular myocardium from tamoxifen-treated MCM Cre– and MCM Cre+ mice show equal transcript levels of *Kcnj8* ($n = 5, 3$). gDNA = genomic DNA; Tg = transgenic; WT = wild-type.

(Figures 2F and 2G). These data showed that loss of SUR2 in adult cardiomyocytes was sufficient to induce a reduction in cardiac performance.

LOSS OF SUR2 PROVIDES RESISTANCE AGAINST ISOPROTERENOL-INDUCED CARDIAC FUNCTIONAL DECLINE. A 6-day course of twice daily injections of high-dose isoproterenol (200 mg/kg) has been shown to induce myocardial injury resulting in cardiac dysfunction with mild hypertrophic remodeling (21). To assess the effect of loss of SUR2 after in vivo cardiac injury and ventricular remodeling, MCM Cre+ and MCM Cre– mice were injected repeatedly with isoproterenol to induce cardiac damage. Two days following the final dose of isoproterenol, cardiac function was assessed through M-mode echocardiography (Figure 3A). Heart weight to body weight ratio was not significantly different between the 2 groups (Figure 3B). MCM Cre– mice had reduced cardiac function after injury as evidenced by decreased percent fractional shortening, while MCM Cre+ mice did not show further deficit beyond the baseline decrease in fractional shortening (Figure 3C). Isoproterenol did not significantly alter diastolic left ventricular internal diameter in either group (Figure 3D). Left ventricular posterior wall thickness was modestly increased after isoproterenol challenge in both the MCM Cre+ and MCM Cre– groups (Figure 3E).

TABLE 1 Summary of Genetic and Phenotypic Differences Among *Abcc9* Mouse Models

Mouse Line	Ex 14/18	Ex5	Fl Ex5
Genetic mutation	Deletion exons 14–18	Deletion exon 5	Floxed exon 5
Isoforms expressed	Sur2-55	–	–
Tissues affected	All	All	Myh6 Cre, cardiac specific
Survival	Survives to adulthood	Early lethality 14–21 days	Survives to adulthood
Phenotype	Cardiac vascular spasm, cardioprotection	Metabolic dysregulation, heart failure	Metabolic dysregulation, heart abnormalities, cardioprotection
Citation	Chutkow et al., 2001 (42)	Fahrenbach et al., 2014 (18)	This report

Ex = exon; FL Ex5 = mice with LoxP sites flanking exon 5.

As expected, *Myh7* and *Nppa* mRNA expression measured by quantitative RT-PCR was increased in both MCM Cre- and MCM Cre in response to isoproterenol (Figure 3F). These results show that while loss of SUR2 in adult cardiomyocytes resulted in mildly depressed cardiac function, the SUR2-deleted hearts displayed resistance to isoproterenol-induced injury in vivo.

PRESERVED CARDIAC FUNCTION AND REDUCED INFARCT SIZE AFTER ISCHEMIA-REPERFUSION INJURY IN MCM Cre+ HEARTS. To further assess whether the loss of total SUR2 in the adult heart was cardioprotective during ischemic injury, MCM Cre+ and MCM Cre- hearts were subjected to ex vivo no-flow ischemia and reperfusion using a Langendorff constant pressure system. Maximum left ventricular developed pressure (LVDP) was decreased at baseline in MCM Cre+ mice (65.5 ± 4.0 mm Hg) compared with MCM Cre- (49.5 ± 2.0 mm Hg) (Figure 4A), consistent with baseline systolic impairment in MCM Cre+ hearts, while the percent recovery of LVDP following ischemia was significantly higher in MCM Cre+ hearts than control mice (Figure 4B). Correspondingly, at baseline, the maximal rate of pressure development was significantly decreased in tamoxifen-injected MCM Cre+ mice compared with MCM Cre- mice (Figure 4C). However, the percent recovery of the maximal rate of pressure development post-ischemia was significantly enhanced in cardiac SUR2-deleted hearts, showing a return to baseline, while the MCM Cre- hearts failed to return to baseline (Figure 4D). The maximal rate of pressure decline during relaxation was impaired at baseline in tamoxifen injected MCM Cre+ mice compared with MCM Cre- mice (Figure 4E). Again, a significantly improved percent recovery of the maximal rate of pressure decline during relaxation post-ischemia was seen in MCM Cre+ hearts compared with MCM Cre- control mice (Figure 4F). After both 30 or 45 min of global ischemia and 60 min of reperfusion, MCM Cre+ mice had significantly smaller infarct areas compared with MCM Cre- control hearts (30 min: MCM Cre- 33 ± 6.3, MCM Cre+ 13.6 ± 1.2; 45 min: MCM Cre- 19.5 ± 4.5, MCM Cre+ 15.5 ± 2.7) (Figures 5A to 5C). These data indicate that, despite causing decreased baseline function, cardiac-specific loss of SUR2 was cardioprotective during ischemic injury.

GLUT4 COMPLEXES WITH SUR2. The findings of cardioprotection in the conditional cardiac SUR2 hearts prompted further analysis. The previously generated SUR2-Ex5 mice developed metabolic abnormalities, failing to fully transition to oxidative metabolism in early postnatal life (18). Using a CO-Regulation gene expression database (25), we queried genes that were concordantly expressed with *ABCC9*/SUR2. Among the list of genes highly co-expressed with *Abcc9* was *KCNJ8*, which encodes Kir6.1, a known partner protein of SUR2 (Table 2) (26). *SLC2A4,* which encodes the insulin-sensitive glucose transporter GLUT4, was >90% concordant with *ABCC9* expression (Table 2). The *Slc2a4* transcript and GLUT4 protein levels were not altered in cardiac SUR2-deleted hearts (Figures 6A and 6B). *Slc2a1*, which encodes GLUT1, and the GLUT1 proteins were also similarly unaffected by cardiac SUR2 ablation. To evaluate the possibility that GLUT4 and SUR2 interact, HEK cells were transfected with constructs to express GLUT4 with SUR2-GFP, SUR55-GFP, or KIR6.2-GFP. Co-immunoprecipitation with GLUT4 from HEK cell lysates showed that SUR2, SUR55, and KIR6.2 each co-associated with GLUT4 (Figure 6C). SUR2 also co-immunoprecipitated with GLUT4 in lysates prepared from normal hearts confirming that this interaction was present with natively expressed proteins (Figure 6D). These data indicated that SUR2 and GLUT4 interact, directly or indirectly, and may be in the same membrane complex.

LOSS OF SUR2 ALTERS GLUCOSE UPTAKE AND GLUT4 LOCALIZATION. Translocation of GLUT4 to the sarcolemma increases glucose uptake by the cell and is directly stimulated by insulin signaling (27,28). To examine if the conditional deletion of SUR2 in

FIGURE 2 Adult Cardiac-Specific Ablation of *Abcc9* Is Associated With Reduced Cardiac Function

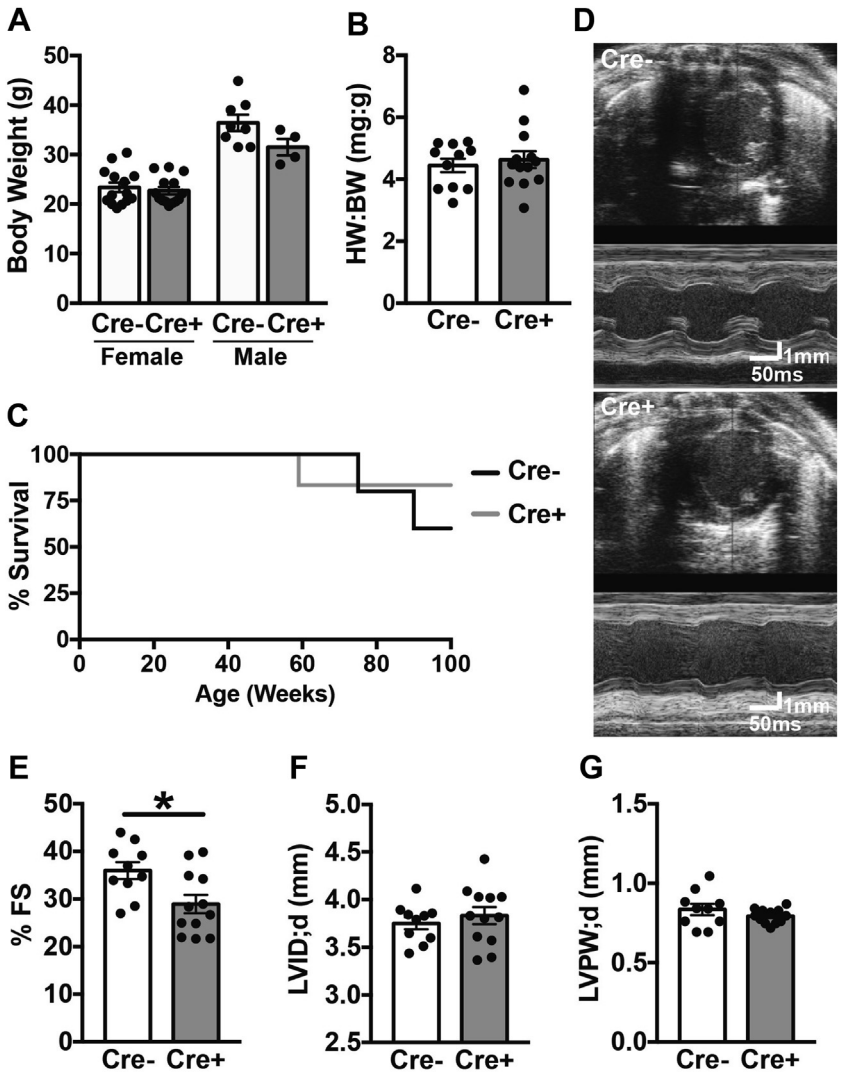

(A) After tamoxifen, cardiac-specific SUR2 deletion (MCM Cre+) mice were compared with identical genotype-drug treatment but without the transgene (MCM Cre–). Body weights were not significantly different between MCM Cre- and MCM Cre+ male or female mice (n = MCM Cre- 8 female mice, 14 male mice; MCM Cre+ 14 female mice, 4 male mice). **(B)** Heart weight to body weight ratios were unchanged when comparing MCM Cre+ to MCM Cre- (n = 11, 13). **(C)** Survival curves showed that MCM Cre+ and MCM Cre- mice had similar life spans (n = 5, 6). **(D)** Representative short-axis M-mode echocardiography images revealed systolic dysfunction. **(E)** Fractional shortening (FS) was decreased in MCM Cre+ mice (n = 10, 12). *p = 10,01. **(F)** Diastolic left ventricular internal diameter (LVID;d) was not altered in MCM Cre+ hearts (n = 10, 12). **(G)** Left ventricular posterior wall diameter (LVPW;d) was not different in MCM Cre+ mice (n = 10, 12). Abbreviations as in Figure 1.

cardiomyocytes had functional implications in glucose handling, cardiomyocytes were isolated from MCM Cre- and MCM Cre+ floxed exon 5 mice and incubated with 2DG. 2DG is an analog of glucose that can be taken up by the cell but cannot be metabolized (29). With insulin exposure, both MCM Cre- and MCM Cre+ cardiomyocytes increased 2DG uptake (Figure 7A). However, SUR2-deleted cardiomyocytes had greater 2DG uptake than those with intact SUR2, indicating enhanced insulin-stimulated glucose uptake in the absence of SUR2 (Figure 7A). We quantified GLUT4 in the plasma membrane of MCM Cre- and MCM Cre+ hearts 30 min after insulin stimulation and found a significant increase in membrane-enriched GLUT4 protein sampled from SUR2-deleted hearts (Figure 7B). The insulin receptor is a membrane

FIGURE 3 Loss of Cardiac *Abcc9* Mitigates Isoproterenol-Induced Cardiac Dysfunction

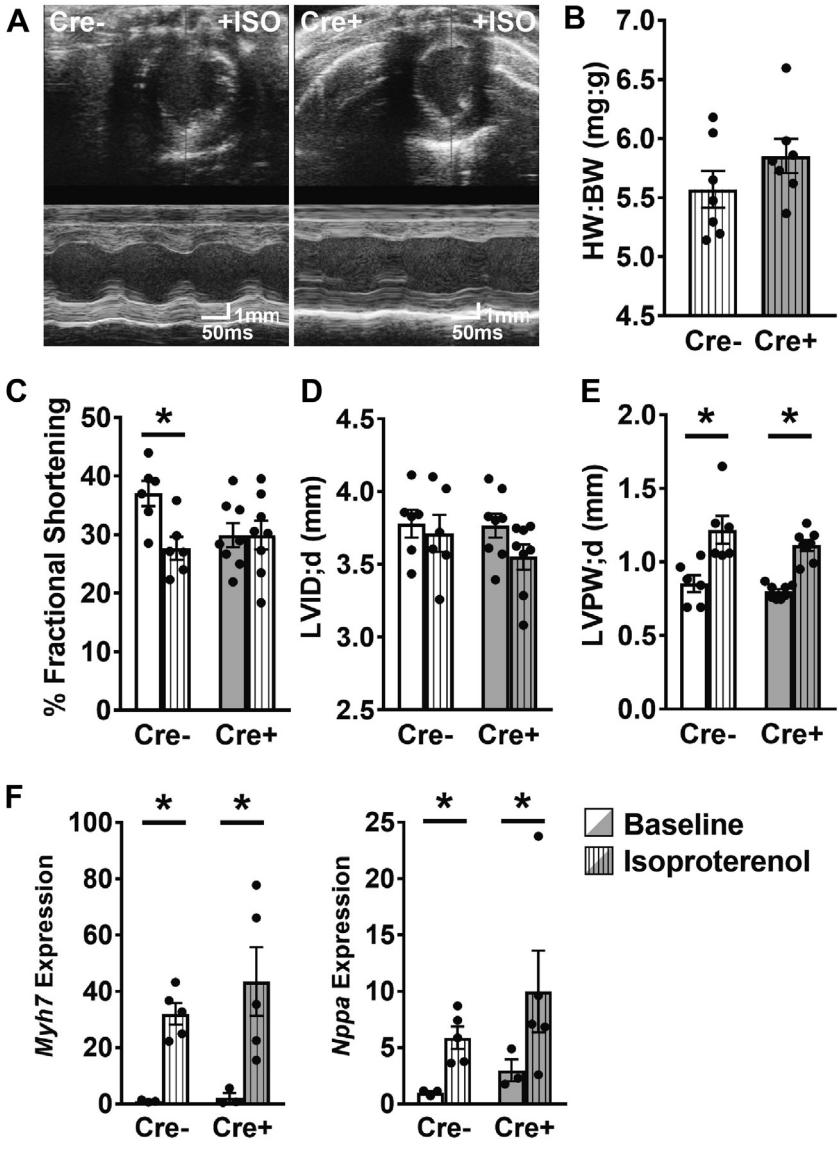

(A) Representative M-mode images of MCM Cre- and MCM Cre+ hearts were examined 2 days after the final isoproterenol injection. **(B)** Heart weight to body weight ratios showed no significant changes between genotypes (n = 7). **(C)** FS decreased with isoproterenol exposure in MCM Cre- mice while no reduction was noted in MCM Cre+ mice indicative of protection (n = 6, 8). *p = 0.03. **(D)** LVID;d was not altered in MCM Cre- or MCM Cre+ hearts with isoproterenol (n = 6, 8). **(E)** LVPW;d increased with isoproterenol exposure in both cohorts as expected (n = 6, 8). *p < 0.002. **(F)** Quantitative RT-PCR of hypertrophic markers *Myh7* and *Nppa* show both MCM Cre- and MCM Cre+ hearts showed the expected significant response to the isoproterenol challenge (n = 3, 5, 3, 5). *p = 0.04 *Myh7*, p = 0.001 *Nppa*. Abbreviations as in Figures 1 and 2.

protein that regulates glucose uptake by signaling through the AKT pathway, resulting in translocation of GLUT4-containing vesicles to the plasma membrane (30). Insulin receptor protein expression levels were similar in MCM Cre- and MCM Cre+ hearts (Figure 7C). However, the ratios of phosphorylated AKT(Thr308) to total AKT and phosphorylated AKT(Ser473) to total AKT were significantly increased in SUR2-deleted hearts after insulin stimulation (Figures 7D and 7E). FOXO1 is a transcription factor that regulates energy metabolism, specifically increasing cardiac fatty acid uptake and inhibiting

FIGURE 4 Adult Cardiomyocyte-Specific Ablation of *Abcc9* Reduced Baseline Cardiac Performance But Enhanced Recovery After Ischemic Injury

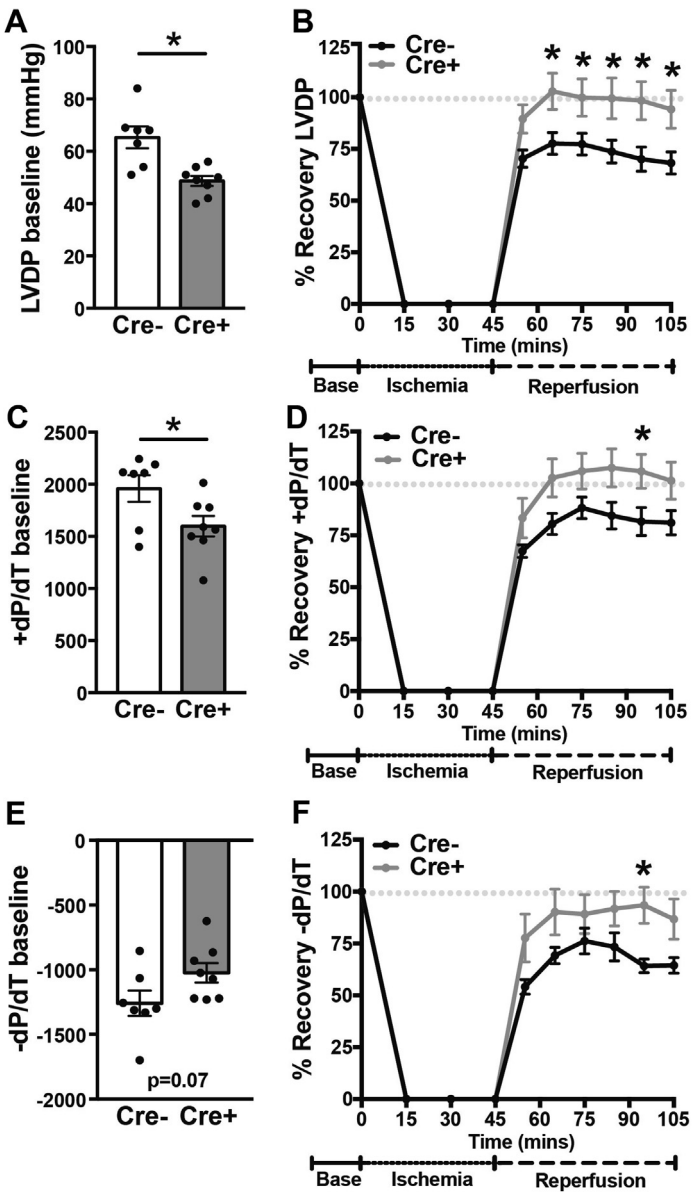

Excised hearts, MCM Cre- and MCM Cre+, were subjected to 30 min of baseline measurement, followed by 45 min of no-flow ischemia, which was followed by 60 min of reperfusion. **(A)** Baseline left ventricular developed pressure (LVDP) was reduced in MCM Cre+ hearts, consistent with echocardiography data. *p = 0.002. **(B)** Following ischemia, MCM Cre+ hearts show improved recovery of LVDP compared with MCM Cre- hearts. *p < 0.02. **(C)** Baseline left ventricular maximal contractility (maximal rate of pressure development [+dP/dT]) was reduced in MCM Cre+ hearts. *p = 0.04. **(D)** Recovery of left ventricular maximal contractility +dP/dT was more efficient in MCM Cre+ hearts than in MCM Cre- hearts (*p = 0.04). **(E)** Baseline left ventricular maximal relaxation (maximal rate of pressure decline during relaxation [-dP/dT]) was reduced in Cre+ hearts. *p = 0.07. **(F)** Recovery of left ventricular maximal relaxation -dP/dT was more efficient in MCM Cre+ hearts than in MCM Cre- hearts (* p = 0.01). **(A to F)** n = 7, 8 hearts. Abbreviations as in Figures 1 and 2.

glucose utilization (31-33). Moreover, the activity of FOXO is known to be negatively regulated through phosphorylation by AKT (34). We found the ratio of pFOXO1(Thr24)/FOXO1 was also significantly increased at baseline and after insulin stimulation in SUR2-deleted cardiomyocytes compared with controls (Figure 7F). These data show that in the absence of SUR2 there is an increase in insulin-dependent cardiac glucose uptake, an increase in GLUT4 in the membrane fraction and enhanced signaling. We conclude that this shift in glucose uptake can be adaptive in response to myocardial stress including isoproterenol infusion or infarct.

LOSS OF SUR2 ALTERS GLUCOSE UTILIZATION IN THE HEART AND LEADS TO INCREASED PHOSPHOCREATINE CONTENT. The cardioprotection observed after ischemia reperfusion without circulating insulin, along with increased baseline insulin signaling in SUR2-deleted cardiomyocytes prompted us to better delineate cardiac metabolism in the absence of insulin using increased glucose uptake by both insulin and non-insulin dependent mechanisms. We profiled 115 hydrophilic metabolites (n = 3 hearts per group) (Supplemental Table 2). Phosphoenolpyruvate, a key metabolite of the glycolysis pathway, was significantly increased in MCM Cre+ hearts compared with MCM Cre- hearts (Figure 8A), and this was accompanied by a significant increase in phosphocreatine, an intracellular energy store (Figure 8B). Glycogen stores were not significantly different in the absence of SUR2/*Abcc9* (Figure 8C). These results indicate altered activity of either the consuming or producing reaction of phosphoenolpyruvate (35). To evaluate whether these findings reflected increased glycolysis, we performed a ^{13}C-glucose labeling fractional enrichment on Langendorff-perfused hearts perfused with ^{13}C-glucose for sufficient time to allow TCA cycle metabolite incorporation of ^{13}C. The protocol included a wash-out with ^{12}C-glucose to unmask possible differences in the rate of early glycolysis marked by ^{13}C (Figure 8D). D-glyceraldehyde-3-phosphate and 3-phosphoglycerate showed a decrease in ^{13}C incorporation in MCM Cre+ compared with MCM Cre-, as reflected by the mass distribution vector MDV (Figure 8D). ^{13}C-pyruvate was differentially labeled between MCM Cre+ and MCM Cre- hearts. This result may be explained either by the duration of the washout time or by the different subcellular localization of pyruvate in the mitochondria versus cytoplasm. Interestingly ^{13}C-alanine-3 incorporation, which reflects the level of mitochondrial pyruvate (36), was increased in the MCM Cre+ hearts, supporting increased mitochondrial pyruvate

production from glucose in the SUR2-deleted heart (Supplemental Figure 1). Tricarboxylic acid cycle metabolites showed no significant differences in these assays (Supplemental Figure 1). Three of the 4 metabolites measured were significantly different between MCM Cre+ and MCM Cre- baseline hearts (**Figure 8E**). These data suggest altered glucose utilization in MCM Cre+ hearts and a low contribution of glucose in the TCA cycle.

DISCUSSION

REDUCED CARDIAC FUNCTION RELATED TO LOSS OF CARDIOMYOCYTE SUR2. Loss of SUR2 during development and in the neonatal window causes cardiomyopathy and death (18). The current investigation examined acute and chronic loss of SUR2 in in the adult myocardium. This genetic deletion moderately reduced cardiac function but generated hearts that were partially protected from ischemia-reperfusion and isoproterenol insults. Cardiac-deleted SUR2 mice had smaller infarct sizes and less functional impairment after isoproterenol infusions. The degree of cardiac functional impairment at baseline was measurable but overall relatively modest in cardiac SUR2-deleted mice, and mice with deletion of SUR2 in the heart did not have shortened life spans. These findings are in contrast to mice carrying this same genetic deletion of exon 5 throughout development and in early postnatal life (18). In SUR2-Ex5 mice, a profound dilated cardiomyopathy developed in perinatal mice and correlated with demise, typically by 3 weeks of age. During early postnatal life, the mammalian heart undergoes a transition from glycolytic to oxidative metabolism as it adapts to high oxygen tension (37,38). Heart failure is similarly accompanied by a shift to glycolytic metabolism, and this state can be viewed as adaptive in the early stage, as the use of glucose requires less oxygen to generate the same amount of ATP (39). However, over the longer term, use of glucose leads to cardiac lipid accumulation and lipotoxicity, and thus becomes maladaptive (40). In contrast, the inability to use glucose in insulin-resistant diabetic hearts and associated diabetic cardiomyopathy is associated with excessive cardiomyocyte reactive oxidative species production by increasing fatty acid flux and oxidation (41). Those models exemplify the important balance of substrate utilization and plasticity in the healthy heart. Substrate prioritization, such as increase in glucose utilization, can provide short-term advantages under stress conditions, but become maladaptive in the long term. The decrease in left ventricular function seen in cardiac-deleted SUR2

FIGURE 5 Adult Cardiac SUR2-Deleted Hearts Were Protected From Ischemia Reperfusion Injury

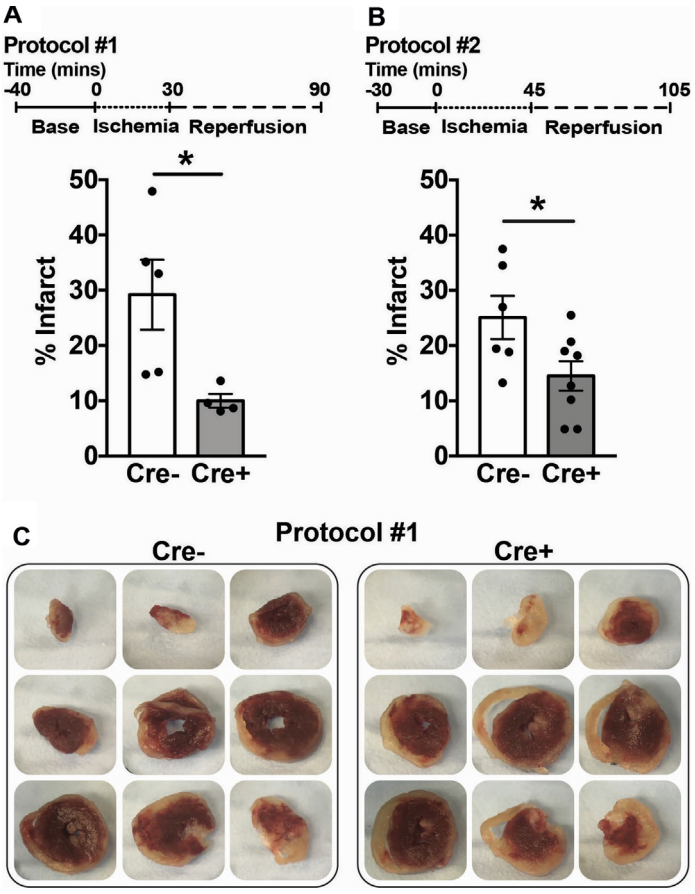

(A) Percent area of infarct was measured after 30 min of ischemia and was reduced in MCM Cre+ hearts (n = 5, 4). *p = 0.03. **(B)** Percent area of infarct after 45 min ischemia was also reduced in MCM Cre+ hearts (n = 6, 8). *p = 0.04. **(C)** Gross images of MCM Cre- and MCM Cre+ are shown after undergoing 30 min ischemia followed by reperfusion. The **white area** shows regions of infarct, while **pink areas** represent uninfarcted regions. Abbreviations as in **Figures 1 and 2**.

TABLE 2 CO-Regulation Database Analysis Shows Genes Concordantly Expressed With *Abcc9*

Gene	Experiments With *Abcc9*	Concordant (%)
ABRA	95	98.9
KCNJ8	403	98.5
YIPF7	117	98.3
ASB10	146	97.3
TCAP	194	91.7
SMR2	142	91.5
SLC2A4	331	91.2
CSRP3	271	91.1
NRAP	303	91.1

FIGURE 6 GLUT4 Is a SUR2-Interacting Protein

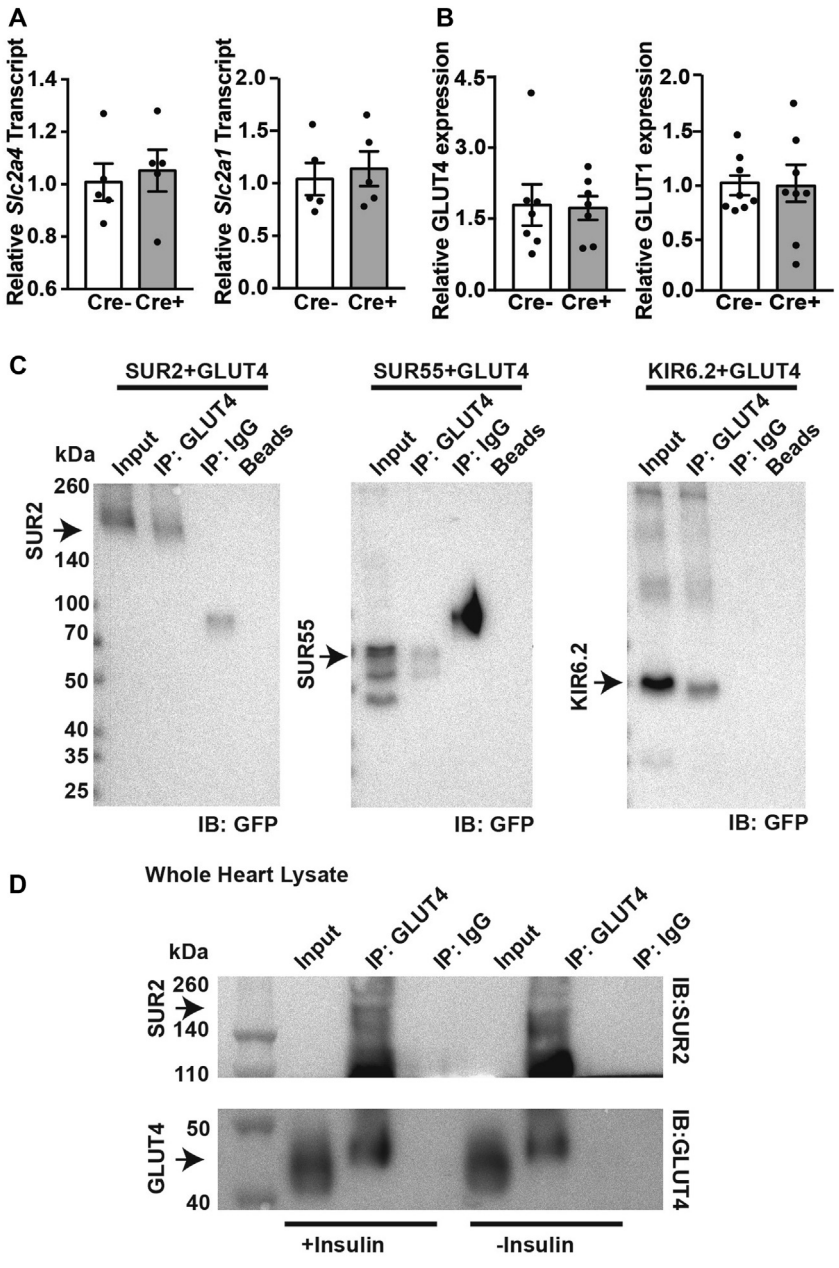

(A) Quantitative PCR analysis of cDNA of whole hearts from tamoxifen-treated Cre– and Cre+ showed similar transcript levels of *Slc2a4*, which encodes glucose transporter 4 (GLUT4), and *Slc2a1*, which encodes GLUT1 (n = 7 per group). **(B)** Cre– and Cre+ hearts express similar levels of GLUT4 and GLUT1 protein (n = 7 per group), as measured by quantitative immunoblotting. **(C)** SUR2, SUR55, and KIR6.2 each co-immunoprecipitated with GLUT4 when co-transfected in human embryonic kidney cells **(arrows)**. Immunoprecipitation with immunoglobulin G (IgG) and beads alone did not result in co-immunoprecipitation and are shown as controls. **(D)** Full-length SUR2 is co-immunoprecipitated with GLUT4 from normal hearts, indicating this interaction occurs with native proteins. The interaction between GLUT4 and SUR2 was not altered in the presence of insulin. Immunoprecipitation (IP) with IgG is shown as a control. IB = immunoblot; GFP = green fluorescent protein; other abbreviations as in Figures 1 and 2.

FIGURE 7 SUR2 Regulates Glucose Uptake and GLUT4 Localization in Adult Hearts

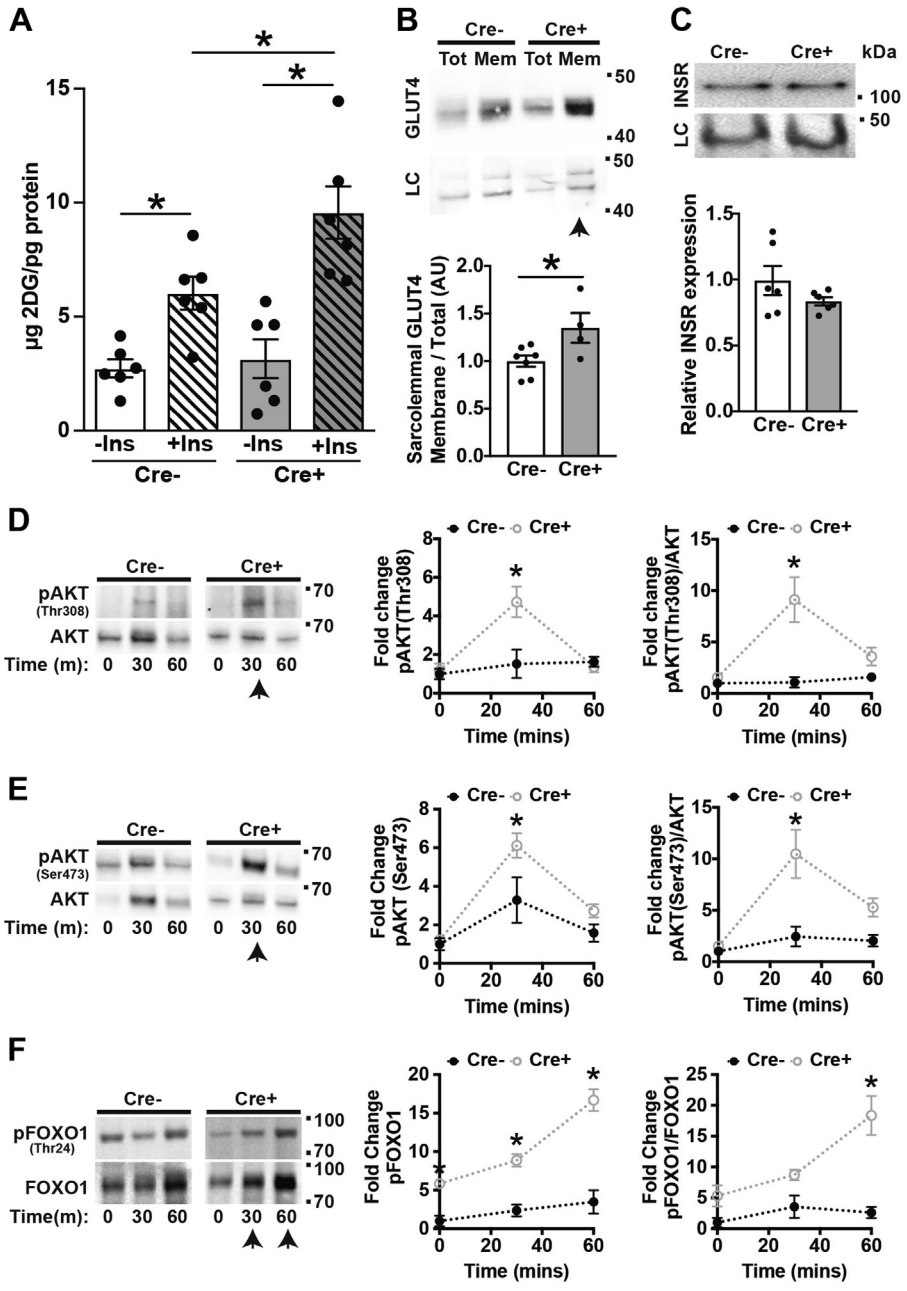

(A) Insulin stimulation significantly increased 2-deoxyglucose (2DG) uptake in both MCM Cre− and MCM Cre+ cardiomyocytes. 2DG levels were significantly elevated in MCM Cre+ cardiomyocytes compared with MCM Cre− cardiomyocytes post-insulin stimulation ($n > 7$). *$p < 0.05$. **(B)** Thirty minutes post-insulin injection MCM Cre+ hearts showed increased GLUT4 in the plasma membrane fraction of prepared microsomes **(black arrow)** ($n \geq 4$ per genotype). Total protein was used as a loading control (LC). Relative sarcolemmal GLUT4 is represented as the ratio of membrane fraction GLUT4 over total GLUT4. *$p < 0.03$. **(C)** Insulin receptor (INSR) protein levels were unchanged between MCM Cre− and MCM Cre+ hearts ($n = 6$); LC, loading control. **(D, E)** Thirty min post-insulin injection MCM Cre+ hearts showed a significant elevation **(black arrow)** in the ratio of phosphorylated AKT (pAKT) (Thr308)/AKT and phosphorylated AKT(Ser473)/AKT ($n = 4$). *$p < 0.001$ Thr308, *$p = 0.003$ Ser473. **(F)** Thirty and 60 min post-insulin injection, MCM Cre+ hearts showed a significant elevation in the ratio of phosphorylated FOXO1 (pFOXO1) (Thr24)/FOXO1 **(black arrows)** ($n = 4$). *$p < 0.0001$. -Ins = without insulin; +Ins = plus insulin; AU = arbitrary units; other abbreviations as in Figures 1 and 2.

FIGURE 8 Increased Glycolysis in SUR2/*Abcc9*-Ablated Hearts

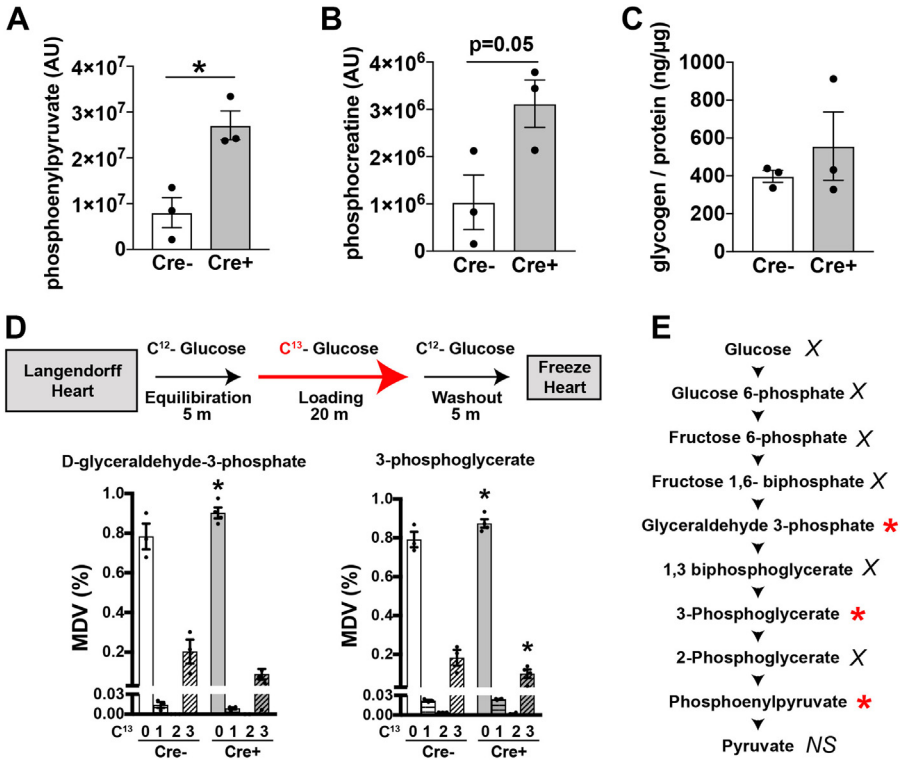

(A) Phosphoenolpyruvate was significantly increased in Cre+ hearts at baseline as measured using metabolomic profiling ($p = 0.01$). **(B)** Phosphocreatine levels were increased in MCM Cre+ hearts ($p = 0.05$). **(C)** The ratio of glycogen over protein was not significantly different between MCM Cre– and MCM Cre+ hearts. **(D)** Whole hearts were equilibrated on a Langendorff apparatus for 5 min and subjected to ^{13}C-glucose uptake for 20 min followed by 5 min with unlabeled ^{12}C-glucose and freezing for analysis. MCM Cre+ hearts had a significant increase in unlabeled carbon (^{13}C-0) D-glyceraldyhade-3-phosphate and 3-phosphoglycerate, while 3-phosphoglycerate also had a significant reduction in (^{13}C-3) ($n = 3$ MCM Cre–, $n = 4$ MCM Cre+ hearts). *$p = 0.05$. **(E)** Steps in the glycolysis pathway. **Red asterisks** indicate substrates that is statistically different between MCM Cre– and MCM Cre+ hearts. *X* indicates substrates that were not measured. *NS* indicates substrates that were measured and were not statistically different between MCM Cre– and MCM Cre+ hearts. AU = arbitrary units; MDV = mass distribution vector; other abbreviations as in Figures 1 and 2.

hearts at baseline is consistent with these same observations; however, this decrease of cardiac function was not associated with a shortened life span.

IMPROVED ADAPTATION TO SHORT-TERM STRESSORS. Strikingly, we observed that adult cardiac-deleted SUR2 hearts were able to withstand short-term cardiac stressors better than normal counterparts. Specifically, 2 different methods, high-dose isoproterenol infusion and ischemia reperfusion, showed that adult cardiac-deleted SUR2 hearts maintained function better after these insults. These findings suggest that the metabolic shift resulting from loss of SUR2 makes cardiomyocytes more resilient to acute stress. We expect that longer-term stressors would more adversely affect hearts lacking SUR2, as glucose utilization is less able to maintain energy supplies. We previously observed that SUR2 Ex14-18 hearts developed vascular spasm (13) and hypothesized that vascular spasm in this setting effectively pre-conditioned the myocardium, rendering it more likely to adapt to ischemic insult (15). We examined cardiac-deleted SUR2 for any evidence of vascular spasm using telemetry to look for ST-segment elevation but did not observe this (Supplemental Figure 2). The current model demonstrates that the loss of SUR2 in the cardiomyocyte itself is responsible for adaptation to short-term stressors.

INCREASED INSULIN SIGNALING IN CARDIOMYOCYTE-SUR2 HEARTS. We previously observed that SUR2 Ex14-18 skeletal muscle had increased glucose uptake despite no change in GLUT4 expression (42). In this study, we now found that SUR2-deleted hearts show

increased glucose uptake and utilization through at least 2 distinct mechanisms. First, GLUT4, the major insulin-sensitive transporter in the heart was found in a complex with SUR2. Co-expression of SUR1 and GLUT4 has been noted in some cell types (43). Both SUR2 and GLUT4 are enriched in striated muscles, including both cardiac and skeletal muscle. GLUT4 is dynamic and recruited to and from the plasma membrane in response to insulin (44,45). Consistent with this, we identified excessive glucose uptake in cardiomyocytes lacking SUR2. These data are consistent with a model where GLUT4 internalization and recycling may be delayed, leading to excessive glucose uptake, which alters glucose handling and energy storage as phosphocreatine. Secondly, we show that insulin signaling was increased in cardiac-deleted SUR2 hearts, reflected by an increase in AKT phosphorylation and activation of downstream targets such as FOXO.

Taken together, excessive glucose uptake into the myocardium, mediated by loss of SUR2 in cardiomyocytes, leads to reduced cardiac function and altered handling of glucose in this model that correlates with a cardioprotective metabolic and bioenergetic milieu. This increase in glucose uptake was accompanied by enhanced insulin signaling. Loss of SUR2 in cardiomyocytes and the resulting metabolic shifts generates a myocardium that is resistant to cardiac stress.

ADDRESS FOR CORRESPONDENCE: Dr. Elizabeth M. McNally, Northwestern University Feinberg School of Medicine, Center for Genetic Medicine, 303 East Superior Street, Lurie 7-123, Chicago, Illinois 60611. E-mail: elizabeth.mcnally@northwestern.edu.

PERSPECTIVES

COMPETENCY IN MEDICAL KNOWLEDGE: Sulfonylurea receptor antagonists remain in use to treat diabetes mellitus since they are largely effective. The cardiovascular safety of the sulfonylureas has been debated. Most commonly used sulfonylurea receptor agonists have greater affinity for SUR1, which is expressed in the pancreatic beta cell, compared with their affinity for SUR2.

TRANSLATIONAL OUTLOOK: The presence of agents that react with SURs indicates that these agents can be targeted and, in doing so, may offer a path to protecting the myocardium.

REFERENCES

1. Noma A. ATP-regulated K+ channels in cardiac muscle. Nature 1983;305:147–8.

2. Flagg TP, Enkvetchakul D, Koster JC, Nichols CG. Muscle KATP channels: recent insights to energy sensing and myoprotection. Physiol Rev 2010;90:799–829.

3. Kefaloyianni E, Bao L, Rindler MJ, et al. Measuring and evaluating the role of ATP-sensitive K+ channels in cardiac muscle. J Mol Cell Cardiol 2012;52:596–607.

4. Rubaiy HN. The therapeutic agents that target ATP-sensitive potassium channels. Acta Pharm 2016;66:23–34.

5. Zingman LV, Hodgson DM, Bast PH, et al. Kir6.2 is required for adaptation to stress. Proc Natl Acad Sci U S A 2002;99:13278–83.

6. Liu XK, Yamada S, Kane GC, et al. Genetic disruption of Kir6.2, the pore-forming subunit of ATP-sensitive K+ channel, predisposes to catecholamine-induced ventricular dysrhythmia. Diabetes 2004;53 Suppl 3:S165–8.

7. Tokuyama Y, Fan Z, Furuta H, et al. Rat inwardly rectifying potassium channel Kir6.2: cloning, electrophysiological characterization, and decreased expression in pancreatic islets of male Zucker diabetic fatty rats. Biochem Biophy Res Comm 1996;220:532–8.

8. Chutkow WA, Simon MC, Le Beau MM, Burant CF. Cloning, tissue expression, and chromosomal localization of SUR2, the putative drug-binding subunit of cardiac, skeletal muscle, and vascular KATP channels. Diabetes 1996;45:1439–45.

9. Ashford MLJ, Bond CT, Blair TA, Adelmair JP. Cloning and functional expression of a rat heart KATP channel. Nature 1994;370:456–9.

10. Clement JP, Kunjilwar K, Gonzalez G, et al. Association and stoichiometry of KATP channel subunits. Neuron 1997;18:827–38.

11. Kane GC, Behfar A, Dyer RB, et al. KCNJ11 gene knockout of the Kir6.2 KATP channel causes maladaptive remodeling and heart failure in hypertension. Hum Mol Genet 2006;15:2285–97.

12. Kane GC, Lam CF, O'Cochlain F, et al. Gene knockout of the KCNJ8-encoded Kir6.1 K(ATP) channel imparts fatal susceptibility to endotoxemia. FASEB J 2006;20:2271–80.

13. Chutkow WA, Pu J, Wheeler MT, et al. Episodic coronary artery vasospasm and hypertension develop in the absence of Sur2 K(ATP) channels. J Clin Invest 2002;110:203–8.

14. Miki T, Suzuki M, Shibasaki T, et al. Mouse model of Prinzmetal angina by disruption of the inward rectifier Kir6.1. Nat Med 2002;8:466–72.

15. Stoller D, Kakkar R, Smelley M, et al. Mice lacking sulfonylurea receptor 2 (SUR2) ATP-sensitive potassium channels are resistant to acute cardiovascular stress. J Mol Cell Cardiol 2007;43:445–54.

16. Shi N-Q, Ye B, Makielski JC. Function and distribution of the SUR isoforms and splice variants. J Mol Cell Card 2005;39:51–60.

17. Pu J-L, Ye B, Kroboth SL, McNally EM, Makielski JC, Shi N-Q. Cardiac sulfonylurea receptor short form-based channels confer a glibenclamide-insensitive KATP activity. J Mol Cell Card 2008;44:188–200.

18. Fahrenbach JP, Stoller D, Kim G, et al. Abcc9 is required for the transition to oxidative metabolism in the newborn heart. FASEB J 2014;28:2804–15.

19. Sohal DS, Nghiem M, Crackower MA, et al. Temporally regulated and tissue-specific gene manipulations in the adult and embryonic heart using a tamoxifen-inducible Cre protein. Circ Res 2001;89:20–5.

20. Barefield DY, Puckelwartz MJ, Kim EY, et al. Experimental modeling supports a role for MyBP-HL as a novel myofilament component in arrhythmia and dilated cardiomyopathy. Circulation 2017;136:1477–91.

21. Wallner M, Duran JM, Mohsin S, et al. Acute catecholamine exposure causes reversible myocyte injury without cardiac regeneration. Circ Res 2016;119:865–79.

22. Fuller W, Eaton P, Medina RA, Bell J, Shattock MJ. Differential centrifugation separates cardiac sarcolemmal and endosomal membranes from Langendorff-perfused rat hearts. Anal Biochem 2001;293:216–23.

23. Tepavcevic S, Koricanac G, Zakula Z, Milosavljevic T, Stojiljkovic M, Isenovic ER. Interaction between insulin and estradiol in regulation of cardiac glucose and free fatty acid transporters. Horm Metab Res 2011;43:524–30.

24. Kakkar R, Ye B, Stoller DA, et al. Spontaneous coronary vasospasm in KATP mutant mice arises from a smooth muscle-extrinsic process. Circ Res 2006;98:682–9.

25. Fahrenbach JP, Andrade J, McNally EM. The CO-Regulation Database (CORD): a tool to identify coordinately expressed genes. PLoS One 2014;9: e90408.

26. Bryan J, Munoz A, Zhang X, et al. ABCC8 and ABCC9: ABC transporters that regulate K+ channels. Pflugers Arch 2007;453:703–18.

27. Saltiel AR, Kahn CR. Insulin signalling and the regulation of glucose and lipid metabolism. Nature 2001;414:799–806.

28. Bryant NJ, Govers R, James DE. Regulated transport of the glucose transporter GLUT4. Nat Rev Mol Cell Biol 2002;3:267–77.

29. Yamamoto N, Ueda M, Sato T, et al. Measurement of glucose uptake in cultured cells. Curr Protoc Pharmacol 2011. Chapter 12:Unit 12.14.1–22.

30. Leto D, Saltiel AR. Regulation of glucose transport by insulin: traffic control of GLUT4. Nat Rev Mol Cell Biol 2012;13:383–96.

31. Ronnebaum SM, Patterson C. The FoxO family in cardiac function and dysfunction. Annu Rev Physiol 2010;72:81–94.

32. Chistiakov DA, Orekhov AN, Bobryshev YV. The impact of FOXO-1 to cardiac pathology in diabetes mellitus and diabetes-related metabolic abnormalities. Int J Cardiol 2017;245:236–44.

33. Xin Z, Ma Z, Jiang S, et al. FOXOs in the impaired heart: new therapeutic targets for cardiac diseases. Biochim Biophys Acta 2017;1863: 486–98.

34. Brown AK, Webb AE. Regulation of FOXO factors in mammalian cells. Curr Top Dev Biol 2018;127:165–92.

35. Buescher JM, Antoniewicz MR, Boros LG, et al. A roadmap for interpreting (13)C metabolite labeling patterns from cells. Curr Opin Biotechnol 2015;34:189–201.

36. Groen AK, Wanders RJ, Westerhoff HV, van der Meer R, Tager JM. Quantification of the contribution of various steps to the control of mitochondrial respiration. J Biol Chem 1982;257: 2754–7.

37. Warshaw JB. Cellular energy metabolism during fetal development. IV. Fatty acid activation, acyl transfer and fatty acid oxidation during development of the chick and rat. Dev Biol 1972; 28:537–44.

38. Piquereau J, Novotova M, Fortin D, et al. Postnatal development of mouse heart: formation of energetic microdomains. J Physiol 2010;588: 2443–54.

39. Azevedo PS, Minicucci MF, Santos PP, Paiva SA, Zornoff LA. Energy metabolism in cardiac remodeling and heart failure. Cardiol Rev 2013;21:135–40.

40. van der Vusse GJ, Glatz JF, Stam HC, Reneman RS. Fatty acid homeostasis in the normoxic and ischemic heart. Physiol Rev 1992;72: 881–940.

41. Shah MS, Brownlee M. Molecular and cellular mechanisms of cardiovascular disorders in diabetes. Circ Res 2016;118:1808–29.

42. Chutkow WA, Samuel V, Hansen PA, et al. Disruption of Sur2-containing K(ATP) channels enhances insulin-stimulated glucose uptake in skeletal muscle. Proc Natl Acad Sci U S A 2001;98: 11760–4.

43. Yee KK, Sukumaran SK, Kotha R, Gilbertson TA, Margolskee RF. Glucose transporters and ATP-gated K+ (KATP) metabolic sensors are present in type 1 taste receptor 3 (T1r3)-expressing taste cells. Proc Natl Acad Sci U S A 2011;108:5431–6.

44. Abel ED. Glucose transport in the heart. Front Biosci 2004;9:201–15.

45. Steinbusch LK, Schwenk RW, Ouwens DM, Diamant M, Glatz JF, Luiken JJ. Subcellular trafficking of the substrate transporters GLUT4 and CD36 in cardiomyocytes. Cell Mol Life Sci 2011;68: 2525–38.

KEY WORDS ABCC9, ischemia, potassium ATP channels, sulfonylurea

APPENDIX For supplemental tables and figures, please see the online version of this paper.

JACC: BASIC TO TRANSLATIONAL SCIENCE VOL. 4, NO. 2, 2019
© 2019 THE AUTHORS. PUBLISHED BY ELSEVIER ON BEHALF OF THE AMERICAN COLLEGE OF CARDIOLOGY FOUNDATION. THIS IS AN OPEN ACCESS ARTICLE UNDER THE CC BY-NC-ND LICENSE (http://creativecommons.org/licenses/by-nc-nd/4.0/).

TRANSLATIONAL PERSPECTIVE

Overcoming Barriers to Development of Novel Therapies for Cardiovascular Disease

Insights From the Oncology Drug Development Experience

Aarif Y. Khakoo, MD,[a] Nicole R. Yurgin, PhD,[b] Paul R. Eisenberg, MD, MPH,[c] Gregg C. Fonarow, MD[d]

SUMMARY

Despite the fact that cardiovascular disease (CVD) is the number 1 cause of death globally, investment in drug development and new drug approvals for CVD are precipitously declining. In contrast, the trajectory of both investment in development as well as new drug approvals for oncology have been increasing steadily over the same time frame. The factors that have spurred drug development in oncology may be applicable to new efforts to overcome barriers to drug development for CVD. Greater investment in basic research and application of expedited regulatory pathways have contributed to a lowering of development barriers in oncology. Barriers in implementation are also critical. More rapid adoption of guideline-based therapies and lower access barriers by payers have contributed to fewer implementation barriers for oncology therapeutics. There is substantially greater advocacy among patients and physicians for new oncology therapeutics, and such advocacy efforts are likely to have had a meaningful impact on lowering barriers to develop new oncology therapeutics. Broad support of patient and physician advocacy efforts directed towards CVD may help overcome existing development and implementation barriers to new drug development, thereby spurring more rapid progress in the fight to eradicate cardiovascular disease. (J Am Coll Cardiol Basic Trans Science 2019;4:269–74)
© 2019 The Authors. Published by Elsevier on behalf of the American College of Cardiology Foundation. This is an open access article under the CC BY-NC-ND license (http://creativecommons.org/licenses/by-nc-nd/4.0/).

Cardiovascular disease (CVD) is the number 1 cause of death globally and has been the leading cause of death in the United States for almost 100 years. It also results in substantial impairment of health status, disability, and increased health care expenditures. Because of improvements in lifestyle and treatments, the United States experienced a 60% reduction in age-adjusted death rates for CVD from 1950 to 1999 (1). Despite this extraordinary advancement for public health, recent data show that CVD mortality rates are no longer declining and, in fact, are increasing for some groups (2). The need to develop new therapies for CVD remains high. There have also been remarkable

From [a]Translational Medicine, Amgen, Inc., South San Francisco, California; [b]US Medical, Amgen, Inc., South San Francisco, California; [c]Amgen, Inc., South San Francisco, California; and the [d]Ahmanson-UCLA Cardiomyopathy Center, UCLA Division of Cardiology, Geffen School of Medicine at UCLA, Los Angeles, California. Drs. Khakoo and Yurgin are employees and shareholders of Amgen, Inc. Dr. Eisenberg is a former employee of and a shareholder of Amgen. Dr. Fonorow has received grants from the National Institutes of Health; and personal fees from Amgen, Bayer, AstraZeneca, Abbott, Novartis, Janssen, and Medtronic. All other authors have reported that they have no relationships relevant to the contents of this paper to disclose.

All authors attest they are in compliance with human studies committees and animal welfare regulations of the authors' institutions and U.S. Food and Drug Administration guidelines, including patient consent where appropriate. For more information, visit the *JACC: Basic to Translational Science* author instructions page.

Manuscript received January 17, 2019; accepted January 20, 2019.

ISSN 2452-302X https://doi.org/10.1016/j.jacbts.2019.01.011

ABBREVIATIONS AND ACRONYMS

ARNI = angiotensin receptor neprilysin inhibitor

ASCVD = atherosclerotic cardiovascular disease

CVD = cardiovascular disease

advances in cardiovascular (CV) basic and translational sciences with a plethora of promising targets for new therapies. Notwithstanding this potential for new therapies and great public health need, it is well recognized that over the past couple of decades there have been proportionally fewer CVD therapeutic candidates in all stages of drug development, including fewer new CVD drug approvals (3-6). Although substantial investments in large scale trials for CVD research continue, more investment seem to be shifting toward other therapeutic classes, such as oncology (3,4). CVD and oncology are the first and second leading causes of death, respectively, yet the investment trajectories are completely different. During the time that CVD drug approvals were declining, new drug approvals and investment in oncology increased significantly (3-6). Understanding the differences in trends and reasons for those differences may be informative and provide strategic insights into approaches used in oncology that can be applied in the treatment of CVD.

Several recent articles have thoroughly reviewed different reasons for the recent reduction in CVD drug development and compared it with the growing investment in oncology (3,4,7). Many factors contribute to more uncertainty and a lower near-term return on investment for CVD relative to oncology. Some factors are related to aspects of drug development and regulatory approval whereas others are related to market dynamics once a drug has been approved. For clarity, this paper will group similar barriers together and refer to the former as development barriers and the latter as implementation barriers (**Central Illustration**). Rather than discussing all these reasons in detail, this paper will focus on the barriers that seem to have been lowered for oncology to suggest similar strategies that may be used to overcome barriers and increase investment in CVD.

DRUG APPROVAL TRENDS AND DEVELOPMENT BARRIERS

In the 1980s, approximately 1 in 4 approvals for all new drugs and biologics were in the CVD therapeutic class whereas ~1 in 10 was in the oncology class (5). In relative terms, in the 1980s U.S. Food and Drug Administration (FDA) approvals for oncology therapies were approximately 20% of new CVD approvals; however, this has changed rapidly over the past few decades. Between 2010 and 2017, there were almost 2.5 times as many oncology FDA approvals as CVD approvals (**Figure 1**) (8).

One factor contributing to drug approvals is investment in basic research. A recent article shows that the speed of clinical and regulatory development is significantly shorter if basic science in the field reaches a point of scientific establishment (7). When comparing levels of federal funding, oncology has significantly more funding than CVD. In 2017, there was more than $6 billion in funding for cancer between the National Cancer Institute funding ($5.9 billion) and the Beau Biden Cancer Moonshot funding from the 21st Century Cures Act ($300 million) (9,10). The National Heart Lung and Blood Institute received one-half that amount of funding ($3.1 billion) in 2017 (9). In fact, among all the institutes at the National Institutes of Health, the National Cancer Institute has held the largest proportion of the budget since at least 1980 (3).

Even after this early-stage investment, the cost of clinical development is substantial. Development cost for a drug or class is a critical factor in return on investment calculations. A recent study analyzed cost data from more than 100 compounds beginning human testing from 1995 to 2007 and estimated the cost of developing a new drug at more than $2.5 billion (in 2013 dollars) (11). This cost estimate was almost 1.5 times higher than they had previously estimated for drugs that were approved a little more than a decade earlier (12). These data are consistent with the so-called "Eroom's law" (Moore's law spelled backwards) used to describe the phenomenon of the increasing cost of drug development over time (4). To our knowledge, there are no studies that compare the development costs for oncology and CVD; however, it has been shown that the registration-enabling trials for CVD are, in general, larger and longer trials than oncology trials (3).

Size and duration are 2 of the main determinants of clinical trial costs. Some of the reasons that CVD trials take longer include: 1) the need to show clinically significant improvement in clinical outcomes on a background of guideline-directed therapies instead of relying on surrogate markers; and 2) a very low tolerance for adverse effects. Potentially because of the success in treating large populations and the sheer number of people treated, there is, with few exceptions, a need to show clinically significant improvement in hard outcomes instead of relying on surrogates in CVD. Also, cardiologists are skeptical of surrogates because many have not successfully predicted CV-related outcomes. For example, the promise of high-density lipoprotein increases as a surrogate for CVD outcomes was not fulfilled when the outcomes trials were conducted. In addition, for drugs that have an impact on more-established

CENTRAL ILLUSTRATION The Development and Implementation Barriers That Impede the Generation of Novel Therapies for Cardiovascular Disease Could Be Overcome by a Cardiovascular Disease "Moonshot Program"

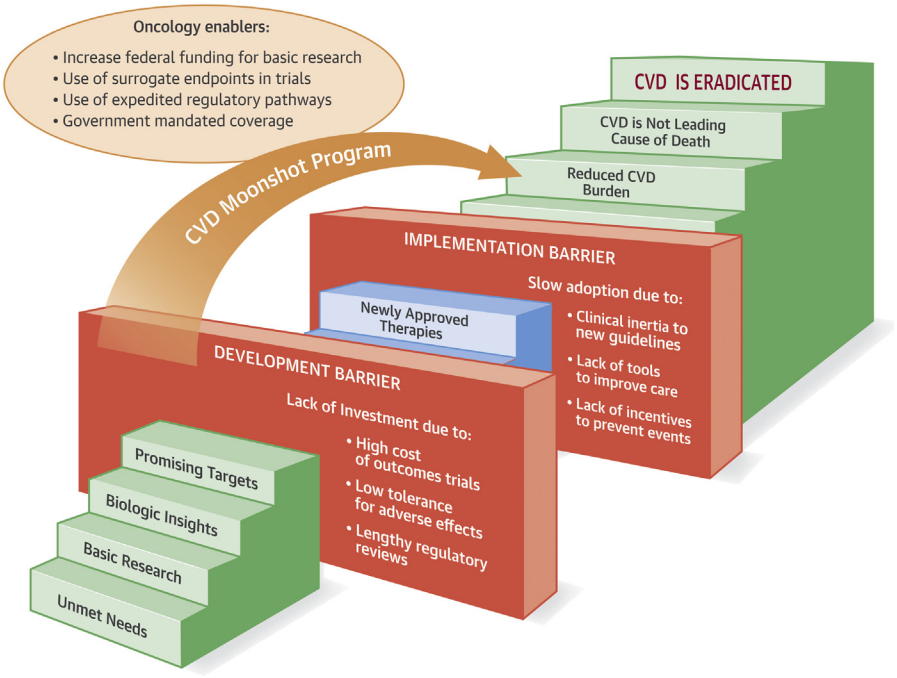

Khakoo, A.Y. et al. J Am Coll Cardiol Basic Trans Science. 2019;4(2):269–74.

The generation of novel cardiovascular therapeutics is impeded by a lack of investment due to barriers that limit investment in research in development as well as barriers that slow adoption of safe and effective therapies that limit their implementation. A "CVD Moonshot Program," consisting of elements that have fueled the rapid development of new cancer therapeutics- increased research funding, novel surrogate endpoints in clinical trials, expedited regulatory pathways, and government mandated coverage- could pave a road towards eradication of CVD. CVD = cardiovascular disease.

surrogate endpoints for CVD such as lowering of low-density lipoprotein cholesterol, large outcomes trials were needed to obtain approval from regulatory and reimbursement authorities. On the other hand, in oncology, because of the recognized importance of getting promising new therapeutics to cancer patients as quickly as possible, there is greater acceptance of drugs being approved based on clinically meaningful surrogate endpoints (13). In addition, there is much greater acceptance of side effects and serious adverse events in oncology. The time for clinical development of new therapies for CVD indications has not changed much since the 1970s (7). Oncology drugs, on the other hand, have taken advantage of expedited regulatory pathways to reduce development times. Of the 4 expedited programs offered by the FDA (orphan, priority review, accelerated approval, and fast track), the greatest number of applications were for oncology drugs. In fact, the proportion of oncology applications for each of these programs ranged from about one-third to more than one-half compared to <10% for CV applications (3).

There is a need to re-envision the development pathways for CVD drugs considering the public health importance of CVD. If this can be accomplished, it will help improve the return on investment and provide more incentive to invest in CVD and further improve public health.

IMPLEMENTATION BARRIERS

Another key factor in return on investment is how rapidly the innovation is adopted into clinical practice. Although there is evidence of geographic differences in the speed of adoption of new cancer drugs (14), there does not seem to be the same general reluctance to adopt new therapies as there is in CVD. For CVD, even when new drugs are adopted into

FIGURE 1 U.S. Food and Drug Administration Approvals for Cardiovascular Disease and Cancer From 1980 to 2017

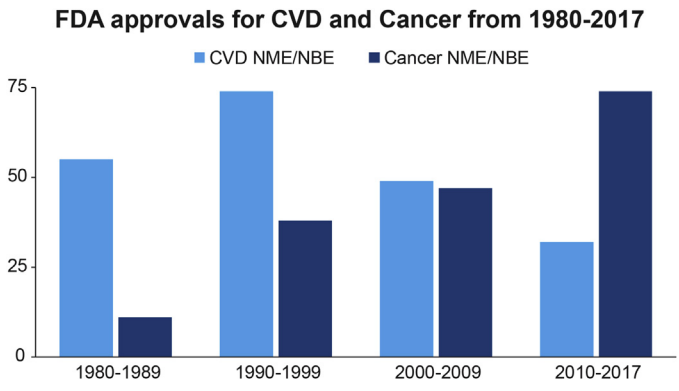

Adapted from Tufts Center for the Study of Drug Development Impact Report 2016 (5). NBE = new molecular entity; NME = new molecular entity.

treatment guidelines, there seems to be clinical inertia regarding adherence to the guidelines. This may be due to the previous success in reducing morbidity and mortality which creates an impression that sufficient progress had been made and underestimates the true burden of CVD. Also, identifying patients at imminent risk of an event is difficult in clinical practice due to a lack of near-term risk prediction tools, particularly for asymptomatic patients (15). Another issue may be that preventing future events is not considered a priority in a system that has a short-term budget view. The current structure of our health care system incentivizes treating conditions that have impact in the short run but does not provide sufficient incentive to prevent or treat conditions that could have enormous long-term impact (e.g., atherosclerotic CVD [ASCVD]).

Even with CV conditions that do have short-term impact and a strong immediate value proposition, such as heart failure (HF), adoption of new therapies is slow. Even though HF has mortality rates comparable to several common cancers (16), when a drug in a new class of HF therapeutics, angiotensin receptor neprilysin inhibition (ARNI), showed a 20% reduction in CV death and similar or better tolerability compared with standard of care, only ~2% of eligible patients were prescribed the drug 1 year after approval (17). This was close to 2 years after the initial report of the benefit of ARNI (18). An analysis by Fonarow et al. (19) estimated that optimal adoption of ARNI therapy could have saved almost 30,000 lives in the United States annually. These better clinical results may actually result in lower total health care costs. Recent analysis of real-world data has shown that, despite the higher pharmacy costs, ARNI reduced total health care costs by 28% compared to standard-of-care because of the much lower medical costs for ARNI-treated patients (20).

Another related barrier for implementation is the reimbursement and access challenges that many new drugs face. When financing new therapies, 2 main questions are typically considered: 1) Can we afford to pay for the drug? 2) Is the drug worth the price? The concern about affordability and the impact of the drug on the budget is particularly relevant for drugs that treat large populations, such as CVD drugs. The most recent report from the American Heart Association (AHA) concludes that almost one-half of all Americans adults (>120 million individuals) have CVD (21). The prevalence of cancer is much lower (>14 million individuals in the United States) (22). The size of the population makes new CVD drugs potentially very difficult to afford. Beyond the budget impact concern, there is a need to convince insurance companies and other payers of the value of these drugs to ensure the drugs are placed onto insurance formularies and can be accessed by patients with an affordable out-of-pocket copayment or coinsurance amount. Often these 2 issues are conflated and what is described as a lack of value is really a concern about the ability to pay for the drug considering the large populations of potential patients.

To deal with financing concerns, payers can resort to erecting major access barriers and this has happened with several recently approved CVD drugs. For example, more than 1 year after proprotein convertase subtilisin/kexin type 9 inhibitors were FDA-approved for treating individuals with familial hypercholesterolemia and established ASCVD, analyses showed that insurance companies were rejecting claims for 63% of familial hypercholesterolemia patients and 58% of ASCVD patients (23). This high rejection rate is due to a failure in any number of steps towards reimbursement, including authorization paperwork that oftentimes requires documentation, and step therapy, often requiring trials of specific doses of medications for prespecified periods. If a patients' insurance rejects a claim, the physician's office may need to go through lengthy appeals processes with insurance companies (24). With oncology drugs, payers are much less likely to impose access restrictions. Government policies often mandate coverage for oncology drugs. For example, Medicare covers all FDA-approved indications for cancer and cancer is 1 of the 6 protected classes required to be covered under Medicare's Part

D drug benefit (25). Although they are not subject to these government mandates for commercially insured patients, payers have been reluctant to impose meaningful restrictions on cancer therapies. This reluctance may be related to previous backlash from advocacy groups when restrictions have been imposed in the past (25).

OVERCOMING BARRIERS THROUGH STRONG ADVOCACY

A common thread in all the differences in oncology and CVD is the strong advocacy in oncology. The level of advocacy by physician groups and patients is not nearly as strong for CVD. For example, if survival outcomes for HF are similar to some cancers, why are people not wearing HF awareness bracelets? This lack of a strong advocacy voice may play into the complacency of payers and health care providers. Greater advocacy from patients and physicians shines the light on problematic barriers that can delay the time to life-changing therapies. There are several potential reasons for the difference in advocacy. Oncology patients tend to skew a little younger, so people are more concerned about life-threatening disease in younger patients. Also, CV patients may blame themselves and their lifestyle choices for their condition. Other than a few very specific conditions in oncology, such as lung cancer, this tends not to be the case for cancer.

With better advocacy for CVD, both development and implementation barriers could be better addressed and reduced. There would be substantial merit in a call to action with a CVD moonshot program and more research funding for CVD like there is for oncology to continue to catalyze innovation in CVD. There is a need for more proactive data-driven discussions with the FDA (as well as the Centers for Medicare and Medicaid Services and other payers) to ensure the right balance between speed and safety is found. Implementation barriers could be reduced through increased support for guideline-based performance improvement programs, systems of care, and training to aid health care systems with rapid adoption (26). Better physician and patient advocacy is critical to bring down payer access barriers. Multiple stakeholders including insurers still seem to underestimate the unmet need in CVD; hence, there is a need for more education about the impact of CVD on patients' health status, wellbeing, and quality of life (27).

Despite the compelling unmet need for additional therapies for CVD that provide meaningful patient-centered benefits, there is underinvestment in CVD compared to other therapeutic areas. However, there are reasons to be optimistic and strategies can be implemented to address these challenges. First, although recent approvals for CVD have declined, data suggests that we may be at a tipping point in basic research for CVD that could spur more successful drug development (7). Innovations in DNA sequencing methodologies have transformed the field of human genetics, holding the promise of identifying causal mechanisms and creating better drug targets for the treatment of common, complex diseases such as CVD (28). Second, as the focus on quality and patient-centered outcomes increases, providing treatments that improve patient outcomes in CVD is well aligned with quality incentive payment programs. Finally, we have seen how advocacy seems to have moved the needle in oncology. If we continue to work together and make a concerted effort to shine the light on the unmet need in CVD, we can help improve investment in this area. We already have large campaigns such as the Center for Disease Control's Millions Heart campaign (29) and the American Heart Association and Duke's Value in Health Care Initiative (30). If cardiologists champion these movements en masse, we will have great momentum. Like they have in oncology, we need to have a CV "moonshot" and we need to be advocates in the fight to eradicate CVD.

ADDRESS FOR CORRESPONDENCE: Dr. Aarif Y. Khakoo, Amgen Inc., 1120 Veterans Boulevard, South San Francisco, California 94080. E-mail: aykhakoo@gmail.com.

REFERENCES

1. Centers for Disease Control. Achievements in Public Health, 1900–1999: Decline in Deaths from Heart Disease and Stroke — United States, 1900–1999. MMWR Weekly 1999;48:649-56. Available at: https://www.cdc.gov/mmwr/preview/mmwrhtml/mm4830a1.htm. Accessed October 15, 2018.

2. Sidney S, Quesenberry CP, Jaffe MG, et al. Recent trends in cardiovascular mortality in the United States and public health goals. JAMA Cardiol 2016;1:594–9.

3. Fordyce BF, Roe MT, Ahmad T, et al. Cardiovascular drug development: is it dead or just hibernating? J Am Coll Cardiol 2015;65:1567–82.

4. Van Norman GA. Overcoming the declining trends in innovation and investment in cardiovascular therapeutics: beyond EROOM's Law. J Am Coll Cardiol Basic Trans Science 2017;2:613–25.

5. Tufts Center for the Study of Drug Development. Outlook 2016. Available at: https://static1.squarespace.com/static/5a9eb0c8e2ccd1158288d8dc/t/5aa2fc9d0852297555747051/1520630944033/Outlook-2016.pdf. Accessed October 1, 2018.

6. Hwang TJ, Lauffenburger JC, Franklin JM, Kesselheim AS. Temporal trends and factors associated with cardiovascular drug development,

1990 to 2012. J Am Coll Cardiol Basic Trans Science 2016;1:301–8.

7. Beierlein JM, McNamee LM, Walsh MJ, Kaitin KI, DiMasi JA, Ledley FD. Landscape of innovation for cardiovascular pharmaceuticals: from basic science to new molecular entities. Clin Ther 2017;39:1409–25.

8. Tufts Center for the Study of Drug Development. CNS Drugs Take 20% Longer to Develop and to Approve vs. non-CNS Drugs. Impact Report 2018;20:1–4.

9. U.S. Department of Health and Human Services. HHS FY 2017 Budget in Brief. Available at: https://www.hhs.gov/about/budget/fy2017/budget-in-brief/nih/index.html. Accessed October 15, 2018.

10. National Cancer Institute. Cancer Moonshot. Available at: https://www.cancer.gov/research/key-initiatives/moonshot-cancer-initiative. Accessed October 15, 2018.

11. DiMasi JA, Grabowski HG, Hansen RW. Innovation in the pharmaceutical industry: New estimates of R&D costs. J Health Econ 2016;47:20–33.

12. DiMasi JA, Hansen RW, Grabowski HG. The price of innovation: new estimates of drug development costs. J Health Econ 2003;22:151–85.

13. Blumenthal GM, Kluetz PG, Schneider J, Goldberg KB, McKee AE, Pazdur R. Oncology drug approvals: evaluating endpoints and evidence in an era of breakthrough therapies. Oncologist 2017;22:762–7.

14. Doyle C. Rapid adoption of oncology drugs improves survival. Value in Oncology 2017;8. Available at: http://www.valuebasedcancer.com/issue-archive/2017/december-2017-vol-8-no-5/rapid-adoption-of-oncology-drugs-improves-survival/. Accessed October 12, 2018.

15. Eagle KA, Ginsburg G, Musunuru K, et al. Identifying patients at high risk of a cardiovascular event in the near future: current status and future directions: report of a National Heart, Lung, and Blood Institute Working Group. Circulation 2010;121:1447–54.

16. Mamas MA, Sperrin M, Watson MC, et al. Do patients have worse outcomes in heart failure than in cancer? A primary care-based cohort study with 10-year follow-up in Scotland. Eur J Heart Fail 2017;19:1095–104.

17. Luo N, Fonarow GC, Lippmann SJ, et al. Early adoption of sacubitril/valsartan for patients with heart failure with reduced ejection fraction: Insights from get with the guidelines-heart failure (GWTG-HF). J Am Coll Cardiol HF 2017;5:305–9.

18. McMurray JJ, Packer M, Desai AS, et al. PARADIGM-HF Investigators and Committees. Angiotensin-neprilysin inhibition versus enalapril in heart failure. N Engl J Med 2014;371:993–1004.

19. Fonarow GC, Hernandez AF, Solomon SD, Yancy CW. Potential mortality reduction with optimal implementation of angiotensin receptor neprilysin inhibitor therapy in heart failure. JAMA Cardiol 2016;1:714–7.

20. Albert, NM, Swindle, JP, et al. Lower hospitalization and total healthcare costs among patients with heart Failure when treated with sacubitril/valsartan versus angiotensin-converting enzyme inhibitor or angiotensin-receptor blocker: re retrospective study of managed care claims. Poster presentation presented at: Academy of Managed Care Pharmacy Annual Meeting; April 23-26, 2018; Boston, MA.

21. Benjamin EJ, Muntner P, Alonso A, et al. Heart disease and stroke statistics—2019 update: a report from the American Heart Association. Circulation 2019;139:e56–528.

22. American Cancer Society. Cancer prevalence: how many people have cancer? Last revised: October 2016. Available at: https://www.cancer.org/cancer/cancer-basics/cancer-prevalence.html. Accessed February 3, 2019.

23. Knowles JW, Howard WB, Karayan L, et al. Access to nonstatin lipid-lowering therapies in patients at high risk of atherosclerotic cardiovascular disease. Circulation 2017;135:2204–6.

24. Baum SJ, Toth PP, Underberg JA, Jellinger P, Ross J, Wilemon K. PCSK9 inhibitor access barriers-issues and recommendations: improving the access process for patients, clinicians and payers. Clin Cardiol 2017;40:243–54.

25. Howard DH, Bach PB, Berndt ER, Conti RM. Pricing in the market for anticancer drugs. J Econ Perspect 2015;29:139–62.

26. Butler J, Fonarow GC, Gheorghiade M. Need for increased awareness and evidence-based therapies for patients hospitalized for heart failure. JAMA 2013;310:2035–6.

27. Plump A. Accelerating the pulse of cardiovascular R&D. Nat Rev Drug Discov 2010;9:823–4.

28. Kamb A, Harper S, Stefansson K. Human genetics as a foundation for innovative drug development. Nat Biotechnol 2013;31:975–8.

29. Wright JS, Wall HK, Ritchey MD. Million hearts 2022 small steps are needed for cardiovascular disease prevention. JAMA 2018;320:1857–8.

30. American Heart Association and Duke Margolis Center for Health Policy. Value in health care initiative. Available at: https://healthpolicy.duke.edu/value-health-care-initiative. Accessed February 3, 2019.

KEY WORDS advocacy, cardiovascular disease, drug development, expedited regulatory pathways

JACC: BASIC TO TRANSLATIONAL SCIENCE VOL. 4, NO. 2, 2019
© 2019 THE AUTHORS. PUBLISHED BY ELSEVIER ON BEHALF OF THE AMERICAN COLLEGE OF CARDIOLOGY FOUNDATION. THIS IS AN OPEN ACCESS ARTICLE UNDER THE CC BY-NC-ND LICENSE (http://creativecommons.org/licenses/by-nc-nd/4.0/).

STATE-OF-THE-ART REVIEW

Cardiac Muscle Membrane Stabilization in Myocardial Reperfusion Injury

Evelyne M. Houang, PhD,[a,*] Jason Bartos, MD,[b,*] Benjamin J. Hackel, PhD,[c] Timothy P. Lodge, PhD,[c,d] Demetris Yannopoulos, MD,[b] Frank S. Bates, ScD,[c] Joseph M. Metzger, PhD[a]

HIGHLIGHTS

- **In myocardial ischemia, the integrity of the cardiac sarcolemma is severely stressed in the critical earliest moments upon reperfusion. Bolstering sarcolemma integrity improves myocyte survival.**
- **This review focuses on cardiac sarcolemma stability and its role as a therapeutic target in ischemia-reperfusion injury.**
- **Synthetic block copolymers have been shown to interface with the muscle membrane to confer membrane stabilization during stress.**
- **Integrated multidisciplinary research teams, spanning cardiology, physiology, chemistry, and chemical engineering are essential to guide future mechanistic and translational studies of novel chemical-based membrane stabilizers for preserving viable heart muscle during ischemia-reperfusion injury in human patients.**

SUMMARY

The phospholipid bilayer membrane that surrounds each cell in the body represents the first and last line of defense for preserving overall cell viability. In several forms of cardiac and skeletal muscle disease, deficits in the integrity of the muscle membrane play a central role in disease pathogenesis. In Duchenne muscular dystrophy, an inherited and uniformly fatal disease of progressive muscle deterioration, muscle membrane instability is the primary cause of disease, including significant heart disease, for which there is no cure or highly effective treatment. Further, in multiple clinical forms of myocardial ischemia-reperfusion injury, the cardiac sarcolemma is damaged and this plays a key role in disease etiology. In this review, cardiac muscle membrane stability is addressed, with a focus on synthetic block copolymers as a unique chemical-based approach to stabilize damaged muscle membranes. Recent advances using clinically relevant small and large animal models of heart disease are discussed. In addition, mechanistic insights into the copolymer-muscle membrane interface, featuring atomistic, molecular, and physiological structure-function approaches are highlighted. Collectively, muscle membrane instability contributes significantly to morbidity and mortality in prominent acquired and inherited heart diseases. In this context, chemical-based muscle membrane stabilizers provide a novel therapeutic approach for a myriad of heart diseases wherein the integrity of the cardiac muscle membrane is at risk.
(J Am Coll Cardiol Basic Trans Science 2019;4:275–87) © 2019 The Authors. Published by Elsevier on behalf of the American College of Cardiology Foundation. This is an open access article under the CC BY-NC-ND license (http://creativecommons.org/licenses/by-nc-nd/4.0/).

From the [a]Department of Integrative Biology and Physiology, University of Minnesota Medical School, Minneapolis, Minnesota; [b]Department of Medicine-Cardiovascular Division, University of Minnesota Medical School, Minneapolis, Minnesota; [c]Department of Chemical Engineering and Materials Science, University of Minnesota, Minneapolis, Minnesota; and the [d]Department of Chemistry, University of Minnesota, Minneapolis, Minnesota. *Drs. Houang and Bartos contributed equally to this work and are joint first authors. Drs. Metzger and Yannopoulos have received grants from the National Institutes of Health. Dr. Metzger is on the scientific advisory board of and holds zero value equity shares in Phrixus Pharmaceuticals Inc., a company developing novel therapeutics for heart failure and DMD, and this is actively managed by the UMN Office of Institutional Compliance. All other authors have reported that they have no relationships relevant to the contents of this paper to disclose.
All authors attest they are in compliance with human studies committees and animal welfare regulations of the authors' institutions and U.S. Food and Drug Administration guidelines, including patient consent where appropriate. For more information, visit the *JACC: Basic to Translational Science* author instructions page.

Manuscript received January 4, 2019; revised manuscript received January 11, 2019, accepted January 26, 2019.

ISSN 2452-302X https://doi.org/10.1016/j.jacbts.2019.01.009

OVERVIEW: CARDIAC MUSCLE MEMBRANE INTEGRITY AND HEART PERFORMANCE

Cardiac muscle membrane instability is a hallmark of myocardial ischemia-reperfusion (I/R) injury (1-29). It is well-documented that in the very earliest moments of reperfusion cardiac myocytes swell markedly due to significant myoplasmic osmolyte accumulation during the ischemic period (21,25,28,30,31). Myocyte swelling, along with myocyte contracture, exerts a severe stress on the cardiac membrane (sarcolemma), leading to membrane tears, pores, blebs, and instability (19,20,25-28). Loss in the primary barrier function of the cardiac membrane leads to catastrophic outcomes in terms of overall myocyte viability and function. It follows that preserving cardiac sarcolemma integrity in I/R holds promise for enhancing cardiac muscle viability thus improving overall heart function during reperfusion (**Figure 1**).

Myocardial I/R causes millions of deaths per year (2,10,15,17,19,32-39) underscoring the urgency for detailed understanding. There are multiple pathological pathways to cardiac reperfusion injury; nonetheless, in the face of this complexity, a key unifying component of I/R injury centers on cardiac muscle membrane instability (19-21,23-26,29,31,37,40). In cardiac I/R, sarcolemmal rupture and necrotic cell death are well documented in the critical minutes of reperfusion after an ischemic event (1-19). Whereas the pathways leading to cardiac I/R injury are multifold and complex (18,41,42), we and others have established a sound premise that a clear approach for a clinically meaningful treatment would be one that would directly enhance cardiac membrane stability in I/R (43). Given that cardiac sarcolemma damage is a well-established hallmark of I/R injury, it is surprising this has received relatively little direct investigation as a possible target for I/R treatment development (44).

In this review, we detail the design and implementation of chemical-based synthetic muscle membrane stabilizers for the diseased heart (**Central Illustration**). Muscle membrane stabilizers target and interface with, but do not transit across, the cell outer membrane to confer sarcolemma stabilization (**Figure 2**) (45-47). We recently showed in several genetic models of cardiac muscle membrane instability that synthetic block copolymer-based membrane stabilizers prevent progressive cardiomyopathy (48,49). We focus here on the mechanism by which block copolymer muscle membrane stabilizers interface with the sarcolemma to preserve cardiac myocyte viability. A structure-function approach is enabled by leveraging insights across disciplinary lines, extending from chemistry to physiology and cardiology. Collectively, we advance synthetic membrane stabilizers as a unique first-in-class cell extrinsic strategy for directly protecting cardiac muscle membranes during I/R in vivo (48-53). We propose that membrane stabilizers, in the form of synthetic copolymers, provide a unique tool to investigate the mechanism of cardiac I/R injury and provide a template toward developing novel therapies designed to stabilize the muscle membrane in acquired heart disease. Thus, this review is centered on novel means and mechanisms to preserve viable myocardium during reperfusion.

FIGURE 1 Health Relevance

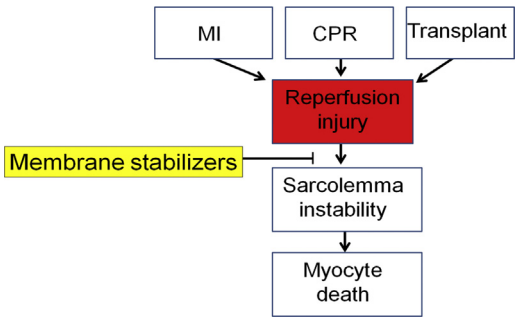

Clinically relevant pathways to cardiac reperfusion injury with focus on cardiac membrane instability and the novel use of synthetic membrane stabilizers. CPR = cardiopulmonary resuscitation; MI = myocardial infarction.

THE CARDIAC MEMBRANE AS A DIRECT THERAPEUTIC TARGET IN MYOCARDIAL I/R

Cardiac I/R injury exacts a tremendous toll on morbidity and mortality in humans (54-59), and recent clinical cardioprotective trials have been disappointing (60). The hypothesis advanced here is that during the critical earliest stages of I/R the cardiac myocyte's endogenous membrane stabilization/repair machinery is overwhelmed and that synthetic copolymers serve to rapidly stabilize the membrane as a bridging mechanism. In this way, copolymers permit the cell intrinsic membrane repair pathways adequate time to fully repair the damaged membrane and preserve cardiac myocyte viability in vivo. Block copolymers offer a direct approach to preserve membrane integrity in I/R, thereby representing a novel therapeutic development opportunity with the potential for high clinical impact.

Heart muscle has multiple cell intrinsic/endogenous mechanisms to stabilize/repair the fragile/damaged sarcolemma during stress (61-64). These include sarcolemma phospholipid fluid mosaic re-structuring that can rapidly repair very small disruptions/injury to the membrane. For more significant damage, which would occur during cardiac I/R, key endogenous mechanisms are activated to repair damage to preserve muscle cell integrity and viability. Published data supports endogenous dysferlin-mediated muscle membrane repair (65,66). Dysferlin repairs muscle membranes in a Ca^{2+}-dependent manner whereby dysferlin regulates fusion of repair vesicles with the sarcolemma to accomplish membrane repair. Mitsugumin 53 has also been identified as a crucial component in membrane repair (67). Recently, a new cell intrinsic membrane stabilization pathway has been elucidated: thrombospondin 4(Thbs4)-mediated striated muscle membrane stabilization (68-70). The Thbs4 mechanism of cell intrinsic membrane stabilization (69) is restricted to cardiac and skeletal muscle and its expression is induced with injury or disease in the heart, including ischemic injury (69-72). Thbs4 is therefore distinct from other Thbs gene family members that are secreted glycoproteins. Within striated muscles, Thbs4 directly enhances intracellular vesicular trafficking and chaperones the critical dystrophin-glycoprotein complex and integrin attachment to the muscle membrane, leading to increased membrane stability of heart muscle (69-73). Data show that genetic ablation of the Thbs4 pathway in otherwise healthy animals directly causes sarcolemma weakness (69). Further, overexpression of Thbs4 markedly enhances vesicular trafficking of dystrophin-glycoprotein complex and integrin complexes to augment muscle membrane integrity to enable efficient membrane repair.

On the physiological timescale, the myocyte's intrinsic membrane repair and stabilization pathways, including dysferlin, mitsugumin 53, Thbs4, and others, can take up to several minutes or longer to repair sarcolemma damage (61,74-77). In I/R, this delay in repair can be catastrophic, leading to the demise of the cell. To address this, we and others have pursued cell-extrinsic synthetic chemistries as a rapid means to protect damaged striated muscle membranes (**Figures 1 to 3**). We were the first to show that the first-in-class synthetic membrane stabilizer, triblock copolymer poloxamer 188 (P188), protects the heart (**Figure 2**) (48). The poloxamer family of block copolymers has been in wide use for drug delivery and other biomedical applications (78). P188 has been safely used in animals and humans, including advanced clinical trials for limiting vaso-occlusive crisis in sickle cell anemia (79-81). As reviewed in detail below, synthetic membrane stabilizers are amphiphilic long-chain macromolecular block copolymers that interact with and protect the muscle sarcolemma during stress (**Central Illustration, Figure 2**). The goal of this review is to illuminate the role of membrane integrity in I/R by disseminating recent insights into copolymer-membrane interactions. We further provide an overview of the potential for translation of this therapeutic approach into clinically relevant beneficial outcomes in the setting of myocardial I/R in vivo.

CENTRAL ILLUSTRATION Chemical-Based Membrane Stabilizer Discovery Platform Integrating Insights From Vesicles to In Vivo

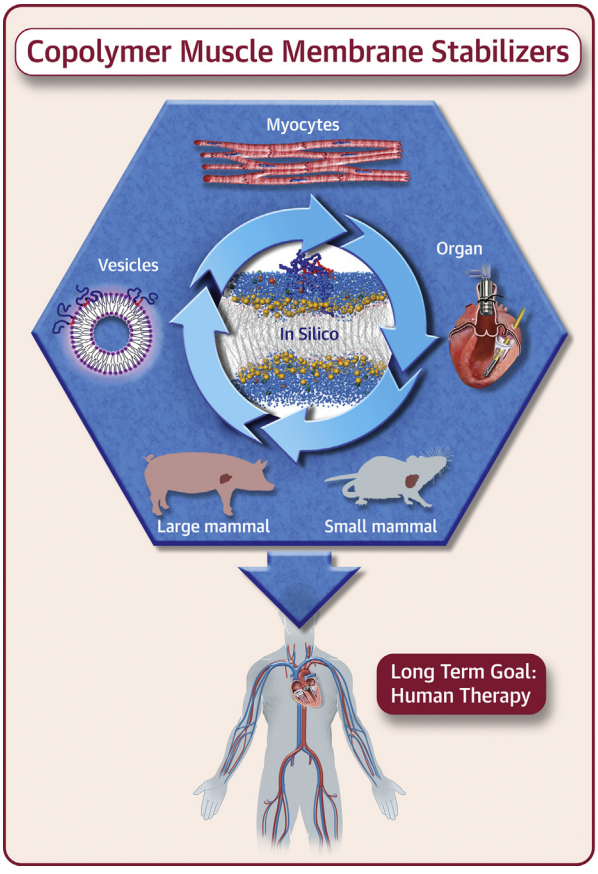

Houang, E.M. et al. J Am Coll Cardiol Basic Trans Science. 2019;4(2):275–87.

Overarching goal: stabilizing the cardiac muscle membrane in disease using synthetic chemistry.

FIGURE 2 Schematic Representation of Block Copolymer P188 Interaction With the Cardiac Sarcolemma

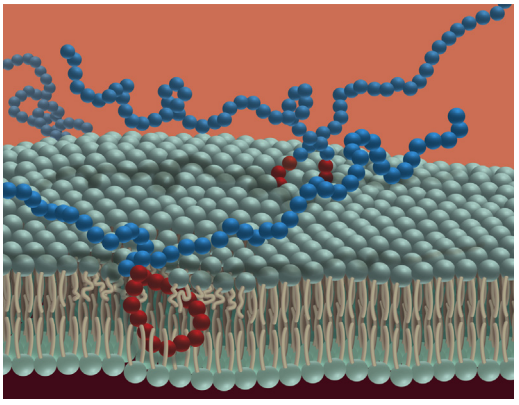

Blue spheres = polyethylene oxide block; **red spheres** = polypropylene oxide block.

MYOCARDIAL I/R INJURY CLINICAL FEATURES

Coronary heart disease is the most common form of human heart disease in the United States, accounting for 20% of all deaths (82). Coronary heart disease most often presents as a myocardial infarction (MI), during which cardiac tissue becomes ischemic due to coronary arterial blockage, and this blockage must be rapidly reversed to help preserve functional heart muscle (4,30,33,34,36,37,83–88). In the United States, >250,000 patients per year have ST-segment elevation MI (STEMI) treated with primary percutaneous coronary intervention (PCI) that involves intracoronary placement of a stent to open up the blocked vessel. Urgent restoration of blood flow, where "time is muscle" is the cardiologist's main imperative. Paradoxically, restoration of blood flow causes a second wave of cardiac muscle damage termed myocardial I/R injury (10,12,38,89).

Along with MI, other clinically relevant scenarios involving myocardial ischemia (or low flow) and reperfusion include cardiopulmonary resuscitation (CPR) and heart organ procurement and transplantation (**Figure 1**) (90,91). In the case of CPR, discordant electrical activity of the heart leads to marked reductions in heart pump performance requiring external compressions of the chest cavity (CPR) to provide low-flow perfusion. Upon reacquisition of sinus rhythm, flow can be restored; however, as in MI, the reintroduction of oxygenated blood results in reperfusion injury. Further, heart organ transplantation necessitates organ procurement and a prolonged ischemic period that can last hours before transplantation and reperfusion (59,92). Each of these common clinical scenarios presents unique conditions for the development of I/R injury, and each provides unique opportunities to assess the efficacy of membrane stabilization to improve myocardial viability and function.

There are 2 basic clinical presentations that result from sudden onset of profound myocardial ischemia. Whereas they differ in the distribution of the ischemia and resulting reperfusion, the underlying mechanisms of cellular injury are similar. The first, MI, occurs in approximately 600,000 people per year. Of these, STEMI accounts for 30% of cases (82). STEMI causes mortality in 6% of cases, with up to 20% of patients going on to develop overt heart failure requiring lifelong therapy (93). STEMI is caused by complete occlusion of a coronary arterial, severely limiting or eliminating blood flow to a region of the heart. This is most commonly caused by sudden formation of thrombus at the site of an atherosclerotic plaque. Advances in treatment of STEMI over the last few decades have focused on reperfusing the muscle by removing the obstruction. This began initially with thrombolytic therapy to dissolve the obstructing thrombus. Presently, front-line clinical treatment focuses on the use of PCI in the cardiac catheterization laboratory, where balloons and/or stents are deployed to resolve the occlusion (94,95). The use of PCI has markedly increased the likelihood of reperfusion, increasing from 40% to 55% with thrombolytics to >90% with PCI (96).

BLOCK COPOLYMERS: FIRST-IN-CLASS SYNTHETIC MUSCLE MEMBRANE STABILIZERS

The scientific premise guiding this review is that maintenance of cardiac membrane integrity is severely challenged from the very earliest moments of reperfusion. Thus, the stability of the muscle membrane represents a potentially highly efficacious target for therapeutic development. In this light, we and others have advanced synthetic chemistries featuring block copolymers as a unique class of molecules with membrane stabilization functionalities (**Central Illustration**). Synthetic block copolymers include a range of soft materials with wide ranging industrial and biological applications (45,81,97). The most well-known synthetic block copolymers in biomedicine are triblock copolymers known as poloxamers (or pluronics), which are composed of a hydrophobic polypropylene oxide (PPO) block flanked

by hydrophilic polyethylene oxide (PEO) chains (**Central Illustration, Figures 2 and 3**). In principle, an immeasurable number of block copolymers of distinct physicochemical properties could be obtained by varying the lengths of the PEO and PPO blocks as well as their architectural assembly. These various combinations give rise to amphiphilic molecules with complex membrane interface behavior that have been found to directly interact with cellular membranes as lysis agents and membrane stabilizers, directly dependent on their unique chemical composition (48,97-101).

Block copolymers can be designed to vary markedly in size, composition, and architecture (**Figures 2 and 4**) (102). By far, the most well-studied block copolymer in biomedical research has been the triblock P188 (or PEO_{75}-PPO_{30}-PEO_{75}, PPO/PEO = 0.20 and MW = 8.4 kDa) (**Figures 2 and 3, Table 1**). P188 was first approved by the Food and Drug Administration as an anti-viscosity agent added to blood and has been previously tested in clinical trials for sickle cell anemia and MI (81,103-110). The pharmacokinetic profile of P188 in healthy males has been obtained in a cohort of volunteers, and it has been determined that elimination occurs primarily through renal clearance (111,112). The formulation of P188 purified from small molecular weight impurities is well tolerated (113). P188's safety profile was further validated for long-term use in human patient sickle cell anemia trials, showing an overall excellent safety profile in humans (81,103,104).

P188 has shown membrane stabilization capability in a diverse range of pathophysiological settings. These include irradiation and burn injury (114,115), blunt impact-induced cartilage damage and joint degeneration (116), amyotrophic lateral sclerosis (117), neuronal cell death (118), traumatic brain injury-induced blood-brain barrier damage, brain edema (119), and apoptosis-induced neuronal cell death after oxygen-glucose deprivation (120). Membrane stabilization by P188 has also been well established in Duchenne muscular dystrophy models (48,49,53,121,122) where purified clinical grade P188 is currently under a Phase II, single-site, open-label clinical trial for Duchenne muscular dystrophy patients. Furthermore, in vivo delivery of P188 was shown to protect neuronal cells during spinal cord compression and acute intracranial hemorrhage (123). P188 has also been used as an additive enhancing blood oxygenation, cardiopulmonary bypass, in heart-lung bypass, and as a rheological agent to lessen blood viscosity and platelet aggregation (124-129).

Of direct relevance to STEMI and I/R injury, a previous study showed that intravenous injection of P188 significantly improved blood flow to ischemic brain areas induced by surgical occlusion of the middle cerebral arterial in a rabbit model of focal cerebral ischemia (130). Because P188 was reported to improve blood flow without reducing blood viscosity and without hemodilution, it has been hypothesized that P188 improves blood flow by reducing adhesive interactions between blood cells and vessel walls and between fibrin and fibrinogen in the microcirculation (130). Moreover, P188 was found in one study to diminish I/R-induced brain injury and improve long-term functional recovery after focal cerebral ischemia in mice (131). There is evidence that P188 can provide long-term protective effects on cerebral I/R injury both in vivo and in vitro and that neuroprotection offered by P188 involves several mechanisms, including preserving blood-brain barrier impermeability, intervening in the nuclear factor kappa light chain enhancer signaling pathway by inhibiting MMP-9, and reducing cell death. P188 was also found to rescue cultured hippocampal neurons after excitotoxicity and oxidative stress (132), both central mechanisms of hypoxia injury-induced neurodegeneration. Another study showed that P188 decreased the activation of autophagy in neuronal cells under oxygen-glucose deprivation in vitro and that intravenous injection of P188 reduced infarct volume and neurological/motor deficits in a mouse model of cerebral ischemia in vivo (133).

A recent investigation further showed that cardiac I/R injury, which is significantly amplified in animal models of sarcolemmal loss-of-function, was abrogated by application of copolymer-based membrane stabilizers (42). P188 treatment of rat cardiac myocytes exposed to simulated ischemia/reperfusion in vitro prevented membrane leakage of intracellular lactate dehydrogenase. Furthermore, P188 mediated

FIGURE 3 Timing and Location of Membrane Stabilizer Delivery are Essential Elements to Clinical Efficacy in STEMI/Percutaneous Coronary Intervention

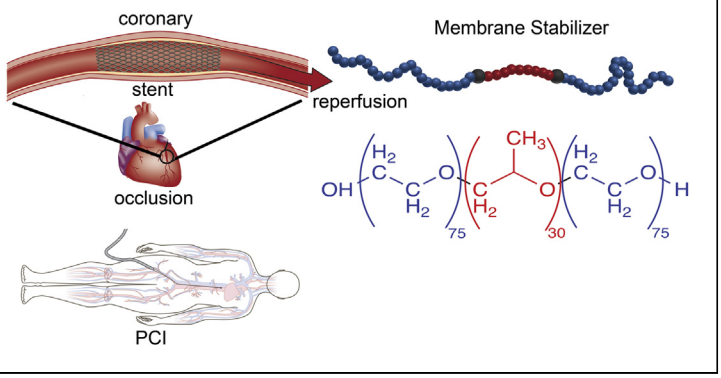

TABLE 1 Chemical Features of Various Synthetic Block Copolymers

Architecture	Polymer	PEO*	PPO*	End Group†	Mass‡	PEO%§
Triblock copolymer/P188‖	$PEO_{75}PPO_{30}PEO_{75}$	150	30	–	8,400	80
Triblock copolymer/P338‖	$PEO_{140}PPO_{44}PEO_{140}$	280	44	–	14,600	84
Triblock copolymer/P331‖	$PEO_{7}PPO_{54}PEO_{7}$	14	54	–	3,700	26
Diblock copolymers	$PEO_{75}PPO_{15}$–H	75	15	–H	4,200	80
	$PEO_{75}PPO_{15}$–C4	75	15	$-C(CH_3)_3$	4,430	77
Control homopolymer	PEO_{198}	198	0	–	8,700¶	100

*Total number of EO or PO monomer units. †Chemical end group. ‡Molecular weight in g/mol by ^{1}H NMR end-group analysis. §PEO weight percent to total molecular weight. ‖Manufacturer BASF, Florham Park, New Jersey. ¶Number average molecular weight.

EO = ethylene oxide; NMR = nuclear magnetic resonance; PEO = polyethylene oxide; PO = propylene oxide; PPO = polypropylene oxide.

membrane stabilization was shown to prevent I/R-functional deficits in isolated hearts ex vivo (42). Taken together, these studies provide strong evidence that the neuronal and cardiac cell membranes can be targeted for membrane stabilization to improve viability and function in I/R.

COPOLYMER-BASED MEMBRANE STABILIZERS IN MYOCARDIAL I/R INJURY

In the setting of reperfusion injury after MI, membrane stabilizers were first tested in small and large animal studies in the 1990s. The first study, published in 1991, used a dog model of left anterior descending arterial occlusion with infusion of P188 for the 15 min before reperfusion and the first 45 min of reperfusion (134). P188 reduced infarct size by 50% in that model. Subsequent studies went on to replicate the reduced infarct size using the same canine model (110). At that time, these positive effects were attributed to the hemorheological and antithrombotic effects of P188, as it was shown to reduce red blood cell aggregation (81), facilitate clot lysis by recombinant tissue plasminogen activator (135), and reduce leukocyte chemotaxis (110). It was later discovered that P188 also stabilizes the sarcolemma (132).

In the clinical setting of I/R, the first human trial enrolled patients from 11 centers between March 1992 and August 1993 (107). All patients had ongoing chest pain of >30 min duration and STEMI on electrocardiogram. Study participants were only included if they were candidates for thrombolytic therapy, as that was the state-of-the-art reperfusion therapy available at that time. The initial phase of the trial randomized the first 45 patients to either control or low-dose P188 (150 mg/kg/h for 1 h then 15 mg/kg/h for 47 h). The second phase randomized the following 69 patients to placebo or high-dose P188 (300 mg/kg/h for 1 h then 30 mg/kg/h for 47 h). P188 showed improvement in infarct size (38% reduction), increased median myocardial salvage (9% absolute increase), and improved left ventricular (LV) function (6% absolute increase in LV ejection fraction [EF]). The P188 group also had a 12% absolute reduction in re-infarcts.

The CORE (Collaborative Organization for RheothRx Evaluation) trial was a phase II open label clinical trial, including 2,948 patients with STEMI receiving thrombolytic treatment, with the trial beginning in 1994 (136). The trial randomized patients to placebo (n = 963) or 1 of multiple dosing regimens with P188. In this large trial, no significant clinical benefit of P188 was observed with similar rates of mortality, reinfarction, and cardiogenic shock between groups. It was also noted in a subset of elderly patients with pre-existing renal dysfunction that acute renal dysfunction was more frequent in the P188 group. In this context, subsequent studies have examined this in detail showing that the commercially available (nonpurified) P188 resulted in vacuolization of the proximal tubule epithelium without signs of irreversible injury or necrosis (113). Purification of P188, which removes low molecular weight contaminants, fully prevented the renal effects of P188 in humans and animal models.

In retrospect, and in the full light of contemporary clinical management of STEMI, it can now be readily discerned that multiple important limitations were inherent in the CORE trial design. First, CORE trial patients were treated with thrombolytics which left at least one-half of the patients without any reperfusion. It follows that the goal of treating reperfusion injury was not possible in the patients that did not achieve reperfusion. As discussed above, PCI is now the standard of care in STEMI, resulting in significantly higher rates of reperfusion. Second, in the CORE trial, P188 was administered intravenously through the PVC approximately 30 min after thrombolytic therapy was administered. This delay is not explicitly described in the publication; however, randomization was recommended within 15 min of thrombolytic infusion, and P188 infusion was initiated within 15 min of randomization. Given the absolute requirement for rapid delivery of therapies targeting reperfusion injury and the rapid decay in benefit over the minutes following reperfusion (137), this 30-min delay is a key parameter in understanding the significantly reduced efficacy of membrane stabilization therapy in the CORE trial. In addition, the trial's PVC delivery dilutes the effect and further minimizes the possibility of detecting a therapeutic benefit.

The methodological limitations of the CORE trial were recently investigated in a porcine model of STEMI (137). Anterior STEMI was established in adult pigs via 45 min of endovascular occlusion of the mid left anterior descending coronary arterial. The pigs were randomized to 1 of 4 groups including vehicle control, immediate intracoronary P188 delivery, delayed peripheral P188, and intracoronary polyethylene glycol (PEG, or PEO)-8,000 infusion serving as a mass equivalent hydrophilic control for P188. After 45 min of ischemia, the endovascular balloon was deflated and removed and the appropriate treatment was infused through the coronary guide catheter in all groups other than the delayed peripheral P188 group where 30 min was allowed to elapse and P188 was then infused via PVC similar to the CORE trial. The pigs were maintained for 4 h at which time the hearts were removed for evaluation of mitochondrial function or staining for quantification of the infarct size. The study revealed significantly improved mitochondrial structure, respiration, and calcium retention in the setting of the immediate intracoronary delivery of P188. Infarct size and serum troponin I levels were reduced by 66% and 75%, respectively, with immediate intracoronary P188 delivery. Importantly, animals receiving the delayed peripheral P188, similar to the CORE trial protocol, resulted in no benefit. In addition, immediate intracoronary PEG infusion also provided no benefit, suggesting that the mechanism was not due to the hemorheological effects of P188. Taken together, these results are evidence that the lack of benefit observed in the CORE trial could be ascribed to a suboptimal treatment protocol rather than a lack of a P188 therapeutic effect. Evidence has accumulated that timing (immediate) and location (intracoronary) are essential parameters of copolymer-based membrane stabilization treatment in STEMI-I/R. It follows that further study in STEMI patients receiving PCI therapy with immediate intracoronary P188 infusion are warranted and should be investigated through future clinical studies (**Figure 3**).

To date, there have been no studies conducted on patients suffering cardiac arrest with P188 intervention. Recently, P188 was studied as part of a bundle of care strategy in a porcine model of prolonged cardiac arrest (138). Here, pigs had ventricular fibrillation induced electrically followed by 17 min of untreated downtime. Animals were then randomized to control CPR or bundle therapy including ischemic postconditioning with stutter CPR, inhaled sevoflurane, and P188. Pigs receiving the bundle of therapy showed improved hemodynamics during CPR, improved rates of return of spontaneous circulation, reduced need for epinephrine and defibrillation after return of spontaneous circulation, reduced troponin and measures of end-organ dysfunction, increased LVEF, and improved neurologic function and freedom from major adverse events. It is difficult to delineate the effect of each component of the bundle in terms of contribution to therapeutic outcome. In this context, it is appropriate that further study be initiated to determine the potential for P188 to prevent cardiac and neurological injury in the setting of cardiac arrest.

Overall, the use of block copolymer-based membrane stabilizers, and the available evidence for their use, is starkly contrasted between the STEMI population and the cardiac arrest population. Membrane stabilizers have a 2-decade history of benefit in controlled animal models of STEMI and inconsistent benefits in human studies of STEMI where duration of ischemia and reperfusion are less well-controlled. Current technologies that increase reperfusion success and provide a definite time of reperfusion, such as PCI, can be expected to improve the consistency of therapeutic benefit in humans. In addition, the opportunity to infuse P188 directly into the coronary artery provides the opportunity for immediate site of action delivery, while minimizing the potential effects on off-target organs such as the kidneys. In contrast to STEMI, evidence is presently lacking for evaluating the efficacy of membrane stabilizers in the setting of cardiac arrest. This population has a broad systemic injury and would then require systemic infusion. In addition, patients often receive bystander or first-responder CPR, which initiates inefficient reperfusion at least 5 to 10 min before initiation of an intravenous catheter, and may limit the benefits of P188 infusion. Alternatively, systemic injury provides a potential opportunity to reduce injury to other organs, including potentially the brain. The dysregulation of the blood-brain barrier and the importance of brain injury in the outcomes after cardiac arrest provide an important target for beneficial effects of membrane stabilizers.

THE COPOLYMER-MEMBRANE INTERFACE: TOWARD THE MECHANISM OF MUSCLE MEMBRANE STABILIZATION

It has been established that block copolymer molecular design impacts molecular interaction with phospholipid membranes and this, in turn, significantly affects muscle membrane stabilization efficacy (50–53,139). From a structure-function perspective, there is a significant opportunity to gain mechanistic insights with the long-range goal to improve and optimize membrane stabilization properties of block

copolymers (**Table 1**). To date, only a very limited subset of the vast possible chemical landscape of the copolymer superfamily has been investigated. There is growing evidence showing that membrane stabilization efficacy is highly dependent on the composition, size, and architecture of the block copolymer. For example, P188 was shown to be superior to a 70% PEO, 13-kDa PEO-PPO-PEO triblock copolymer, but inferior to 60% vinylpyrrolidone-40% vinyl acetate random copolymer VA64 in resealing cortical and hippocampal cells after controlled cortical impact (140). Conversely, the same 70% PEO, 13-kDa hydrophilic PEO-PPO-PEO triblock copolymer was superior to P188 in maintaining cell viability after transient photoacoustic permeabilization for molecular delivery (141). On the other hand, increased molecular weight, while maintaining 80% PEO content, improved dystrophic myofiber protection in culture, and also impacted its pharmacodynamics in dystrophic skeletal muscles in vivo (50,51).

Physicochemical models of cellular membranes have been developed to provide new mechanistic insights into copolymer-membrane interactions. Copolymer interactions with lipid membranes were first described via Langmuir trough experiments in which compression and expansion of simple model lipid monolayers were used to assess the surface pressures at which copolymer insertion occurred (98). P188 was found to only insert at surface pressure below that of an intact cell membrane and then was squeezed out above that threshold (97). This experiment directly correlates copolymer insertion with membrane lipid packing density. Additionally, the surface pressure of insertion depends on copolymer hydrophobicity. Copolymers with comparatively higher PPO/PEO ratios show higher squeeze-out pressures. Furthermore, hydrophobic copolymers insert at faster rates and can increase membrane permeability (142,143). These findings indicate an important relationship between the PPO/PEO ratio and molecular weight in determining copolymer-membrane interactions. These experimental studies are supported by recent in silico studies using molecular dynamics to simulate interactions of copolymers with a lipid bilayer under lateral mechanical stress (52). P188 insertion into stretched lipid bilayers significantly increases the lateral pressure at which membrane rupture occurs. In contrast, highly hydrophobic copolymers (e.g., PEO_7-PPO_{54}-PEO_7) decrease the lateral pressure required for membrane rupture. This is consistent with experimental findings showing that above a specific hydrophobicity threshold copolymer insertion leads to increased susceptibility to mechanical stress (52).

Copolymer-bilayer interactions have also been investigated using pulsed-field gradient nuclear magnetic resonance spectroscopy to measure the diffusion of block polymers in the presence and absence of phospholipid vesicles (144). This technique further confirmed that increased copolymer molecular weight and increased relative hydrophobicity caused increased binding and liposome coverage relative to smaller, more hydrophilic copolymers. This differential diffusivity enables quantification of the extent of copolymer interaction with the phospholipid membrane. Recent studies have shown higher interaction with increased copolymer molecular weight and hydrophobicity. For example, surface plasmon resonance (SPR) experiments have been used to measure binding kinetics for copolymers with supported phospholipid bilayers (139). These SPR experiments further quantify the extensive duration of P188-bilayer interaction and revealed the ability of the hydrophilic PEO block itself to engage phospholipid membranes at high concentrations. These findings support the hypothesis that the hydrophilic block of poloxamers is not merely a passive bystander to the hydrophobic block's interaction with the core of the phospholipid bilayer, but rather also contributes to membrane interaction. These results motivate further design and engineering of the copolymer hydrophilic block(s) for improved membrane interactions.

Block copolymers can be synthesized with distinct chemical blocks in a variety of sizes, compositions, and architectures (**Figure 4, Table 1**) (102). Recent papers have addressed the impact of block copolymer architecture on membrane stabilization (50–53,139,144). In particular, a PEO_{75}-PPO_{16} diblock, essentially half of P188 (**Figure 4**), was shown to provide protection to cultured myoblasts in response to hypotonic shock and isotonic recovery (51) Moreover, it was shown that addition of a single hydrophobic tert-butoxy moiety to the PPO end of the diblock enhances membrane stabilization efficacy both in vitro and in vivo in a muscular dystrophy mouse model (50). Molecular dynamics studies further showed that the tert-butoxy moiety acts like an anchor, keeping the PPO end of the diblock deep within the acyl chains of the bilayer, whereas absence of this moiety led to the PPO group preferring to interact with interfacial water (50). From these studies, an "anchor and chain" model of copolymer-membrane interface has emerged (50,51). Stronger interaction with the bilayer without actual percolation across the membrane could be envisioned to be beneficial to pharmacokinetics and pharmacodynamics properties in vivo. The benefit of such a hydrophobic anchor was further substantiated by the

lack of efficacy of diblocks with shortened hydrophobic PPO blocks. The ability to modulate performance with focused investigation of copolymer composition and architecture leads to substantial optimism for mechanistic insight and enhanced activity with broader systematic changes in copolymer design. Notably, such systematic evaluation is facilitated by the use of the diblock architecture, which is more synthetically efficient than the triblock architecture and affords the opportunity to manipulate end-group chemistry independent of the hydrophobic block characteristics.

Studies using dynamic light scattering and isothermal titration calorimetry suggest that copolymers that adsorb but do not insert into the intact bilayer affect the hydration shell at the bilayer-solvent interface (143). P188 and its mass equivalent PEO homopolymer PEG8000 were shown to prevent the diffusion of a free radical lipid peroxidation initiator into the lipid bilayer (100,145). In contrast, more hydrophobic copolymers such as P335 (PEO_{38}-PPO_{54}-PEO_{38}), P333 (PEO_{20}-PPO_{54}-PEO_{20}), and P181 (PEO_2-PPO_{30}-PEO_2) did not prevent free radical-induced lipid peroxidation. This result was confirmed by Cheng et al. (143) using dynamic light scattering, isothermal titration calorimetry, and small molecule-directed lipid peroxidation of liposomes. The PPO/PEO ratio was shown to be a key feature in effectively protecting intact liposomes from peroxidation. Copolymers that adsorb at the membrane surface without penetration into the bilayer core, such as P188 and PEG8000, presumably affect the initial hydration shells of the bilayer via interactions with water molecules at the interface. Presence of a "water shield" of hydrated copolymers would physically suppress the diffusion of the free radical lipid peroxidation initiator into the lipid bilayer, thereby preventing the initiation of lipid peroxidation. More hydrophobic poloxamers, for example P335 (PEO_{38}-PPO_{54}-PEO_{38}), P333 (PEO_{20}-PPO_{54}-PEO_{20}), and P181 (PEO_2-PPO_{30}-PEO_2) have significant heat of partitioning indicative of insertion into the liposomal membrane (143) and do not prevent lipid peroxidation (146).

More detailed structure-function analysis of copolymer block chemistry, length, and structural characteristics will be important. Future experiments are needed to expand our understanding of copolymer-membrane interactions. In addition to the use of physicochemical models to quantify the kinetics and extent of membrane interaction for different polymers and membrane compositions, it will be important to develop more extensive biophysical methods to determine the localization of polymers within the membrane and within organs/tissues to help determine engagement with target tissues and the pharmacokinetic profile of copolymer variants. The vast unexplored copolymer chemical landscape and novel structure-function insights to follow will help guide copolymer design for advancing copolymers in applications for I/R injury and STEMI.

FIGURE 4 Copolymer-Muscle Membrane Interface

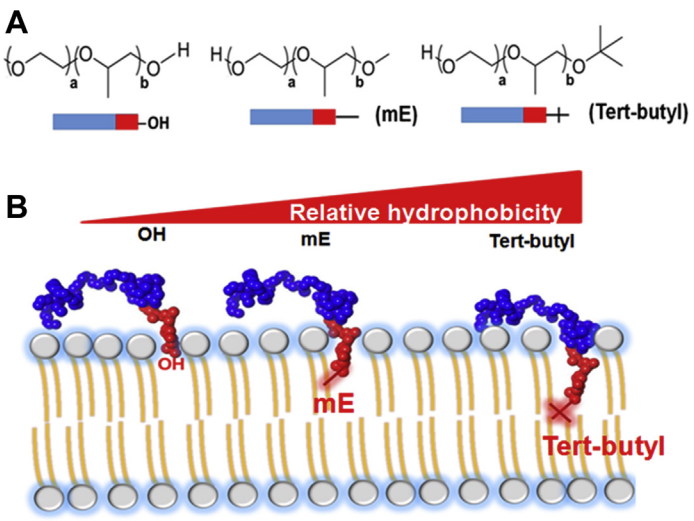

(A) Diblock copolymer structures with unique single chemical end groups where **blue** represents polyethylene oxide units and **red** represents polypropylene oxide units. **(B)** Conceptualization of anchor and chain working model, wherein the relatively more hydrophobic tert-butyl end group anchors the polypropylene oxide block more deeply in the phospholipid bilayer **(right).**

SUMMARY AND FUTURE OPPORTUNITIES

Block copolymers represent a class of organic materials with unique biological properties, including direct interfacing with biological membranes. In the context of a myriad of acquired and inherited heart diseases that involve, directly or indirectly, destabilization of the cardiac muscle membrane, block copolymers provide a unique potential therapeutic strategy to preserve myocyte and heart organ function.

By combining diverse expertise in chemistry, chemical engineering, muscle physiology, and cardiology, the design and implementation of synthetic block copolymers as novel membrane stabilizing agents has come to the forefront as a potential therapy for clinical disorders involving loss in muscle membrane integrity. Structure-function studies, guided by strategic molecular design, provide

insights into the fundamental basis of the copolymer-membrane interface. An anchor-and-chain working model has been proposed to account, mechanistically, for the copolymer-membrane interface that leads to membrane stabilization during stress, including I/R. Exciting opportunities lie ahead to decipher atomic to organ physiology levels of discovery in this research space.

There is a significant opportunity to advance mechanistic insights and enhanced performance into how copolymers function as membrane stabilizers. To date, structure-function and efficacy studies have been achieved with a comparatively limited evaluation, in terms of the vast chemical space of copolymers. The ability to strategically modulate copolymer-membrane function with detailed investigations of copolymer size, composition, and architecture leads to substantial optimism for mechanistic insights—and ultimately enhanced activity—with expansive and systematic changes in copolymer design. Notably, such systematic evaluation is facilitated by the use of the diblock architecture (**Figure 4**), which is more synthetically efficient than triblocks, and affords the opportunity to manipulate end-group chemistry independent of the hydrophobic block characteristics. Moreover, well-designed cellular and molecular assays enable efficient evaluation of copolymer designs and mechanisms.

The localization of P188 both within the membrane hydrophobic core and along the hydrophilic head groups is consistent with the anchor-and-chain mechanism, while hinting at more extensive interaction of the PEO component with the hydrophilic head groups than initially considered; notably, this is consistent with the aforementioned SPR results that indicate significant PEO-membrane interaction. Moreover, the discovery that P188 is distributed throughout the 1-palmitoyl-2-oleoyl-sn-glycero-3-phosphocholine bilayer alters the perception of the depth of interaction. More extensive studies with copolymer variants and altered membrane composition will further elucidate copolymer localization and the mechanism of interaction. These insights, in turn, will lead to deeper understanding of the mechanism of membrane stabilization.

Future directions in clinical models are essential to extend basic science discoveries toward clinical impact. Along with reperfusion studies in the context of STEMI, studies are warranted in CPR and organ transplantation. Having demonstrated the essential features of copolymer-based membrane stabilization, shown to be critically dependent upon time of delivery and precise location of delivery (**Figure 3**), there is now a significant opportunity to conduct STEMI patient trials with these key parameters clearly aligned in clinical protocols during PCI-based therapeutic trials.

ACKNOWLEDGMENTS This work was supported by grants from the NIH, MDA and AHA. The authors thank Cynthia DeKay for the schematics presented in **Figures 2 and 3**.

ADDRESS FOR CORRESPONDENCE: Dr. Joseph M. Metzger, Department of Integrative Biology and Physiology, University of Minnesota Medical School, 6-125 Jackson Hall, 321 Church Street Southeast, Minneapolis, Minnesota 55455. E-mail: metzgerj@umn.edu.

REFERENCES

1. Hausenloy DJ, Yellon DM. Preconditioning and postconditioning: united at reperfusion. Pharmacol Ther 2007;116:173–91.

2. Hausenloy DJ, Yellon DM. The therapeutic potential of ischemic conditioning: an update. Nat Rev Cardiol 2011;8:619–29.

3. Hausenloy DJ, Yellon DM. "Conditional Conditioning" in cardiac bypass surgery. Basic Res Cardiol 2012;107:1–6.

4. Hausenloy DJ, Boston-Griffiths E, Yellon DM. Cardioprotection during cardiac surgery. Cardiovasc Res 2012;94:253–65.

5. Yellon DM, Downey JM. Spotlight on preconditioning. Cardiovasc Res 2002;55:425–8.

6. Yellon DM, Downey JM. Preconditioning the myocardium: from cellular physiology to clinical cardiology. Physiol Rev 2003;83:1113–51.

7. Yellon DM, Hausenloy DJ. Realizing the clinical potential of ischemic preconditioning and postconditioning. Nat Clin Pract Cardiovasc Med 2005;2:568–75.

8. Yellon DM, Opie LH. Postconditioning for protection of the infarcting heart. Lancet 2006;367:456–8.

9. Yellon DM, Hausenloy DJ. Myocardial reperfusion injury. N Engl J Med 2007;357:1121–35.

10. Piper HM, Meuter K, Schafer C. Cellular mechanisms of ischemia-reperfusion injury. Ann Thorac Surg 2003;75:S644–8.

11. Piper HM, Balser C, Ladilov YV, et al. The role of Na+/H+ exchange in ischemia-reperfusion. Basic Res Cardiol 1996;91:191–202.

12. Piper HM, Garcia-Dorado D. Prime causes of rapid cardiomyocyte death during reperfusion. Ann Thorac Surg 1999;68:1913–9.

13. Piper HM, Garcia-Dorado D, Ovize M. A fresh look at reperfusion injury. Cardiovasc Res 1998;38:291–300.

14. Piper HM, Siegmund B, Ladilov YV, Schluter KD. Myocardial protection during reperfusion. Thorac Cardiovasc Surg 1996;44:15–9.

15. Piper HM, Abdallah Y, Schafer C. The first minutes of reperfusion: a window of opportunity for cardioprotection. Cardiovasc Res 2004;61:365–71.

16. Piper HM, Garcia-Dorado D. Cardiac protection takes off. Cardiovasc Res 2009;83:163–4.

17. Piper HM, Garcia-Dorado D. Reducing the impact of myocardial ischaemia/reperfusion injury. Cardiovasc Res 2012;94. 167–7.

18. Kung G, Konstantinidis K, Kitsis RN. Programmed necrosis, not apoptosis, in the heart. Circ Res 2011;108:1017–36.

19. Jennings RB. Historical perspective on the pathology of myocardial ischemia/reperfusion injury. Circ Res 2013;113:428–38.

20. Jennings RB, Steenbergen C Jr., Reimer KA. Myocardial ischemia and reperfusion. Monogr Pathol 1995;37:47–80.

21. Jennings RB, Reimer KA. The cell biology of acute myocardial ischemia. Annu Rev Med 1991; 42:225–46.

22. Jennings RB, Murry CE, Steenbergen C Jr., Reimer KA. Development of cell injury in sustained acute ischemia. Circulation 1990;82:II2–12.

23. Jennings RB, Murry C, Reimer KA. Myocardial effects of brief periods of ischemia followed by reperfusion. Adv Cardiol 1990;37:7–31.

24. Jennings RB, Reimer KA. Pathobiology of acute myocardial ischemia. Hosp Pract (Off Ed) 1989;24:89–101. 105.

25. Sage MD, Jennings RB. Myocyte swelling and plasmalemmal integrity during early experimental myocardial ischemia in vivo. Scanning Microsc 1988;2:477–84.

26. Steenbergen C, Hill ML, Jennings RB. Cytoskeletal damage during myocardial ischemia: changes in vinculin immunofluorescence staining during total in vitro ischemia in canine heart. Circ Res 1987;60:478–86.

27. Jennings RB, Reimer KA, Steenbergen C. Myocardial ischemia revisited. The osmolar load, membrane damage, and reperfusion. J Mol Cell Cardiol 1986;18:769–80.

28. Steenbergen C, Hill ML, Jennings RB. Volume regulation and plasma membrane injury in aerobic, anaerobic, and ischemic myocardium in vitro. Effects of osmotic cell swelling on plasma membrane integrity. Circ Res 1985;57:864–75.

29. Reimer KA, Jennings RB, Tatum AH. Pathobiology of acute myocardial ischemia: metabolic, functional and ultrastructural studies. Am J Cardiol 1983;52:72A–81A.

30. Mirzaei M, Truswell AS, Taylor R, Leeder SR. Coronary heart disease epidemics: not all the same. Heart 2009;95:740–6.

31. Ganote CE, Seabra-Gomes R, Nayler WG, Jennings RB. Irreversible myocardial injury in anoxic perfused rat hearts. Am J Pathol 1975;80: 419–50.

32. Wijns W, Naber CK. Reperfusion delay in patients with high-risk ST-segment elevation myocardial infarction: every minute counts, much more than suspected. Eur Heart J 2018;39:1075–7.

33. Yannopoulos D, Bartos JA, Raveendran G, et al. Coronary arterial disease in patients with out-of-hospital refractory ventricular fibrillation cardiac arrest. J Am Coll Cardiol 2017;70:1109–17.

34. Yannopoulos D, Bartos JA, Martin C, et al. Minnesota Resuscitation Consortium's Advanced Perfusion and Reperfusion Cardiac Life Support Strategy for Out-of-Hospital Refractory Ventricular Fibrillation. J Am Heart Assoc 2016;5. pii: e003732.

35. Frank A, Bonney M, Bonney S, Weitzel L, Koeppen M, Eckle T. Myocardial ischemia reperfusion injury: from basic science to clinical bedside. Semin Cardiothorac Vasc Anesth 2012;16: 123–32.

36. Garcia-Dorado D, Barba I, Inserte J. Twenty-five years of preconditioning: are we ready for ischaemia? From coronary occlusion to systems biology and back. Cardiovasc Res 2011;91:378–81.

37. Schwartz LL, Kloner RA, Arai AE, et al. New horizons in cardioprotection: recommendations from the 2010 National Heart, Lung, and Blood Institute Workshop. Circulation 2011;124:1172–9.

38. Garcia-Dorado D, Ruiz-Meana M, Piper HM. Lethal reperfusion injury in acute myocardial infarction: facts and unresolved issues. Cardiovasc Res 2009;83:165–8.

39. Garcia-Dorado D. Myocardial reperfusion injury: a new view. Cardiovasc Res 2004;61:363–4.

40. Jennings RB, Reimer KA, Hill ML, Mayer SE. Total ischemia in dog hearts, in vitro. 1. Comparison of high energy phosphate production, utilization, and depletion, and of adenine nucleotide catabolism in total ischemia in vitro vs. severe ischemia in vivo. Circ Res 1981;49: 892–900.

41. Whelan RS, Kaplinskiy V, Kitsis RN. Cell death in the pathogenesis of heart disease: mechanisms and significance. Annu Rev Physiol 2010;72:19–44.

42. Martindale JJ, Metzger JM. Uncoupling of increased cellular oxidative stress and myocardial ischemia reperfusion injury by directed sarcolemma stabilization. J Mol Cell Cardiol 2014;67: 26–37.

43. Wong SW, Yao Y, Hong Y, et al. Preventive effects of poloxamer 188 on muscle cell damage mechanics under oxidative stress. Ann Biomed Eng 2017;45:1083–92.

44. See Hoe LE, May LT, Headrick JP, Peart JN. Sarcolemmal dependence of cardiac protection and stress-resistance: roles in aged or diseased hearts. Br J Pharmacol 2016;173:2966–91.

45. Padanilam JT, Bischof JC, Lee RC, et al. Effectiveness of poloxamer 188 in arresting calcein leakage from thermally damaged isolated skeletal muscle cells. Ann N Y Acad Sci 1994;720: 111–23.

46. Lee RC, River LP, Pan FS, Ji L, Wollmann RL. Surfactant-induced sealing of electropermeabilized skeletal muscle membranes in vivo. Proc Natl Acad Sci U S A 1992;89:4524–8.

47. Lee RC, Canaday DJ, Hammer SM. Transient and stable ionic permeabilization of isolated skeletal muscle cells after electrical shock. J Burn Care Rehabil 1993;14:528–40.

48. Yasuda S, Townsend D, Michele DE, Favre EG, Day SM, Metzger JM. Dystrophic heart failure blocked by membrane sealant poloxamer. Nature 2005;436:1025–9.

49. Townsend D, Turner I, Yasuda S, et al. Chronic administration of membrane sealant prevents severe cardiac injury and ventricular dilatation in dystrophic dogs. J Clin Invest 2010;120:1140–50.

50. Houang EM, Haman KJ, Kim M, et al. Chemical end group modified diblock copolymers elucidate anchor and chain mechanism of membrane stabilization. Mol Pharm 2017;14:2333–9.

51. Kim M, Haman KJ, Houang EM, et al. PEO-PPO diblock copolymers protect myoblasts from hypoosmotic stress in vitro dependent on copolymer size, composition, and architecture. Biomacromolecules 2017;18:2090–101.

52. Houang EM, Bates FS, Sham YY, Metzger JM. All-atom molecular dynamics-based analysis of membrane-stabilizing copolymer interactions with lipid bilayers probed under constant surface tensions. J Phys Chem B 2017;121:10657–64.

53. Houang EM, Haman KJ, Filareto A, et al. Membrane-stabilizing copolymers confer marked protection to dystrophic skeletal muscle. Mol Ther Methods Clin Dev 2015;2:15042.

54. Benjamin EJ, Blaha MJ, Chiuve SE, et al. Heart disease and stroke statistics–2017 Update: a report from the American Heart Association. Circulation 2017;135:e146–603.

55. Murray CJ, Vos T, Lozano R, et al. Disability-adjusted life years (DALYs) for 291 diseases and injuries in 21 regions, 1990–2010: a systematic analysis for the Global Burden of Disease Study 2010. Lancet 2012;380:2197–223.

56. Lozano R, Naghavi M, Foreman K, et al. Global and regional mortality from 235 causes of death for 20 age groups in 1990 and 2010: a systematic analysis for the Global Burden of Disease Study 2010. Lancet 2012;380:2095–128.

57. Helis E, Augustincic L, Steiner S, Chen L, Turton P, Fodor JG. Time trends in cardiovascular and all-cause mortality in the "old" and "new" European Union countries. Eur J Cardiovasc Prev Rehabil 2011;18:347–59.

58. Mathers CD, Boerma T, Ma FD. Global and regional causes of death. Br Med Bull 2009;92: 7–32.

59. Lopez AD, Murray CC. The global burden of disease, 1990–2020. Nat Med 1998;4:1241–3.

60. Fordyce CB, Gersh BJ, Stone GW, Granger CB. Novel therapeutics in myocardial infarction: targeting microvascular dysfunction and reperfusion injury. Trends Pharmacol Sci 2015;36:605–16.

61. McNeil PL, Steinhardt RA. Plasma membrane disruption: repair, prevention, adaptation. Annu Rev Cell Dev Biol 2003;19:697–731.

62. Miyake K, McNeil PL. Mechanical injury and repair of cells. Crit Care Med 2003;31:S496–501.

63. McNeil PL, Vogel SS, Miyake K, Terasaki M. Patching plasma membrane disruptions with cytoplasmic membrane. J Cell Sci 2000;113 Pt 11: 1891–902.

64. McNeil PL, Steinhardt RA. Loss, restoration, and maintenance of plasma membrane integrity. J Cell Biol 1997;137:1–4.

65. Doherty KR, McNally EM. Repairing the tears: dysferlin in muscle membrane repair. Trends Mol Med 2003;9:327–30.

66. Bansal D, Campbell KP. Dysferlin and the plasma membrane repair in muscular dystrophy. Trends Cell Biol 2004;14:206–13.

67. Cai C, Weisleder N, Ko JK, et al. Membrane repair defects in muscular dystrophy are linked to altered interaction between MG53, caveolin-3, and dysferlin. J Biol Chem 2009;284:15894–902.

68. Stenina-Adognravi O, Plow EF. Thrombospondin-4 in tissue remodeling. Matrix Biol 2019;75-76:300–13.

69. Vanhoutte D, Schips TG, Kwong JQ, et al. Thrombospondin expression in myofibers stabilizes muscle membranes. Elife 2016;5. pii:e17589.

70. Lynch JM, Maillet M, Vanhoutte D, et al. A thrombospondin-dependent pathway for a protective ER stress response. Cell 2012;149:1257–68.

71. Brody MJ, Schips TG, Vanhoutte D, et al. Dissection of thrombospondin-4 domains involved in intracellular adaptive endoplasmic reticulum stress-responsive signaling. Mol Cell Biol 2016;36:2–12.

72. Frolova EG, Sopko N, Blech L, et al. Thrombospondin-4 regulates fibrosis and remodeling of the myocardium in response to pressure overload. FASEB J 2012;26:2363–73.

73. Cingolani OH, Kirk JA, Seo K, et al. Thrombospondin-4 is required for stretch-mediated contractility augmentation in cardiac muscle. Circ Res 2011;109:1410–4.

74. McNeil PL, Kirchhausen T. An emergency response team for membrane repair. Nat Rev Mol Cell Biol 2005;6:499–505.

75. Bansal D, Miyake K, Vogel SS, et al. Defective membrane repair in dysferlin-deficient muscular dystrophy. Nature 2003;423:168–72.

76. Blazek AD, Paleo BJ, Weisleder N. Plasma membrane repair: a central process for maintaining cellular homeostasis. Physiology (Bethesda) 2015;30:438–48.

77. Cai C, Masumiya H, Weisleder N, et al. MG53 nucleates assembly of cell membrane repair machinery. Nat Cell Biol 2009;11:56–64.

78. Kabanov AV, Batrakova EV, Alakhov VY. Pluronic block copolymers as novel polymer therapeutics for drug and gene delivery. J Control Release 2002;82:189–212.

79. Guler N, Abro S, Emanuele M, Iqbal O, Hoppensteadt D, Fareed J. The protective effect of poloxamer-188 on platelet functions. Clin Appl Thromb Hemost 2017;23:987–91.

80. Emanuele RM. FLOCOR: a new anti-adhesive, rheologic agent. Expert Opin Investig Drugs 1998;7:1193–200.

81. Adams-Graves P, Kedar A, Koshy M, et al. RheothRx (poloxamer 188) injection for the acute painful episode of sickle cell disease: a pilot study. Blood 1997;90:2041–6.

82. Go AS, Mozaffarian D, Roger VL, et al. Heart disease and stroke statistics—2014 update: a report from the american heart association. Circulation 2014;129:e28–292.

83. Hausenloy DJ, Yellon DM. Myocardial ischemia-reperfusion injury: a neglected therapeutic target. J Clin Invest 2013;123:92–100.

84. Gershlick AH, Banning AP, Myat A, Verheugt FW, Gersh BJ. Reperfusion therapy for STEMI: is there still a role for thrombolysis in the era of primary percutaneous coronary intervention? Lancet 2013;382:624–32.

85. O'Gara PT, Kushner FG, Ascheim DD, et al. 2013 ACCF/AHA guideline for the management of ST-elevation myocardial infarction: executive summary: a report of the American College of Cardiology Foundation/American Heart Association Task Force on Practice Guidelines: developed in collaboration with the American College of Emergency Physicians and Society for Cardiovascular Angiography and Interventions. J Am Coll Cardiol 2013;62:485–510.

86. Braunwald E. The rise of cardiovascular medicine. Eur Heart J 2012;33:838–45.

87. McMurray JJ. Clinical practice. Systolic heart failure. N Engl J Med 2010;362:228–38.

88. Aronow WS. Heart disease and aging. Med Clin North Am 2006;90:849–62.

89. Kass RS, Lindegger N, Hagen B, Lederer WJ. Another calcium paradox in heart failure. J Mol Cell Cardiol 2008;45:28–31.

90. Yannopoulos D, Halperin HR. During CPR, push hard and fast and please do not stop! Resuscitation 2011;82:1475–6.

91. Yannopoulos D, Aufderheide T. Acute management of sudden cardiac death in adults based upon the new CPR guidelines. Europace 2007;9:2–9.

92. Rickenbacher P, Pfisterer M, Burkard T, et al. Why and how do elderly patients with heart failure die? Insights from the TIME-CHF study. Eur J Heart Fail 2012;14:1218–29.

93. Kontos MC, Rennyson SL, Chen AY, Alexander KP, Peterson ED, Roe MT. The association of myocardial infarction process of care measures and in-hospital mortality: a report from the NCDR(R). Am Heart J 2014;168:766–75.

94. Doost HA, Moloi S, Chandrasekhar J, Farshid A. Mortality pattern and cause of death in a long-term follow-up of patients with STEMI treated with primary PCI. Open Heart 2016;3:e000405.

95. Frohlich GM, Meier P, White SK, Yellon DM, Hausenloy DJ. Myocardial reperfusion injury: looking beyond primary PCI. Eur Heart J 2013;34:1714–22.

96. Armstrong PW, Gershlick AH, Van de Werf F. Fibrinolysis or primary PCI in myocardial infarction. N Engl J Med 2013;369:280–1.

97. Maskarinec SA, Hannig J, Lee RC, Lee KY. Direct observation of poloxamer 188 insertion into lipid monolayers. Biophys J 2002;82:1453–9.

98. Frey SL, Zhang D, Carignano MA, Szleifer I, Lee KY. Effects of block copolymer's architecture on its association with lipid membranes: experiments and simulations. J Chem Phys 2007;127:114904.

99. Wu G, Lee KY. Interaction of poloxamers with liposomes: an isothermal titration calorimetry study. J Phys Chem B 2009;113:15522–31.

100. Wu G, Majewski J, Ege C, Kjaer K, Weygand MJ, Lee KY. Interaction between lipid monolayers and poloxamer 188: an x-ray reflectivity and diffraction study. Biophys J 2005;89:3159–73.

101. Wang JY, Chin J, Marks JD, Lee KY. Effects of PEO-PPO-PEO triblock copolymers on phospholipid membrane integrity under osmotic stress. Langmuir 2010;26:12953–61.

102. Bates FS, Hillmyer MA, Lodge TP, Bates CM, Delaney KT, Fredrickson GH. Multiblock polymers: panacea or Pandora's box? Science 2012;336:434–40.

103. Orringer EP, Casella JF, Ataga KI, et al. Purified poloxamer 188 for treatment of acute vaso-occlusive crisis of sickle cell disease: a randomized controlled trial. JAMA 2001;286:2099–106.

104. Ballas SK, Files B, Luchtman-Jones L, et al. Safety of purified poloxamer 188 in sickle cell disease: phase I study of a non-ionic surfactant in the management of acute chest syndrome. Hemoglobin 2004;28:85–102.

105. Toth K, Bogar L, Juricskay I, et al. The effect of RheothRx injection on the hemorheological parameters in patients with acute myocardial infarction. Clin Hemorheol Microcirc 1997;17:117–25.

106. Chareonthaitawee P, Gibbons RJ, Roberts RS, Christian TF, Burns R, Yusuf S. The impact of time to thrombolytic treatment on outcome in patients with acute myocardial infarction. For the CORE investigators (Collaborative Organisation for RheothRx Evaluation). Heart 2000;84:142–8.

107. Schaer GL, Spaccavento LJ, Browne KF, et al. Beneficial effects of RheothRx injection in patients receiving thrombolytic therapy for acute myocardial infarction. Results of a randomized, double-blind, placebo-controlled trial. Circulation 1996;94:298–307.

108. Kelly RF, Hursey TL, Patel RB, Parrillo JE, Schaer GL. Effect of poloxamer 188 on collateral blood flow, myocardial infarct size, and left ventricular function in a canine model of prolonged (3-hour) coronary occlusion and reperfusion. J Thromb Thrombolysis 1998;5:239–47.

109. O'Keefe JH, Grines CL, DeWood MA, et al. Poloxamer-188 as an adjunct to primary percutaneous transluminal coronary angioplasty for acute myocardial infarction. Am J Cardiol 1996;78:747–50.

110. Schaer GL, Hursey TL, Abrahams SL, et al. Reduction in reperfusion-induced myocardial necrosis in dogs by RheothRx injection (poloxamer 188 N.F.), a hemorheological agent that alters neutrophil function. Circulation 1994;90:2964–75.

111. Grindel JM, Jaworski T, Piraner O, Emanuele RM, Balasubramanian M. Distribution, metabolism, and excretion of a novel surface-active agent, purified poloxamer 188, in rats, dogs, and humans. J Pharm Sci 2002;91:1936–47.

112. Grindel JM, Jaworski T, Emanuele RM, Culbreth P. Pharmacokinetics of a novel surface-active agent, purified poloxamer 188, in rat, rabbit, dog and man. Biopharm Drug Dispos 2002;23:87–103.

113. Emanuele M, Balasubramaniam B. Differential effects of commercial-grade and purified poloxamer 188 on renal function. Drugs R D 2014;14:73–83.

114. Greenebaum B, Blossfield K, Hannig J, et al. Poloxamer 188 prevents acute necrosis of adult skeletal muscle cells following high-dose irradiation. Burns 2004;30:539–47.

115. Collins JM, Despa F, Lee RC. Structural and functional recovery of electropermeabilized skeletal muscle in-vivo after treatment with surfactant poloxamer 188. Biochim Biophys Acta 2007;1768:1238–46.

116. Coatney GA, Abraham AC, Fischenich KM, Button KD, Haut RC, Haut Donahue TL. Efficacy of P188 on lapine meniscus preservation following blunt trauma. J Mech Behav Biomed Mater 2015;47:57–64.

117. Riehm JJ, Wang L, Ghadge G, et al. Poloxamer 188 decreases membrane toxicity of mutant SOD1 and ameliorates pathology observed in SOD1 mouse model for ALS. Neurobiol Dis 2018;115:115–26.

118. Serbest G, Horwitz J, Jost M, Barbee K. Mechanisms of cell death and neuroprotection by poloxamer 188 after mechanical trauma. FASEB J 2006;20:308–10.

119. Bao H, Yang X, Zhuang Y, et al. The effects of poloxamer 188 on the autophagy induced by traumatic brain injury. Neurosci Lett 2016;634:7–12.

120. Shelat PB, Plant LD, Wang JC, Lee E, Marks JD. The membrane-active tri-block copolymer pluronic F-68 profoundly rescues rat hippocampal neurons from oxygen-glucose deprivation-induced death through early inhibition of apoptosis. J Neurosci 2013;33:12287–99.

121. Townsend D, Yasuda S, Metzger J. Cardiomyopathy of Duchenne muscular dystrophy: pathogenesis and prospect of membrane sealants as a new therapeutic approach. Expert Rev Cardiovasc Ther 2007;5:99–109.

122. Markham BE, Kernodle S, Nemzek J, Wilkinson JE, Sigler R. Chronic dosing with membrane sealant poloxamer 188 NF improves respiratory dysfunction in dystrophic Mdx and Mdx/utrophin-/- Mice. PLoS One 2015;10:e0134832.

123. Borgens RB, Bohnert D, Duerstock B, Spomar D, Lee RC. Subcutaneous tri-block copolymer produces recovery from spinal cord injury. J Neurosci Res 2004;76:141–54.

124. Adams JE, Owens G, Mann G, Headrick JR, Munoz A, Scott HW Jr. Experimental evaluation of pluronic F68 (a non-ionic detergent) as a method of diminishing systemic fat emboli resulting from prolonged cardiopulmonary bypass. Surg Forum 1960;10:585–9.

125. Miyauchi Y, Inoue T, Paton BC. Adjunctive use of a surface-active agent in extracorporeal circulation. Circulation 1966;33:171–7.

126. Hymes AC, Safavian MH, Gunther T. The influence of an industrial surfactant Pluronic F-68, in the treatment of hemorrhagic shock. J Surg Res 1971;11:191–7.

127. Hymes AC, Robb HJ, Margulis RR. Influence of an industrial surfactant (pluronic F-68) on human amniotic fluid embolism. Am J Obstete Gynecol 1970;107:1217–22.

128. Hymes AC, Beck K. A comparison of pluronic F-68, low molecular weight dextran, mannitol, and saline as priming agents in the heart-lung apparatus. II. The in vitro influence on oxygen consumption of certain fluids used as priming agents in a heart-lung bypass apparatus. J Thorac Cardiovasc Surg 1968;56:23–7.

129. Hymes AC, Safavian MH, Arbulu A, Baute P. A comparison of pluronic F-68, low molecular weight dextran, mannitol, and saline as priming agents in the heart-lung apparatus. I. Pluronic F-68: first use as a plasma substitute. J Thorac Cardiovasc Surg 1968;56:16–22.

130. Colbassani HJ, Barrow DL, Sweeney KM, Bakay RA, Check IJ, Hunter RL. Modification of acute focal ischemia in rabbits by poloxamer 188. Stroke 1989;20:1241–6.

131. Gu JH, Ge JB, Li M, Xu HD, Wu F, Qin ZH. Poloxamer 188 protects neurons against ischemia/reperfusion injury through preserving integrity of cell membranes and blood brain barrier. PLoS One 2013;8:e61641.

132. Marks JD, Pan CY, Bushell T, Cromie W, Lee RC. Amphiphilic, tri-block copolymers provide potent membrane-targeted neuroprotection. FASEB J 2001;15:1107–9.

133. Wang T, Chen X, Wang Z, et al. Poloxamer-188 can attenuate blood-brain barrier damage to exert neuroprotective effect in mice intracerebral hemorrhage model. J Mol Neurosci 2015;55:240–50.

134. Justicz AG, Farnsworth WV, Soberman MS, et al. Reduction of myocardial infarct size by poloxamer 188 and mannitol in a canine model. Am Heart J 1991;122:671–80.

135. Carr ME Jr., Powers PL, Jones MR. Effects of poloxamer 188 on the assembly, structure and dissolution of fibrin clots. Thromb Haemost 1991;66:565–8.

136. Effects of RheothRx on mortality, morbidity, left ventricular function, and infarct size in patients with acute myocardial infarction. Collaborative Organization for RheothRx Evaluation (CORE). Circulation 1997;96:192–201.

137. Bartos JA, Matsuura TR, Tsangaris A, et al. Intracoronary poloxamer 188 prevents reperfusion injury in a porcine model of ST-segment elevation myocardial infarction. J Am Coll Cardiol Basic Trans Science 2016;1:224–34.

138. Bartos JA, Matsuura TR, Sarraf M, et al. Bundled postconditioning therapies improve hemodynamics and neurologic recovery after 17 min of untreated cardiac arrest. Resuscitation 2015;87:7–13.

139. Kim M, Vala M, Ertsgaard CT, et al. Surface plasmon resonance study of the binding of PEO-PPO-PEO triblock copolymer and PEO homopolymer to supported lipid bilayers. Langmuir 2018;34:6703–12.

140. Mbye LH, Keles E, Tao L, et al. Kollidon VA64, a membrane-resealing agent, reduces histopathology and improves functional outcome after controlled cortical impact in mice. J Cereb Blood Flow Metab 2012;32:515–24.

141. Sengupta A, Dwivedi N, Kelly SC, Tucci L, Thadhani NN, Prausnitz MR. Poloxamer surfactant preserves cell viability during photoacoustic delivery of molecules into cells. Biotechnol Bioeng 2015;112:405–15.

142. Cheng CY, Wang JY, Kausik R, Lee KY, Han S. An ultrasensitive tool exploiting hydration dynamics to decipher weak lipid membrane-polymer interactions. J Magn Reson 2012;215:115–9.

143. Cheng CY, Wang JY, Kausik R, Lee KY, Han S. Nature of interactions between PEO-PPO-PEO triblock copolymers and lipid membranes: (II) role of hydration dynamics revealed by dynamic nuclear polarization. Biomacromolecules 2012;13:2624–33.

144. Zhang W, Haman KJ, Metzger JM, Hackel BJ, Bates FS, Lodge TP. Quantifying binding of ethylene oxide-propylene oxide block copolymers with lipid bilayers. Langmuir 2017;33:12624–34.

145. Wu G, Majewski J, Ege C, Kjaer K, Weygand MJ, Lee KY. Lipid corralling and poloxamer squeeze-out in membranes. Phys Rev Lett 2004;93:028101.

146. Wang JY, Marks J, Lee KY. Nature of interactions between PEO-PPO-PEO triblock copolymers and lipid membranes: (I) effect of polymer hydrophobicity on its ability to protect liposomes from peroxidation. Biomacromolecules 2012;13:2616–23.

KEY WORDS copolymer, heart, ischemia, reperfusion

JACC: BASIC TO TRANSLATIONAL SCIENCE VOL. 4, NO. 2, 2019
© 2019 THE AUTHOR. PUBLISHED BY ELSEVIER ON BEHALF OF THE AMERICAN COLLEGE OF CARDIOLOGY FOUNDATION. THIS IS AN OPEN ACCESS ARTICLE UNDER THE CC BY-NC-ND LICENSE (http://creativecommons.org/licenses/by-nc-nd/4.0/).

COMMENTARY

JACC: Basic to Translational Science 2018 Young Author Award Winner

Douglas L. Mann, MD, *Editor-in-Chief JACC: Basic to Translational Science*

On March 16, 2018, during the *JACC* Journals' reception, *JACC: Basic to Translational Science* was proud to recognize and congratulate the following recipient of the *JACC: Basic to Translational Science* 2017 Young Author Award.

Haiyang Tang, PhD

Paper: Pathogenic Role of mTORC1 and mTORC2 in Pulmonary Hypertension

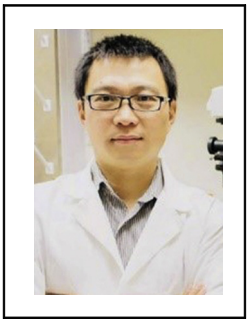

Dr. Haiyang Tang currently is a research assistant professor working in the Division of Translational and Regenerative Medicine, Department of Medicine, The University of Arizona. Dr. Tang's research interests include pathogenic mechanisms of idiopathic and hypoxic pulmonary hypertension, cellular and molecular mechanisms of hypoxic pulmonary vasoconstriction and pulmonary vascular pathophysiology. He has diligently and successfully developed animal models of pulmonary hypertension, as well as successfully established state-of-the-art approaches for the study of pulmonary hypertension, including right ventricular pressure measurements using the Millar system and hypoxic pulmonary vasoconstriction measurements by isolated/ventilated and perfuse lung system.

Mentor: Jason J.-X. Yuan, MD, PhD

Dr. Jason Yuan is a professor of medicine and physiology at the University of Arizona. He is the chief of the Division of Translational and Regenerative Medicine and leading the development of impactful and sustainable translational health strategies at the University of Arizona. Dr. Yuan has previously held appointments as professor of medicine and pharmacology, vice chair for scholarly activities for the Department of Medicine, director of the Pulmonary Hypertension Translational Research Program in the Institute for Personalized Respiratory Medicine, and director of the Program in Pulmonary Vascular Disease and Right Heart Function in the Center for Cardiovascular Research at the University of Illinois at Chicago. He also has held faculty positions in the Department of Medicine, School of Medicine, University of California, San Diego, and the Department of Physiology, University of Maryland School of Medicine, Baltimore.

ISSN 2452-302X https://doi.org/10.1016/j.jacbts.2019.01.007

JACC: BASIC TO TRANSLATIONAL SCIENCE VOL. 4, NO. 2, 2019
© 2019 THE AUTHOR. PUBLISHED BY ELSEVIER ON BEHALF OF THE AMERICAN COLLEGE OF CARDIOLOGY FOUNDATION. THIS IS AN OPEN ACCESS ARTICLE UNDER THE CC BY-NC-ND LICENSE (http://creativecommons.org/licenses/by-nc-nd/4.0/).

EDITOR'S PAGE

Scott Gottlieb's Resignation as FDA Commissioner Is a Loss for Translational Medicine

Douglas L. Mann, MD, *Editor-in-Chief: JACC: Basic to Translational Science*

On March 5, 2019, Dr. Scott Gottlieb announced that he was resigning as the commissioner of the U.S. Food and Drug Administration (FDA). Although many people were initially skeptical that Dr. Gottlieb would be effective leader at the FDA, given his prior antiregulatory comments as well as his ties to major pharmaceutical firms, there is a growing consensus that he has been an effective champion for important public health care policies, including the opioid epidemic, drug pricing, and teen vaping. Moreover, as will be discussed below, he has also been a strong advocate for the development of new drug and device therapies, which will have important implications for cardiovascular translational medicine.

Under Dr. Gottlieb's leadership, the FDA's Center for Drug Evaluation and Research (CDER) approved a record high of 62 new therapeutic drugs in 2018, which exceeded the prior record of 53 approvals in 1996 (1). Dr. Gottlieb also announced that the FDA was planning to create a 52-person Office of Drug Evaluation and Science that would have its own director and 3 separate divisions, including a Division of Biomedical Information and Safety Analytics, charged with use of information technology in clinical trial decision making; a Division of Clinical Outcomes Assessment, responsible for patient-focused efficacy and patient safety endpoints; and a Division of Research and Biomarker Development that monitors genetic scans and new biomarkers (2,3). Dr. Gottlieb indicated that "The office is just one component of a very broad reorganization of the Office of New Drugs," and "This is going to be the new paradigm and it's going to be how we modernize the drug review process" (3).

Dr. Gottlieb also modernized the review process for new regenerative medicine products, including novel cell and gene therapies. On November 16, 2017, the FDA expanded upon the regenerative medicine provisions in the 21st Century Cures Act by releasing 4 guidance documents that were designed to expedite the review and approval processes for regenerative medicine therapies. Although the review process would still require performing clinical trials, the guidance documents provided increased clarity with respect to the pathways for developing new therapies in the field of regenerative medicine, while still ensuring the safety of these new products (4). In the same news briefing, Dr. Gottlieb also took aim at unproven stem cell therapies: "Alongside all the promise, we've also seen products marketed that are dangerous and have harmed people….With the policy framework the FDA is announcing today, we're adopting a risk-based and science-based approach that builds upon existing regulations to support innovative product development while clarifying the FDA's authorities and enforcement priorities. This will protect patients from products that pose potential significant risks, while accelerating access to safe and effective new therapies" (4).

Finally, Dr. Gottlieb pushed for a new regulatory framework to evaluate the safety and efficacy of the proliferation of novel diagnostic tests that are being offered to personalize medical care. He indicated that the FDA would endorse "a more modern, flexible approach to promote the extraordinary innovation that's already well underway in this space, while ensuring patient protections." He also stated that he hoped that there would be "a compelling new paradigm for the cancer research community," and "the FDA would seek to establish collaborative communities of scientists, clinicians, test developers, and patients to help support the agency's decision making" (5).

ISSN 2452-302X https://doi.org/10.1016/j.jacbts.2019.03.001

JACC: BASIC TO TRANSLATIONAL SCIENCE VOL. 4, NO. 2, 2019
APRIL 2019:289–90

I suspect that there will be many who believe that Dr. Gottlieb could have done more during his tenure as the FDA commissioner. However, as the Editor-in-Chief of a journal that seeks to accelerate the translation of new scientific discoveries into new therapies that improve clinical outcomes for patients afflicted with or at risk for cardiovascular disease, I would like to join with the many other health care organizations and patient advocacy groups who have praised Dr. Gottlieb for his efforts to use innovation as way to improve the public health. As always, we welcome comments and suggestions from investigators in academia and industry, patients, societies, and all of the governmental regulatory agencies about your thoughts about Dr. Gottlieb's tenure at the FDA, either through social media (*#JACC:BTS*) or by e-mail (jaccbts@acc.org).

ADDRESS FOR CORRESPONDENCE: Dr. Douglas L. Mann, Editor-in-Chief, *JACC: Basic to Translational Science*, American College of Cardiology, Heart House, 2400 N Street NW, Washington, DC 20037. E-mail: JACC@acc.org.

REFERENCES

1. Mullard A. 2018 FDA drug approvals. Nat Rev Drug Discov 2019;18:85-9.

2. Mullard A. FDA plans Office of Drug Evaluation Science. Nat Rev Drug Discov 2019;18:164.

3. Rosenberg J. Gottlieb touts launch of new FDA office to improve drug review process. American Journal of Managed Care 2019. Available at: https://www.ajmc.com/newsroom/gottlieb-touts-launch-of-new-fda-office-to-improve-drug-review-process. Accessed March 7, 2019.

4. U.S. Food and Drug Administration. FDA announces comprehensive regenerative medicine policy framework. FDA News Release 2017. Available at: https://www.fda.gov/newsevents/newsroom/pressannouncements/ucm585345.htm. Accessed March 7, 2019.

5. Gottlieb S. Blueprint for breakthroughs - charting the course for precision medicine. FDA News 2018. Available at: https://www.fda.gov/NewsEvents/Speeches/ucm620375.htm. Accessed March 7, 2019.